• U C •

FCTUC FACULDADE DE CIÊNCIAS
E TECNOLOGIA
UNIVERSIDADE DE COIMBRA
DEPARTAMENTO DE
ENGENHARIA CIVIL

COASTAL SEDIMENT DYNAMICS UNDER ASYMMETRIC WAVES AND CURRENTS: MEASUREMENTS AND SIMULATIONS

DINÂMICA SEDIMENTAR LITORAL SOB A ACÇÃO DE ONDAS ASSIMÉTRICAS E CORRENTES: MEDIÇÃO E MODELAÇÃO

Tiago André Martins de Azevedo Abreu

A dissertation presented to the Faculty of Sciences and Technology of the University of Coimbra for the degree of Doctor in Civil Engineering.

Supervisors:

Francisco Eduardo da Ponte Sancho (Assistant Professor, University of Coimbra);

Paulo Manuel Cruz Alves da Silva (Assistant Professor, University of Aveiro).

POPH PROGRAMA OPERACIONAL POTENCIAL HUMANO

QREN QUADRO DE REFERÊNCIA ESTRATÉGICO NACIONAL PORTUGAL 2007.2013

UNIÃO EUROPEIA
Fundo Social Europeu

ABSTRACT

As waves travel and shoal towards a beach, their surface elevation becomes peaky (sharp crests) and asymmetric relative to the vertical. Within a wave period, the corresponding orbital velocity near the bottom shows a similar (time) variation, presenting both velocity and acceleration skewnesses. These local nonlinearities are inextricably linked to sediment transport, but the processes involved are not well understood. This research intends to increase the understanding of cross-shore sediment transport processes under combined nonlinear waves plus currents, focusing on the importance of the velocity and acceleration skewnesses in sheet flow layer dynamics. For that purpose, new experimental and modelling work are presented in this thesis.

Firstly, new experiments under sheet flow conditions conducted in an oscillating water tunnel (OWT) are reported, enabling to study the effects of flow acceleration on instantaneous velocities and sediment concentrations and fluxes. The measured net transport rates show that (i) the acceleration skewness in an oscillatory flow is responsible for a net sediment transport in the direction of the highest (onshore) acceleration; (ii) the net transport in the presence of an opposing current is negative, against the direction of the highest acceleration, and reduces with an increase in flow acceleration; and (iii) the velocity skewness increases the values of the net onshore transport rates. This trend is also confirmed through detailed velocity and concentration measurements in the sheet-flow layer. Two mechanisms play a key role in the sediment transport of acceleration skewness flows, namely, skewed bed shear stresses and unsteady phase-lag effects between the velocity and sediment concentration: they both drive a positive net transport in the direction of the largest acceleration.

Afterwards, a new simple analytical formulation that reproduces a skewed, nonlinear, near-bed wave orbital velocity is presented. Two input parameters are related to the velocity and acceleration skewnesses. The equation is compared with other models and validated against field and laboratory experiments. The results reveal that it can simulate accurately a wide range of nonlinear wave shapes. The new expression is used to derive a new bed shear stress estimator accounting for these nonlinear effects. When tested against bed shear stress measurements of the OWT experiment, a good agreement with the momentum-integral method estimate is obtained. The parameterisation is incorporated in a quasi-steady bed load formula and is tested against the measured net transport rates in several OWT experiments. When compared with other sediment transport formulations the new model accurately reproduces transport rates under nonlinear, nonbreaking waves with and without an opposing current.

Finally, the same bedload shear stress predictor is applied to predict the bed changes in the surf region in front of a collapsing coastal dune, in a laboratory experiment.

RESUMO

À medida que uma onda se propaga para a costa e a profundidade diminui, a superfície livre evolui, tornando-se pontiaguda sobre a crista da onda, mais achatada na cava e relativamente íngreme na face frontal da crista, previamente à rebentação. No período da onda, a velocidade orbital junto ao fundo exibe variações temporais semelhantes, apresentando assimetrias na velocidade e na aceleração. Estas não linearidades estão inextrincavelmente ligadas ao transporte sedimentar, mas subsiste um desconhecimento dos processos envolvidos. Este trabalho de investigação pretende contribuir para um melhor entendimento dos processos de transporte sedimentar na direcção transversal à costa, sob a acção combinada de ondas assimétricas e correntes, evidenciando a importância das assimetrias da velocidade e da aceleração na dinâmica da camada de sedimentos em regime de leito plano superior ("sheet flow"). Com esse propósito, esta tese apresenta novos trabalhos experimentais e de modelação.

Inicialmente, apresentam-se novas experiências realizadas em túnel de ondas em condições (configuração de fundo) de leito plano superior, que permitem avaliar o efeito da aceleração em escoamentos oscilatórios, no campo de velocidade orbital e na concentração e fluxos de sedimentos. As taxas de transporte sedimentar calculadas experimentalmente revelam que (i) a assimetria da aceleração de um escoamento oscilatório é responsável por um transporte efectivo no sentido da maior aceleração (para sotamar); (ii) o transporte é negativo na presença de uma corrente colinear oposta ao do sentido da maior aceleração, mas é minorado com um aumento da aceleração; (iii) a assimetria da velocidade aumenta os valores da taxa de transporte sedimentar em direcção à linha de costa. Esta tendência é igualmente confirmada através de medições detalhadas de velocidades e concentrações dentro da camada de "sheet flow". Os resultados evidenciam dois mecanismos que desempenham um papel primordial no transporte sedimentar de escoamentos oscilatórios na presença de acelerações assimétricas, nomeadamente, a assimetria das tensões de atrito junto ao fundo e efeitos associados ao desfasamento entre velocidades e concentrações de sedimentos: ambos conduzem a um transporte positivo na direcção da maior aceleração.

Posteriormente, apresenta-se uma expressão analítica eficaz na reprodução de velocidades orbitais junto ao fundo sob a acção de ondas não lineares. Dois parâmetros intervenientes nesta expressão estão relacionados com as assimetrias da velocidade e aceleração do escoamento. A equação é comparada com outros modelos e validada com resultados experimentais de trabalhos de campo e laboratoriais. Mostra-se que a expressão simula adequadamente um vasto número de formas de ondas assimétricas. A nova expressão é utilizada na obtenção de um estimador de tensões de atrito que entra com essas formas não lineares. Quando comparada com estimativas de tensões de atrito obtidas através do método "momentum-integral", em experiências em túnel de onda, obtém-se uma boa concordância. A parametrização é incorporada num modelo de transporte por arrastamento quase-estacionário e o seu desempenho é avaliado para medições de transporte obtidos em diversos túneis de

ondas. Confrontada com outras formulações, o novo modelo revela-se promissor na estimativa do transporte sedimentar sob ondas não rebentadas assimétricas e que possam coexistir com correntes opostas.

Finalmente, o mesmo modelo de transporte é aplicado para prever mudanças morfológicas, medidas em laboratório, na região de espalho ("surf") em frente a uma duna colapsante.

ACKNOWLEDGEMENTS

To all who have accompanied me during my PhD journey, family, friends and colleagues that, through their friendship, understanding and presence, contributed to the achievement of this work, here I express my sincere gratitude. Nonetheless, I have to present special thanks:

- to my supervisors Professors Francisco Sancho and Paulo Silva for providing all the necessary resources for the development of the experimental work, for encouraging me to participate in important international conferences, for challenging me with interesting and rewarding projects, for sharing their experience and knowledge, for their important contributions on some of the experimental work, for their example of commitment to achieve the best results, for their patience and friendship, for the final review of the text and, most important, for the total willingness to support, motivate and guide me throughout my academic career. It has been a great privilege to work with both of you;

- to the Portuguese Science Foundation (FCT) that supported me through a PhD grant (SFRH/BD/41827/2007). Furthermore, both TRANSKEW and BOB experimental works were supported by the European Community's Sixth Framework Programme through the grant to the budget of the Integrated Infrastructure Initiative HYDRALAB III within the Transnational Access Activities, Contract no. 022441. This financial support is greatly acknowledged;

- to the leaders of the projects TRANSKEW and BOB, namely, Professors Paulo Silva and Roberto Tomasicchio, and to the rest of the participants involved in the experiments. It was a pleasure and a privilege to work with you;

- to Doctor Hervé Michallet and Professor André Temperville, from *Laboratoire des Ecoulements Géophysiques et Industriels* (France), for receiving me at their group in Grenoble during several times, for their hospitality, for the generous insights they gave me in the processing of the data collected at Delft, for several comments, discussions and suggestions contributing to improvements of this thesis;

- to Professor Tom O'Donoghue and Doctor Dominic van der A, from the University of Aberdeen (UK), for their hospitality during my short stay in Aberdeen, for sharing with me several interesting ideas and publications, and for their helpful comments and stimulating discussions;

- to Professor Gerben Ruessink, from Utrecht University (The Netherlands), for the fruitful opinions, constructive suggestions and research contributions;

- to Professor Peter Nielsen, from The University of Queensland (Australia), for giving me suggestions to improve my work and for his invaluable teachings, particularly, on the velocity defect function;

- to Professor Mário Franca for introducing me into the wavelet world, sharing with me several interesting ideas that revealed to be very useful for this work;

- to my work colleagues and friends Carla Macedo, Célia Rodrigues, Elsa Carvalho, Filipe Magalhães, Gilberto Rouxinol, João Vieira, Lino Borges, Luís Vasconcelos, Nuno Simões, Patrícia Sousa, Paulo Costeira, Maria Bezerra, Renata Gomes, Teresa Lopes (and many more), partners of enjoyable times, lunches, dinners and extra-work activities, for their fellowship which helped me keeping up a good spirit essential to balance the moments of intense work;

- à minha família e, em particular, aos meus pais, aos meus irmãos Pedro e Cátia, aos meus cunhados Carolina e Mário e à minha sobrinha Lia pelo apoio e afecto, que alimentam o meu entusiasmo, e pelo encorajamento nas minhas decisões.

CONTENTS

LIST OF FIGURES

LIST OF TABLES

NOTATION

Roman symbols

a horizontal acceleration (m/s^2)

a_1 Fourier coefficient of the first harmonic (-)

a_c acceleration coefficient (-)

a_{cr} critical value of a_{spike} (m/s^2)

a_i fitting coefficient (i=1, 2 and 3 for Eq.s (4.17), (4.18) and (4.19), accordingly) (-)

a_{max} maximum value of a (m/s^2)

a_{min} minimum value of a (m/s^2)

a_n Fourier coefficient of nth harmonic (-)

a_{spike} parameter in Eq. (4.55) (m/s^2)

A water particle semi-excursion (m)

A_m approximation of the signal c at the scale m (kg/m^3)

A_{rms} root-mean-square value of A (m)

As_u velocity asymmetry (-)

b_1 Fourier coefficient of the first harmonic (-)

b_i fitting coefficient (i=1, 2 and 3 for Eq.s (4.17), (4.18) and (4.19), accordingly) (-)

b_n Fourier coefficient of nth harmonic (-)

c sediment concentration (kg/m^3)

$\tilde{c}$ oscillatory sediment concentration (kg/m^3)

$\overline{c}$ mean value of the sediment concentration (kg/m^3)

$\hat{c}$ bin-averaged sediment concentration (kg/m^3)

c_0 undisturbed bed concentration (kg/m^3)

c_b reference concentration (kg/m^3)

c_i fitting coefficient (i=1, 2 and 3 for Eq.s (4.17), (4.18) and (4.19), accordingly) (-)

$\hat{c}_w$ continuous wavelet transform of c (kg/m^3)

C correction factor applied to the measured net transport rates in the wave-current flows (-)

C_f correction factor proposed by Tanaka and Thu (1994) (-)

C_v volumetric sediment concentration (-)

D_1 complex velocity defect function (-)

d diameter of a spherical sediment particle (m)

d_{50} median grain size (m)

d_e erosion depth (m)

d_{eE} erosion depth quantified from the concentration measurements above d_e (m)

d_i fitting coefficient (i=1, 2 and 3 for Eq.s (4.17), (4.18) and (4.19), accordingly) (-)

d_t top of the sheet flow layer thickness (m)

D_* dimensionless particle size parameter (-)

e_i fitting coefficient (i=1, 2 and 3 for Eq.s (4.17), (4.18) and (4.19), accordingly) (-)

e_{rms} root-mean-square absolute errors (same unit as the base quantity)

f non-dimensional factor that allows the velocity amplitude to be equal to U_w (-)

$f_{2.5}$ roughness friction coefficient using a roughness equal to 2.5 d_{50} (-)

f_w wave friction factor (-)

f_{cw} wave-current friction factor (-)

F_B buoyancy force (N)

F_D drag force (N)

F_G gravity force (N)

F_L lift force (N)

F_P pressure force (N)

F_S seepage force (N)

g gravitational acceleration (m/s^2)

$G_{l/r}$ total (dry) weight of the sand collected in the trap (kg)

h water depth (m)

h_0 offshore water depth (m)

H wave height (m)

H_{rms} root-mean-square wave height (m)

k wave number ($k = 2\pi/L$) (m^{-1}); turbulent kinetic energy (m^{2}s^{-2})

k_b represents all constants in the Bailard (1981) equation associated to bed load transport (m^{-1}s^2)

k_s bed roughness (m)

k_{ss} represents all constants in the Bailard (1981) equation associated to suspended load transport (m^{-2}s^3)

K_a constant in Eq. (4.55) (ms)

l position parameter (-)

L wave length (m)

L_0 offshore wave length ($L_0 = \left(g/2\pi\right)T^2$) (m)

m scale parameter (-)

M number of experimental conditions (-)

n $r = 2n/\left(1+n^2\right)$ (-)

N number of runs for each experimental condition (-)

N_c number of flow cycles (-)

N_p number of data points in a time series (-)

p pressure (Pa)

p_1 parameter derived from an analysis of the primary harmonic (-)

q_b volumetric bed load transport (m^2/s)

q_{ba} additional term representing acceleration effects on bed load transport (m^2/s)

q_{on} positive (onshore) transport rate in the sheet flow layer (kg/m/s)

q_{off} negative (offshore) transport rate in the sheet flow layer (kg/m/s)

q_s net transport rate (kg/m/s)
q_{sc} corrected net transport rate (kg/m/s)
q_{sm} measured net transport rate (kg/m/s)
q_{ss} volumetric suspended load transport (m^2/s)
$q_{s,left}$ left-computed net transport rates along the tunnel – Eq. (3.3) (kg/m/s)
$q_{s,right}$ right-computed net transport rates along the tunnel – Eq. (3.4) (kg/m/s)
$q_{s,x}$ net transport rate at x coordinate (kg/m/s)
r nonlinearity measure ($-1 < r < 1$) (-)
r_1 Fourier magnitude coefficient of the first harmonic (-)
r_∞ free-stream value of r_1 (-)
R velocity skewness coefficient (-)
Re Reynolds number (-)
Re_* grain Reynolds number (-)
s ratio between sediment and water densities (-)
S acceleration parameter (m/s^2)
S_m detail of the signal c at the scale m (kg/m^3)
S_q skill (-)
t time (s)
t_0 reference time (s)
T flow period (s)
T_0 dimensionless instant used in Elfrink et al.'s (2006) model (-)
T_1 dimensionless instant used in Elfrink et al.'s (2006) model (-)
T_2 dimensionless instant used in Elfrink et al.'s (2006) model (-)
T_c time duration of the positive half cycle of the near bed velocity (s)
T_p wave peak period (s)
T_{pc} time interval measured from the zero up-cross point to wave crest (s)
T_t time duration of the negative half cycle of the near bed velocity (s)
u horizontal flow velocity (m/s)
$\tilde{u}$ oscillatory horizontal flow velocity (m/s)
$\overline{u}$ mean value of the horizontal flow velocity (m/s)
$\hat{u}$ phase-average of the horizontal flow velocity (m/s)
u_c equivalent sinusoidal velocity amplitude at the crest (m/s)
u_d defect velocity of u (m/s)
u_{max} maximum value of u (m/s)
u_{min} minimum value of u (m/s)
u_s velocity of the sediment particles (m/s)
u_t equivalent sinusoidal velocity amplitude at the trough (m/s)
u_θ sediment mobilization velocity (m/s)
u_∞ free-stream horizontal velocity (m/s)
u_* shear velocity (m/s)

U_0 mean current velocity (m/s)

$U_{0,max}$ maximum velocity in the middle of the tunnel (m/s)

U_c velocity amplitude at crest used in Elfrink et al.'s (2006) model (m/s)

U_t velocity amplitude at trough used in Elfrink et al.'s (2006) model (m/s)

U_r Ursell number ($Ur = (H/L)\times(L/h)^3$) (-)

U_{rms} root-mean-square value of the oscillatory velocity (m/s)

U_w oscillatory velocity amplitude (m/s)

U_{zc} velocity amplitude used in Elfrink et al.'s (2006) model (m/s)

x spatial coordinate (m)

w vertical flow velocity (m/s)

w_s sediment fall velocity (m/s)

W width of the tunnel test section (m)

z vertical coordinate (m)

z_0 roughness length scale (m)

z_1 velocity defect function decay length scale (m)

z_a reference height ($z_a = 2d_{50}$) (m)

Greek symbols

α wave skewness parameter (-)

α_{β_s} parameter in Eq. (4.63) (-)

β acceleration skewness coefficient (-)

β_{cw} velocity-leaning index (-)

β_s local bed slope (-)

β_t $\beta_t = \tan^{-1}(\cos\beta_s \tan\beta_s)$ (-)

β_τ bed shear-stress skewness (-)

γ constant in Eq. (4.57) (-)

Γ parameter in Eq. (4.57) (-)

δ boundary layer thickness (m)

δ_t time shift used in the cross correlations technique (s)

δ_s sheet flow layer thickness (m)

Δt time lag (s)

Δt_{run} duration of each run (s)

$\Delta V_{l/r}$ total eroded volume (m^3)

Δx distance between ADV velocimeters (m)

Δx_{CCM} distance between the two CCM sensors (m)

Δz translation of the vertical axis (m)

ε dissipation rate of turbulent energy (m^2/s^3)

ε_0 sand porosity (-)

ε_s sediment diffusivity (m^2/s)

η elevation of the water surface (m)

θ Shields parameter (-)

θ_{max} maximum Shields parameter (-)

θ_{cr} critical Shields parameter (-)

θ_1 Shields parameter in Eq.s (4.59) and (4.60) (-)

$\theta_{cr,slope}$ critical Shields parameter that accounts for the bed slope (-)

Θ_1 coefficient used in Isobe and Horikawa's (1982) model (-)

Θ_2 coefficient used in Isobe and Horikawa's (1982) model (-)

κ von Kármán's constant (-)

λ scale parameter (-)

λ_0 base dilatation (-)

$\mu_{3,a}$ acceleration skewness (-)

$\mu_{3,u}$ velocity skewness (-)

$\mu_{3,\tau}$ bed shear stress skewness (-)

μ_T coefficient used in Isobe and Horikawa's (1982) model (-)

μ_u coefficient used in Isobe and Horikawa's (1982) model (-)

ν kinematic viscosity (m^2/s)

ν_T eddy viscosity (m^2/s)

ξ surf similarity parameter (-)

ρ water density (kg/m^3)

ρ_m density of the sediment/fluid mixture (kg/m^3)

ρ_s sediment density (kg/m^3)

σ_g sand geometric standard deviation (m)

σ_q relative standard deviation of the net transport rates (-)

σ_T Prandtl-Schmidt number (-)

σ_u standard deviation of u (m/s)

σ_τ standard deviation of τ ($kg/m/s^2$)

υ constant in Eq. (4.57)

τ bed shear stress ($kg/m/s^2$)

$\tau_{y=0}$ bed shear stress in the middle of the tunnel ($kg/m/s^2$)

$\bar{\tau}$ average value of τ ($kg/m/s^2$)

τ_{max} maximum value of τ ($kg/m/s^2$)

τ_{min} minimum value of τ ($kg/m/s^2$)

φ phase difference between τ and u_∞ (°)

φ_s phase difference between τ and u_∞ for the sinusoidal case (°)

ϕ waveform parameter ($-\pi/2 \le \phi \le \pi/2$) (rad)

ϕ' waveform parameter ($\phi' = \phi + \pi/2$) (rad)

ϕ_1 Fourier phase coefficient of the first harmonic (º)

ϕ_f horizontal sediment flux (kg/m^2/s)

$\hat{\phi}_f$ bin-averaged sediment flux (kg/m^2/s)

ϕ_d depth-integrated sediment flux (kg/m/s)

ϕ_i internal angle of friction of bed material (º)

ϕ_m angle of moving friction (º)

ϕ_s angle of static friction (º)

ϕ_t time-averaged sediment flux (kg/m^2/s)

$\tilde{\phi}_t$ time-averaged oscillatory sediment flux (kg/m^2/s)

$\overline{\phi}_t$ current-related sediment flux (kg/m^2/s)

ϕ_u phase difference between u_∞ and u (º)

ϕ_∞ free-stream value of ϕ_1 (º)

Φ non-dimensional transport rate (-)

Ψ mobility number (-)

Ψ_{max} mobility number based on $u = u_{max}$ (-)

ψ wavelet function (-)

$\overline{\psi}$ conjugate of the wavelet function (-)

ω angular frequency ($\omega = 2\pi/T$) (rad/s)

ω_1, ω_{cr} parameters in Eq.s (4.59) and (4.60) (-)

Ω_i , Ω_i' parameters in Eq. (4.58) (-)

$\mathcal{H}$ Hilbert transform (-)

ς position parameter (-)

Acronyms

ABS Acoustic Backscatter Sensor

ADV Acoustic Doppler Velocimeter

ADVP Acoustic Doppler Velocity meter Profiler

AOFT Oscillatory Flow Tunnel

AWG Acoustic Wave Gauges

BOB Beach Overwashing and Breaching

CCM Conductivity Concentration Meter

CIEM *Canal d'Investigació i Experimentació Marítima*

EMF ElectroMagnetic Flow meter

LBP Laser Bed Profiler

LIM Maritime Engineering Laboratory

LOWT Large Oscillating Water Tunnel

OPCON	Optical Concentration Meter
RWG	Resistence Wave Gauges
SFL	Sheet Flow Layer
TRANSKEW	Sand TRANsport induced by SKEWed waves and currents
TSS	Transverse Suction System
UPC	Catalonia University of Technology
UVP	Ultrasonic Velocity Profiler
VAT	Visual Accumulation Tube

Chapter 1

INTRODUCTION

"Adamastor" painted by Jorge Colaço in 1933, in *Centro Cultural Rodrigues de Faria*, Forjães (Portugal)

1. INTRODUCTION

1.1 Research Context

Studies on sediment transport are of paramount importance in marine coastal environments. Nowadays, one verifies, even to a world scale, coastal management problems associated to littoral morphological changes. The transformations of the coastal zones might compromise, in medium and long-terms, the stability of the shoreline. In particular, the retreat of the shoreline due to beach erosion poses many problems to the coastal communities. However, due to the complexity of the processes involved, there are no global engineering solutions to tackle it and, sometimes, the need to maintain or minimize the changes of a particular stretch of coastline requires large investments.

These morphological changes can be induced by natural or human causes. For example, modifications in the wave field and mean sea level caused by global climate changes (e.g., Andrade et al., 2006), or the regulation of rivers through the construction of dams, reducing the supply of sediments to coastal zones, cause an imbalance in the transport of sediments, both across and alongshore, affecting the shape of the shoreline. Figure 1.1 presents an overview over sediment sources and losses to the coastal zone. Whenever the equilibrium between sources and losses is broken, the beach morphology changes.

To tackle the problems associated to erosion, some engineering projects involve the construction of coastal defence structures (groins, seawalls...). However, it is recognised that these solutions solve the problem locally, but do not avoid the erosion at neighbouring places. Moreover, the erosion is even intensified downdrift of these places, particularly for groins.

The processes that intervene in the mechanisms of sediment transport are complex (e.g., forces at mobile beds, sediment-flow interactions) and the evolution of the shoreline and coastal geomorphology can also be affected spatially as well as temporally (on a daily, weekly, seasonal, decadal, ... and millennium time-scales). Due to the central importance of this issue, and often motivated by undesirable morphologic changes, the scientific community has been engaged in improving our understanding and modelling capabilities of beach morphodynamics. Though several progresses have been made in the past decades, this issue remains a challenge to researchers.

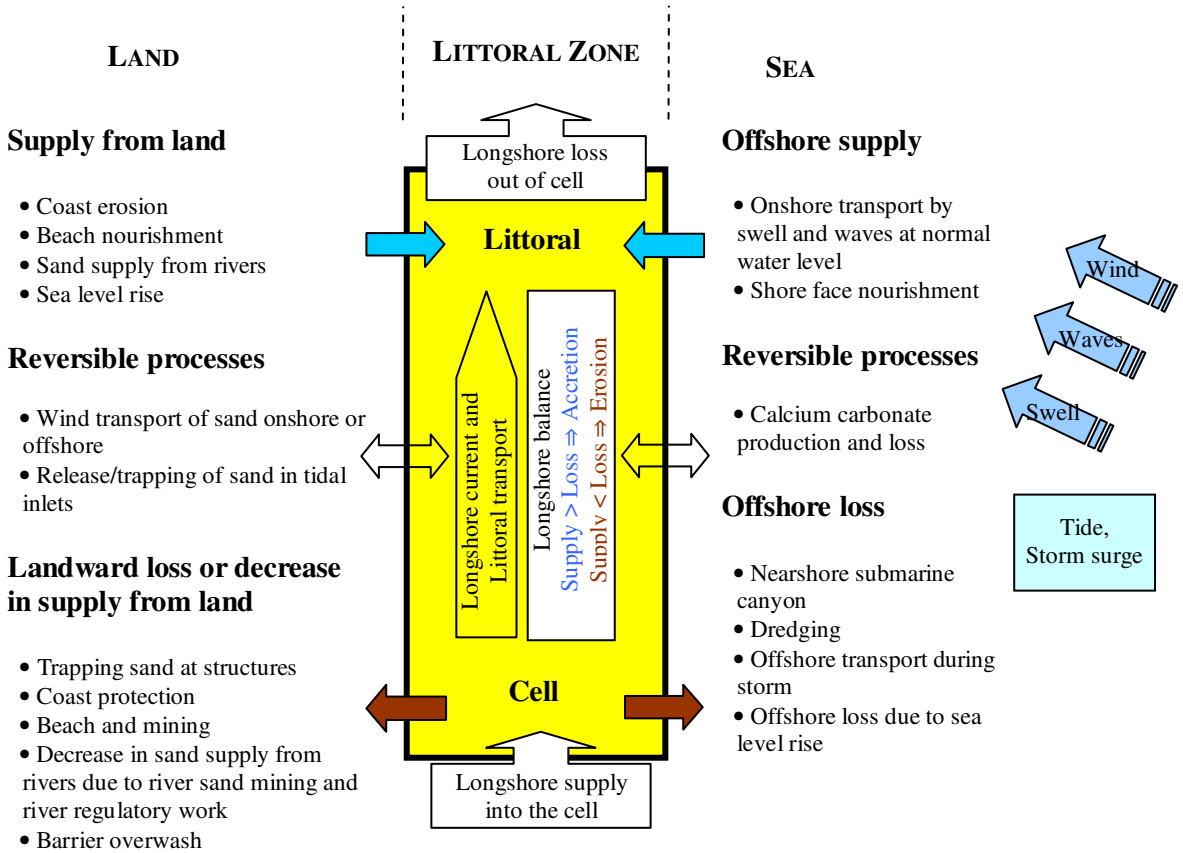

Figure 1.1 – Overview of sediment sources and losses to the coastal zone (adapted from Coastal Wiki, 2011).

1.2 Motivation and objectives of the thesis

Sediment transport is mainly caused by the action of waves or currents or, a combination of both. For increasingly shallow waters, these hydrodynamic processes induce motions on the seabed and if the grains are exposed to large enough velocities they start to move. The transport may occur as either bedload, if the grains are in more or less continuous contact with the bed (by rolling, sliding and saltating), or as suspended load if the sediments particles are entrained into the water column and they move as suspended particles, not having continuous contact with the bed during the transport. Particularly, under high energy conditions, and thus high shear stresses at the bed, the sediments are mainly transported within a thin bottom boundary layer of few centimeters or less near the seabed, leading to larger transport rates compared to those found at lower shear stresses (Pugh and Wilson, 1999). This thin layer is characterised by high sand concentrations and is usually termed as sheet flow.

The interplay between sediment transport and water motion is also affected by nonlinear interactions owing to propagating waves. As ocean surface waves approach the coast and propagate into shallower water they transform in appearance, becoming asymmetric and skewed (Elgar and Guza, 1985;

Doering and Bowen, 1995). While in deep waters the free-surface and wave orbital velocity correspond closely to those of linear waves, i.e., they can be accurately described by a sinusoidal function, in the shoaling zone they become more peaked at the crest and flatter at the trough. Hence, the orbital velocity presents skewness. Also, in the inner surf zone and swash, past wave breaking, a rapid change in the wave velocity during the steep wave front gives rise to large fluid accelerations, while, at the sloping rear face of the wave, the corresponding flow accelerations are much smaller. This asymmetry of the wave leads to acceleration-skewed orbital motions. In nature, waves possess both velocity and acceleration skewnesses (e.g., Doering and Bowen, 1995; Elfrink et al., 2006). These local nonlinearities are reflected on the near-bed oscillatory flow and are inextricably linked to sediment transport.

In this work the effects of the wave hydrodynamics interacting with the sea floor are analysed in the direction of wave propagation, resulting into a two-dimensional analysis (2D). Since, often, the incoming waves become almost perpendicular to the nearshore bathymetry, this study can be considered to contribute to the cross-shore transport problem.

The knowledge and modelling of sand transport induced by waves and currents still has considerable shortcomings. Two large knowledge gaps in sand transport processes are: i) sand transport induced by skewed waves and ii) sand transport due to combined influence of waves and currents.

The prediction of morphological changes and sediment budgets in the coastal zone may be obtained from numerical simulation of hydrodynamic and sediment transport processes. Battjes (2006) distinguished two different approaches to investigate the modelling of the processes determining the coupled evolution of sea bed topography and the wave-current field. In conformity, the predictive models can follow a holistic approach where, on a typical large-scale coastal modelling system, the dominant process variables are identified and their effects on sediment transport processes and the overlying hydrodynamics are generally parameterized (e.g., Reniers et al., 2004a; Warner et al., 2008). By merely including essential details of important processes, these parametric models have shown a high degree of success in long-term predictions of profile evolution (e.g., Masselink, 2004; Plant et al., 2004; Mariño-Tapia et al., 2007a). The second approach considers smaller scales and includes as much of the physics of the system as possible. In this so called reductionist (bottom-up) approach the processes that occur on the grain-scale near the bed are resolved for each individual wave cycle and integrated through time to obtain results at larger scales. For example, by accounting for accelerations of wave-orbital velocities in the formulation of sediment transport due to (nearly) breaking waves, Hoefel and Elgar (2003) managed to reproduce the cross-shore migration of a shore-parallel bar over a 45-day period, by using the measured fluid velocities as input. Although, these process-based models

should, theoretically, provide most realistic results in long-term predictions, in practice, this is not utterly true. There are several intervenient processes that are not yet well understood and, consequently, are not accounted in the models. Hence, long-term predictions accumulate errors, resulting in an inability to produce accurate results.

The poor understanding of the processes is partially due to the complexity of the energetic nearshore and to the scarcity of available comprehensive and high quality datasets about detailed sediment transport mechanisms. Also, measurements of the complex sediment-flow interactions and forces still pose challenging technical difficulties. To validate theories and improve our understanding and modelling capabilities, one needs small-scale measurements concerning sediment transport. Measurements can be performed in the field or in laboratory facilities, but the benefits of controlled laboratory experiments is evident when the objective is to obtain an accurate response of the sediments to the dominant selected forces. In these physical models a simplified version of the reality is obtained and the forcing conditions are usually imposed within certain ranges due to restrictions of the facilities. Thus, they provide a good understanding of the underlying mechanisms and a lot of research effort has been made recently, offering insights into the physical processes involved, contributing significantly to our understanding of small-scale sediment transport processes (e.g., Ribberink and Al-Salem, 1995; McLean et al., 2001; Dohmen-Janssen and Hanes, 2002, 2005; O'Donoghue and Wright, 2004a; van der A et al., 2010, Ruessink et al., 2011).

A hindrance to the construction of these datasets is associated with financial costs of these experiments and to the time required to prepare, perform and analyse them. The European Community recognizes the importance of such studies and through the "Integrated Infrastructure Initiative HYDRALAB III" allows groups of researchers from across Europe to use unique and costly experimental facilities. Part of this thesis presents results of the experimental project TRANSKEW (sand TRANsport induced by SKEWed waves and currents) carried out in the Large Oscillating Water Tunnel of Deltares (formerly, WL|Delft Hydraulics), supported by the European Community's Sixth Framework Programme. The general aim of this project was to obtain a new reliable dataset of detailed flow and sand transport processes under flat-bed/sheet flow conditions that allow analysing the effects of wave nonlinearities and of a net current on the sediment transport processes (e.g., Silva et al., 2008, 2011; Ruessink et al., 2011).

Taking into account the needs identified previously, this thesis aims the achievement of the following main objectives:

- increase the understanding of the cross-shore sediment transport processes under combined nonlinear waves plus currents, particularly, the importance of the velocity and acceleration skewness in the sheet flow layer dynamics;

- present a simple analytical formulation that reproduces a skewed, nonlinear near-bed wave orbital velocity and derive a new bed shear stress estimator, accounting for those effects;

- develop an improved sediment transport model for sheet flow conditions under currents and waves of arbitrary shape.

These objectives will be tackled by analysing in detail the physical model data and by using suitable analytical mathematical models. The transport rates obtained during the TRANSKEW experiment will allow to study the importance of velocity and acceleration skewness effects on net transport rates in the presence or absence of collinear currents under sheet flow conditions. The detailed measurements of velocity and sediment concentrations collected for selected test conditions will be processed in order to see how the sediment fluxes and mobilization of sediments from the bed vary during the wave period. Such analysis provides insights about the nature of the wave boundary layer hydrodynamics and will be used for the validation and development of existing models.

1.3 Organization of the thesis

This thesis is organized in six chapters. A description of the contents of each chapter is given in the following paragraphs.

Chapter 1 – Introduction – introduces the thesis with a contextualization of the developed research, followed by the presentation of the motivations and main objectives of this work and by the present description of the organization of the text.

Chapter 2 – Fundaments – is essentially dedicated to describe the physical fundaments associated with the structure of the flow and with the sediment dynamics in the boundary layer generated by a wave or by the combination of waves and currents.

Chapter 3 – Physical Modelling – presents the experimental project TRANSKEW performed in the Large Oscillating Water Tunnel. The chapter starts with a description of the experimental set-up and the measuring program. It is followed by the methodologies applied to process the measured data. At the end, results of net sediment transport rates, detailed measurements of velocity and concentrations,

sediment fluxes within the sheet flow layer and bed shear stresses are shown. The analysis is focused on the influence of the effect of velocity and acceleration skewness and of a net current in mobile beds.

Chapter 4 – Analytical Modelling – provides some advances in analytical modelling including the effects of nonlinear oscillatory motion. It starts by presenting a new analytical function able to reproduce wave shapes for any combination of velocity and acceleration skewness. Then, a comparison is performed between existing bed shear stress parameterisations that account for non-linear waves. A new estimator is developed, aiming to improve the previous formulations. The chapter ends with the application of different sediment transport models to predict the TRANSKEW measured net transport rates, including a new formula based on the above new bed shear stress predictor. This sediment transport formulation is tested and extended to other experimental data.

Chapter 5 – Application to a large-scale dune erosion experiment – presents a set of experiments on dune erosion processes conducted at the large-scale wave flume CIEM (*Canal d'Investigació i Experimentació Marítima*) at the Maritime Engineering Laboratory (LIM) from the Catalonia University of Technology (UPC) in Barcelona. Attending the hydrodynamics obtained in front of the collapsing dunes, the applicability of the formulations developed in the previous chapter is assessed.

Chapter 6 – Conclusions and future research – summarizes the conclusions of this thesis and points out some future research topics.

Chapter 2

FUNDAMENTS

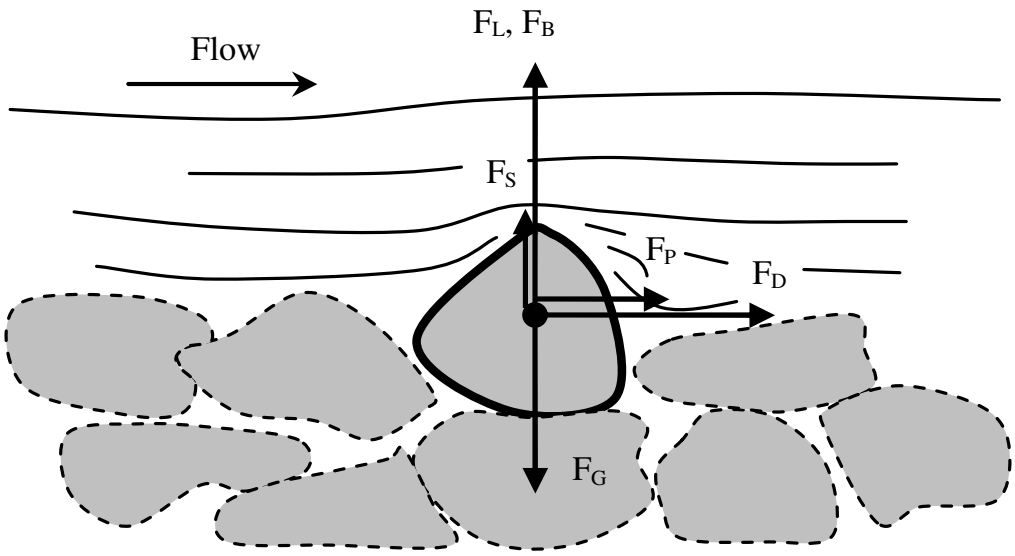

2. FUNDAMENTS

2.1 Introduction

Sediment transport usually occurs in a region referred as the inner shelf. In this region there is an important link between hydrodynamic forcing and the morphological response of the bottom. The activity at the interface between a moving fluid and an erodible boundary is extremely complex, involving many considerations and difficulties caused by the current, the wave orbital velocity or a combination of both. Once the sediments on the seabed are exposed to large enough forces induced by the water movements, the particles are entrained into the water column and the flow is no longer a simple fluid flow, since two materials are involved.

Classically, the sediment transport is conceived as occurring in two principal modes: bedload transport and suspended transport. Figure 2.1 presents an introductory overview of the sediment transport modes on a beach. Bedload transport is characterized by particles that move by rolling, sliding and/or jumping (saltating) along the bottom. Suspended transport occurs when the sediment is carried above the bottom by the turbulent eddies of the water, becoming available to be transported at higher elevations of the water column.

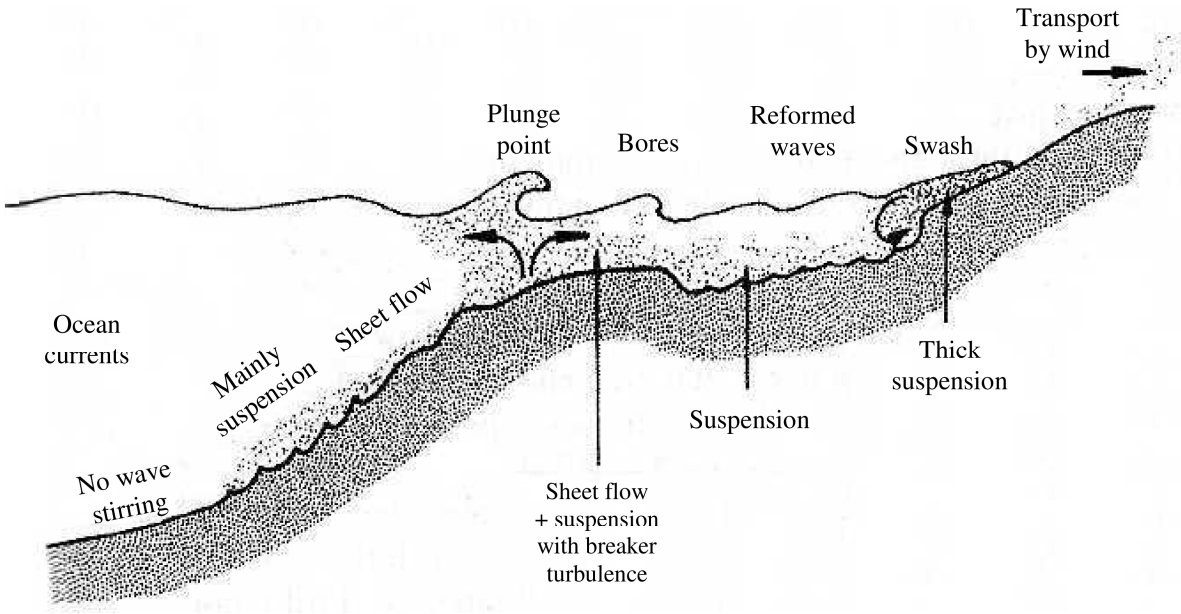

Figure 2.1 – Sediment transport modes on a beach (Nielsen, 2009).

Considering low velocity flows acting over a plane movable bottom, bedload transport becomes the dominant mode since most of the transport takes place in close proximity of the bed. However, if the available energy increases, the bottom will no longer remain plane, starting to exhibit bed forms and ripples. Under such conditions, the wave stirring enhances the suspension and suspended load often

prevails over bedload. At even stronger flow conditions, the bed shear stress increases and ripples and dunes are smoothed out and the stationary bed is capped by a thin layer of bedload particles in intense motion, leading to large transport rates. This transport regime is known as sheet flow regime.

This chapter intends to provide an understanding of the physics involved in cross-shore transport of cohesionless sediments. For the purpose of this work, attention is given to cases where bedload transport is considered the dominant mode and, particularly, under the sheet flow regime. The following description is limited to the main processes involved under incident short (wind forced) wave motions (frequencies of 0.05~0.4 Hz). The concepts introduced here give a short insight of the wave hydrodynamics, oscillatory boundary layers and sediment dynamics. A more exhaustive discussion about sediment transport processes in the nearshore zone can be found in the literature, for example, Fredsøe and Deigaard (1992), Nielsen (1992, 2009), van Rijn (1993) and Soulsby (1997).

The chapter starts with a brief presentation of the wave hydrodynamics, providing a descriptive overview of their transformation as they approach the shoreline. Initially, the solutions of the linear wave theory are provided, explaining the main mechanisms involved during wave propagation and the induced orbital motion. Then, attention is given to nonlinear processes that occur for shallow water waves. During the description importance is given to different parameters that enable the characterisation of the nonlinear wave properties and of the corresponding orbital motions that are acknowledged to be linked to the sediment transport.

Afterwards, the nature and structure of the oscillatory boundary layer is presented. This thin layer near the bed is recognized to be relevant to sediment transport modelling. Through viscosity effects, the water transfers shear forces that are responsible for the entrainment and transport of sediment particles. The main features of the boundary layer flow are identified and the influence of nonlinear motions is also assessed.

Finally, a succinct introduction to the sediment transport problem is provided. It starts by a description of the main forces acting on the particles, leading to incipient motion, and it is followed by a description of the sheet flow regime. The structure of the sheet flow layer is assessed and it is illustrated that this layer is also affected by the orbital motion.

In short, this chapter presents the most important nearshore physical mechanisms that are referred in the following chapters.

2.2 Wave hydrodynamics

2.2.1 Linear waves

Wave motion is often thought of as pure sinusoidal movement. This simplest representation of ocean water waves corresponds to the solution of the most elementary wave theory developed by Airy (1841) and it is known as *small-amplitude* or *linear wave theory*. Even though the assumptions made in developing the theory carry some restrictions (e.g., Le Méhauté, 1976), linear theory provides a most useful first approximation to the wave motion and can be used in many coastal engineering applications due to its simplicity. Nonetheless, ocean waves are generally not "small in amplitude", implying the use of nonlinear wave theories in coastal projects.

Figure 2.2 shows a definition sketch of a sinusoidal, progressive wave. A simple description of the sinusoidal surface variation, η, can be expressed by its length L (the horizontal distance between corresponding points on two successive waves), height H (the vertical distance from crest to trough) and period T (the time for two successive crests to pass a given point):

$$\eta(x,t) = \frac{H}{2}\cos(kx - \omega t) \tag{2.1}$$

where x is the horizontal spatial coordinate, k is the wave number ($k = 2\pi/L$) and ω is the wave angular frequency ($\omega = 2\pi/T$). Linear theory is restricted to waves of relatively small height in comparison to their wave length and water depth.

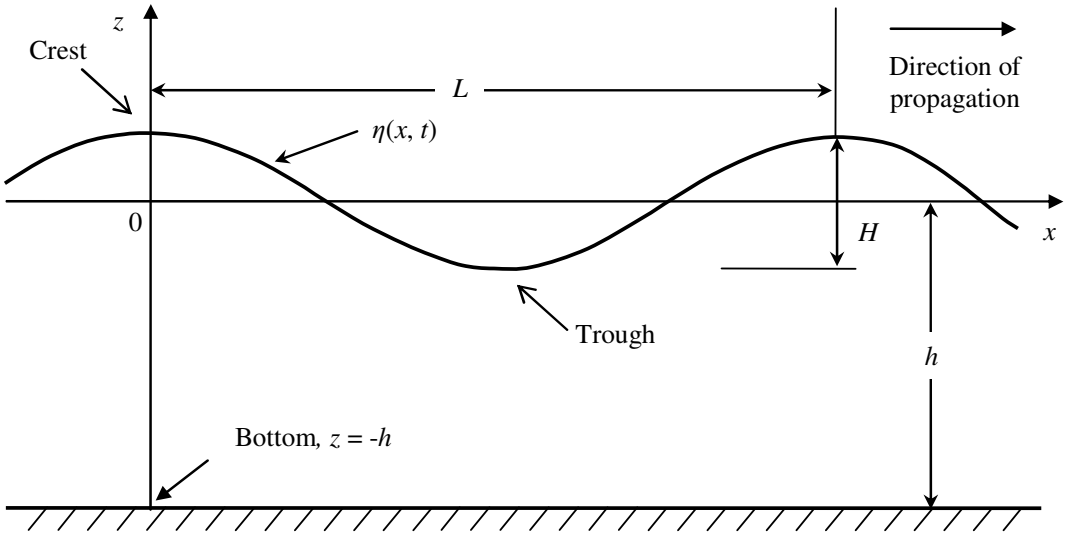

Figure 2.2 – Definition sketch of a sinusoidal, progressive wave.

Below the surface, the passage of a progressive wave induces fluid velocities, whose horizontal component, u, is given by:

$$u(x,z,t) = \frac{H}{2}\frac{gT}{L}\frac{\cosh\left(k\left(h+z\right)\right)}{\cosh\left(kh\right)}\cos\left(kx-\omega t\right) \tag{2.2}$$

where z is the vertical spatial coordinate, g is the gravitational acceleration and h is the water depth.

The corresponding local fluid particle acceleration, a, can be obtained by differentiating Eq. (2.2) in time. Accordingly, it is written as:

$$a(x,z,t) = \frac{g\pi H}{L}\frac{\cosh\left(k\left(h+z\right)\right)}{\cosh\left(kh\right)}\sin\left(kx-\omega t\right). \tag{2.3}$$

To maintain a constant energy flux of the wave motion during the shoaling process, there is an increase in wave height for decreasing depths, which is also reflected in the induced orbital motions (e.g., Dean and Dalrymple, 1991). An important issue that results from the wave induced motion is the displacement of individual water particles within the wave cycle. Linear wave theory imply that the orbital motion is circular for deep waters ($h/L>0.5$), and elliptical in shallow ($h/L<0.05$) or transitional depths ($0.05<h/L<0.5$). The ellipses become flatter for increasingly shallow water depths. Also, the horizontal particle displacement near the bottom can be large, affecting directly the mobilisation of the sediments in that region.

Exemplifying, for a wave with $T = 10$ s and $H = 1$ m, the linear theory produces near bottom velocity exceeding 0.15 m/s with corresponding maximum horizontal displacements greater than 0.5 m in depths less than 30 m. However, it is pointed that due to the perfectly sinusoidal movement of Airy waves, in the absence of currents, the sediment transport within the flow cycle is zero. However, that is not the case in shallow waters. As waves propagate from deep into shallow waters, they begin to interact with the sea floor and they undergo through several changes due to nonlinear effects.

2.2.2 Nonlinear wave properties

Stokes (1847) was one of the first to note and analyse the nonlinearities prior to wave breaking. He observed that, as waves approach the coast and propagate into shallower water, the waves present shorter and higher crests and longer and shallower troughs than in the sinusoidal profile. Apart from becoming peaky with sharp wave crests and long wave troughs, once waves approach breaking and enter the surf zone, they also attain a sawtooth shape, with a steep front face and more gently sloping

rear face (e.g., Svendsen et al., 1978; Elgar et al., 1988). The transformations of the surface elevation are illustrated in Figure 2.3 and are usually designated as skewed and asymmetric waves (e.g., Elgar and Guza, 1985).

Moreover, the corresponding orbital velocity near the bottom shows a similar (time) variation. Under the steep front face the velocity varies rapidly from a maximum negative (offshore) value to a maximum positive (onshore) value, giving rise to rapid fluid accelerations. The accelerations induced by the motion of the rear face of the wave are much smaller. This effect is related with the acceleration skewness.

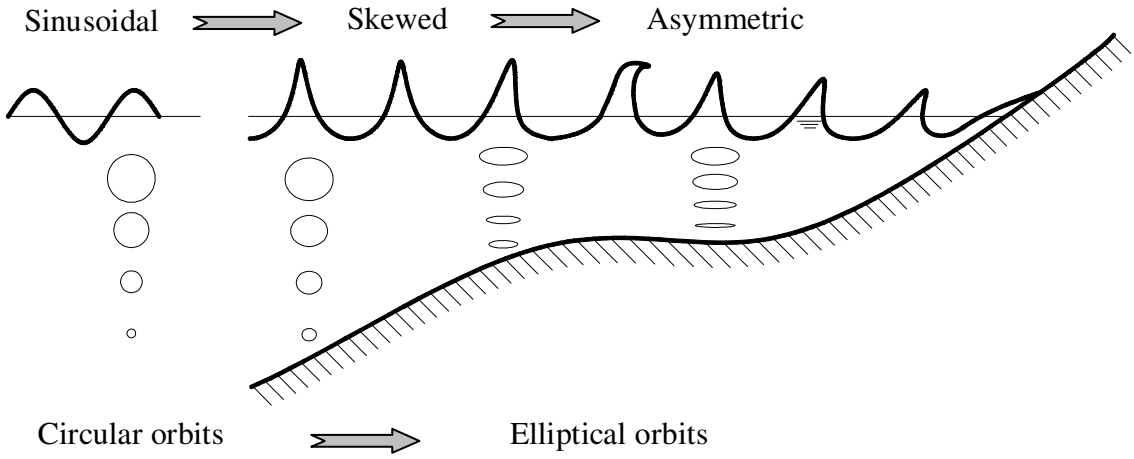

Figure 2.3 – Sketch of wave shape transformation and corresponding orbital motions as waves propagate from deep to shallow waters.

There are alternative approaches in the literature to assess these nonlinear effects. This can be done through the computation study of some statistical moments or from other simple parameters determined from the analysis of notable points in the velocity and acceleration time series. For example, Elgar et al. (1988) use statistical definitions to compute the velocity skewness and asymmetry. In such cases, the velocity skewness of a time series u is given by

$$\mu_{3,u} = \left\langle u^3 \right\rangle \Big/ \left\langle u^2 \right\rangle^{3/2}, \tag{2.4}$$

with the angle brackets denoting a time-average and the asymmetry is

$$As_u = \left\langle \left(\mathcal{H}(u) \right)^3 \right\rangle \Big/ \left\langle u^2 \right\rangle^{3/2}, \tag{2.5}$$

with $\mathcal{H}(u)$ the Hilbert transform of u. The velocity asymmetry is closely related with the acceleration skewness (Elgar, 1987), which can be represented as $\mu_{3,a} = \langle a^3 \rangle / \langle a^2 \rangle^{3/2}$, where a represents the time series of the fluid horizontal acceleration (e.g., Drake and Calantoni, 2001).

Alternatively, the velocity and acceleration skewness are often defined in terms of the following coefficients, R and β, respectively:

$$R = \frac{u_{\max}}{u_{\max} - u_{\min}} \tag{2.6}$$

$$\beta = \frac{a_{\max}}{a_{\max} - a_{\min}} \tag{2.7}$$

where $u_{\max}$ and $u_{\min}$ are the maximum positive and maximum negative velocities, respectively, and $a_{\max}$ and $a_{\min}$ have the same meaning, but for the fluid horizontal acceleration, a. Figure 2.4a shows a sketch of a pure velocity-skewed oscillatory flow. In such case, the magnitude of velocity at the crest is larger than that at the trough, leading to $R > 0.5$, but β remains constant at 0.5 since $|a_{\max}|$ equals $|a_{\min}|$. For symmetric waves, R equals 0.5, whereas the case of $R < 0.5$ occurs when the absolute value of the velocity at the trough is larger than that at the crest, which is less common in nearshore propagating waves. Analogously, Figure 2.4b shows a sketch of pure acceleration-skewed flow. This corresponds to the sawtooth wave case, where the oscillatory velocity is symmetric with respect to the horizontal axis in a time series graph (R = 0.5) but is asymmetric with respect to the vertical axis within each wave cycle, giving rise to skewed accelerations (i.e., $\beta > 0.5$).

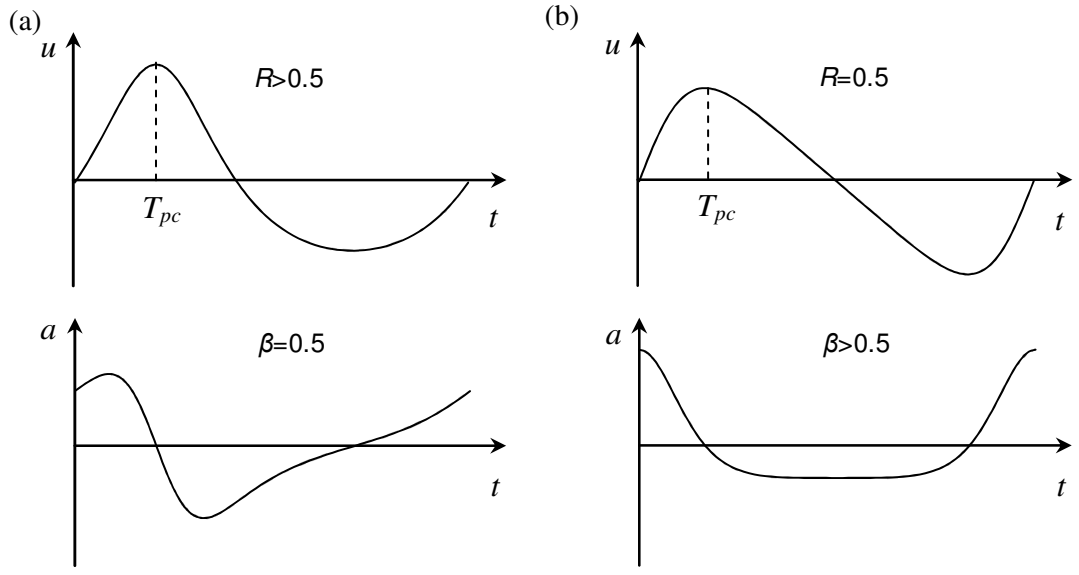

Figure 2.4 – Sketch of: (a) a velocity-skewed (Stokes) flow; (b) an acceleration-skewed flow (sawtooth).

Watanabe and Sato (2004) formulate the acceleration skewness coefficient, β, in terms of an equivalent parameter denoted "velocity-leaning index" β_{cw}:

$$\beta_{cw} = 1 - \frac{2T_{pc}}{T}, \tag{2.8}$$

where, T_{pc} is the time interval measured from the zero up-cross point to wave crest in the time variation of free-stream velocity (see Figure 2.4). Recently, Suntoyo et al. (2008) classified their experiments in terms of the "wave skewness parameter" α, closely related to β_{cw}:

$$\alpha = 2T_{pc}/T = 1 - \beta_{cw}. \tag{2.9}$$

It is noted that the final purpose of the previous definitions is the same. All of them intend to characterize nonlinear wave properties through the identification of the velocity and acceleration skewnesses, which are recognized to be inextricably linked to the movement of sediments.

2.3 Oscillatory boundary layers

2.3.1 Introduction

As mentioned in the previous section, as the waves propagate from deepwater to shallow waters, the horizontal particle displacements near the bottom become large, as well as the horizontal velocities near the bottom. This implies that to satisfy the no-slip condition at the seabed where the velocity is zero, there is a thin region where the wave-induced water motion is strongly influenced by the bed. This layer is called the boundary layer and is characterized by strong velocity gradients, leading to noticeable shear stresses. This region is particularly relevant to sediment transport modelling because it is responsible by the mobilization and transport of the sediment particles, and for bringing them into suspension above the seabed. It is also within this region of the water column that high levels of turbulence intensities are produced and, consequently, where most of the energy dissipation of the flow occurs.

In general, the boundary layer thickness, δ, depends on the flow period and on the eddy viscosity, ν_T (e.g., Nielsen, 1992), obeying

$$\delta \propto \sqrt{\nu_T T} \,. \tag{2.10}$$

For fixed eddy viscosity, Eq. (2.10) shows that for short wave components (frequencies of 0.05-0.4 Hz) due to the oscillatory nature of the wave orbital velocity the bottom boundary layer has only a limited time to grow, resulting in the development of a thin layer, a few centimetres in thickness (over flat beds of loose sediments). Conversely, a current, wind-driven or tidal, will vary over a much longer time leading to thicker boundary layers which can extend to the entire water column. This is of great importance to entrain and transport sediment particles because the shear stresses exerted at the bed depend directly on the vertical velocity gradient ($\tau = \rho \nu_T \, du/dz$, with ρ the fluid density), which is inversely proportional to the boundary layer thickness. Therefore, a thinner boundary layer due to wave motion implies mean larger shear stresses. In consequence, a wave is capable to entrain a significant portion of sand from the bottom, whereas a steady flow with a comparable velocity might not be even able to initiate the movement of the sediment particles. This clarifies the importance of waves for initiating the motion of the sediments.

Experimental evidence does not show significant effects on the wave bottom boundary layer flow structure and on the wave shear stresses due to the presence of moderate superimposed currents

(Nielsen, 1992; Simons et al., 2000). However, when the currents are combined with waves, their contribution may play a major role to the net sediment transport.

From dimensional analysis, Jonsson (1966) concluded that the structure of oscillatory boundary layers depends mainly on the Reynolds number ($Re = A^2\omega/\nu$) and on the relative bed roughness A/k_s, where A represents the water particle semi-excursion and k_s the bed roughness. The values of Re and A/k_s help to classify if the boundary layer is either laminar or turbulent. Moreover, Jonsson showed that the wave friction factor, f_w, which is a dimensionless factor that links the bottom shear stress to the free-stream velocity, can be expected to depend only on Re and A/k_s. The maximum value of τ was defined by:

$$\tau_{\max} = \frac{1}{2}\rho f_w (A\omega)^2 . \tag{2.11}$$

Eq. (2.11) can be applied to arbitrary wave shapes if $A\omega$ is replaced with the maximum orbital velocity. The advantage to use such friction factor is that one does not need to resolve the details of the boundary layer flow in order to calculate the shear stress from flow information outside the boundary layer.

2.3.2 Defect law

To describe the water motion within the wave boundary layer, the Navier-Stokes momentum equation must be solved. The governing equation of the horizontal component of a 2D flow in the vertical x-z plane yields

$$\frac{\partial u}{\partial t} + u\frac{\partial u}{\partial x} + w\frac{\partial u}{\partial z} = -\frac{1}{\rho}\left(\frac{\partial p}{\partial x} - \frac{\partial \tau}{\partial z}\right). \tag{2.12}$$

where p is the pressure and w is the vertical flow velocity. Inside the boundary layer the flow can be considered essentially horizontal ($w \approx 0$). Moreover, within U-tubes[1] the flow is uniform in the x-direction and, if the disturbances introduced by the individual roughness elements are restricted to a layer considerably thinner than the boundary layer itself, the convective acceleration term $u\partial u/\partial x$ can be neglected. In such case, Eq. (2.12) can be reduced to

[1] See Chapter 3.

$$\rho \frac{\partial u}{\partial t} = -\frac{\partial p}{\partial x} + \frac{\partial \tau}{\partial z} . \tag{2.13}$$

Outside the boundary layer the shear stresses vanish and Eq. (2.13) can then be simplified to

$$\rho \frac{\partial u_\infty}{\partial t} = -\frac{\partial p}{\partial x} , \tag{2.14}$$

where u_∞ represents the free-stream velocity.

Subtracting Eq. (2.14) with Eq. (2.13), the equation of motion can be written as

$$\rho \frac{\partial}{\partial t}\left(u_\infty - u\right) = -\frac{\partial \tau}{\partial z} , \tag{2.15}$$

where u_∞-u is the so-called velocity defect (= u_d).

The laminar boundary layer over flat beds provides a good basis to gain insight about the main features of the wave boundary layer structure. In such case and for a Newtonian fluid, τ is related to the velocity gradient and the fluid kinematic viscosity, ν, by

$$\frac{\tau}{\rho} = \nu \frac{\partial u}{\partial z} . \tag{2.16}$$

Introducing Eq. (2.16) into Eq. (2.15), the equation of motion reads

$$\rho \frac{\partial}{\partial t}\left(u_\infty - u\right) = -\nu \frac{\partial^2 u}{\partial z^2} . \tag{2.17}$$

Eq. (2.17) has the advantage to enable the development of analytical expressions for u and τ if u_∞ is provided.

In the following, one considers a pure accelerated skewed flow (sawtooth wave) where the free-stream velocity consists of six harmonics (van der A et al., 2010):

$$u_\infty(t) = A\omega \sum_{n=1}^{6} \frac{(2\beta - 1)^{n-1} \sin(n\omega t)}{n} , \tag{2.18}$$

where β is the acceleration skewness parameter (Eq. (2.7)). Similarly to the sinusoidal approach, introducing Eq. (2.18) in Eq. (2.17) the velocity within the boundary layer yields

$$u(z,t) = A\omega\sum_{n=1}^{6}\frac{(2\beta-1)^{n-1}}{n}\left[\cos(n\omega t)\sin\left(\sqrt{n}\frac{z}{\sqrt{2\nu/\omega}}\right)\exp\left(-\sqrt{n}\frac{z}{\sqrt{2\nu/\omega}}\right)+\right.$$
$$\left.+\sin(n\omega t)\left(1-\cos\left(\sqrt{n}\frac{z}{\sqrt{2\nu/\omega}}\right)\exp\left(-\sqrt{n}\frac{z}{\sqrt{2\nu/\omega}}\right)\right)\right] \quad (2.19)$$

and the corresponding bed shear stress results in

$$\tau(0,t) = \rho A\omega\sqrt{\omega\nu}\sum_{n=1}^{6}\frac{(2\beta-1)^{n-1}\sqrt{n}\sin(n\omega t+\pi/4)}{n}. \quad (2.20)$$

Eq. (2.19) illustrate that u scales with the Stokes length $\sqrt{2\nu/\omega}$, which is often assumed as the boundary layer thickness of the laminar flow ($\delta \propto \sqrt{\nu T}$).

Figure 2.5 shows the results of Eq.s (2.18), (2.19) and (2.20) for three cases of the acceleration skewness coefficient, β = 0.5, 0.65 and 0.8. The first case, β = 0.5, corresponds to the sinusoidal flow. In general, the velocity profiles for all the tree cases present various well-known features of oscillatory boundary layers: the velocity decays toward zero as the bed is approached; near the bed, the velocity turns before the free-stream velocity, i.e., it is leading in phase the free-stream velocity; and an "overshoot" velocity is observable close to the bed because at certain elevations the velocity amplitude exceeds the maximum free-stream velocity. However, some differences can be perceived due to the introduction of the acceleration skewness in u_∞. With an increase of β, the onshore velocity increases in magnitude faster than the offshore velocity, and the associated boundary layer has a shorter time to develop. This becomes clearer for β = 0.8, where under the crest the overshoot velocity is maximum at $z \approx 1.7\sqrt{2\nu/\omega}$ with $|u/u_\infty| \approx 1.22$, whereas, under the trough is maximum at $z \approx 2.9\sqrt{2\nu/\omega}$ with $|u/u_\infty| \approx 1.10$. As a consequence, the onshore velocity generates a thinner boundary layer and therefore a larger bed shear stress. Moreover, the difference in phase between the free-stream velocity and the bed shear stress is also affected. In the particular case of sinusoidal flow, τ leads u_∞ by 45º, but for β = 0.65 and 0.8 it results in 44º and 34º, respectively.

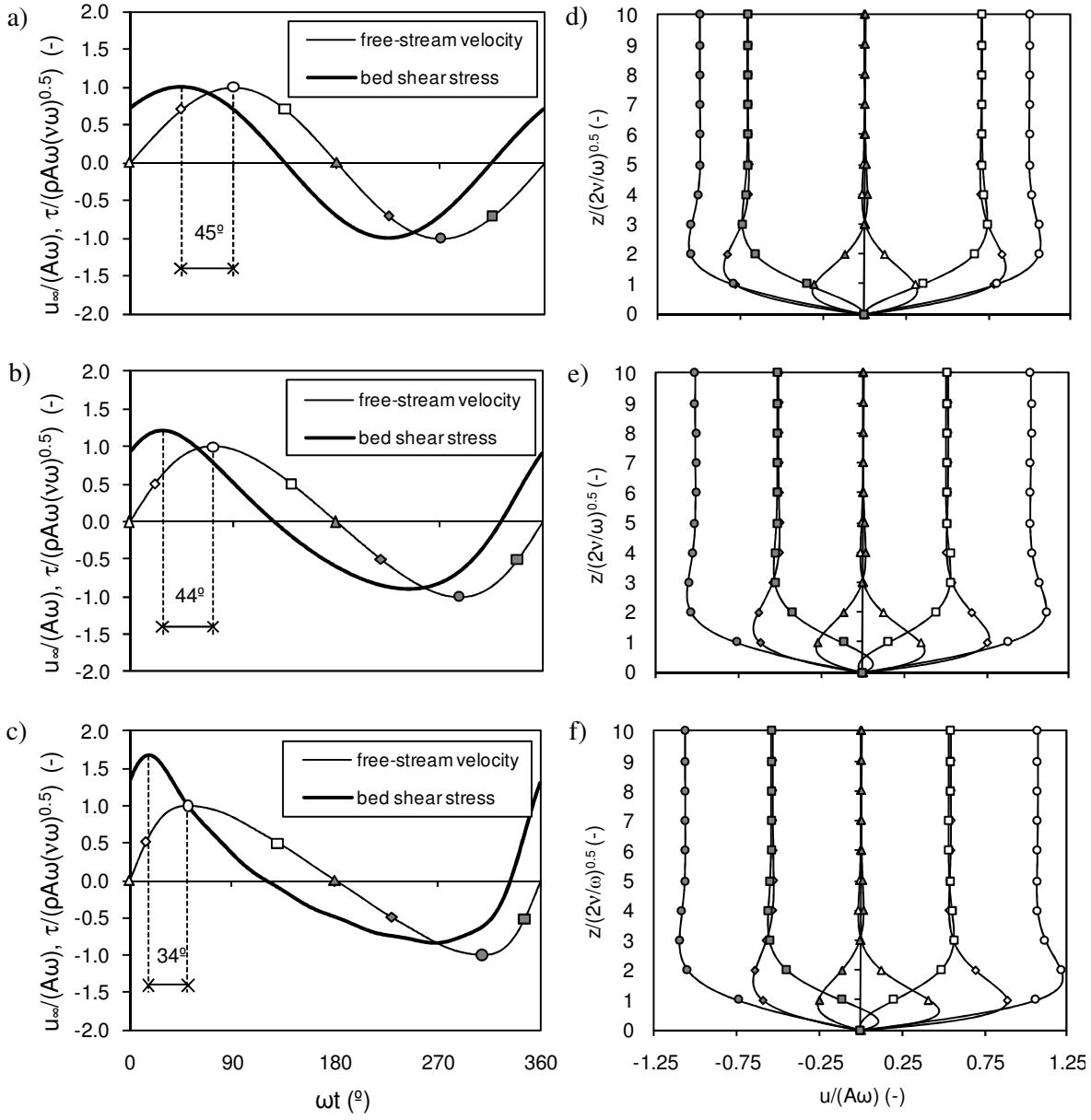

Figure 2.5 – Dimensionless time-series of free-stream velocity and bed shear stress using Eqs. (2.19) and (2.20) for: (a) $\beta = 0.5$, (b) $\beta = 0.65$ and (c) $\beta = 0.80$. The symbols identify selected phases of the flow cycle for which the corresponding vertical velocity profiles obtained by Eq. (2.19) are represented in (d) – (f).

Though the previous results concern only laminar boundary layers over flat beds, similar results can be observed for turbulent wave boundary layers in general. For example, Figure 2.6 shows the ensemble-averaged velocity profiles and velocity time-series at selected elevations for a rough turbulent flow over fixed beds, for one of the experiments performed by van der A et al. (2008) at the Aberdeen Oscillatory Flow Tunnel ($\beta = 0.75$ in Eq. (2.18)). Figure 2.6 demonstrates that all the boundary layer flow features observed for laminar flows are well reproduced for turbulent flows. In addition, the influence of the acceleration skewness leads to a stronger overshoot velocity and a thinner boundary layer under the positive (onshore) velocities similar to laminar flows (see Figure 2.5f).

For the measure of the boundary thickness, δ, different definitions can be found in the literature. For instance, Jonsson (1966) define δ as the lowest elevation where $u = u_\infty$, Sleath (1987) at the level where the velocity defect equals 5% of u_∞ ($u_d = 0.05\ u_\infty$), Jensen et al. (1989) at the elevation of maximum velocity ($u = u_{max}$) and Kajiura (1968) proposes

$$\delta = \frac{1}{A\omega} \max\left\{\int_0^\infty (u_\infty - u)\, dz\right\}. \tag{2.21}$$

Nevertheless, for rough turbulent flows, expressions based on A/k_s, seem to characterise well the boundary layer thickness (e.g., Sleath, 1987; Fredsøe and Deigaard, 1992).

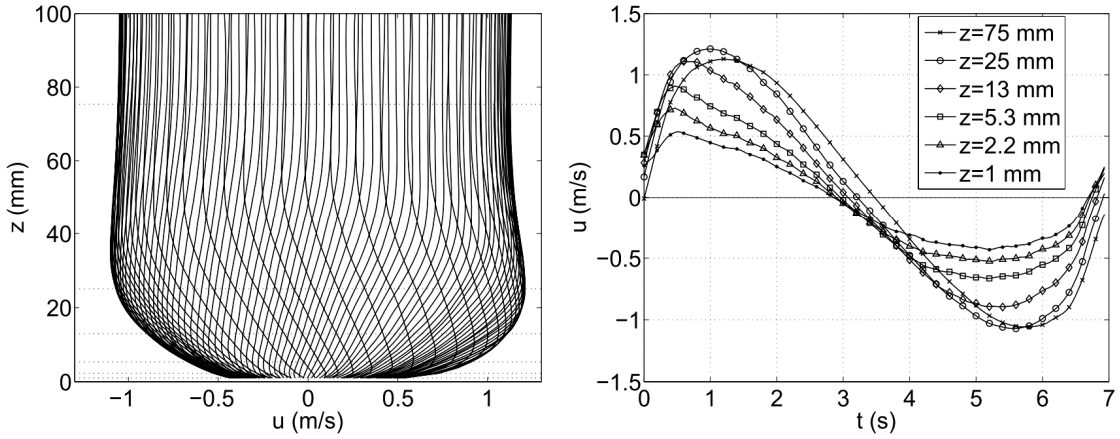

Figure 2.6 – Ensemble-averaged velocity profiles (left) and velocity time-series (right) at selected elevations (indicated by dotted lines in left plot). Experiment S757012g (gravel bed, $T = 7$s, $\beta = 0.75$); $z = 0$ corresponds to the top of the roughness elements. (van der A et al., 2008)

2.4 Sediment dynamics

2.4.1 Threshold of motion

A sediment particle on the bed is mobilized by the flow if it induces a force sufficient to overcome the natural resistance to motion of the particle. Thus, the threshold of motion is usually associated with the balance of forces acting on a sediment particle. If a certain ratio between mobilizing and stabilizing forces is exceeded the incipient motion occurs.

Figure 2.7 shows the intervenient forces acting on a grain over a flat erodible bed: buoyancy force F_B, drag force F_D, gravity force F_G, lift force F_L, pressure force F_P, and seepage force, F_S (e.g., Nielsen, 2009). However, the forces that mainly contribute to the mobilization of the sediment are the drag, lift and pressure forces.

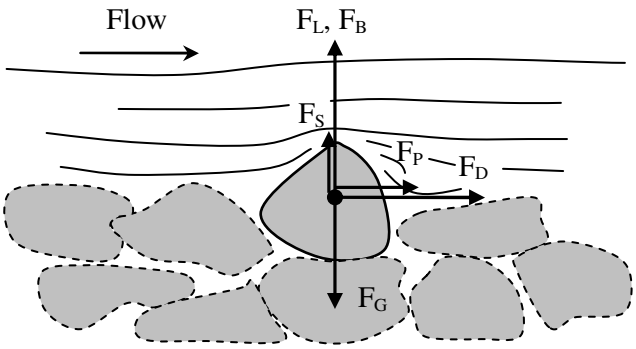

Figure 2.7 – Forces acting on a grain over a flat erodible bed.

The vertical mobilizing force (lift force) results from the curvature of the streamlines which locally contract over the particle, decreasing the pressure to be lower than the hydrostatic pressure at the top of the grains. This leads to a vertical pressure gradient and consequently to a lift force.

The total horizontal mobilizing force on sediment particles comprises the sum of a drag force and inertial (pressure) forces ($F_D + F_P$). This results from the frictional forces that the fluid exerts on the surface of the grains (the bed shear stress) and from the horizontal pressure gradients generated by the wave-induced accelerations of unsteady flows.

From tunnel experiments, Sleath (1993) proposed a parameter representing the ratio of the inertial to gravity force (corrected for buoyancy) that determines the dominant mode of sediment transport:

$$S(t) = \frac{\rho a(t)}{(\rho_s - \rho) g}, \tag{2.22}$$

with ρ_s the sediment density. Sleath (1999) suggested that if $S > 0.3$ the pressure gradients become dominant, whereas $S < 0.3$ indicates that the sediment transport process is dominated by bed shear stresses. Recently, Foster et al. (2006) observed that, in the field, the pressure gradient dominance occurs at lower values of S ($S > 0.1$), which is probably due to the additional presence of vertical velocities.

To determine dimensionless parameters involved in the incipient motion of a sediment particle, Shields (1936) applied dimensional analysis. He established a diagram from experimental results as a function of two dimensionless quantities: the grain Reynolds number Re_*, and the Shields parameter, θ

$$Re_* = \frac{u_* d}{\nu}, \tag{2.23}$$

$$\theta = \frac{\tau}{(\rho_s - \rho) g d}. \tag{2.24}$$

In Eq. (2.23) the Reynolds number enters with the friction velocity $u_* (= \sqrt{\tau/\rho})$.

The Shields parameter establishes the ratio of a shear force to a gravity force (corrected for buoyancy), i.e., the ratio between the main stabilising and mobilising forces acting on a grain. Eq. (2.24) accounts for both pressure gradients and drag forces, inasmuch as the acceleration effects are incorporated in τ.

Many bedload transport formulas define the transport rate to be proportional to 3/2 power of the Shields parameter (e.g., Meyer-Peter and Müller, 1948, Wilson, 1966; Nielsen, 1992; Soulsby, 1997). Soulsby and Damgaard (2005) provide a comprehensive description about the underlying derivation of such formulae.

The critical value of Shields, θ_{cr}, defining the threshold of motion, is usually expressed in terms of sediment and fluid characteristics, which is more convenient and explicit than the use of the traditional Shields diagram (e.g., Tanaka and To, 1995; Soulsby, 1997). For example, Soulsby and Whitehouse (1997) proposed an expression for θ_{cr} as a function of a dimensionless particle size parameter D_*:

$$\theta_{cr} = \frac{0.3}{1 + 1.2 D_*} + 0.055\left(1 - \exp\left(-0.02 D_*\right)\right), \tag{2.25}$$

with

$$D_* = \left(\frac{g\left(s-1\right)}{\nu^2} \right)^{1/3} d \,. \qquad (2.26)$$

Eq. (2.26) shows that for $d = 0.2$ mm, θ_{cr} results in 0.05, which is a reference value widely used for sand in water.

Beside the definition for the incipient motion under waves, θ and D_* have been used to produce diagrams, identifying the bedforms that are generated under certain hydraulic and sediment conditions (see Figure 2.8). This figure shows that the bed states of "no motion", "wave ripples", "suspension" and "sheetflow" appear in crescentic order of the Shields parameter, and also depend on D_*. Although the Shields parameter has been widely used by engineers as a criterion for incipient motion, this criterion still presents some limitations. For example, the experiments conducted by Terrile et al. (2006) in a wave flume indicate that the wave shape also has a strong influence on the threshold of motion.

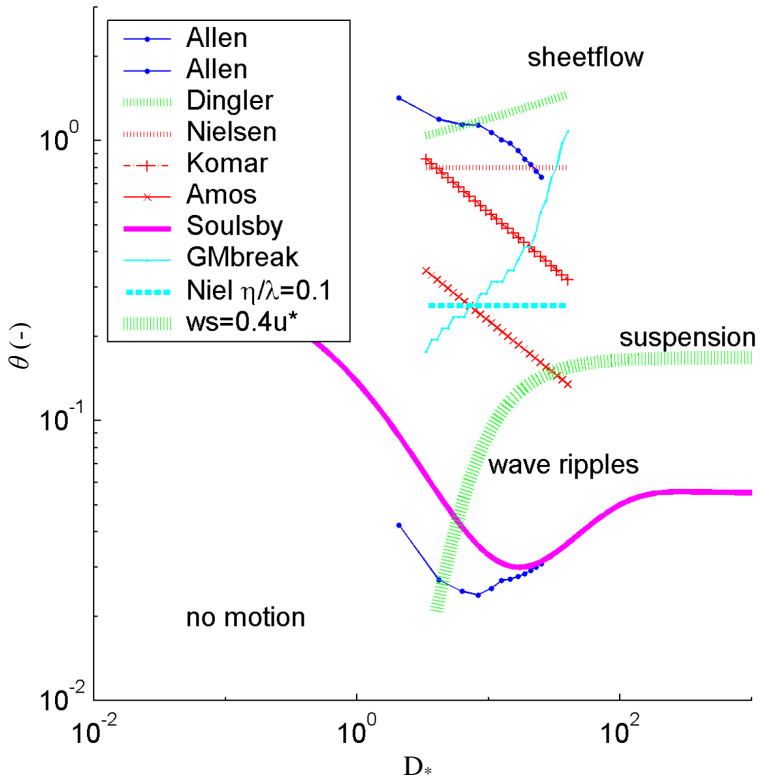

Figure 2.8 – Wave bedform stability diagram and criteria plotted in terms of the Shields parameter and the dimensionless particle size parameter (adapted from kleinhans, 2005)

2.4.2 Bedload and sheet flow

Intense wave orbital velocities near the bed, occurring typically in the ocean surf zone or even at intermediate water depths during storm conditions, can cause the sand bed to move as a sheet layer. This happens for large Shields numbers ($\theta > 0.8$) and defines the so-called sheet flow layer (SFL) (see Figure 2.8).

This layer generally possess a thickness of the order of mm to cm and the sand concentrations reach values between 200g/l to near 1600 g/l at the stationary bed. Due to the high concentration values, inter-granular forces and sediment-flow forces are important. As shown by the experimental works of Ribberink and Al-Salem (1995), McLean et al. (2001) and Ruessink et al. (2011), most of the sediment transport in this regime can occur within the SFL. Hence the study of the SFL structure along the wave cycle is an important research issue (Dohmen-Jansen, 1999; O'Donoghue and Wright, 2004a; Hsu and Hanes, 2004; Myrhaug and Holmedal, 2007).

In the sheet flow regime the transport is partly bedload and partly suspended load. The boundary between the SFL and the upper suspension layer usually delimits two flow regions with distinct driving forces for the sediment movement: turbulent mixing in the suspension layer and inter-granular forces in the SFL. Although the distinction of sediment transport in two modes may be made conceptually, the quantitative separation of both is quite difficult. As for volumetric concentrations greater than 8% (≈210 g/l) the inter-granular forces are expected to be important, this reference concentration value can be assumed to define the top level of the SFL, d_t (Dohmen-Janssen and Hanes, 2002).

The sheet flow layer is divided into two distinct layers: a lower layer where the sediment particles are picked up from the bed and an upper layer in which they are entrained into the flow (see Figure 2.9). The level $z = 0$ corresponds to the stationary bed prior to wave action.

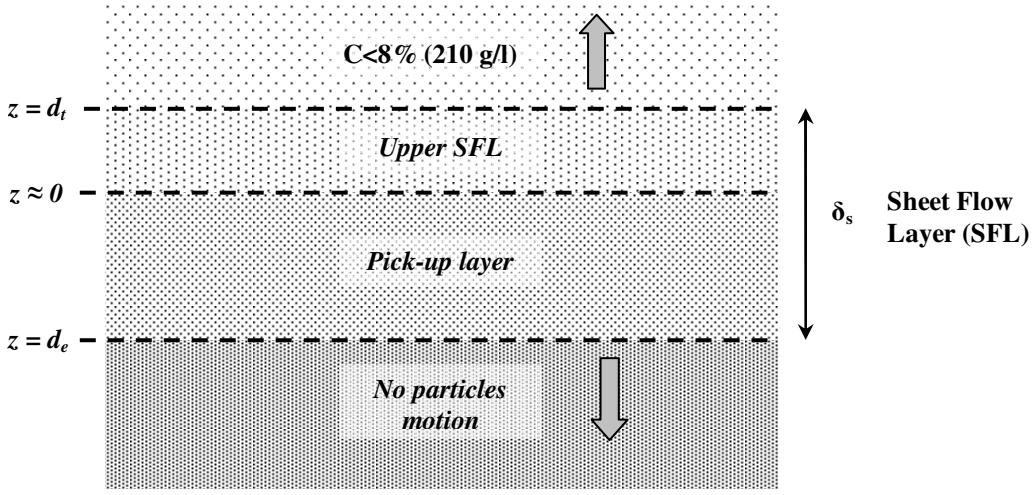

Figure 2.9 –Diagram illustrating the sheet flow layer structure.

The lower level of the SFL, d_e, is considered as the instantaneous location of the interface between the moving and stationary grains. The difference between this level and the initial stationary bed, prior to wave motion, is considered by some authors as the erosion depth (e.g., Zala-Flores and Sleath, 1998). The boundary between the pick-up layer and the upper part of the SFL is normally found at $z = 0$, the initial stationary bed. Following Dohmen-Janssen and Hanes (2002) and Ribberink et al. (2008), the SFL thickness is therefore defined as the distance between the top and lower levels:

$$\delta_s = d_t - |d_e| . \tag{2.27}$$

Figure 2.10 presents an example of the measured ensemble-averaged volumetric concentrations at different elevations under the sheet flow regime obtained by Dohmen-Janssen and Hanes (2002). The experiments were performed in a large wave flume and the sand bed was formed by well-sorted quartz with a median grain diameter of 0.24 mm. Figure 2.10 illustrates the typical behaviour of the sheet flow under velocity skewed waves, providing a good insight about the sheet flow layer structure. In the upper sheet flow layer the concentrations are in phase with the free-stream velocity, i.e., when the velocity increases the concentrations increase too, because sediment is entrained from below into the flow, and when the velocity decreases, concentrations decrease too. In the pick-up layer the concentrations are higher, but vary in antiphase with the free-stream velocity. Moreover, the effect of the shape of the waves, inducing larger crest velocities than trough velocities, is clearly reflected in the concentrations both in the pick-up layer and in the upper sheet flow layer. The figure also shows that at the pick-up layer the concentrations are nearly instantaneously related to the near-bed velocity and that, above this layer, the peak in concentration occurs after the moment of maximum velocity, showing increasing phase lags with increasing distance above the bed. These observations affect the SFL structure and, consequently, the sediment fluxes.

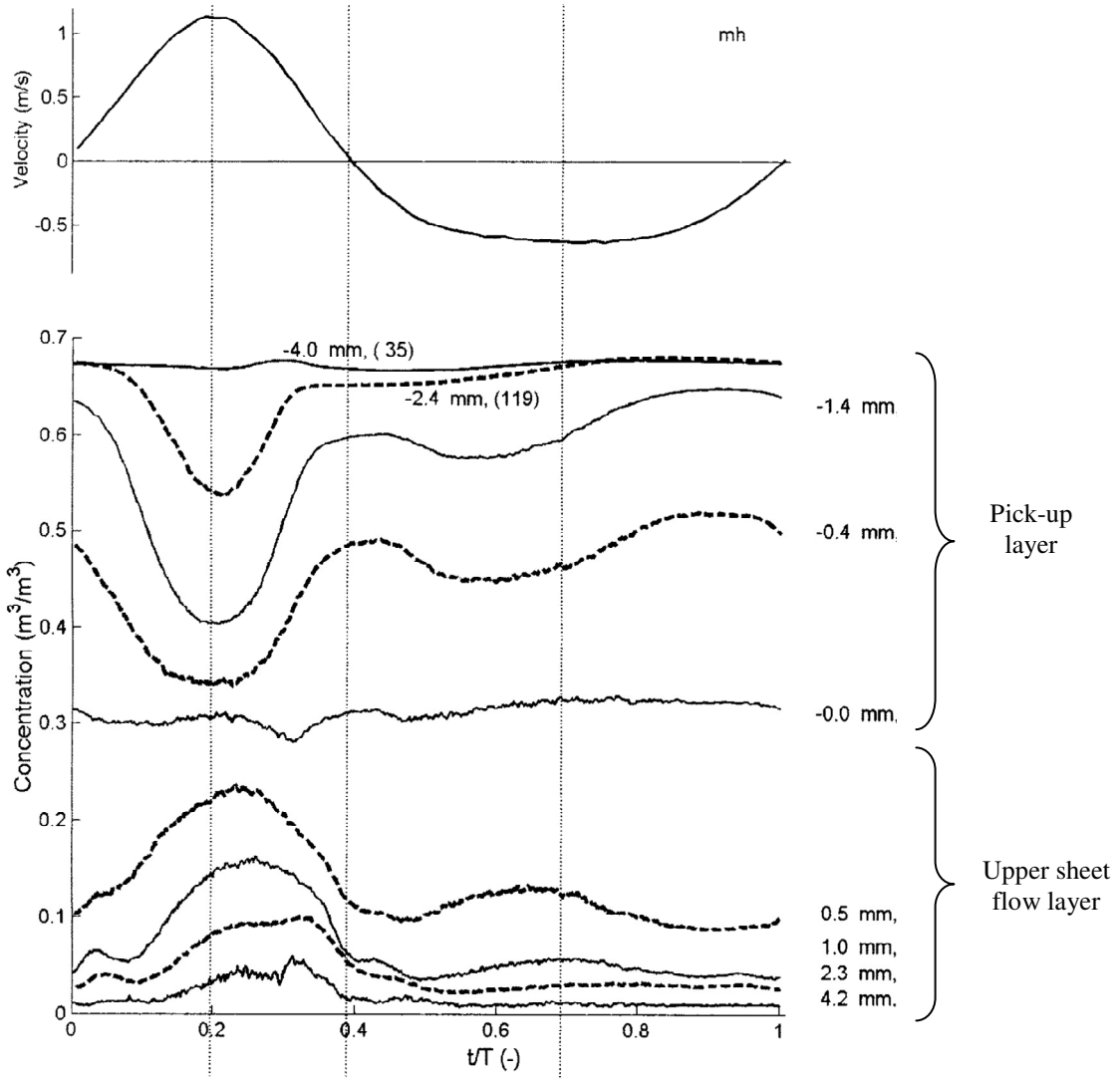

Figure 2.10 – Measured ensemble-averaged concentrations at different elevations in the sheet flow layer for condition mh (Dohmen-Janssen and Hanes, 2002).

Chapter 3

PHYSICAL MODELLING

3. PHYSICAL MODELLING

3.1 Introduction

Studies under controlled experimental conditions that consider the effect of wave asymmetry and fluid acceleration on sediment transport are scarce. King (1991) performed a series of experiments in the oscillatory flow tunnel of the Scripps Institute of Oceanography under half-cycle sawtooth waves. Dibajnia and Watanabe (1998) and Watanabe and Sato (2004) have conducted experiments in the oscillatory flow tunnel of the University of Tokyo with irregular and regular oscillatory flows, respectively. The Dibajnia and Watanabe (1998) data refer to velocity- and acceleration-skewed oscillatory flow while the Watanabe and Sato (2004) experiments refers to sawtooth shaped oscillatory flow with or without a net current superimposed. These experiments were performed with relatively short flow periods, between 3 and 5s. Longer periods could not be considered because of limitations of the facility. Recently, van der A et al. (2010) have conducted a series of experiments in the Aberdeen Oscillatory Flow Tunnel (AOFT) with sawtooth oscillatory flows with varying degrees of acceleration skewness, three sand sizes and wave periods ranging from 5 to 9s. All these experiments were performed in the sheet flow (flat-bed) regime.

Among the existing data only the experiments performed in the AOFT provide detailed measurements of flow velocities and sediment concentrations which enable the study of small scale sediment transport processes (van der A et al., 2008; van der A et al., 2009). Furthermore, only the AOFT data are representative for the typical wave periods found in energetic shoaling and surf zones.

The existing experimental data show that acceleration-skewed oscillatory flows result in a net sediment transport in the direction of the largest acceleration (shorewards) and that its magnitude increases with acceleration skewness (Watanabe and Sato, 2004; Silva et al., 2008, 2011; van der A et al., 2010). The key mechanism driving the net transport is believed to be the larger bed shear stress under the rapidly accelerating half cycle compared to the slowly accelerating half cycle, which occur as a result of time limitation on the boundary layer growth, as suggested by Nielsen (1992) and shown in van der A et al.'s (2008) fixed bed experiments and in Ruessink et al. (2011) mobile bed experiments. The numerical study of Ruessink et al. (2009) with a 1DV bottom boundary layer model also suggests that the time-dependent sediment transport can be parameterised in terms of the instantaneous bed shear-stress for grain sizes larger than 0.2 - 0.25 mm. For finer sediments however, their modelling results showed that phase lag effects between flow velocities and sediment concentrations enhance the net transport in the wave direction, in the opposite direction of what was found previous for velocity-skewed oscillatory flows (Dohmen-Janssen et al., 2002; Hassan and

Ribberink, 2005). The potential importance of phase lag effects for acceleration-skewed flows and fine sands was already pointed out by Dibajnia and Watanabe (1998) and Silva et al. (2007), but only shown recently in the mobile bed experiments of van der A et al. (2009). Furthermore, results of the two-phase model of Hsu and Hanes (2004) also suggest that sediment fluxes are correlated with the flow acceleration and can be enhanced when bed failure occurs.

In the present chapter, results of the experimental project TRANSKEW (sand TRANsport induced by SKEWed waves and currents) carried out in the Large Oscillating Water Tunnel (LOWT) of Deltares (formerly, WL|Delft Hydraulics) are presented. The general aim of this project was to obtain a new reliable dataset of detailed flow and sand transport processes under flat-bed/sheet flow conditions that allow analyzing the effects of wave nonlinearities and of a net current on the sediment transport processes. The experimental conditions were selected to simulate the near-bed cross-shore sediment motion in various wave conditions representative of the upper shoreface, particularly in the surf zone. They mimic the degree of velocity and acceleration skewness found before and after wave breaking, and the cross-shore mean flow associated to the undertow. Both net sediment transport rates and detailed time-dependent sediment concentrations and flow velocity measurements were carried out. The present experiments extend the previously experimental conditions of Watanabe and Sato (2004) and van der A et al. (2010) by considering oscillatory flows with longer periods (7-10 s), oscillatory flows with a net current and the combined effect of velocity and acceleration skewness.

The chapter starts with a description of the experimental program and of the instruments deployed. Subsequent sections present the data-processing methodologies developed and applied and the results obtained, discussing their dependence on velocity skewness, acceleration skewness and net currents.

3.2 *TRANSKEW* experimental set-up and measurements

3.2.1 Large Oscillating Water Tunnel (LOWT)

The LOWT is a U-tube with a rectangular horizontal test section (14 m long, 0.3 wide and 1.1 m hight with a 0.3m thick sand bed) and two cylindrical risers at either end (Figure 3.1 and Figure 3.2). A steel piston system housed in one of the cylinders drives the flow in the test section over the sand bed. The other cylinder is open to the atmosphere. The LOWT is fitted with a recirculation system that enables the generation of a mean current that is superimposed on the oscillatory flow. Sediment traps existing beneath both cylinders and at the recirculation system allow capturing the eroded sand transported out off the test section during a run.

The LOWT allows the simulation of near bed horizontal oscillatory flow at full scale (1:1) over the sand bed, representative of a wide range of flow conditions found in the nearshore zone. Scale effects, typical of sediment-transport studies in smaller laboratory wave flume facilities, are therefore avoided. Nonetheless, the oscillatory flow within the test section of the tunnel is an approximation of the flow experienced at the seabed under real waves as pointed out by Ribberink et al. (2000), Dohmen-Janssen and Hanes (2002) and Schretlen et al. (2009). Among other processes, the nonlinear boundary layer streaming induced by wave surface effects is absent. Schretlen et al. (2009) indicated that these induced small net currents are especially important for the transport of fine sands (median grain size $d_{50} \leq 0.15$ mm). Also, in the U-tube facilities, vertical velocities are absent or quite small, unlike those under real free-surface waves. Hence, velocities in U-tubes are one-dimensional, whereas under long-crested waves they are bi-dimensional.

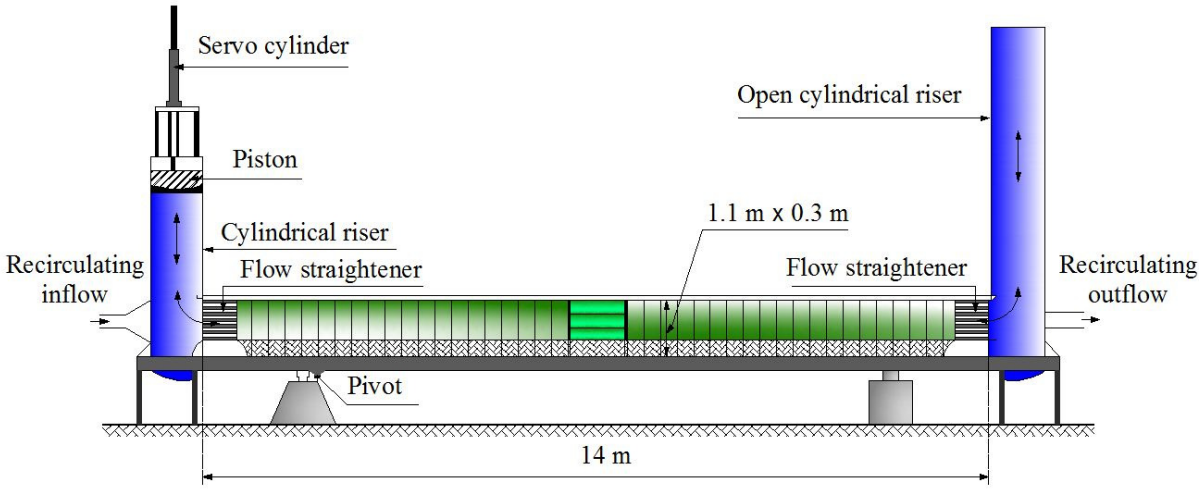

Figure 3.1 – General outline of the LOWT.

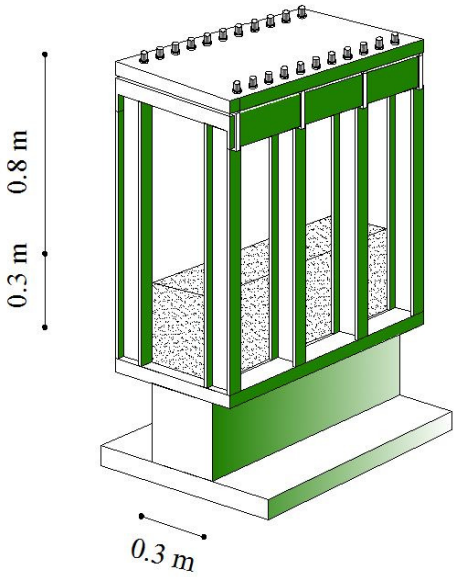

Figure 3.2 – Sketch of the cross-section of the LOWT.

The LOWT has been used since 1989 in several extensive experimental studies, contributing to an improvement of the knowledge of the bottom boundary layer structure and sediment transport mechanisms in wave and combined wave-current conditions (see Ribberink et al., 2008 and van der Werf et al., 2009 for a review). Further details of the LOWT can be found in Ribberink and Al-Salem (1994) and Dohmen-Janssen (1999).

3.2.2 Steering Signal

The steering signal of the piston has to be formulated in order to reproduce the desired hydraulic conditions in the test section. In the present experiments a regular sawtooth oscillatory flow with different degrees of acceleration skewness was devised (with or without a net current) as well as an oscillatory flow with both velocity and acceleration skewness. Previous experimental and theoretical work with sawtooth-shaped waves considered different expressions for the velocity (e.g., Hamm et al., 1998, Drake and Calantoni, 2001, Watanabe and Sato, 2004, van der A et al., 2010). In the TRANSKEW experiments a more general expression for velocity- and acceleration-skewed oscillatory flows was developed (Abreu et al., 2010b) and used to drive the LOWT piston, surpassing some limitations of the previous existing formulas. The new formulation is presented in detail in the next chapter. The regular horizontal free-stream velocity is given by the general form:

$$u(t) = U_w f \frac{\left[\sin(\omega t) + \dfrac{r\sin\phi}{1+\sqrt{1-r^2}}\right]}{\left[1 - r\cos(\omega t + \phi)\right]}, \tag{3.1}$$

where the parameter r is an index of skewness or nonlinearity ($-1 < r < 1$), ϕ is a waveform parameter related to the biphase (e.g., Elgar and Guza, 1985; Leykin et al., 1995) and f is a non-dimensional factor that forces the velocity amplitude to be equal to U_w ($f = \sqrt{1-r^2}$). Eq. (3.1) represents a wide range of nearshore nonlinear wave orbital velocity shapes, depending on the value that the waveform parameter ϕ ($-\pi/2 \le \phi \le \pi/2$) takes. A purely acceleration-skewed flow (i.e., sawtooth wave) is obtained for $\phi = 0$. A pure velocity-skewed flow (e.g., cnoidal wave) is achieved for $\phi = -\pi/2$. Values of ϕ between 0 and -π/2 yield wave forms with both velocity and acceleration skewnesses ($\langle u^3 \rangle \neq 0$ and $\langle a^3 \rangle \neq 0$).

For the particular conditions of combined oscillatory-current flow, a net current, U_0, was added to the oscillatory signal imposed by Eq. (3.1).

3.2.3 Experimental test conditions

The hydraulic conditions in the LOWT test section consisted of a repetition of regular oscillatory flows. Three major flow categories were considered: Series A (4 conditions) consisted of regular oscillatory flows with different degrees of acceleration skewness, β, and flow periods, T; Series B (4 conditions) considered acceleration-skewed oscillatory flows with an opposing collinear net current (U_0) of different strengths that mimics the undertow; and Series C (3 conditions) consisted of oscillatory flows of different periods with both velocity and acceleration skewness, R and β, respectively. The test parameters were planned to obtain sheet flow regime for every test condition (as shown in Section 3.3.2) and to satisfy the working limits of the LOWT, as the range of possible velocity and acceleration amplitudes and oscillating periods within the test section are restricted by the limited movement of the piston (Ribberink and Al-Salem, 1994).

Table 3.1 – TRANSKEW experimental conditions (target values).

Condition	U_w (m/s)	U_0 (m/s)	T (s)	r (-)	ϕ (rad)	β (-)	R (-)
A1	1.2	0	7	0.30	0	0.65	0.50
A2	1.2	0	10	0.30	0	0.65	0.50
A3	1.2	0	7	0.50	0	0.75	0.50
A4	1.2	0	10	0.50	0	0.75	0.50
B1	1.2	-0.2	7	0.30	0	0.65	0.50
B2	1.2	-0.4	7	0.30	0	0.65	0.50
B3	1.2	-0.2	7	0.50	0	0.75	0.50
B4	1.2	-0.4	7	0.50	0	0.75	0.50
C1	1.2	0	7	0.50	-π/4	0.65	0.60
C2	1.2	0	10	0.50	-π/4	0.65	0.60
C3	1.2	0	7	0.38	-π/2	0.50	0.60

Table 3.1 lists the target characteristics of the 11 hydraulic conditions tested in the tunnel. To exemplify some results obtained from Eq. (3.1), Figure 3.3 plots the target free-stream velocities and the corresponding accelerations, *a*, for tests A3, C1 and C3. Clearly the most striking difference is the acceleration curve for test A3.

The maximum opposing current magnitude of tests B2 and B4 (U_0 = -0.4 m/s) is representative of the conditions found in nature under large waves (Masselink and Black, 1995; Reniers et al., 2004b).

Figure 3.4 presents the grain size distribution of the quartz sand (ρ_s = 2650 kg/m^3) considered in the experiments as resulting from VAT (Visual Accumulation Tube) analysis. The sand (Figure 3.5) is well-sorted with a median grain diameter, d_{50} = 0.20mm and geometric standard deviation σ_g = 1.18. The porosity of the sand, ε_0, was also determined experimentally during the various tests considering different samples of the same sediment type: the average value was equal to 0.4.

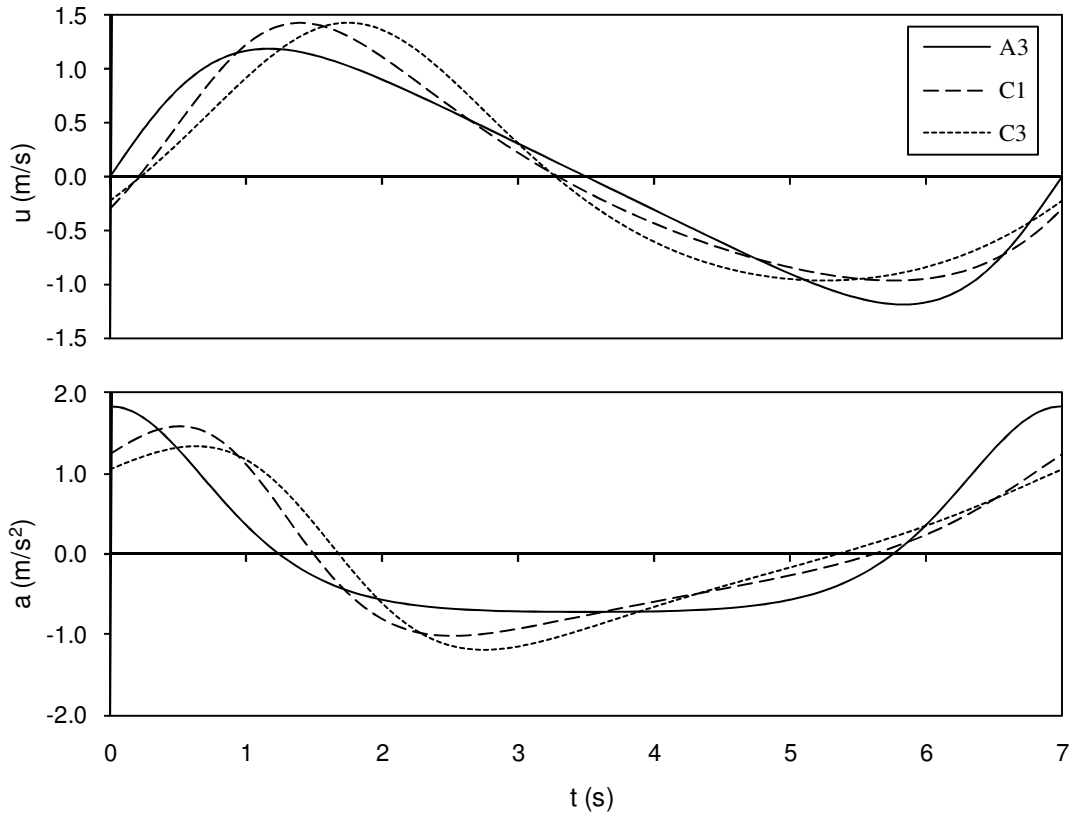

Figure 3.3 – Time series of the free-stream target velocities and corresponding accelerations for A3, C1 and C3.

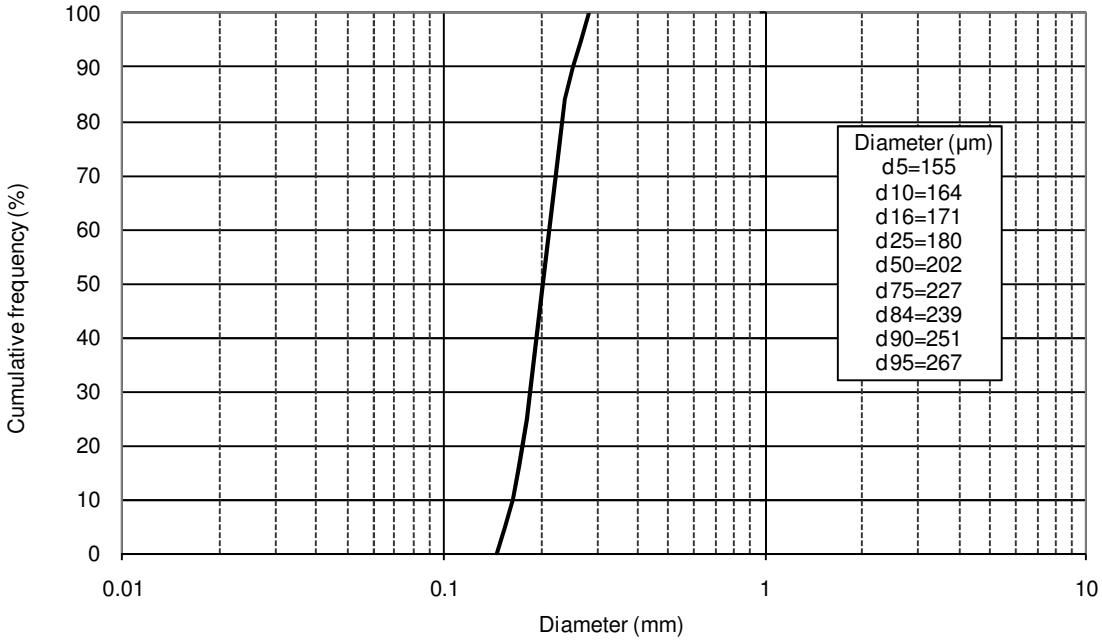

Figure 3.4 – Grain size distribution of the sand used in the experiments.

Figure 3.5 – Close-up photograph of the sand used in the experiments.

3.2.4 Instrumentation

During the experiments different instruments were deployed along the tunnel section. A brief description of the measuring instruments used during the present experiments is offered in the following.

Laser Bed Level Profiler System (LBP)

The Laser Bed Profiler, LBP, consists of a trolley moving along the tunnel test section which is fitted with a laser diode that sends out an across-flow vertical laser sheet approximately 0.5 mm thick over the entire tunnel width, and a camera positioned at an angle of 45º which records the reflected light

from the bed (Figure 3.6 and Figure 3.7). The main hardware and data processing algorithms were developed by Deltares. The output of the bed profiler is the bed elevation in x,y,z-coordinates with a vertical resolution of 1 mm. At every centimetre along the tunnel length, the bed level was recorded, providing a detailed description of the height of the sand bed. A more detailed description of LBP system can be found in van der A (2010), section 3.6.

Figure 3.6 – Laser Bed Level Profiler in the LOWT (front view and side view).

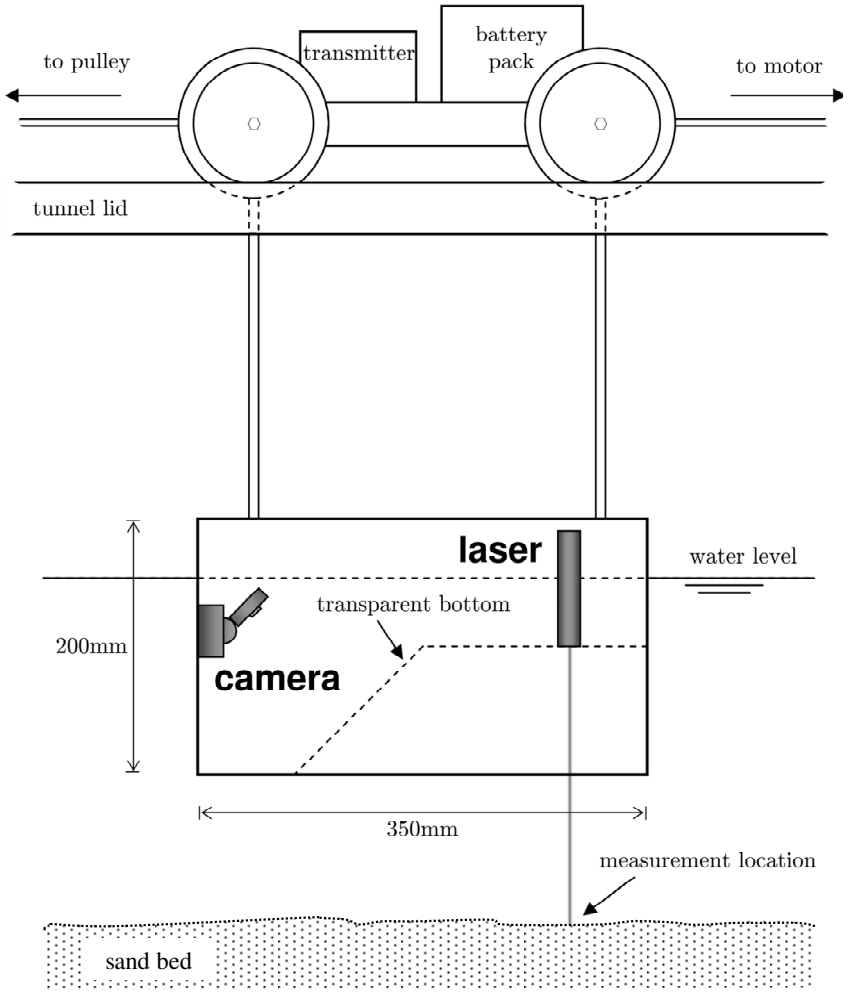

Figure 3.7 – Sketch of the Laser Bed Level Profiler (adapted from van der A, 2010).

ElectroMagnetic Flow meter (EMF)

The flow velocity measurements above the oscillatory flow boundary layer were performed using an Electromagnetic Flow Meter (EMF) (Figure 3.8). The device employs Faraday's Induction Law for the measurement of the velocity of a conductive liquid moving across the magnetic field. The sampling frequency was 100 Hz and the signals were collected 30cm above the bed in a cylindrical control volume 5 mm thick by 50 mm diameter.

Figure 3.8 – ElectroMagnetic Flow meter (EMF).

Vectrino Velocimeter (ADV)

A single-point Acoustic Doppler Velocimeter (ADV - Nortek Vectrino) was used to obtain time-dependent velocities in the tunnel (Figure 3.9). The probe consists of three receive transducers, each mounted inside the receiver arm, and a transmit transducer located at the bottom end of the stem. The Vectrino velocimeter measures the fluid velocity using the Doppler effect, by transmitting short pairs of sound pulses, listening to their echoes and measuring the change in pitch or frequency of the returned sound. The instrument allows the measurement of the three velocity components in relatively high concentrations of sediments.

Figure 3.9 – Acoustic Doppler Velocimeter (ADV).

Acoustic Doppler Velocitymeter Profiler (ADVP)

The Acoustic Doppler Velocitymeter Profiler (Hurther and Lemmin, 2001) provides detailed velocity measurements from approximately 150 mm above the bed to within the sheet flow layer. It is composed of a sensor emitting at 2 MHz and two receivers positioned at the same depth (in this experiment about 35 cm above the bed) and 7.9 cm to the centre of the emitter (Figure 3.10). The acoustic pulse is repeated at 1.6 kHz. The phase shift of the backscattered acoustic signal is recorded every 4 μs. This enables to deduce velocities along the receivers beam axis over a whole profile with a vertical resolution of about 3 mm. Horizontal and vertical velocities are geometrically reconstructed from these components. Thirty two successive phase shifts are used to derive one value of the velocity, leading to an equivalent acquisition frequency of 50 Hz. The analysis of the intensity of the received acoustic signal also enables the estimation of the SFL boundary evolution with time.

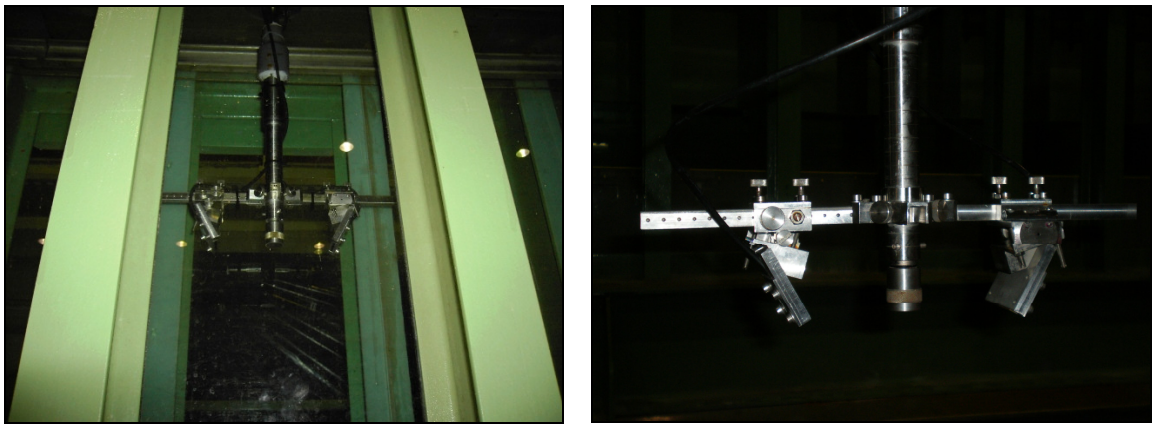

Figure 3.10 – Acoustic Doppler Velocity meter Profiler (ADVP).

Ultrasonic Velocity Profiler (UVP)

The Ultrasonic Velocity Profiler (UVP, MetFlow) provides detailed velocity profiles consisting of 128 points measured along the axis of the probe (Figure 3.11). The probe transmits a short emission of ultrasound along the axis in which the probe is pointing and, when this hits a moving particle, part of the ultrasound energy scatters from the particle, echoing back. The UVP software calculates the position and velocity of the particle and the time lag between the transmission of ultrasound and the reception of echoes. During the experiments, the probe was fitted in a plastic mounting which was connected to a stainless steel rod at a 45° angle to the horizontal. Known the angle of the probe, the horizontal velocity can be determined from the velocity component measured along the beam axis.

Figure 3.11 – Ultrasonic Velocity Profiler (UVP).

Transverse Suction System (TSS)

Time-averaged concentrations were measured using ten transverse suction samplers with an inner diameter of 3 mm (Figure 3.12). The device is described in Bosman et al. (1987) and the measurements typically concern the z = [25 − 250] mm range. The left panel of Figure 3.13 shows the 10 peristaltic pumps used to drive the suction in a direction normal to the flow at different levels. Some of the buckets used to collect the sand/water samples are also shown. The right panel of Figure 3.13 shows the calibrated tubes from where the volume of sand was obtained. The median grain size was determined with a sediment settling tube (VAT - Figure 3.14), from the fall velocity.

Figure 3.12 – Probe of Transverse Suction System .

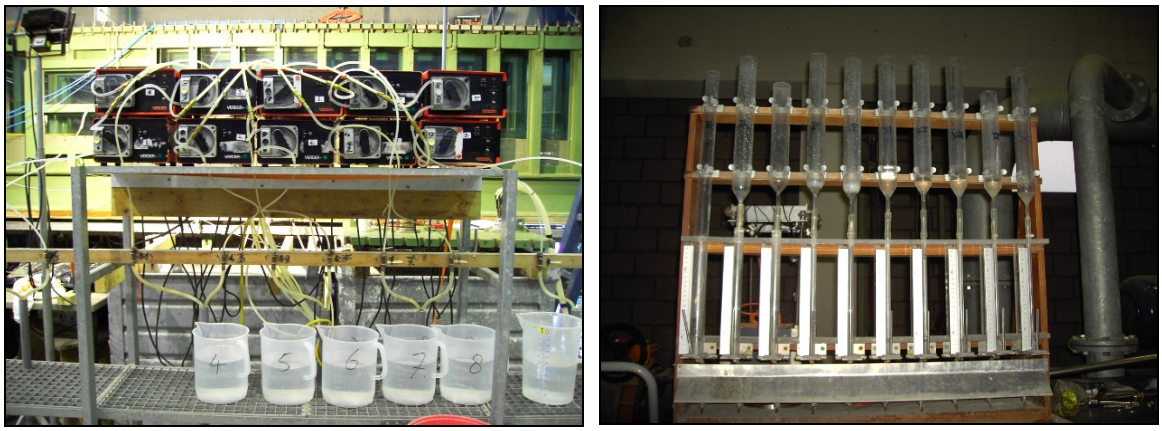

Figure 3.13 – Left panel: peristaltic pumps to drive the suction and buckets to collect the sand samples. Right panel: calibrated tubes used to obtain the volume of sand.

Figure 3.14 – Visual Accumulation Tube (VAT).

Optical Concentration Meter (OPCON)

The optical concentration meter (OPCON) provides time dependent suspended concentration measurements in the range of 0.1-50 g/l (Figure 3.15). The device emits a horizontal light beam between a transmitter and a receiver that is orientated perpendicular to the oscillatory flow. The volume concentration is measured based on the extinction of the infra-red light.

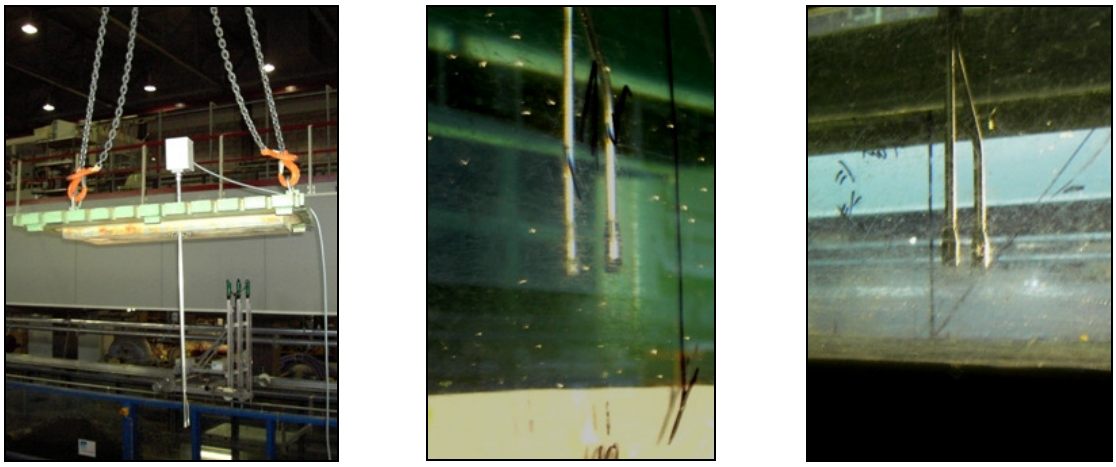

Figure 3.15 – Optical concentration meter (OPCON).

Conductivity Concentration Meter (CCM)

Detailed measurements of instantaneous sediment concentration in the sheet flow layer were done with two conductivity concentration meter (CCM) probes. The CCM probes were developed for the measurement of large sediment concentrations, in the range of 100-1600 g/l. Through a four-point electro-resistance method, the electrical conductivity of the sand/water mixture is measured with a sampling frequency of 1000 Hz and can be converted in sand concentrations (see Ribberink and Al-Salem, 1995, for further details).

The two probes were positioned 11 mm apart in the streamwise direction and were inserted through the bottom of the tunnel, as shown in Figure 3.16 (left panel). The system could be moved vertically, and placed at different elevations in the flow, with a precision of 0.1 mm, penetrating in the sheet flow layer from bellow. When the sensors were above the bed level, the intrusive nature of the probes lead to some residual scour holes that could interfere somewhat with the results (Figure 3.16, right panel). However, as the measurement volume is made above the probe tips, where the flow was relatively unobstructed, the results are reliable and an important step towards the understanding of the processes inside this thin sand/water mixture layer. At present, this is still the most reliable device to measure sediment concentrations within the sheet flow layer.

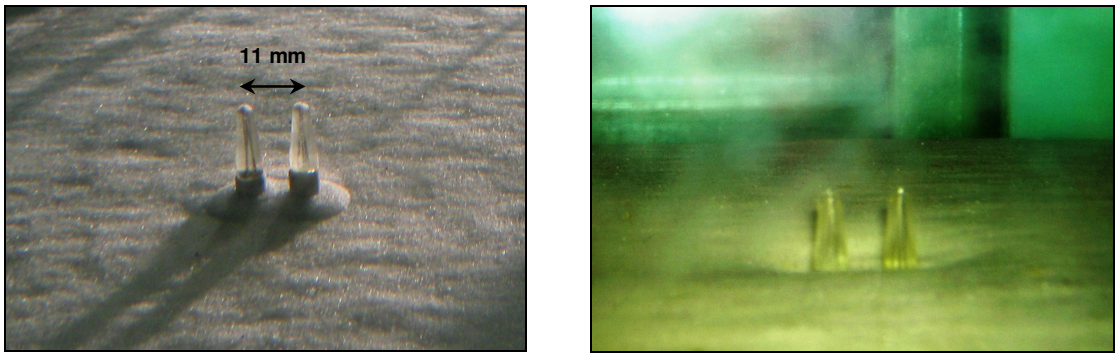

Figure 3.16 – Left panel: distance between the probes. Right panel: residual scour holes due to the insertion of the probes.

Acoustic Backscatter Sensor (ABS)

The Acoustic Backscatter Sensor (AQUAScat 1000R, by AquaTec) provides detailed concentration measurements down to 5 mm above the no-flow bed (Thorne and Hanes, 2002). The ABS was mounted in one of the top lids of the LOWT and did not perturb the flow (Figure 3.17). The device comprises three transducers working, respectively, at 1.0, 2.0 and 4.0 MHz, that operate as transceivers, transmitting and receiving. The backscatter profiles were collected at 80 Hz with a 5-mm bin size up to the top of the sheet flow layer.

Figure 3.17 – Acoustic Backscatter Sensor (ABS).

3.2.5 Measuring plan

The measuring program was divided in two phases:

- the first part (M1) consisted of net sand transport rates measurements;

- the second part (M2) consisted of detailed measurements of time-dependent sand concentrations and flow velocities.

In the M1 experiments, a total of 43 runs corresponding to the 11 hydraulic conditions listed in Table 3.1 were conducted. In average, each run had a duration of 580 s. The bed profile before and after each run was measured with the Laser Bed level Profiler system (LBP) and the free-stream velocity was measured with the ElectroMagnetic Flow meter (EMF). The sand collected from the sediment traps located at both ends of the tunnel (and for Series B, also in the recirculation system trap) were weighed underwater and analysed in the Visual Accumulation Tube (VAT) to determine the particle size distribution. Net transport rates were then computed from masses of sand and the volume change of sand along the tunnel test section, using a mass conservation method (see section 3.3).

In the M2 tests, different measuring instruments were deployed at different sections of the LOWT: ABS – Acoustic Backscatter System, UVP – Ultrasonic Velocity Profiler, ADVP - Acoustic Doppler Velocity meter Profiler, ADV – Vectrino Velocimeter, CCM – Conductivity Concentration Meter and OPCON - Optical Concentration meter. These allowed the measurement of time-dependent flow and sand concentrations in the suspension and sheet flow layer. The vertical distribution of time-averaged suspended sediments concentrations and the suspended sand grain size were measured with the TSS - Transverse Suction System.

The M2 measurements were made for 5 selected conditions (A1, A3, B2, B4, C1) and around 80 runs were carried out. In average, each run had a duration of 250 s. These measurements allow the estimation of important quantities in sediment transport dynamics, such as bed shear-stresses, roughness heights, sediment fluxes and sheet flow layer characteristics (e.g., thickness of the layer, erosion depth). It is noticed that the flow is ideally horizontally-uniform along the LOWT. Hence, theoretically, all instruments could be placed simultaneously at different sections. However, as most of the instruments are intrusive, affecting the flow near them, the placement of the probes was carefully selected to interfere the least as possible with the measurements.

Each run of a given test is designated as M######, where the second number is either 1 or 2, corresponding to M1 or M2, the 3rd and 4th cases are the condition name (see Table 3.1), and the last three cases are a sequential integer starting at 1 corresponding to the run number of a given test condition.

This chapter concerns the measurements obtained from sediment traps, LBP, EMF, ADVP and CCM. Results from other devices are presented elsewhere (e.g., Ruessink et al., 2011).

3.3 Net transport rates

3.3.1 Methodologies

The mass conservation method was used to compute the net transport rates. For that purpose, the sediment continuity equation was integrated along the test section from the LBP data with corresponding boundary conditions. These consist of the sand mass collected in the traps of the two cylindrical risers on both ends of the LOWT and in the recirculation pipe in the case of a net current (Figure 3.1). As two boundary conditions are available, the sediment continuity equation

$$\frac{\partial q_s}{\partial x} + \frac{\partial z}{\partial t}(1-\varepsilon_0) = 0 \tag{3.2}$$

can be integrated from the left side and also from the right side of the test section, giving two estimations of the net transport rates, q_s. The following equations were used:

$$\text{Left estimate: } q_{sm} = \frac{1}{\Delta t_{run} W}\left(\Delta V_l (1-\varepsilon_0) - \frac{G_l}{\rho_s}\right) \tag{3.3}$$

$$\text{Right estimate: } q_{sm} = -\frac{1}{\Delta t_{run} W}\left(\Delta V_r (1-\varepsilon_0) - \frac{G_r}{\rho_s}\right) \tag{3.4}$$

where $\Delta V_{l/r}$ represents the total eroded volume (including pores) from the x-position of the tunnel test section to the left/right of the measurement location during one test [m^3]; ε_0 the porosity; $G_{l/r}$ the total weight of the sand collected in the left/right trap [kg]; ρ_s the density of sand [2650 kg/m^3]; W the width of the tunnel test section [0.30 m]; Δt_{run} the test duration [s] and q_{sm} the net transport rate without pores per unit width and time for one test at the measurement location [m^2/s].

As an example, Figure 3.18 (upper panel) represents the bed levels measured before and after one of the C3 runs. The oscillations observed near the extremities of the test section are end effects. Between x = 2 to 9 m both bed levels are almost equal denoting a constant transport rate not influenced anymore by the end effects. The middle panel of Figure 3.18 represents the computed net mass transport rates [kg/m/s] along the tunnel test section. Between x = 2 to 4 m the transport rate values are nearly constant and therefore representative of the q_{sm} within the tunnel for this test.

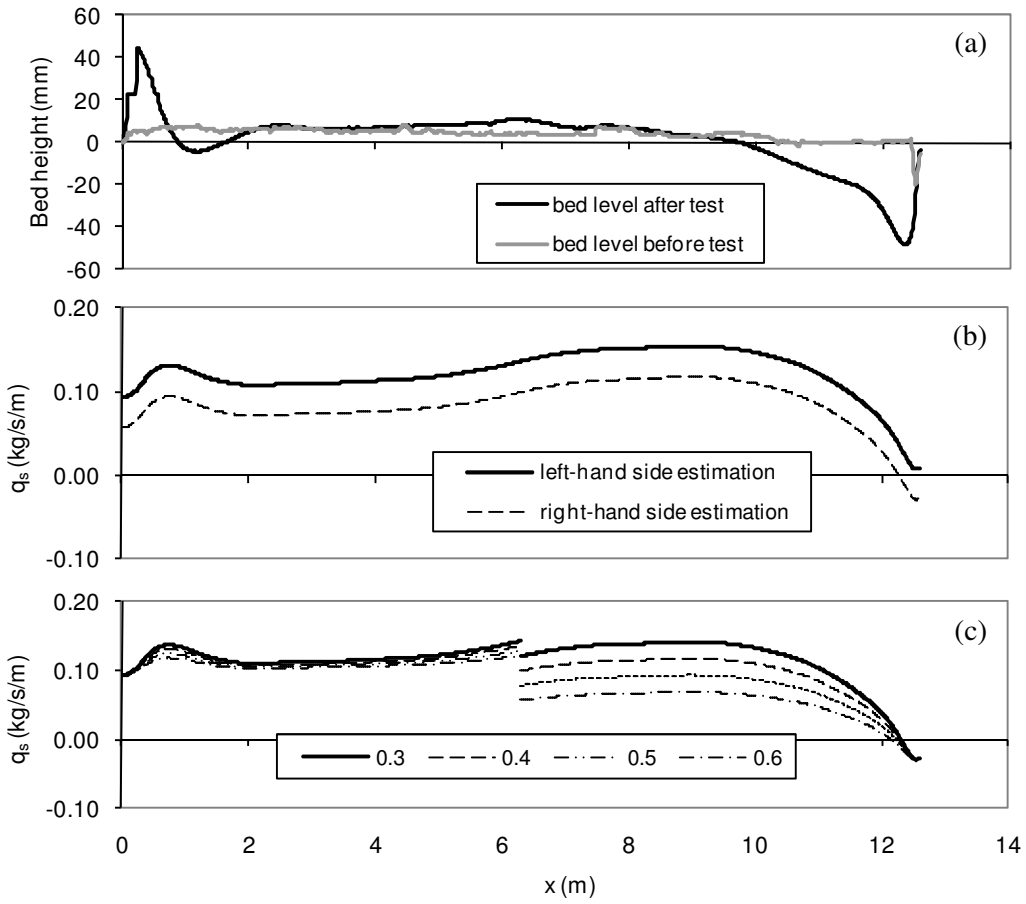

Figure 3.18 – (a) Bed levels measured before and after the test C3 (run M1C3004); (b) Left- and right-computed net transport rates along the tunnel and (c) Sensitivity of $q_{s,left}$ and $q_{s,right}$ for change of porosity.

Generally the right and left estimates of q_{sm} did not match precisely. This is due to the presence of measurement errors: uncertainty or change in porosity (due to the compaction of sand due to the removal and refilling of sand after each new test), error in the bed level measurement and loss of sand from the system during the emptying of sand traps (this is more likely to occur in the trap of the recirculation system). Figure 3.18c exemplifies that the net sand transport rate estimates are sensitive to the porosity ε_0 if the boundary condition is based on the trap with the least amount of sand (in this case the right end). To better elucidate the differences obtained from Eq.s (3.3) and (3.4), only part of the resulting curves are presented in Figure 3.18c, resulting in the discontinuity in the middle of the tunnel. On the left, the curves correspond to the estimates obtained from Eq. (3.3), whereas, on the right, they were obtained using Eq. (3.4). The differences due to ε_0 are expected whenever the last term in Eq.s (3.3) and (3.4) is not dominant in relation to the preceding term.

To complement the previous analysis, Figure 3.19 shows a test where a superimposed current coexist with the oscillatory motion. The results concern one of B2 condition runs. The end effects are now more evident at the left end of the test section and the transport rate remains reasonably constant for

$x > 3$ m. The analysis to the porosity confirms that it is in the left end, where the trap has less amount of sand, that the sand transport rates are more sensitive to ε_0.

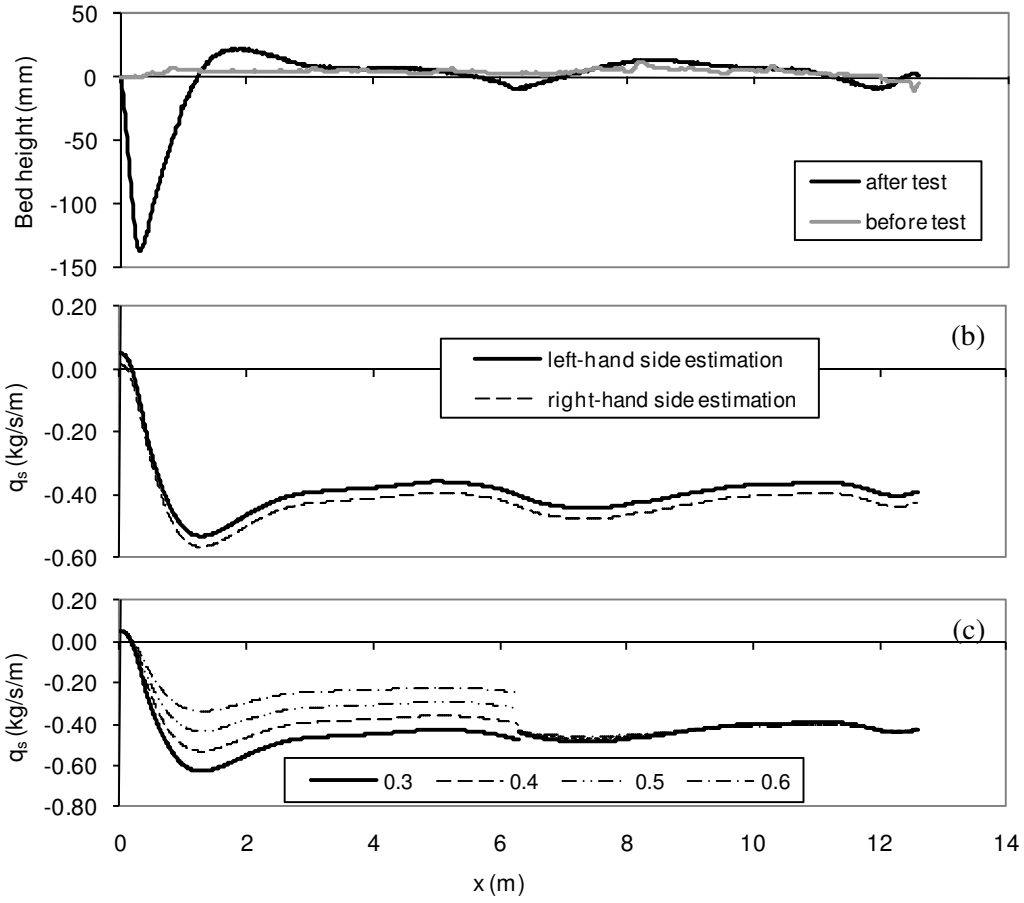

Figure 3.19 – (a) Bed levels measured before and after the test B2 (run M1B2001); (b) Left- and right-computed net transport rates along the tunnel and (c) Sensitivity of $q_{s,left}$ and $q_{s,right}$ for change of porosity.

The net transport rates presented here are based on ε_0 =0.4 (see section 3.2.3) and use the largest of the weights as boundary condition. For most of the conditions the difference between this estimate and the transport rate based on the mean value of the right and left estimative is less than 5% except for B1, B3 and C3 conditions, for which is equal to 11.5%, 40% and 15%, respectively.

As described in Koelewijn and Ribberink (1994), measurements of the velocity profile across the tunnel (with a sinusoidal wave and a net current) show that the oscillating component of the flow is almost constant over the cross-section, while the mean velocity is changing due to a thicker side wall boundary layer. Hence, the effect of the lateral boundary layers in the flow means that in combined oscillatory flow-current tests the bulk measurements of net transport rates, as they are width-averaged values, have to be corrected to obtain equivalent transport rates without the presence of the tunnel's lateral walls (e.g., Koelewijn and Ribberink, 1994; Dohmen-Janssen et al. 2002). Koelewijn and

Ribberink (1994) describe a method to correct the net sediment transport rates based on the hypothesis that the net transport rate, q_s, is proportional to the third-order velocity moment, $\langle u^3 \rangle$.

For the present flow conditions in Series B, one assumes a proportionality between q_s and $<\tau^{3/2}>$, following Nielsen's (2006) bedload formulation. According to this, the following expression is derived between the corrected (q_{sc}) and the measured (q_{sm}) net transport rate:

$$q_{sc} = \frac{\overline{\langle \tau_{y=0}^{3/2} \rangle}}{\overline{\langle \tau^{3/2} \rangle}} q_{sm} \tag{3.5}$$

where the over bar denotes averaging over the cross-section, the angle brackets denote a time-averaging, and $\tau_{y=0}$ represents the bed shear-stress in the middle of the tunnel. The ratio in Eq. (3.5) represents a correction factor, C. Assuming that $\tau(t) = 1/2 \cdot \rho f_{cw} u(t)^2$ with $u(t) = U_0 + \tilde{u}(t)$ and $\tilde{u}(t)$ is given by Eq. (3.1) and that the wave-current friction factor f_{cw} is in a first approximation constant in time and along the tunnel cross section, the expression for the correction factor C in Series B is equal to the one obtained in Koelewijn and Ribberink (1994):

$$C = \frac{\overline{< u_{max}{}^3 >}}{\overline{< u^3 >}} = \frac{\overline{U_{0,max}{}^3} + 3\overline{U_{0,max} U_{rms}{}^2}}{\overline{U_{0,max}{}^3} + 3\overline{U_{0,max}} \overline{U_{rms}{}^2}} \tag{3.6}$$

where $U_{0,max}$ represents the maximum velocity in the middle of the tunnel and U_{rms} the root-mean-square value of the oscillatory flow. The values of C in Eq. (3.6) can be computed for each test condition, using the measured U_{rms} and U_0 values (Table 3.2). For the B test conditions, the values of C are equal to 1.16 for B1 and B3 and 1.17 for B2 and B4.

3.3.2 Results

Table 3.2 lists the characteristics of the oscillatory flow velocity measured 30 cm above the bed during the M1 experiments, presenting, for each flow condition, the average corrected net transport rate, q_{sc}, and the relative standard deviation, σ_q, obtained from the number of runs (N) performed for each test:

$$\sigma_q = \sqrt{\frac{1}{N-1} \sum_{i=1}^{N} \left(\frac{q_{s,i} - q_{sc}}{q_{sc}} \right)^2} \,. \tag{3.7}$$

The root-mean-square value of the oscillatory velocity, U_{rms}, was maintained nearly constant for all the conditions (≈ 0.88 m/s). The amplitude Reynolds number $\left(Re = U_w A/\nu\right)$ and the relative roughness (A/k_s) enable to classify the boundary layer regime. Here, A is the near-bed wave orbital amplitude, ν is

the fluid kinematic viscosity and k_s is the Nikuradse's (1932) equivalent roughness, defined as $k_s = 30z_0$ in the fully rough turbulent regime, in which z_0 is the roughness height (roughness length scale). For the present study, involving a plane sand bed in the sheet flow regime, the Nikuradse's equivalent roughness was assumed to be proportional to the median grain size $k_s = 2.5d_{50}$ (e.g., Nielsen and Callaghan, 2003). The values of A/k_s and Re are within the range of $10^3 < A/k_s < 10^4$ and $10^6 < Re < 10^7$, locating the experiments in the limit between rough to smooth turbulent regimes (see Figure 3.20). The delineation of the flow regimes in Figure 3.20 represented by solid lines correspond to Jonsson's (1980) recommended criteria, whereas the dashed lines indicate the transition from the rough turbulent to the very rough turbulent regime according to Davies and Villaret (1997).

Table 3.2 – TRANSKEW experimental conditions (measured values).

Cond.	U_0 (m/s)	U_w (m/s)	U_{rms} (m/s)	T (s)	r (-)	ϕ (rad)	β (-)	R (-)	Re (-)	A/k_s (-)	Ψ_{max} (-)	θ_{max} (-)	N (-)	q_{sc} (kg/m/s)	σ_q (%)
A1	0	1.32	0.90	7	0.28	0.00	0.64	0.50	$1.9\cdot10^6$	$2.9\cdot10^3$	540	2.11	5	0.0539	21.6
A2	0	1.27	0.88	10	0.26	0.15	0.63	0.49	$2.5\cdot10^6$	$4.0\cdot10^3$	484	1.83	2	0.0443	2.9
A3	0	1.33	0.88	7	0.44	0.00	0.72	0.50	$2.0\cdot10^6$	$3.0\cdot10^3$	554	2.14	5	0.1137	8.3
A4	0	1.29	0.86	10	0.45	0.09	0.72	0.49	$2.5\cdot10^6$	$4.0\cdot10^3$	496	1.88	4	0.0847	4.7
B1	-0.22	1.30	0.89	7	0.28	0.00	0.64	0.50	$1.8\cdot10^6$	$2.9\cdot10^3$	516	2.05	7	-0.1133	21.0
B2	-0.44	1.28	0.88	7	0.28	0.00	0.64	0.50	$1.8\cdot10^6$	$2.9\cdot10^3$	511	2.00	3	-0.3826	24.0
B3	-0.22	1.31	0.86	7	0.42	0.00	0.71	0.50	$1.9\cdot10^6$	$2.9\cdot10^3$	533	2.09	4	-0.0489	21.0
B4	-0.44	1.30	0.86	7	0.42	-0.09	0.71	0.51	$1.9\cdot10^6$	$2.9\cdot10^3$	538	2.06	3	-0.2241	9.3
C1	0	1.25	0.86	7	0.43	-0.93	0.61	0.59	$2.4\cdot10^6$	$3.3\cdot10^3$	668	1.94	4	0.1845	3.4
C2	0	1.35	0.94	10	0.42	-0.98	0.60	0.59	$4.1\cdot10^6$	$5.1\cdot10^3$	801	2.06	2	0.2797	3.6
C3	0	1.22	0.87	7	0.36	-1.37	0.53	0.59	$2.3\cdot10^6$	$3.2\cdot10^3$	636	1.85	4	0.1244	9.4

The Ψ_{max} and θ_{max} indicated in Table 3.2 represent the maximum values of the mobility number (Ψ) and of the Shields parameter (θ), respectively. Here, Ψ_{max} is given by

$$\Psi_{max} = \frac{u_{max}^2}{(s-1)\, g d_{50}}, \tag{3.8}$$

where $s = \rho_s/\rho$ is the ratio between sediment and water densities and u_{max} is the measured maximum velocity in the free-stream.

The values of the (effective) Shields parameter were computed following Nielsen (2006):

$$\theta(t) = \frac{u_\theta^{\,2}(t)}{(s-1)\, g d_{50}},\ u_\theta(t) = \sqrt{f_{2.5}/2}\left(u\cos\varphi + \frac{a}{\omega}\sin\varphi\right) \tag{3.9}$$

where the angle φ roughly represents the phase lead of bed shear stress over the free-stream velocity, u_θ (t) is the "sediment mobilization velocity", which essentially is a friction velocity that incorporates the combined effect of the bed shear-stress, proportional to u, and the pressure gradient, proportional to the near-bed flow acceleration, and $f_{2.5}$ is the roughness friction coefficient which is computed from Swart (1974) using a roughness equal to 2.5 d_{50}:

$$f_{2.5} = \begin{cases} \exp\left[5.213\left(\dfrac{A}{2.5d_{50}}\right)^{-0.194} - 5.977\right] & , \dfrac{A}{2.5d_{50}} > 1.57 \\ 0.3 & , \dfrac{A}{2.5d_{50}} \le 1.57 \end{cases}, \tag{3.10}$$

The phase difference φ in Eq. (3.9) was set to 51°, following Nielsen (2006). Although apparently similar, it is noted that due to the differences in u_{max} and u_θ, Ψ_{max} and θ_{max} will yield strikingly different numbers in magnitude.

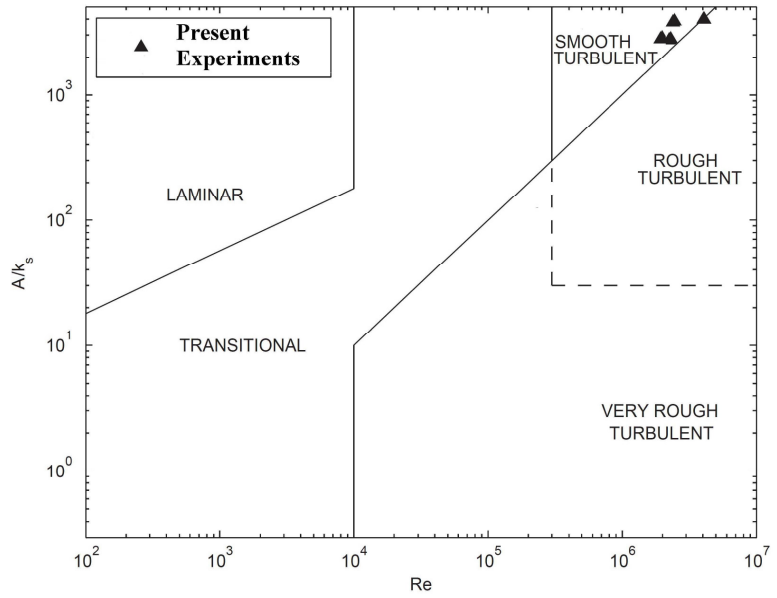

Figure 3.20 – Delineation of flow regimes illustrating the range of the present experiments (adapted from van der A, 2010)

Table 3.2 shows that all the values of Ψ_{max} and θ_{max} are greater than 300 (O'Donoghue et al., 2006) and 0.8 (Wilson, 1987), accordingly, confirming the visual observations where sheet flow plane-bed conditions were achieved for all the runs.

Figure 3.21 shows the measured net transport rates as a function of different parameters. Figure 3.21a illustrates that an increase in the acceleration skewness β leads to a larger net transport in the (positive) implied wave direction. Figure 3.21b shows a similar behaviour, only the transport rates are much larger due to the added effect of velocity skewness, R. This is better illustrated in Figure 3.21c, which

show the transport rates as a function of R. Note however, that in Figure 3.21a the net transport rates are lower for the largest flow period. However, the conditions with $R \approx 0.6$ in Figure 3.21c show an increase in transport rate with increasing flow period. This is possibly due to the 9% larger U_{rms} for the $T = 10$ s condition (C2) than for the $T = 7$ s condition (C1) (see Table 3.2).

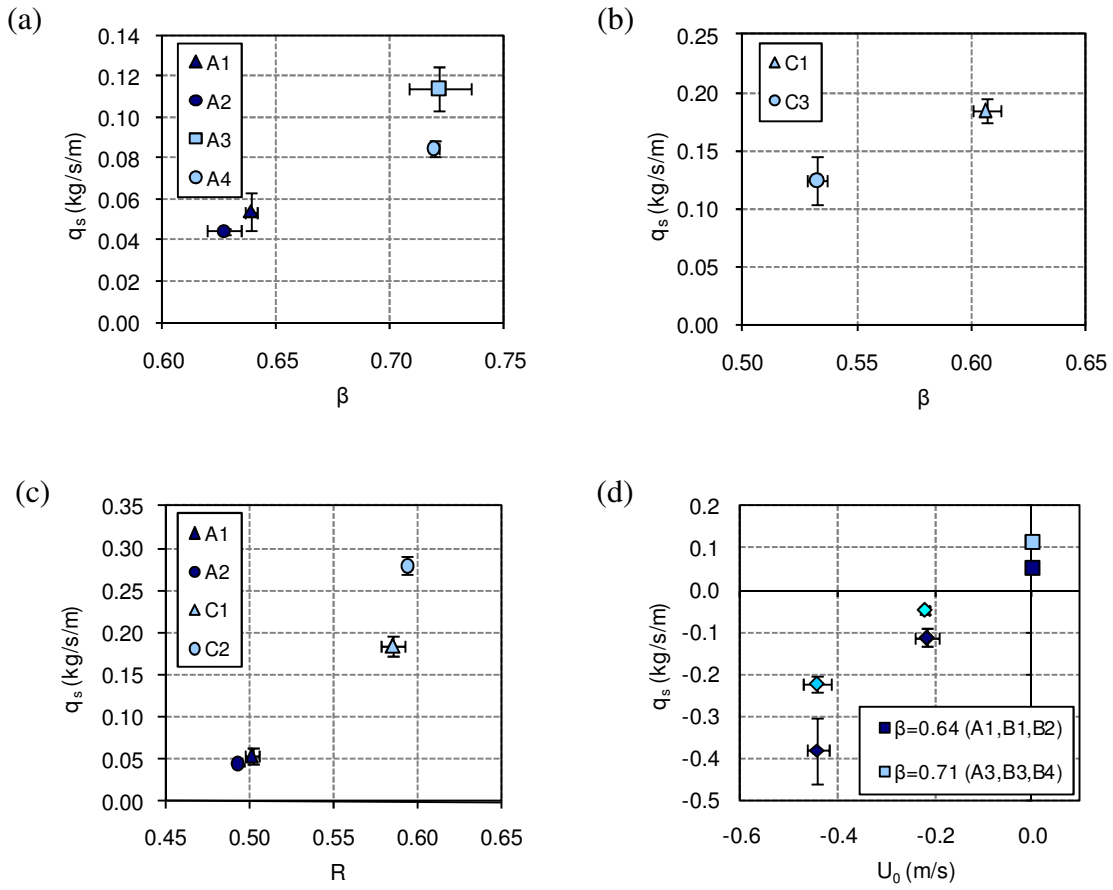

Figure 3.21 – Measured net transport rates for conditions (a) A1-A4; (b) C1, C3; (c) A1, A2, C1, C2 and (d) A1, A3, B1-B4. The error bars correspond to the standard deviation.

In Figure 3.21d, the measured net transport rates are shown for different values of the mean current velocity and two different values of $\beta \approx 0.64$ and ≈ 0.71 corresponding, respectively, to the two sets of conditions (A1, B1, B2) and (A3, B3, B4), all with the same flow period, $T = 7$ s. The results with negative U_0 show a net negative transport rate (i.e., against the direction of maximum acceleration). Also, an increase in the acceleration skewness reduces the amount of sediment transported in the negative direction.

Figure 3.22 compares the previous experimental results of net transport rates with acceleration-skewed oscillatory flows in sheet flow conditions (WS04 - Watanabe and Sato, 2004; AOFT10 - van der A. et al., 2010) with the present Series A results as a function of the maximum Shields parameter. The values of θ_{max} were computed from Eq. (3.9). The WS04 data corresponding to $\beta = 0.6$ and 0.7 are

well grouped together (open circles) while $\beta = 0.8$ show a different behaviour (open triangles). The use of a constant phase difference of $\varphi = 51°$ in Eq. (3.9), gives more importance to the acceleration effects for the bed shear stress calculations than the velocity term (first term in the brackets). Perhaps the importance of the effect of accelerations is overestimated for $\beta = 0.8$ giving rise to unrealistic high values for θ_{max}. Furthermore, the WS04 data corresponds to $d_{50} = 0.2$ and 0.74 mm. However, the coarser sediment data was not taken into account in this analysis because the q_s values show an unexpected trend with θ (see also Gonzalez-Rodriguez and Madsen, 2007). For the AOFT10 data three median grain sizes, 0.15, 0.27 and 0.46 mm were considered. The net transport rates are represented by the filled circles and the corresponding values of β are contained within $0.56 < \beta < 0.78$. The Series A data is represented by the gray squares and the corresponding values of β are $0.63 < \beta < 0.72$ (see Table 3.2). As can be seen in Figure 3.22, all data sets show an increase in q_s with θ_{max} and the values of q_s obtained in Series A are consistent with the AOFT10 and WS04 data for the same range of β.

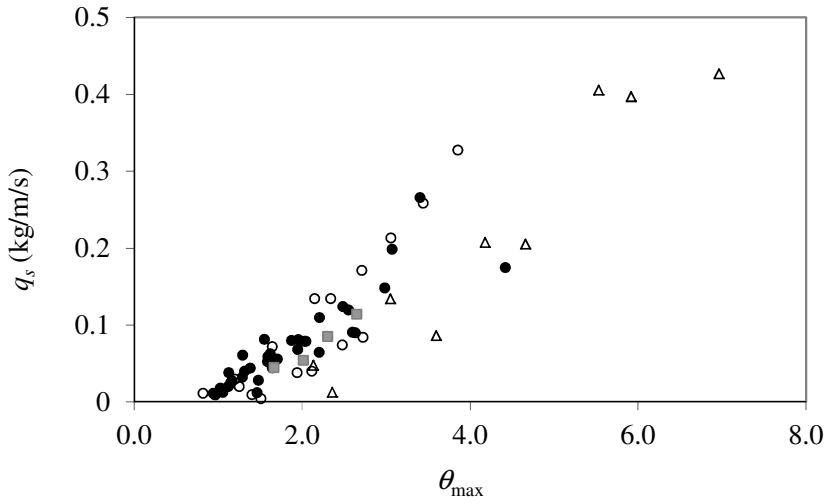

Figure 3.22 – Measured net transport rates in purely acceleration-skewed oscillatory flows: WS04 data (open circles - $\beta = 0.6, 0.7$; open triangles - $\beta = 0.8$); AOFT10 data (filled circles) and the present results in Series A (gray squares), as a function of the maximum Shields parameter.

The LOWT data also allows establishing the relative importance of the velocity and acceleration skewness in the net transport rates. The difference between the values of q_s in conditions C1 and C3 (≈0.06 kg/m/s) (see Figure 3.21b) is approximately equal to the measured value in condition A1. This result suggests that in the present experiments the contribution of velocity skewness to the total net transport rate is larger than that of the acceleration skewness for the same degree of parameter increase (β and R). This is more likely due to an increase of the skewness of the bed shear stress in the presence of velocity skewed flows as will be seen later.

3.4 Flow velocities

3.4.1 Methodologies

Phase-averaged velocities

The time-varying velocities considered in this work were measured with the Electromagnetic Flow Meter (EMF) and the Acoustic Doppler Velocity meter Profiler (ADVP).

An example of the instantaneous velocity obtained with the ADVP is shown in Figure 3.23 for Test A3. The vertical coordinate denoted z is positive upward and $z = 0$ is defined as the initial bed level at the beginning of the experiments, prior to wave action. Figure 3.23 shows that 3 cm above the bed the vertical velocity w is very small compared to the horizontal velocity u as expected for the LOWT. Also, at the reference level $z = 0$ the flow does not present velocities equal to zero. This is due to the development of the sheet flow layer structure that mobilizes fluid and particles at lower levels. In addition, during each experiment, there were some small bed level changes of the order of a few millimetres that were accounted for in the ADVP post processing.

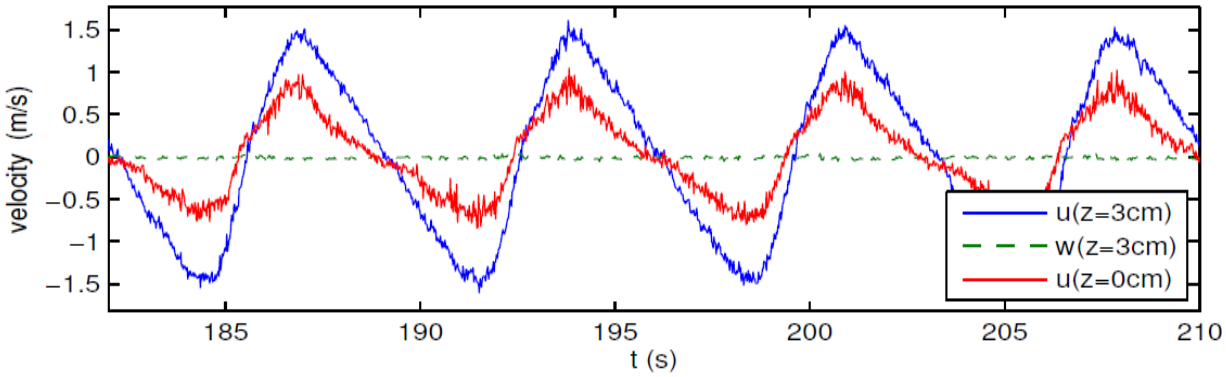

Figure 3.23 – Instantaneous velocities measured with the ADVP for Test A3: horizontal velocities u at $z = 0$ and z = 3cm and vertical velocity w for z = 3cm.

From the available number of flow cycles, N_c (≈ 36), the phase-averaged velocities, $\hat{u}$, are computed according to:

$$\hat{u}(z,t) = \frac{1}{N_c}\sum_{n=1}^{N_c} u\left(z, t+(n-1)T\right),\ 0 \le t < T\ , \tag{3.11}$$

where N_c represents the number of flow cycles.

The phase-averaged velocity $\hat{u}$ can be decomposed into mean and orbital velocities denoted, respectively, by $\bar{u}$ and $\tilde{u}$. These components are calculated as follows:

$$\overline{u}(z)=\frac{1}{N_p}\sum_{n=1}^{N_p}\hat{u}(z,n), \tag{3.12}$$

$$\tilde{u}(z,t)=\hat{u}(z,t)-\overline{u}(z), \tag{3.13}$$

where N_p is the total number of data points registered within the flow period T.

Defect law

Following Nielsen (1992), the velocities $u(z,t)$ inside the wave bottom boundary layer can be written in terms of the free-stream velocity, $u_\infty(t)$, and a velocity defect $u_d(z,t)$: $u(z,t)=u_\infty(t)-u_d(z,t)$. This equation can be written in terms of a dimensionless velocity defect complex function $D_1(z)$:

$$u(z,t)=\left(1-D_1(z)\right)u_\infty(t) \tag{3.14}$$

For laminar oscillatory flows it can be deduced (Nielsen, 1992) that:

$$D_1(z)=\exp\left(-(1+i)\frac{z}{\sqrt{2\nu/\omega}}\right) \tag{3.15}$$

Eq. (3.15) implies that the vertical scale of the laminar oscillatory flow is the Stokes length $\sqrt{2\nu/\omega}$. For turbulent flows, Nielsen (1992, p. 44) suggests that a similar expression can be used:

$$D_1(z)=\exp\left(-(1+i)\left(\frac{z}{z_1}\right)^{p_1}\right) \tag{3.16}$$

which reduces to (3.15) for p_1=1 and $z_1=\sqrt{2\nu/\omega}$. Hence, z_1 represents the velocity decay length scale, whereas p_1 is associated to the velocity gradients. For example, smaller values of p_1 imply larger velocity gradients and, consequently, enhanced bed shear stress. The parameters z_1 and p_1 are derived from an analysis of the primary harmonic of the velocity records.

It is noticed that if z_1 and p_1 adjust well our data, it means that the vertical velocity profile can be estimated with somewhat reduced information. They allow to obtain $D_1(z)$, which combined with $u_\infty(t)$, provide values for $u(z,t)$ through Eq. (3.14) (e.g., Abreu et al., 2010a). In addition, the velocity gradients resulting from this process can be used to assess bed shear stresses.

To obtain z_1 and p_1 the measured velocities $u(z,t)$ are decomposed in a Fourier series:

$$u(z,t)=\frac{a_0(z)}{2}+\sum_{n=1}^{+\infty}\left(a_n(z)\cos(n\omega t)+b_n(z)\sin(n\omega t)\right), \tag{3.17}$$

where n represents the rank of the harmonics (n = 1 corresponds to the fundamental component) and a_n and b_n are the Fourier coefficients. Then, the first harmonic coefficients a_1 and b_1 are computed:

$$a_1(z) = \frac{2}{N_p}\sum_{j=1}^{N_p}\hat{u}\left(z, j\frac{T}{N_p}\right)\cos\left(\omega j\frac{T}{N_p}\right), \tag{3.18}$$

$$b_1(z) = \frac{2}{N_p}\sum_{j=1}^{N_p}\hat{u}\left(z, j\frac{T}{N_p}\right)\sin\left(\omega j\frac{T}{N_p}\right), \tag{3.19}$$

and are converted to magnitude, r_1, and phase coefficients, ϕ_1:

$$r_1(z) = \sqrt{a_1^2(z) + b_1^2(z)}, \tag{3.20}$$

$$\phi_1(z) = \tan^{-1}\left(b_1(z)/a_1(z)\right). \tag{3.21}$$

These coefficients are directly linked to the real and imaginary parts of $D_1(z)$ (see Figure 3.24):

$$\mathrm{Re}\{D_1(z)\} = 1 - \frac{r_1(z)}{r_\infty}\cos\left(\phi_1(z) - \phi_\infty\right) \tag{3.22}$$

$$\mathrm{Im}\{D_1(z)\} = \frac{r_1(z)}{r_\infty}\sin\left(\phi_1(z) - \phi_\infty\right) \tag{3.23}$$

where r_∞ and ϕ_∞ represents the free-stream values of r_1 and ϕ_1.

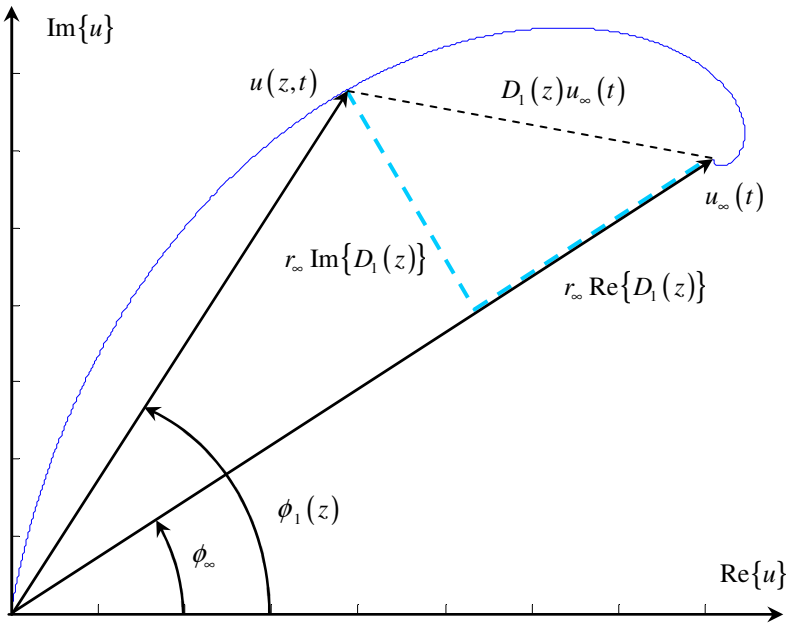

Figure 3.24 – Visualisation of $u(z,t)$ in the complex plane.

Figure 3.24 schematises the result of Eq. (3.14) in which $u(z,t)$ is constructed geometrically in the complex plane (Nielsen, 1992, Figure 1.2.6). The solution gives a spiral that starts at the origin of the coordinates, corresponding to the bed where the velocity is zero, and ends at the free-stream velocity, where the distance to the origin equals the amplitude of u_∞. The free-stream velocity and a generic point $u(z,t)$ are represented as rotating vectors in the complex plane. For a certain elevation z, the module of the vector $u(z,t)$ represents the velocity amplitude and $\phi_1 - \phi_\infty$ correspond to the differences in phase between $u(z,t)$ and $u_\infty(t)$. The values of these phase differences, $\phi_u(z)$, can be calculated from $D_1(z)$:

$$\phi_u(z) = \phi_1(z) - \phi_\infty = \tan^{-1}\left(\frac{\mathrm{Im}\{D_1(z)\}}{1-\mathrm{Re}\{D_1(z)\}}\right). \tag{3.24}$$

The real and imaginary parts of $D_1(z)$ can be rewritten as:

$$\mathrm{Re}\{D_1(z)\} = \sqrt{|D_1(z)|^2 - \mathrm{Im}\{D_1(z)\}^2}\,, \tag{3.25}$$

$$\mathrm{Im}\{D_1(z)\} = \frac{|D_1(z)|}{\sqrt{1+\dfrac{1}{\tan^2\left(-A\mathrm{rg}\{D_1(z)\}\right)}}}\,. \tag{3.26}$$

With $ln|D_1(z)|$ and Arg $D_1(z)$ derived from the measurements, the two parameters z_1 and p_1 are derived as shown in Figure 3.25.

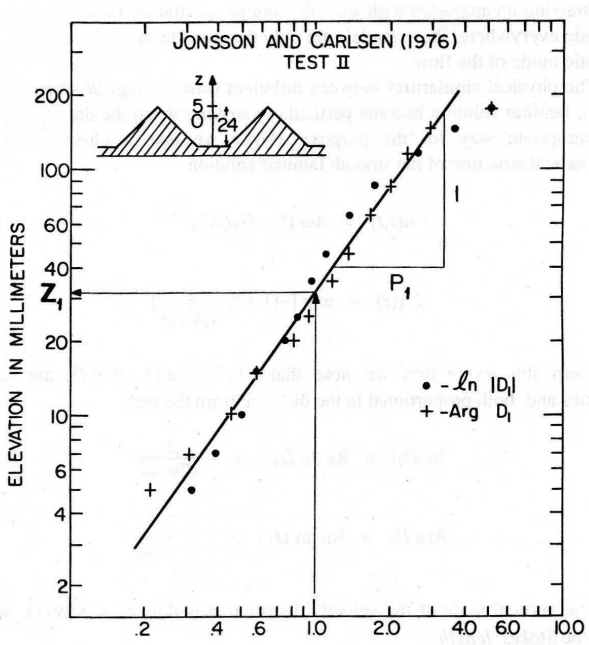

Figure 3.25 – $-ln|D_1(z)|$ and -Arg $D_1(z)$ derived from the measurements of Jonsson and Carlsen (1976), T = 7.9 s, $A\omega$ = 1.53 m/s and k_s/A = 0.035. The corresponding values of z_1 and p_1 are determined from the straight line on log-log (adapted from Nielsen, 1992).

3.4.2 Results

Phase-averaged velocities

Figure 3.26 exemplifies the target velocity time-series against the phase-averaged and low-pass filtered (cut-off frequency 0.53 Hz) measured values by the EMF for some of the runs. They report to the first set of experiments (M1) and concern A1, A3, B1, B4, C1 and C3 conditions. The corresponding acceleration time series were obtained by numerical differentiation of the filtered velocity time series, and are also plotted in Figure 3.26. The accelerations obtained by this procedure are local accelerations at each point $\left(a = \partial u / \partial t\right)$.

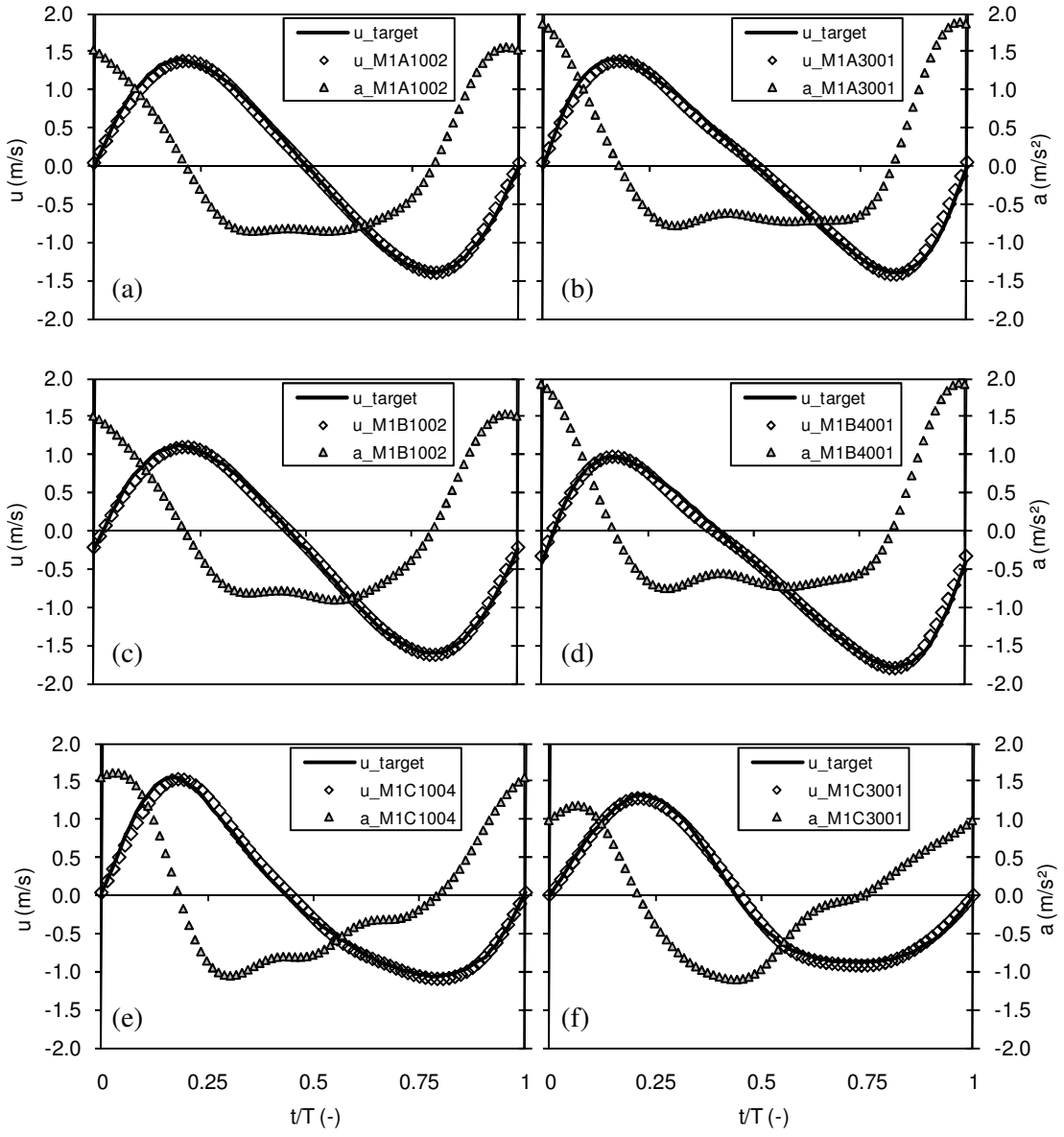

Figure 3.26 – Time series of the measured (phase-averaged) and target velocities for several runs, and the corresponding accelerations. Experimental conditions: (a) A1; (b) A3; (c) B1; (d) B4; (e) (C1) and (f) C3.

Figure 3.26 shows that the target velocities were accurately reproduced inside the LOWT. Nevertheless, some minor differences can be found between the curves, leading to somewhat different values of the velocity and acceleration skewness coefficients R and β as listed previously in Table 3.1 and Table 3.2. This is also illustrated in Figure 3.27 where the target and measured values of R and β are given for each flow condition. One observes that the values of M1 experiments are practically the same as for M2 experiments. In general, all the values of R are well reproduced, regarding the target values. This suggests that Series A and B reproduce quite well the pure accelerated skewed flows ($R = 0.5$ and $\beta \neq 0.5$). Nonetheless, with the exception of Test C3, the target values of β are slightly higher than the experimental values. For test C3 the value of β is somewhat larger than the expected 0.5, meaning that a small degree of acceleration skewness is present. Thus, this condition is not completely representative of a pure velocity-skewed flow as it was planned.

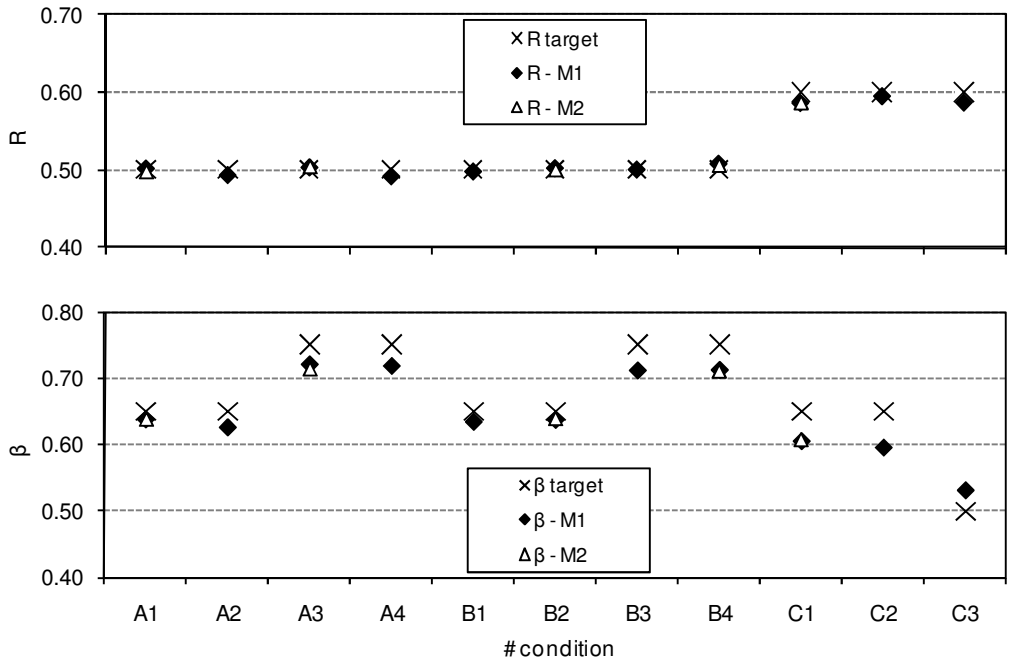

Figure 3.27 – Measured *versus* target values of the velocity and acceleration skewness coefficients, R and β, in M1 and M2 experiments.

Figure 3.28 and Figure 3.29 show results of the phase-averaged velocities for the oscillatory flow conditions without and with a net current superimposed, respectively. The data refer to the second part of the experiments (M2), where detailed measurements of time-dependent flow velocities provide a good insight of the vertical structure of $u(z)$. The results exhibit typical features of the oscillatory bottom boundary layer: the velocity magnitude first increases with distance from the bed, with an overshoot velocity within the range z = 10-30 mm from the bed and, near the bottom, the velocity times-series lead the free-stream velocity in phase. In addition, as observed in Chapter 2, the influence

of the acceleration skewness leads to a stronger overshoot velocity and a thinner boundary layer under the positive (onshore) velocities.

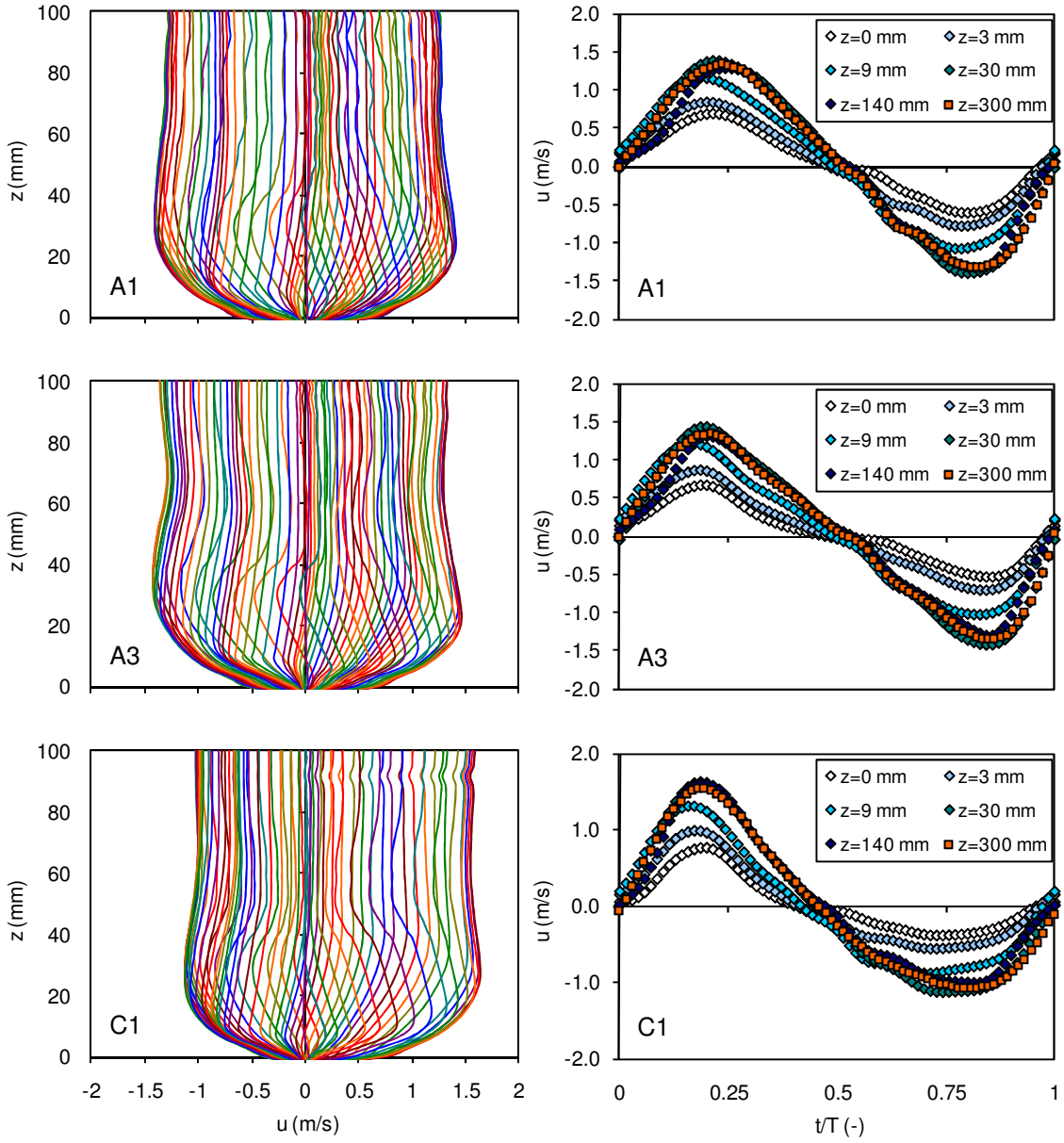

Figure 3.28 – First column: ADVP phase-averaged velocity profiles every 0.10 s for condition A1, A3 and C1. Second column: velocity times-series at z = 0, 3, 9, 30 and 140 mm (ADVP) and at z =300 mm (EMF) for the same conditions.

The comparison of the velocity times-series at the upper level (z = 140 mm) obtained with the ADVP and with the EMF (z = 300 mm), shows that the tests without a counter current (Figure 3.28) present some mismatches around flow reversal. This is probably due to the low seeding in the upper part (z > 3 cm), during part of the wave cycle (Ruessink et al., 2011), affecting the ADVP measurements.

The first column of Figure 3.29 also plots the mean horizontal velocity profile, $\bar{u}(z)$, for test B2 and B4. The results indicate that the counter current increases from the bottom reaching the free-stream value of U_0 at approximately z = 80 ~ 90 mm.

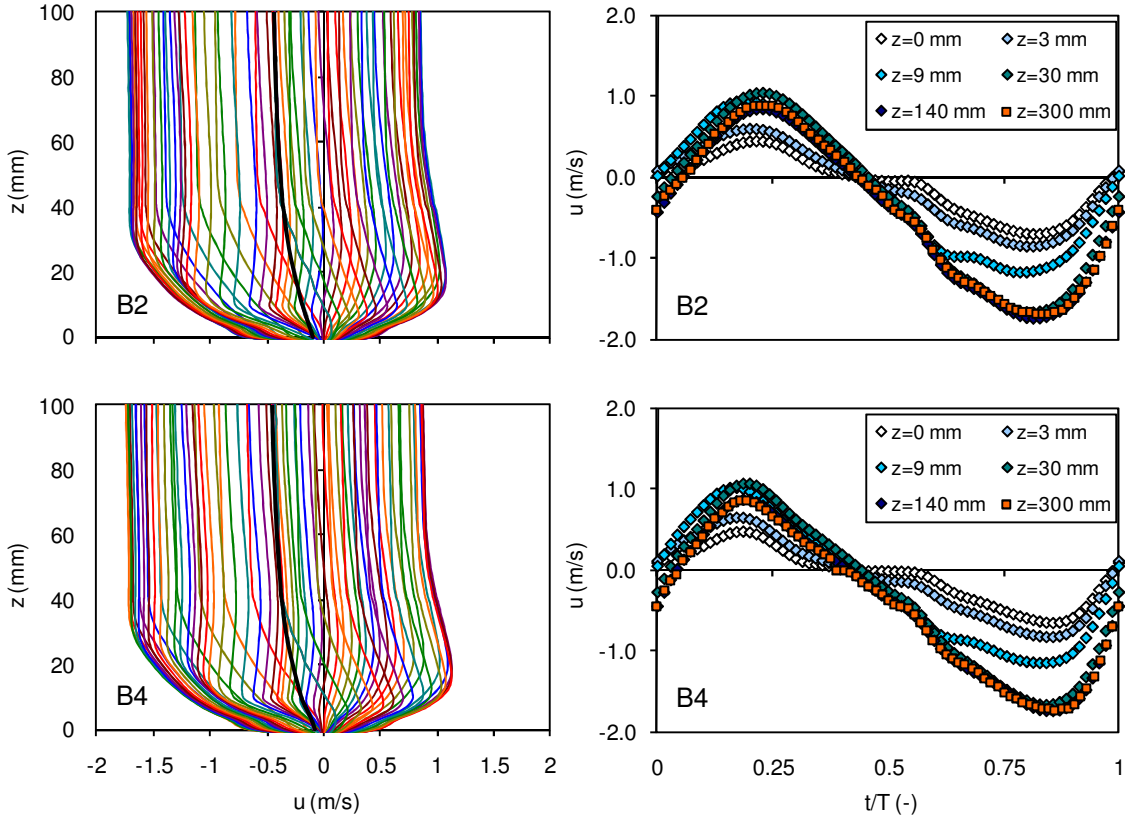

Figure 3.29 – First column: ADVP phase-averaged velocity profiles every 0.10 s for condition B2 and B4 (the bold line indicates the mean horizontal velocity profile). Second column: velocity times-series at z = 0, 3, 9, 30 and 140 mm (ADVP) and at z =300 mm (EMF) for the same conditions.

The vertical structure of $\bar{u}(z)$ for A1, A3 and C1 can be seen in Figure 3.30. As expected for turbulent oscillatory boundary layers, non-linear intra-wave processes produce a time-averaged residual flow near the bottom (Davies et al., 2008). Figure 3.30 shows that C1 has a different vertical behaviour comparing to the others. Close to the bed ($z \lesssim 6$ mm) there is a positive streaming, followed by a negative streaming in the range $z \approx$ 6-30 mm, which is balanced higher up in the vertical by a positive mean flow. This is consonant to Davies and Li (1997) observations in which this behaviour of the boundary layer streaming is due to turbulence asymmetries. In addition, the vertical structure of $\bar{u}(z)$ in Test C1 resembles the structure described by Ribberink et al. (2008) for velocity-skewed oscillatory flows, pointing that the positive streaming close to the bed ($z \lesssim 6$ mm) is due to a mobile-bed effect. The differences between C1 and the other two conditions might be attributed to different degrees of turbulence asymmetry during successive oscillatory flow half-cycles (Ruessink et al., 2009, 2011). Tests A1 and A3 show positive residual flows in the entire vertical ($z < 50$ mm), but it is very close to

the bed ($z \lesssim 6$ mm) that the streaming seems relevant. Furthermore, the increase of acceleration skewness seems to enhance the positive residual flow. These results contrast with the negative near-bed $\bar{u}(z)$ observations of van der A et al. (2008) for fixed-bed experiments under acceleration-skewed flows, where increasing β lead to an increase in magnitude of negative near-bed streamings. Possibly, as suggested by Ribberink et al. (2008), the near-bed positive streamings observed in Figure 3.30 result from a mobile-bed effect.

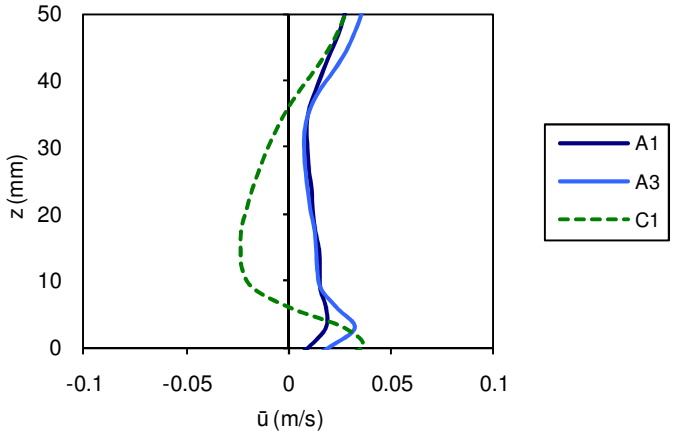

Figure 3.30 – Vertical structure of the mean horizontal velocity profile, $\bar{u}(t)$, for A1, A3 and C1 conditions.

Defect law

A first harmonic analysis was obtained from the ADVP detailed measurements, providing good insights of the oscillatory boundary layer structure of the flows. Figure 3.31 shows the vertical structure of r_1/r_∞ and ϕ_u (see Eq.s (3.20) and (3.24)) and plots the real and imaginary parts of $D_1(z)$ (Eq.s (3.22) and (3.23)). The first column evidences that the local velocity amplitude (r_1) increases from the bed and oscillates as a dampened wave around the free-stream value (r_∞) for higher elevations. At about $z \approx 30$ mm the overshoot velocity is reached, leading to r_1/r_∞ = 1.12, 1.14, 1.09, 1.06 and 1.05 for A1, A3, C1, B2 and B4, correspondingly.

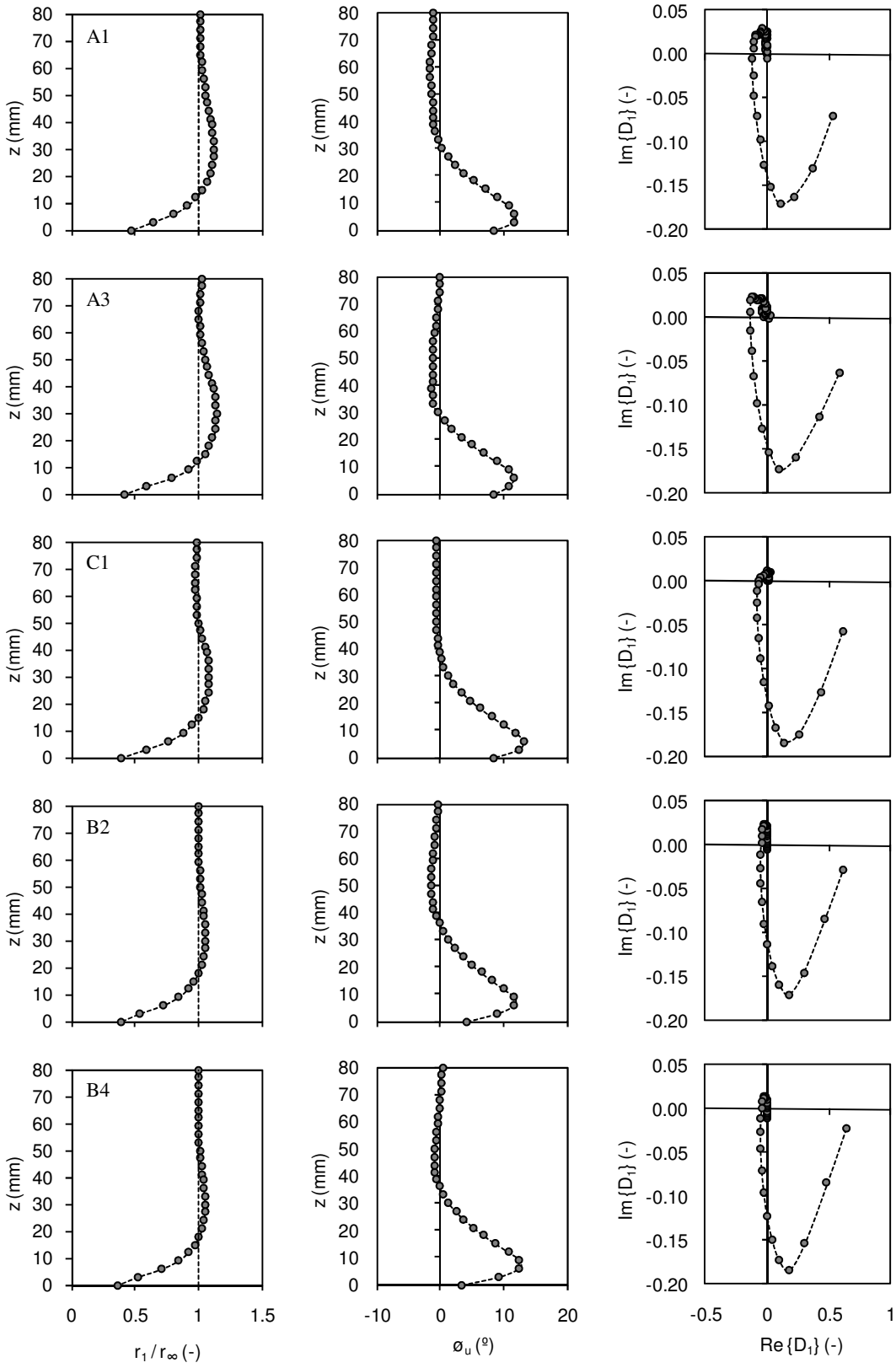

Figure 3.31 – First harmonic analysis for A1, A3, C1, B2 and B4. (first column) Vertical structure of r_1/r_∞. (second column) Vertical structure of ϕ_u. (third column) Im$\{D_1\}$ *versus* Re$\{D_1\}$.

The second column of Figure 3.31 shows a positive phase lead ϕ_u from 0 at $z > 30$ mm, peaking to values of approximately 15º at $z = 6$ mm for all five flows. Bellow $z = 6$ mm the values of ϕ_u reduce to less than 10º for A1, A3 and C1, and even to close to 0º for B2 and B4 at $z = 0$. These phase leads and differences can also be observed at the right-side plots of Figure 3.28 and Figure 3.29, evidencing that the 1st harmonic from the defect law method captures immediately these features. This contrasts with the acceleration-skewed, fixed-bed experiment results of van der A et al. (2008) where ϕ_u continuously increase towards the bed. However, other mobile-bed experiments (McLean et al., 2001; Malarkey et al., 2009) and two-phase model simulations (Dong and Zhang, 2002; Malarkey et al., 2009) present similar vertical structures of ϕ_u as those observed in the TRANSKEW experiments. The differences between fixed and mobile-bed experiments may point to an effect to the high near-bed sand concentrations on the flow in the wave boundary layer (Malarkey et al., 2009). Furthermore, the oscillatory flow experiments with superimposed currents of McLean et al. (2001) also suggest a stronger reduction in ϕ_u close to the bed. Thus, apparently, the mean-flow further contributes to the stronger reduction in ϕ_u.

The third column of Figure 3.31 plots the real and imaginary parts of $D_1(z)$ showing that the defect function $D_1(z)$ moves along a logarithmic spiral presenting a similar behaviour to that of a simple harmonic, oscillatory laminar flow over a smooth bed (Nielsen, 1992, Figure 1.2.6). At the bed, where the velocity vanishes, the spiral would start in $\mathrm{Re}\{D_1\}=1$ and $\mathrm{Im}\{D_1(z)\}=0$. Then, as z increases, the values approach 0 ($\mathrm{Re}\{D_1\}=0$ and $\mathrm{Im}\{D_1(z)\}=0$), corresponding to the free-stream velocity.

The vertical structure of the real and imaginary parts of $D_1(z)$ is shown in Figure 3.32 for A1, A3, C1, B2 and B4. For the five flows, a similar trend is noticeable. For higher elevations, both the real and imaginary parts of $D_1(z)$ are practically zero. Going down into the boundary layer, the imaginary part increases from 0 at $z > 30$ mm and peaks at approximately $z = 9$ mm, starting to decay toward 0 as the bed is approached. The real part increases continuously from 0 at $z \approx 15$ mm to 1 at lower elevations. In Figure 3.32 the data trend is extrapolated (represented by squares) beyond the lowest measurement location in order to find the level of the non-moving bed ($\mathrm{Re}\{D_1\}=1$ and $\mathrm{Im}\{D_1(z)\}=0$). The results consistently indicate that around $z = -5$ mm the velocity seems to vanish.

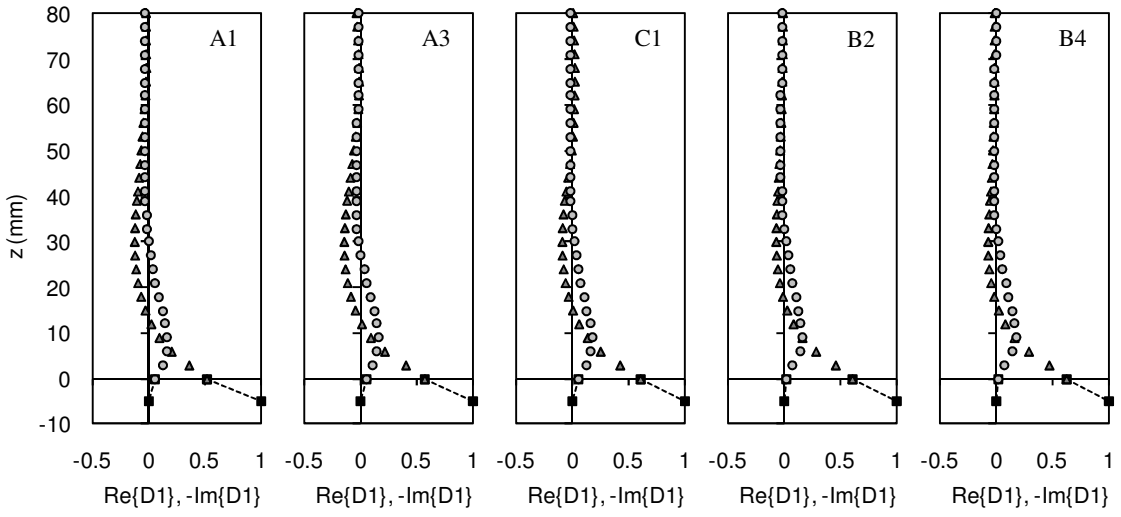

Figure 3.32 – Vertical structure of $\mathrm{Re}\{D_1(z)\}$ (triangles) and -$\mathrm{Im}\{D_1(z)\}$ (circles) for A1, A3, C1, B2 and B4. The lowest points (squares), at $z \approx$ -5 mm, is extrapolated from the data trends to obtain $\mathrm{Re}\{D_1\}$=1 and $\mathrm{Im}\{D_1\}$=0, corresponding to "no motion".

Figure 3.33 plots the vertical evolution of $-ln|D_1(z)|$ and $-\mathrm{Arg}\{D_1\}$ on a log-log scale. According to the above, the z origin was replaced, adding 5 mm to all the ADVP levels to account for the presumable location of the non-moving bed. The power p_1 in Eq. (3.16) relies on the slope of the best straight-line fit of $-ln|D_1(z)|$ (left panel of Figure 3.33). The vertical scale z_1 is obtained from $-ln|D_1(z_1)|=1$. For the overall experiments, one founds that the values of z_1 are within the range 9-10 mm and $p_1 \approx 0.90$. The tests without a counter current (A1, A3 and C1) have some mismatches in the upper part (z >30 mm) regarding the fitting to a straight-line, which might be attributed to the low suspended concentrations during parts of the flow cycle (Ruessink et al., 2011).

Moreover, it is possible to observe in the right panel of Figure 3.33 that for higher elevations ($\gtrsim$ 20 mm) -$\mathrm{Arg}\{D_1(z)\}$ follow quite reasonably the linear trend found for -$ln|D_1(z)|$ (black line). This agrees with Nielsen (1992) observations, where the structure of the turbulent boundary layer is very similar to that of smooth, laminar flow in which the real and imaginary parts of the complex logarithm of the defect function are approximately identical along the water column ($\mathrm{Re}\{ln(D_1(z))\} = \mathrm{Im}\{ln(D_1(z))\}$, or equivalently, $-ln|D_1(z)| = -\mathrm{Arg}\{D_1(z)\}$). Nevertheless, the TRANSKEW experiments reveal some divergence between $ln|D_1(z)|$ and $\mathrm{Arg}\{D_1(z)\}$ at lower elevations and other linear trends could be assumed.

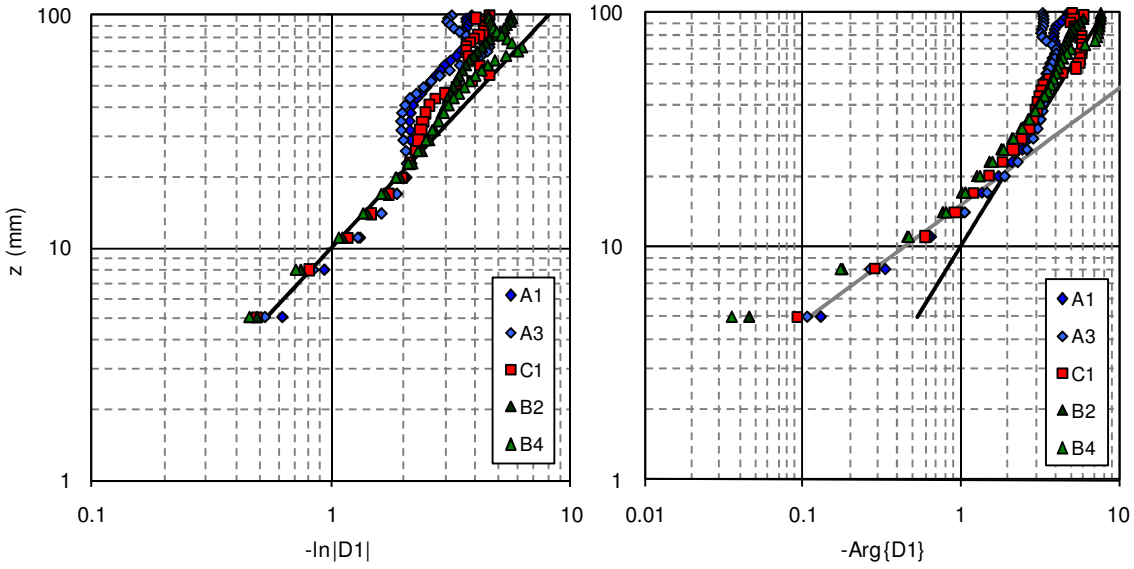

Figure 3.33 –Vertical evolution of $-ln(D_1)$ and $-\mathrm{Arg}\{D_1\}$ for the five test conditions. The continuous lines refer to Eq.s (3.27) (black) and (3.28) (grey).

The following expressions represent the continuous lines shown in Figure 3.33 which roughly approximate the trends of the five flow conditions:

$$\left|D_1(z)\right| = e^{-(z/0.010)^{0.90}}, \tag{3.27}$$

$$-\mathrm{Arg}\{D_1(z)\} = \begin{cases} (z/0.010)^{0.90}, z > 0.021m \\ (z/0.015)^{2.0}, z \le 0.021m \end{cases}. \tag{3.28}$$

The value of $z = 0.021$ m in Eq. (3.28) was chosen to obtain the continuity between the two straight-lines with different slopes. Figure 3.34 plots the vertical evolution of the phase lead ϕ_u using Eq. (3.24), with the results expressed by Eq.s (3.27) and (3.28). Additionally the identity of $\mathrm{Arg}\{D_1(z)\}$ and $ln\left|D_1(z)\right|$ is assumed through the use of Eq. (3.27). The results reveal that the reduction of the phase lead ϕ_u closer to the bed, observed in Figure 3.31 is recreated when $ln\left|D_1(z)\right| \neq \mathrm{Arg}\{D_1(z)\}$. As depicted in Figure 3.31, B2 and B4 present a stronger decay toward 0 as the bed is approached, suggesting a somewhat lower slope in the second branch of Eq. (3.28). That can be confirmed in the right panel of Figure 3.33.

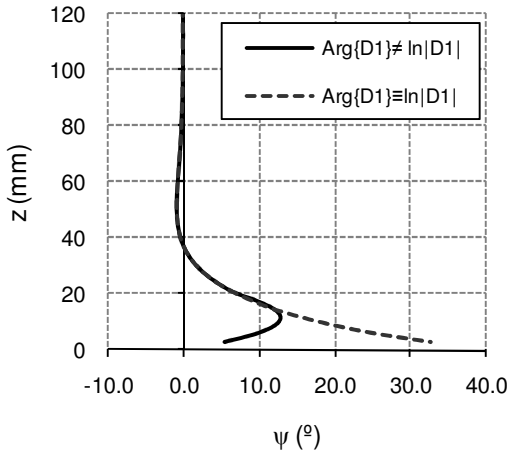

Figure 3.34 –Velocity phase difference, ϕ_u, assuming $ln(D_1) \equiv \mathrm{Arg}\{D_1\}$ and $ln(D_1) \neq \mathrm{Arg}\{D_1\}$.

As the vertical structure of the velocity, through $D_1(z)$, was shown to be well defined by Eq.s (3.27) and (3.28) with the use of simple parameters (z_1 and p_1), it is possible to convert them into magnitude and phase coefficients, $r_1(z)$ and $\phi_1(z)$, using Eq.s (3.22) and (3.23). This procedure surpasses the incongruent measurements associated with low seeding in the upper part ($z > 3cm$) observed for A1, A3 and C1 during part of the wave cycle. Such information, combined with the EMF free-stream velocity, $u_\infty(t)$, enables the reconstruction of $u(z,t)$. Figure 3.35 plots, for all five flow conditions, the ADVP phase-averaged velocities and the predicted velocities according to the defect law analysis. Though the reconstruction relies only on the 1st harmonic component, the results agree fairly well with the ADVP measurements, showing that the defect law reproduces the typical features of the wave boundary layer: (1) the velocity magnitude generally increases with distance from the bed, (2) at different levels the velocities are not in phase, (3) an overshoot of the velocity occurs at a certain elevation (2-4 cm) above the bed.

The consistence of the values suggests that the defect law is verified with the TRANSKEW data and that the use of the defect law can be useful to correct and predict the values where the ADVP failed. In addition, when applied to mobile beds, the methodology provides an estimate of the non-moving bed elevation and replicates the reduction of velocity phase differences, ϕ_u, if different values of z_1 and p_1 are assumed for lower elevations in $\mathrm{Arg}\{D_1(z)\}$. It is noted that, according to Nielsen (1992, p.46), the parameters z_1 and p_1 could be prescribed as function of the relative roughness (A/k_s) and the Reynolds number $(Re = A^2\omega/\nu)$. Therefore, in the future, it would be interesting to investigate such relations in different flow regimes for several experiments. Furthermore, this simple methodology appears promising in many engineering applications that require the knowledge of the wave boundary layer flow, such as bed shear stresses and sediment transport.

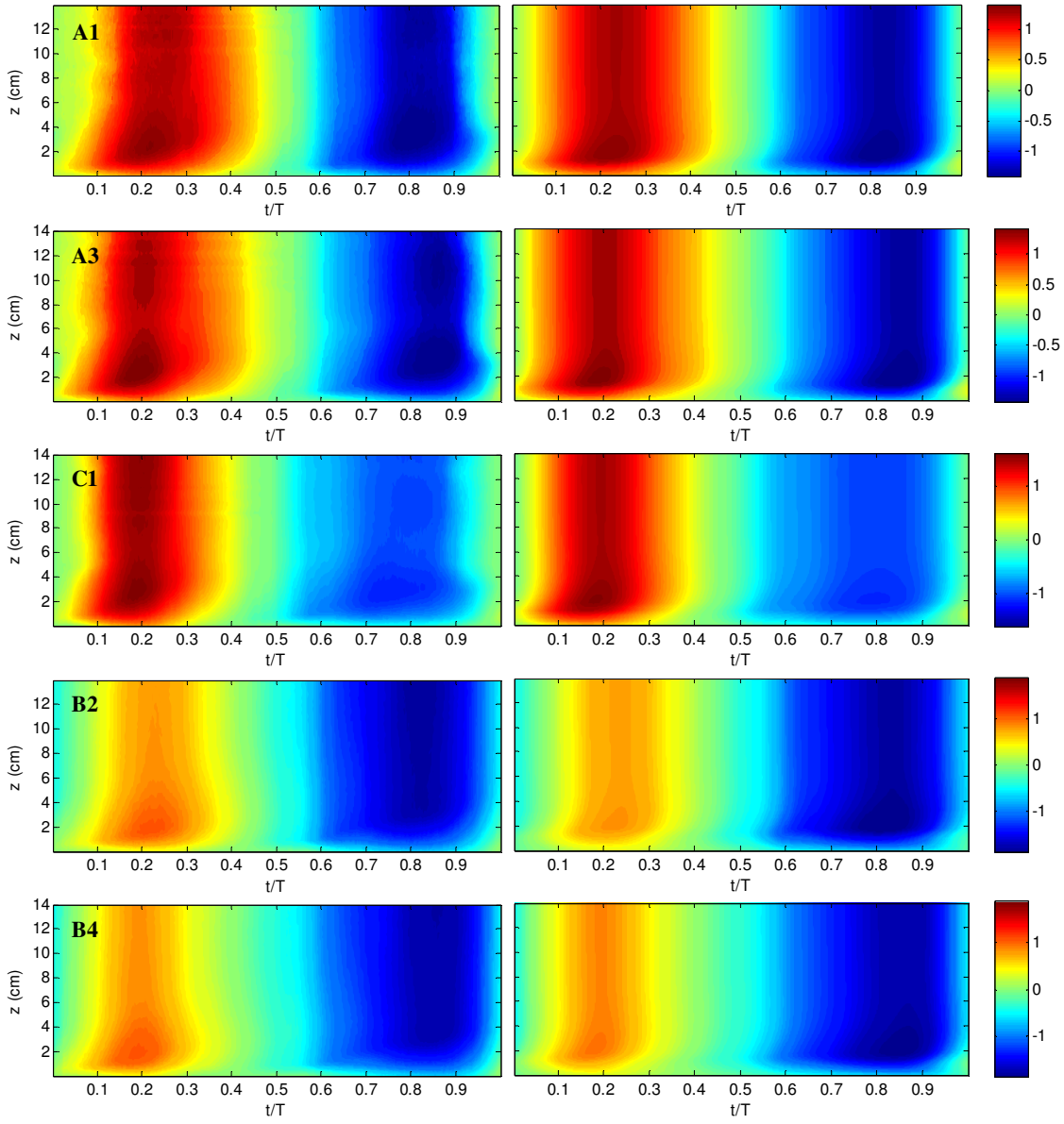

Figure 3.35 – ADVP phase-averaged velocities (first column) and predicted velocities according to the defect law for A1, A3, C1, B2 and B4.

3.5 Sediment concentrations within the sheet flow layer

3.5.1 Methodologies

Bin-averaging technique

During each experiment, the CCM probes were kept at the same initial position, but, as the bed level changed up and down at the site where they were deployed, the levels of the sensors relative to the bed also changed and must be updated in time. The knowledge of the gradual bed level changes is very important because in the sheet flow layer the vertical concentration gradients are very high. Therefore, in order to get accurate concentration data at specific heights with respect to a known reference level (e.g., $z = 0$ the initial bed level), the CCM concentration series had to be carefully post processed. For that purpose, the bed level at rest was measured during the runs by means of a rule placed in the glass wall of the tunnel and a video system. The measurements were registered every 60 s at flow reversal, when it is believed that most part of the sediments settled down. The temporal evolution of these bed level measurements showed a good adjustment to a 3rd degree polynomial fit, and the time series of the conductivity probes were then associated to these continuous bed level changes.

Figure 3.36 exemplifies the bed level changes during one of test A3 runs. The experiment was performed during 6 minutes and, at the beginning of the test, the CCM probes were referred to $z = 0$. After 51 flow cycles (≈ 6 min), a general accretion of 4 mm was verified. The measurements show that a good agreement is obtained with a 3rd degree polynomial fit. In general, the bed level changes were lower than 5mm for all the runs.

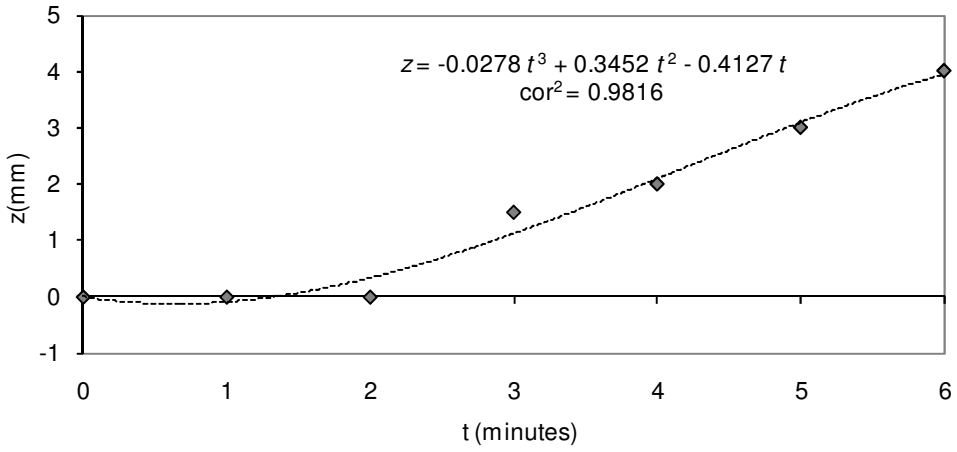

Figure 3.36 – Bed level changes for test A3 during run M2A3013 measured by means of a rule placed in the glass wall of the tunnel (dots) and a 3rd degree polynomial fit (dotted lined).

For the present analysis only integer and intermediate values of z have been considered, resulting in a 0.5 mm resolution. Further, it was accepted that the time series corresponding to each value of z comprehend all measurement values in the range of ± 0.2 mm, corresponding to a 0.4 mm bin height. For example, if the analysis is performed for z = 0.5mm, the time series considered concern the data for which the bed-levels are between the vertical elevations z = 0.7 mm and z = 0.3 m.

With a sampling frequency of 1 kHz, each flow period was divided into 36 time intervals (phases) defining a temporal bin size that, for a 7 s flow period, encompasses 194 data points (≈ 7000/36). With every concentration measurement, c, assigned to a particular (ωt,z) bin, the data values can then be averaged, yielding $\hat{c}(z,t)$.

The bin-averaged concentration $\hat{c}$ can be decomposed into mean and orbital components $\overline{c}$ and $\tilde{c}$, respectively. These components are calculated as follows

$$\overline{c}(z) = \frac{1}{N_p}\sum_{n=1}^{N_p}\hat{c}(z,n), \tag{3.29}$$

$$\tilde{c}(z,t) = \hat{c}(z,t) - \overline{c}(z). \tag{3.30}$$

3.5.2 Erosion depth and sheet flow layer thickness

The structure of the sheet flow layer (SFL) along the wave cycle is considered an important research issue because most of the sediment transport occurs within this thin layer (e.g., Ribberink and Al-Salem, 1995; McLean et al., 2001). This region is characterized by high concentration values where inter-granular forces and sediment-flow forces play an important role.

The top and the lower level of the sheet flow layer during the oscillatory motion can be established based on different methodologies. Reference concentrations provided by the CCM probes can be used to establish the SFL structure. In addition, the intensity of the backscattered acoustic signal over the depth obtained with the ADVP can be used to determine the bed position and the top of the SFL as shown by Silva et al. (2009). Moreover, observations of video recorded during the measurements, near the side glass of the LOWT, have enabled to estimate the erosion depth, d_e. In this case, d_e is the distance between the bed level at flow reversal after the maximum positive velocity (when almost sediment has settled) and the lowest bed level observed during the flow cycle (at maximum velocity). This determination is not very accurate because it is difficult to distinguish the bed level at maximum velocities and because the observations were made at the test section wall. The video observations

were mainly used as a check of the other measurements. In this work, the results obtained from the CCM data are presented.

The instantaneous sand volume concentration equal to 8% of ρ_s ($\approx$ 210 kg/m^3) is adopted to define the top of the SFL, $d_t(t)$. According to Dohmen-Janssen and Hanes (2002), at lower concentrations, the inter-granular stresses are negligible and the concentration profile is determined by turbulent diffusion processes. The intra-wave lower level of the SFL, $d_e(t)$, was computed by identifying the levels where the measured sediment concentration did not change in time, equalling the undisturbed bed concentration c_0. Following Dohmen-Janssen and Hanes (2002), the SFL thickness, is therefore defined as the distance between the top and lower levels, given above:

$$\delta_s(t) = d_t(t) + \left| d_e(t) \right| . \tag{3.31}$$

Ruessink et al. (2011) evaluated the accuracy of the measured erosion depth following Malarkey et al. (2009). According to their methodology, an instantaneous erosion depth, d_{eE}, is estimated from the integration of all concentration measurements in the water column above d_e:

$$d_{eE}(t) = -\frac{1}{c_0}\int_{d_e(t)}^{\infty} \hat{c}(t)\, dz . \tag{3.32}$$

This resulted in differences between d_e and d_{eE} of about 1-2 mm, being d_{eE} consistently higher. Apparently, the water column had more sand than the values of d_e imply. Nonetheless, it is not possible to detect if the error comes from the concentration data in the sheet flow layer or in the suspension layer (or both). It is noted that the differences are practically in the same order of the uncertainty associated with the positioning of the CCM probes.

3.5.3 Results

The time-dependent and time-averaged concentrations, $\hat{c}$ and $\overline{c}$, respectively, within the sheet flow layer are plotted in Figure 3.37 for A1, A3 and C1 and in Figure 3.38 for B2 and B4 conditions. In addition, according to the method described in Section 3.5.2, the lower and upper levels of the SFL, d_t and d_e, are indicated over $\hat{c}$. On top of each time-dependent concentration diagram, the free-stream velocity is given for reference. Some symbols are marked over the free-stream velocity, indicating particular phases for which the sediment flux computations will be presented.

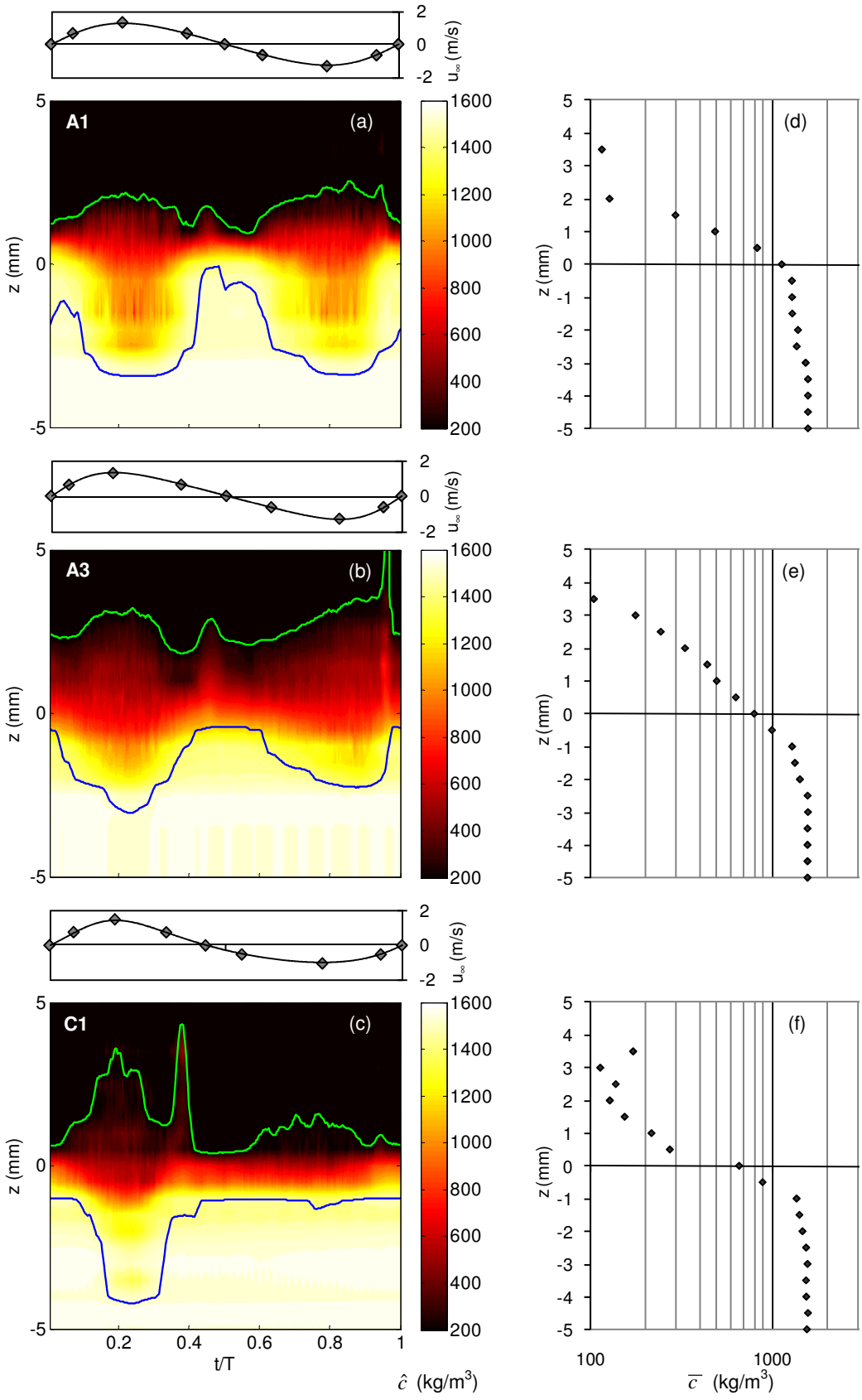

Figure 3.37 – Time dependent phase-average concentrations, $\hat{c}$, and time-averaged concentrations, $\overline{c}$, at (from top to bottom) A1, A3 and C1. Lower and upper levels of the SFL are indicated with continuous lines over $\hat{c}$. On top of each diagram the free-stream velocity is given. The diamonds over the free-stream velocity indicate phases for which results are presented in other figures.

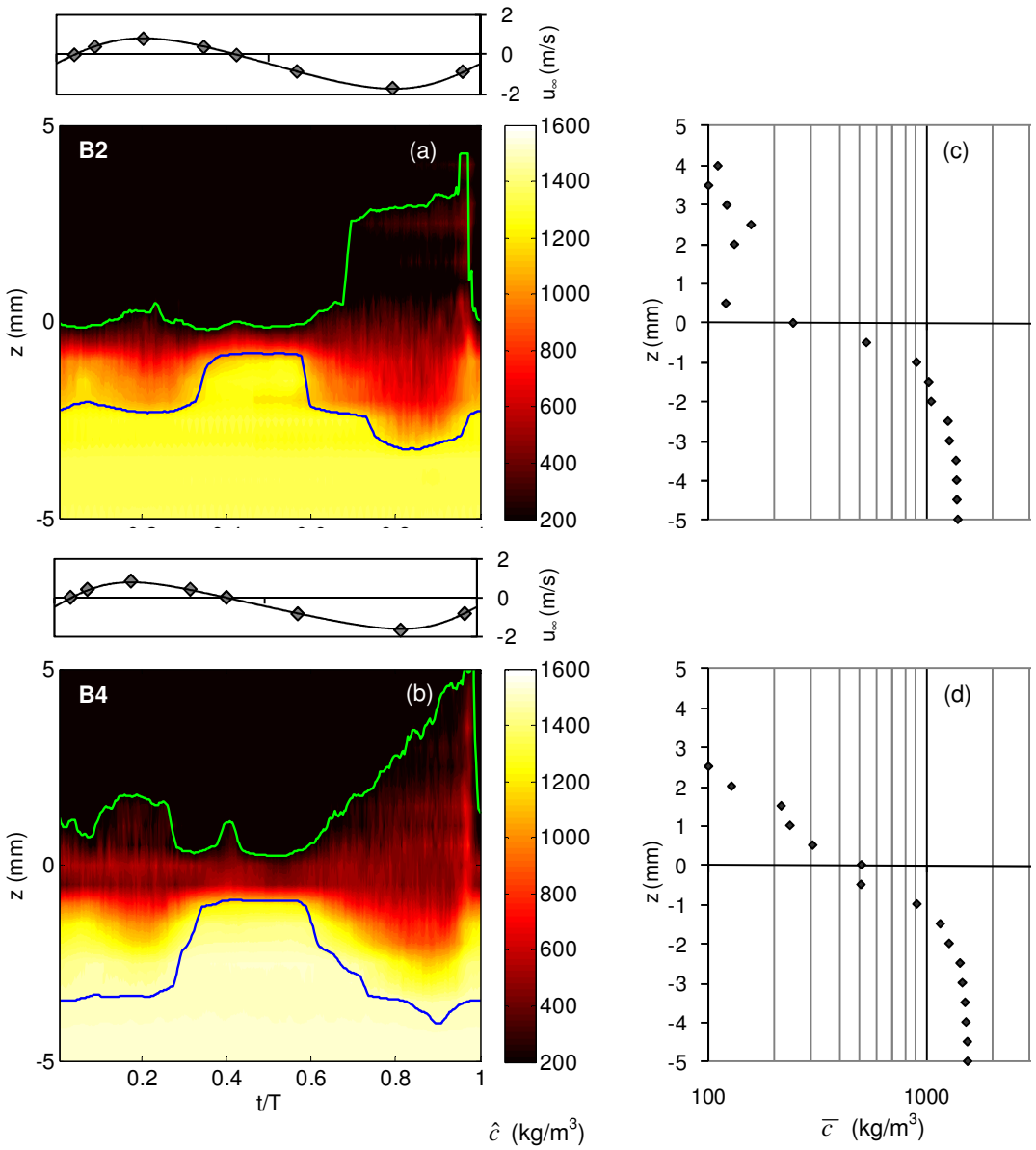

Figure 3.38 – Time dependent phase-average sediment concentrations, $\hat{c}$, and time-averaged concentrations, $\overline{c}$, at (from top to bottom) B2 and B4. Lower and upper levels of the SFL are indicated with continuous lines over $\hat{c}$. On top of each diagram the free-stream velocity is given. The diamonds over the free-stream velocity indicate phases for which results are presented in other figures.

For all the conditions, during the oscillatory motion, the concentration at z = -5 mm did not change and is equal to the still bed value c_0. The value of c_0 differs slightly between the five flow conditions, varying from about 1400 to 1550 kg/m^3. Similar c_0 values were reported in previous experiments (e.g., Dohmen-Janssen et al., 2002; Hassan and Ribberink, 2005). Moreover, it is reassuring to see that the "no motion" level at z = -5 mm corroborates the extrapolated value obtained from the defect law analysis.

Above z = -5 mm one observes the development of the sheet flow layer structure which has an expected behaviour, similar to that of previous experiments (e.g., Zala-Flores and Sleath, 1998;

Dohmen-Janssen et al., 2002; O'Donoghue and Wright, 2004a; Hassan and Ribberink, 2005; van der A et al., 2009), enabling a division into two distinct layers: a pick-up layer ($d_e \leq z \lessapprox 0$) and an upper sheet flow layer ($0 \lessapprox z \leq d_t$). The pick-up layer is characterized by high concentrations that vary in antiphase with the free-stream velocity, i.e., at a given vertical, when the velocity increases, the concentrations decrease. In the upper sheet flow layer, the sediment is entrained from below into the flow and the concentrations are lower, but approximately in phase with the velocity. At $z \approx 0$ mm there is the transition between these layers and a practically constant concentration during the entire flow cycle is observed. The results of the time-averaged concentrations $\overline{c}$ evidence that along the sheet flow layer there are large vertical concentrations' gradients. Moreover, the lower and upper levels of the SFL reveal a very thin layer thickness ($\delta_s < 10$ mm). Note that, according to Dohmen-Janssen and Hanes (2002), as the sampling volume of the CCM probes has a height of 1-1.5 mm, values of SFL thickness less than 1.5 mm are not very accurate. This leads to uncertainties associated with the positioning of the CCM probes. Moreover, the cross-tube uniformity occasionally lacked during the experiments, introducing some errors in the measurements. Thus, the corresponding accuracy on the estimation of the SFL thickness δ_s is approximately 2 mm.

Observing the development of the SFL in Figure 3.37 and Figure 3.38, as the velocity increases from zero values, at each flow reversal, sediment particles are mobilized from the bed, causing local erosion associated with a deepening of the bed level and an increase in the erosion depth. These particles are entrained into the flow above the initial bed level ($z = 0$) causing an increase of sediment concentration at those levels and, consequently, raising the top level of the SFL. When the magnitude of the velocity decreases, the processes that sustain the sediment particles either in the sheet flow or in the suspension layer tend to vanish, and sediment particles have a tendency to settle down to the bed, causing a decrease in the SFL thickness. It is noticed that the temporal evolution of the erosion depth is progressive, suggesting that the particles do not start to move as a single block as it occurs for plug flows (Sleath, 1999), where the forces acting on the sediment particles become dominated by the free-stream pressure gradient. In the TRANSKEW experiments, the mobile layer appears to react instantaneously to flow velocity changes due to the temporal variation of the bed shear stress.

For the A3, B2, B4 and C1 conditions, the upper limit of the SFL computed from the CCM data show a sudden increase just before flow reversal. These maxima are connected to short duration concentration peaks measured by the CCM. Nonetheless, these secondary peaks were not captured by the two non-intrusive acoustic techniques used in the experiments (ABS and ADVP). As suggested by Dick and Sleath (1992), the CCM probe tip at the bed could enhance flow separation locally, producing a local vortex shedding during certain stages of the oscillatory flow and, accordingly, an

artificial increase on the concentration estimates very close to the bed at these phases. However, irrespective of the question whether the secondary peaks are true aspects of sheet flow dynamics or are instrument-induced, they have little impact on sand transport rates since the flow reversal concentration peaks concur with near-zero velocities.

With the exception of test C1, under the largest acceleration values, i.e., when the velocity changes rapidly from the negative (offshore) maximum to a positive (onshore) maximum, the SFL remains thicker than at the opposite positive-to-negative flow reversal (on-offshore) where much smaller flow accelerations are found. The sand that is stirred in the negative flow phase has short time to settle back to the bed during the negative-to-positive flow cycle and, consequently, part of the sand persists for the positive flow phase, becoming available for transport in the opposite direction during the next half wave cycle. This is a result of the acceleration skewness present in the experiments and supports the existence of phase-lag effects between the sediment particles and the flow. This was also confirmed by video observations of the bed behaviour. However, the importance of the phase-lag found for the TRANSKEW experiments is rather limited compared to that for finer sediments, as reported by van der A et al. (2009) for a median grain size of d_{50} = 0.15 mm.

The upper and lower bounds of the SFL at maximum velocity are well related to the physical forcing parameters. In test A3 (oscillatory flow with acceleration skewness) the erosion depth is larger under the crest than under the trough. This is in consonance with the numerical results of Hsu and Hanes (2004) and outcomes solely from the acceleration skewness, as the velocity skewness is zero in this test. This behaviour is also observed at the upper level of the SFL and then consequently in δ_s. Note that test A1 does not show this tendency because the acceleration skewness is weak. It is also evident from Figure 3.37 and Figure 3.38 that d_e, d_t and δ_s are proportional to the maxima flow velocity attained during the crest and trough. This can be achieved either by adding a mean current to the oscillatory flow, as in B2 and B4 tests, or increasing the onshore velocity in C1 test, resulting from an increase in the velocity skewness. For example, since C1 presents a stronger maximum positive velocity, it is possible to observe large differences between the positive and negative flow cycles. Under the maximum positive flow, the sand is entrained higher and the erosion depth reaches a deeper value, comparing to the results obtained for the maximum negative flow.

The effect of the acceleration skewness described above is also perceptible in the combined oscillatory-current flow tests. As the (implied) wave propagation direction and the current are opposite, an increase in the acceleration skewness (from B2 to B4 test) leads to an increase of the d_e and d_t (δ_s) during the crest in comparison to the values observed for the trough. By combining the

CCM with the ABS data, Ruessink et al. (2011) shows that the sand reaches further in the suspension layer for B2 and B4, presenting larger time-averaged concentrations gradients than A1, A3 and C1.

3.6 Sediment velocities within the sheet flow layer

3.6.1 Methodologies

Simple cross-correlation technique

To determine the velocities inside the sheet flow layer the correlation technique described by McLean et al. (2001) was applied. For that purpose, the flow period was divided into 36 time intervals (phases), yielding for a flow period equal to 7 s 194 samples at each phase, as before. The cross-correlations were calculated between the two CCM series for these samples, considering time shifts or phase-lags up to ±90 ms between two time series. The observation of maxima peaks in correlations gives a direct indication of the time lag (δ_t) between the grains seen at the two sensors. Since the spacing of the two CCM sensors was constant and equal to Δx_{CCM} = 11 mm, the velocity of the sediment particles can be directly obtained ($u_s = \Delta x_{CCM} / \delta_t$). Attending a maximum absolute time shift of 90 ms, velocities below 0.12 m/s cannot be measured.

An example of the ensemble average of all the cross-correlation estimates *versus* time lag for Test B4 at elevation z = 4 mm and phase t/T = 0.70 is shown in Figure 3.39. In this figure, a maximum is clearly visible at δ_t = -25 ms, implying a velocity equal to 0.44 m/s. However, for most of the 36 time intervals of the flow cycle for all test cases, no clear maxima in the cross-correlations were observed. Due to the low cross-correlations found, instead of considering the "centroid" of all cross-correlation values exceeding one-half the maximum value to lead to Δt, as defined by McLean et al. (2001), one decided to change the definition for the values exceeding two-thirds the maximum value. To exemplify, the two-thirds of the maximum value is signalised in Figure 3.39 with the horizontal dotted line, leading to an average value of -21.5 ms for the new centroid, resulting in u_s = -0.51 m/s. If more than one "centroid" was found within the time shifts interval $-90 < \delta_t < 0$ ms (associated with the positive flow) or within $0 < \delta_t < 90$ ms (associated with the negative flow) the values were rejected because it was assumed that no clear peak was observable.

The application of the above simple cross-correlation technique to the data showed that only the grain velocities at certain phases of the oscillatory motion could be determined. Most of the valid results were obtained solely during the periods when the SFL was thicker. The same kind of hindrance was reported by Dohmen-Janssen and Hanes (2002) who have only reported valid grain velocities around

the wave crest and for some z-levels. Dohmen-Janssen and Hanes argued that, probably due to the variation of the thickness of the sheet flow layer over the wave cycle, which in turn depends on the asymmetry of the waves, this layer can be very thin and no clear peak in correlation is detectable.

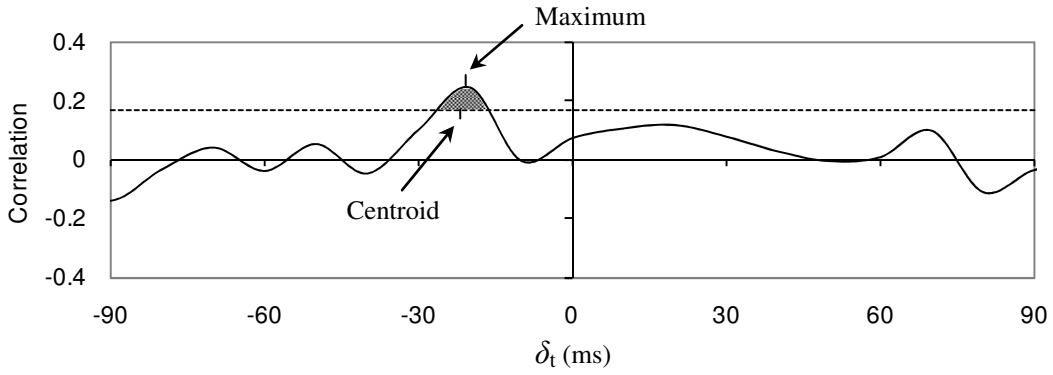

Figure 3.39 – Ensemble average of all the cross-correlation estimates *versus* time lag for Test B4 at the elevation z = 4 mm and the phase t/T = 0.70 (continuous line). The horizontal dotted line marks two-thirds of the maximum correlation value.

Cross-correlation and wavelet decomposition

To tackle the problem described above, a methodology for the estimation of the grain velocity inside the sheet flow layer, which combines cross-correlation techniques and wavelet multilevel decomposition (Mallat, 1999; Franca and Lemmin, 2006), was applied. The wavelet is a waveform, $\psi(t)$, of limited duration that has an average value of zero. Basically, like sinus and cosines are used in Fourier analysis to decompose continuous or discreet time dependent functions, wavelets constitute an alternative basis functions to decompose these latter.

Considering a time function $c(t)$, the continuous wavelet transform is given by

$$\hat{c}_w(\lambda,\varsigma) = \int_{-\infty}^{+\infty} c(t)\,\overline{\psi}_{\lambda,t}(t)\,dt\,, \tag{3.33}$$

where λ is a scale parameter (scale), ς a location parameter (position, herein representing position in dimension time), t the integration variable (herein over time) and $\overline{\psi}_{\lambda,\varsigma}(t)$ the conjugate of the wavelet function $\psi(t)$:

$$\overline{\psi}_{\lambda,\varsigma}(t) = \frac{1}{\sqrt{\lambda}}\psi\left(\frac{t-\varsigma}{\lambda}\right). \tag{3.34}$$

Similar to Fourier analysis, where the signal is decomposed into sine waves of various frequencies, the wavelet analysis decomposes the signal into shifted and scaled versions of the original wavelet through ς and λ, respectively.

Since the signal of the CCM probes was measured at a discrete time, instead of the continuous wavelet transform, the discrete wavelet transform is applied. What distinguishes both approaches is the set of scales and positions at which they operate. Rather than real values of λ and ς, the discrete wavelet transform is parameterised by the integers m and l. These parameters have a similar meaning in both transforms, and can be considered the scale and position parameters, respectively. The relation between these parameters to those of the continuous wavelet transform can be obtained by considering an adequate base dilatation λ_0 and reference time t_0:

$$\lambda = \lambda_0^{\,m}, \tag{3.35}$$

$$\varsigma = l t_0 \lambda_0^{\,m}. \tag{3.36}$$

Thus, the discrete wavelet function, $\psi_{m,l}(t)$, assumes the form

$$\psi_{m,l}(t) = \frac{1}{\sqrt{\lambda_0^{\,m}}} \psi\left(\frac{t - l t_0 \lambda_0^{\,m}}{\lambda_0^{\,m}} \right). \tag{3.37}$$

In the present study the wavelet function of type “D4” (Daubechies, 1988) is used to perform the wavelet transform (Figure 3.40). The discrete transform can be written as:

$$\hat{c}_w(m,l) = \frac{1}{\sqrt{\lambda_0^{\,m}}} \int_{-\infty}^{+\infty} c(t) \psi\left(\frac{t - l t_0 \lambda_0^{\,m}}{\lambda_0^{\,m}} \right) dt\,. \tag{3.38}$$

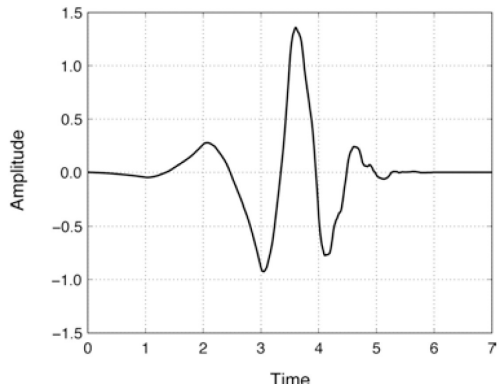

Figure 3.40 – Daubechies wavelet function of type D4 (Daubechies, 1988)

A wavelet frame can be associated to each of the wavelets, being characterized by the scale parameter m ($\lambda = \lambda_0^{\,m}$). This process is called the wavelet multilevel decomposition. To obtain the original signal without loss of information from those components, an inverse discrete wavelet transform can be used.

This process is called reconstruction (or synthesis) and, for an orthogonal decomposition, the reconstruction formula of the discrete wavelet transform follows:

$$c(t) = \sum_{m=-\infty}^{+\infty} \sum_{l=-\infty}^{+\infty} \hat{c}_w(m,l)\psi_{m,l}(t). \tag{3.39}$$

Often, a partial reconstruction of the signal contains important parts of the original signal, though with a lower resolution. This can be obtained by restricting m, which corresponds to one wavelet frame scale defined by λ_0^m. The wavelet multiresolution analysis is based on a hierarchically organized process where the original signal is decomposed into one coarse approximation and successive others with lower scale resolutions. Figure 3.41 exemplifies that it is possible to reconstruct the original signal from the approximations (A_m) and consecutive details (S_m).

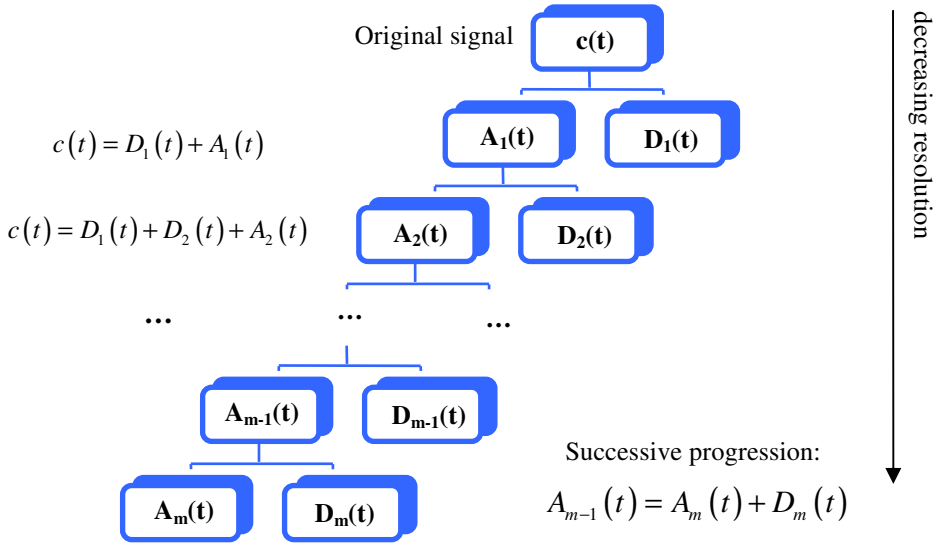

Figure 3.41 – Hierarchical organization of the wavelet multiresolution analysis applied to a time data set $c(t)$.

The CCM original signals were stored in ASCII files and imported to MATLAB © Software for further processing. They were decomposed into 10 resolution wavelet levels, obtaining one coarse large-scale approximation and several others with progressively smaller scale resolutions by using the MATLAB wavelet toolbox.

3.6.2 Results

The application of wavelet transforms to the signals of the two conductivity probes allowed the application of scale-conditioned cross-correlation techniques. It is expected that most correlated events passing through both probes are prone to have similar resolution levels. As an example, Figure 3.42 shows the cross-correlation results obtained for each of the 10 resolution levels for A3 at z = 6 mm.

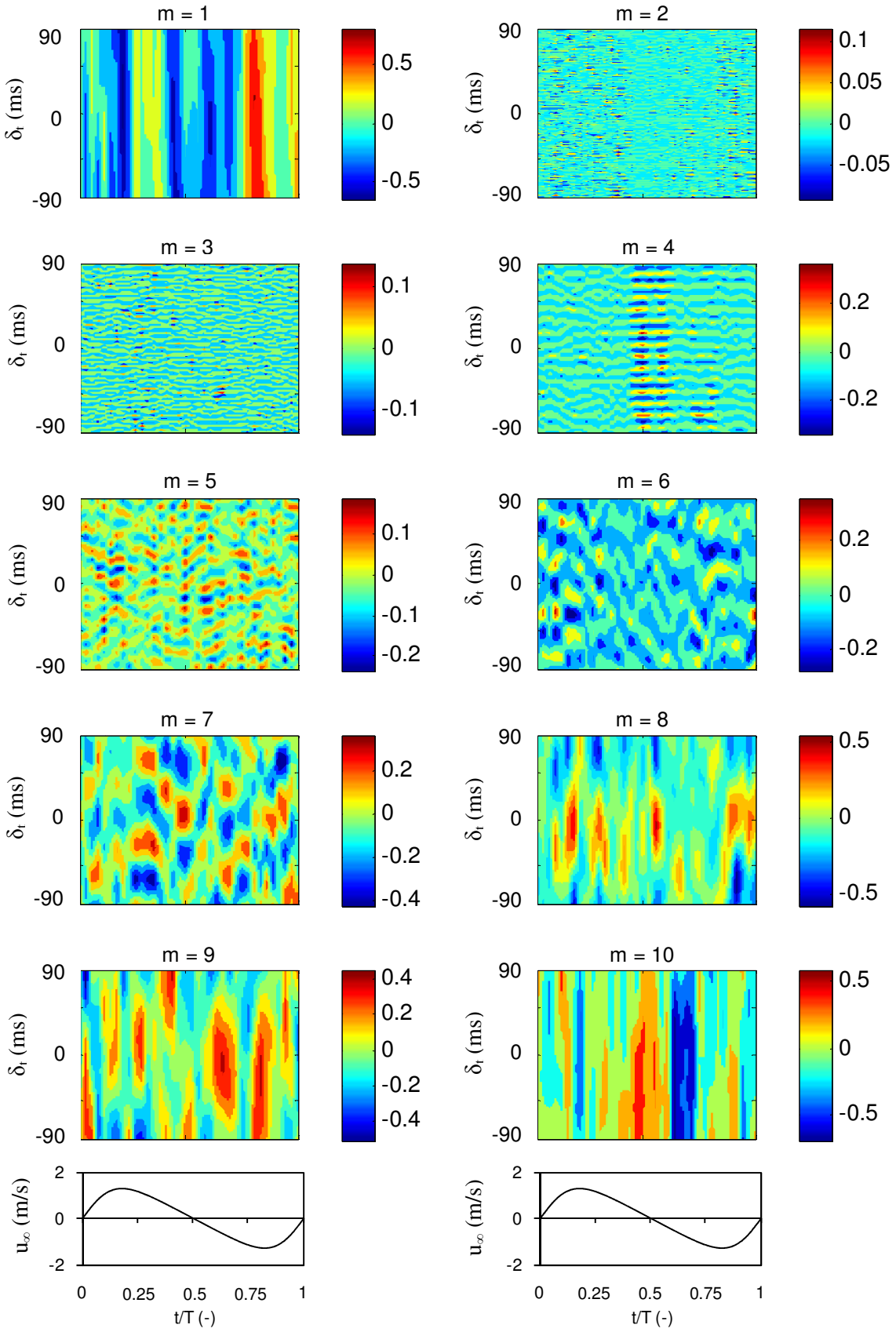

Figure 3.42 – Ensemble averaged cross-correlation between the two CCM sensors for A3 at z = 6 mm, using wavelet decomposition with 10 resolution levels. The bottom panel shows the free-stream velocity u_∞.

Besides the 6th and 7th resolution levels, the cross-correlation values are very homogenous and do not suggest any particular trend that could indicate peaks to obtain grain velocities along the flow cycle. It is noted, that the methodology is usually applied only for a certain resolution level (e.g., Franca and Lemmin, 2006). However, the 6th and 7th resolution levels show different patterns, but by themselves do not clarify a clear trend of the cross-correlation peaks. For that reason, the results of both resolution levels were combined, by attributing them the same weight. Figure 3.43 shows a comparison between the cross-correlation results without applying the wavelet technique and by combining the 6th and 7th resolution levels. Moreover, phase averaged velocities obtained by the ADVP at z = 6 mm were converted to time-lag δ_t and are represented through continuous lines over the cross-correlation results. As explained before, the time lag δ_t yields the grain velocities during the flow cycle ($\delta_t = \Delta x_{CCM} / u_s$). Figure 3.43 reveals that without the wavelet technique there is already a trend, which approximately follows the continuous lines of the ADVP but with very low correlations (see the scale bar). Combining the 6th and 7th resolution levels of the wavelet decomposition, the correlation peaks are enhanced, improving the capability of determining the sediment velocities in other instants of the flow cycle. The rest of the data followed similar trends, helping to decide that the 6th and 7th resolution levels could be significant of sediment transport, resulting in clearer cross-correlation peaks and allowing a better estimate of particle velocities. In the future, it would be interesting to investigate if better results could be provided, by testing different combinations with other resolution levels and/or different weights.

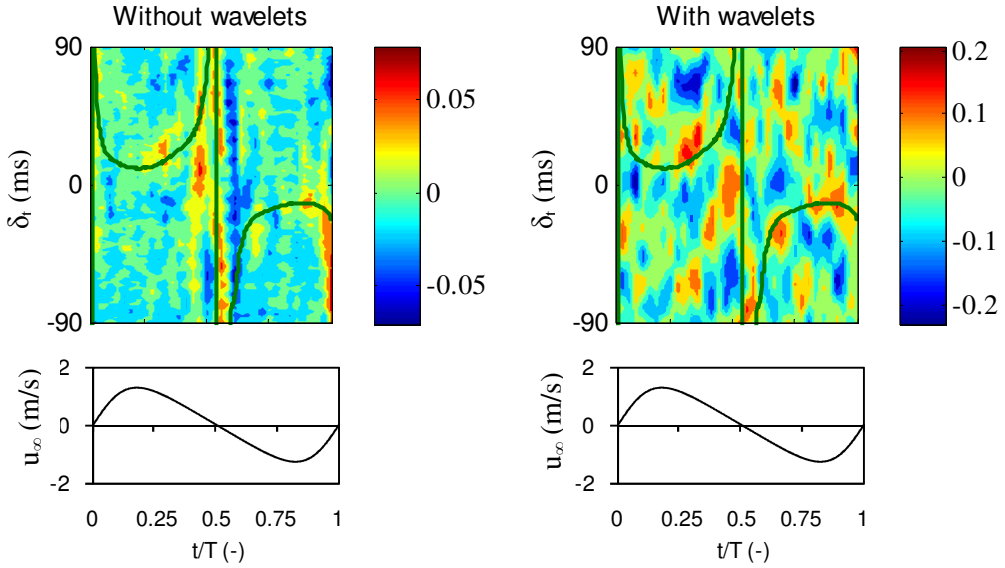

Figure 3.43 – Ensemble averaged cross-correlation between the two CCM sensors for A3 at z= 6 mm. First column: without wavelet decomposition. Second column: with wavelet decomposition. The bottom panel shows the free-stream velocity u_∞. The velocities obtained with the ADVP for that level are represented with continuous lines over the cross-correlation values.

Figure 3.44 and Figure 3.45 synthesize the ensemble averaged cross-correlation between the two CCM sensors for A3 and C1, respectively. The other conditions give comparable results and, consequently, are not shown. The cross-correlation shown corresponds to three elevations: 0, 3 and 6 mm. These levels were selected because they allowed a direct comparison with the ADVP velocity data. The first and second columns present the ensemble averaged cross-correlations without and with the wavelet multilevel decomposition, respectively. The free-stream velocity u_∞ is given for reference at the lower panel. The peak values, obtained using the centroid criterion in wavelet analysis (recall Figure 3.39), are signalized with circles over both columns and the results attained by the ADVP are represented through continuous lines.

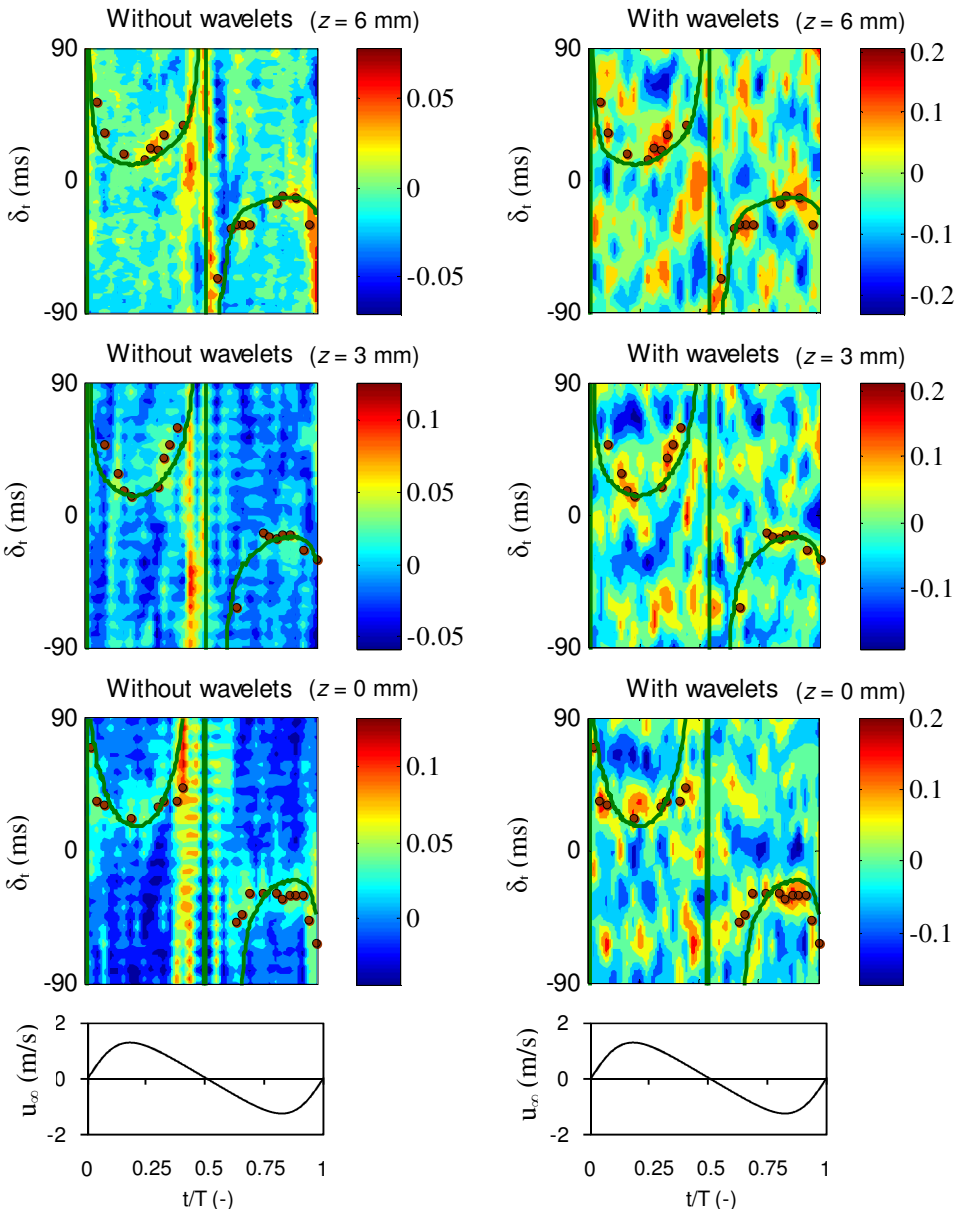

Figure 3.44 – Condition A3: ensemble averaged cross-correlation between the two CCM sensors for z = 6, 3 and 0 mm. First column: without wavelet decomposition. Second column: with wavelet decomposition. The bottom panel shows the free-stream velocity u_∞. Overlapping the cross-correlation values, one finds the solutions obtained with the wavelet technique (circles) and with the ADVP (continuous lines).

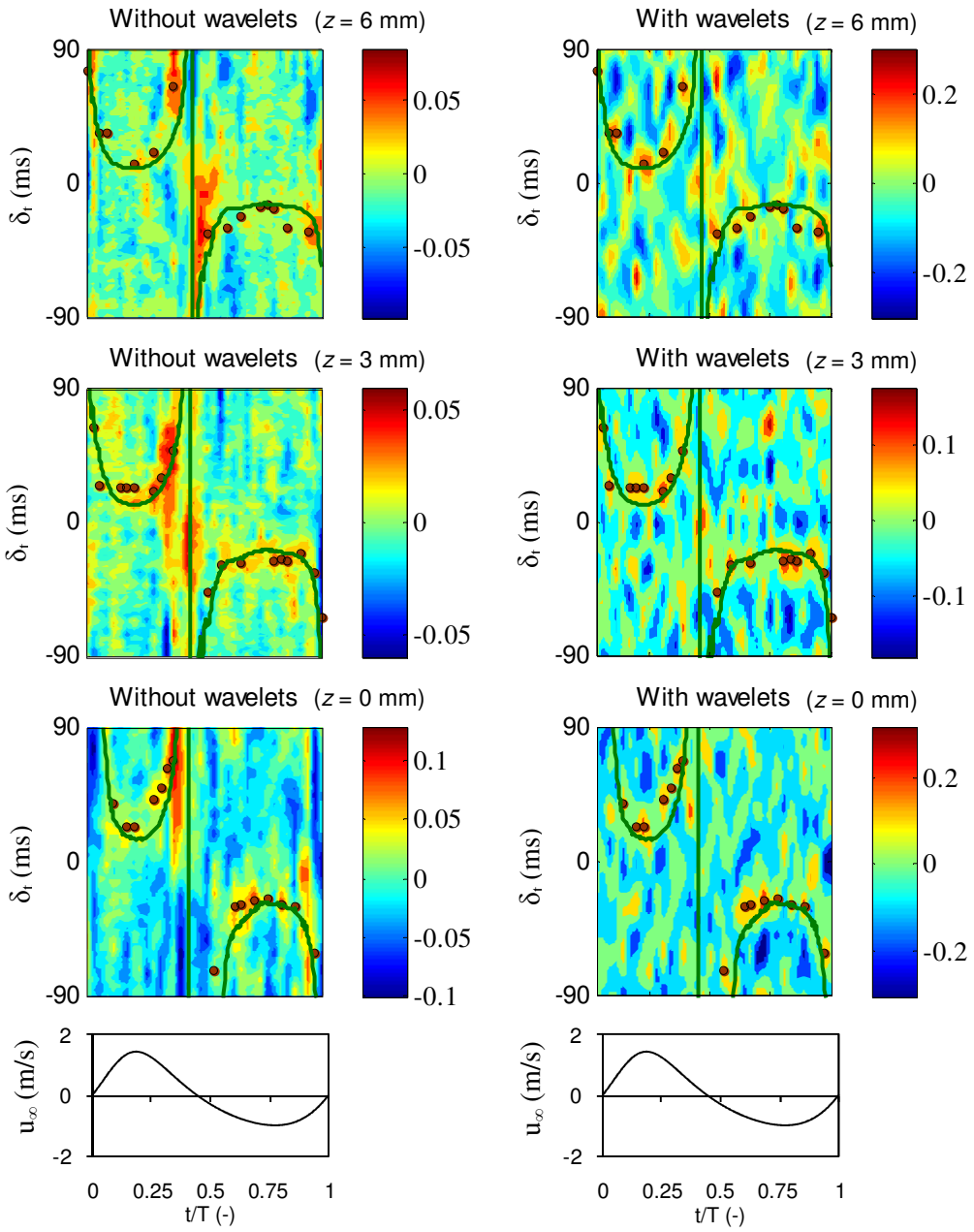

Figure 3.45 – Condition C1: ensemble averaged cross-correlation between the two CCM sensors for z = 6, 3 and 0 mm. First column: without wavelet decomposition. Second column: with wavelet decomposition. The bottom panel shows the free-stream velocity u_∞. Overlapping the cross-correlation values, one finds the solutions obtained with the wavelet technique (circles) and with the ADVP (continuous lines).

The differences between both methods are herein examined. It is noted that, using the "pure" CCM signals, the correlation values are very low in the first column of each figure (note the different bar-scales on each figure). The correlations become higher using the new approach. However, for more than one half of the 36 phase intervals the results remain unclear. Interestingly, the ADVP velocities show a good agreement with the solutions found through the cross-correlation technique. This suggests that the acoustic device penetrates well in the sheet flow layer.

For the lower levels than $z = 0$, the new analysis also appeared to be very consistent. As an example, Figure 3.46 presents the results at z=-3 mm for condition C1. This corresponds to one of the lowest bed level value where the movement of the particles was detected (see Figure 3.37). From the ensemble averaged cross-correlations of the signals, without wavelet decomposition, it was already possible to see a clear pattern indicating that the movement of the grains occurred, only, during part of the positive flow cycle. In that region, the correlations were fairly high and the change of the pattern associated with the different sand concentration values helped to support that conclusion.

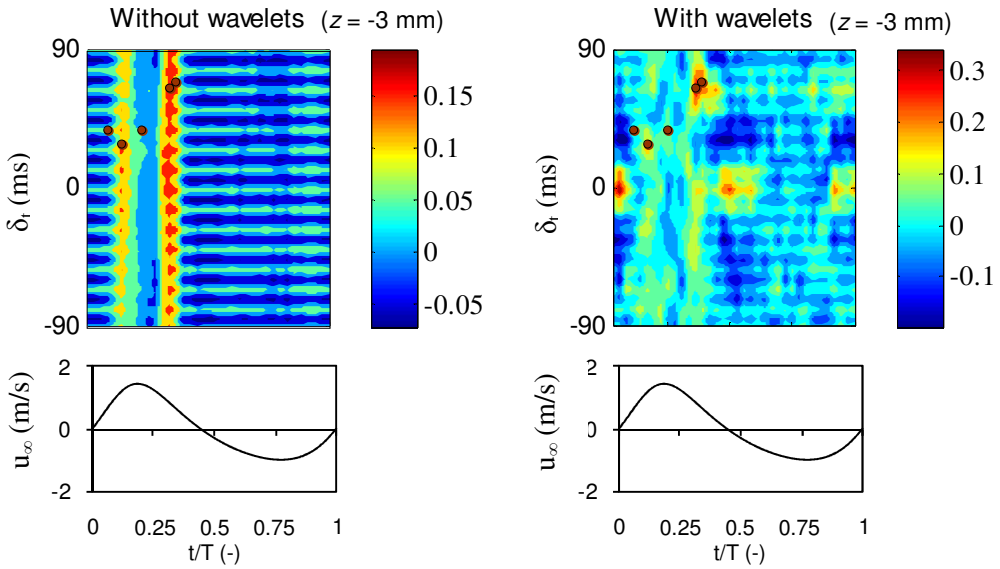

Figure 3.46 – Condition C1: ensemble averaged cross-correlation between the two CCM sensors for z= -3 mm. First column: without wavelet decomposition. Second column: with wavelet decomposition. At the bottom, the free-stream velocity u_∞ is given. The solutions obtained with the wavelet technique are marked with circles over the cross-correlation values.

From the change of pattern one has established the positions where the velocity was effectively zero. Still, the wavelet decomposition helped to detect some peak values in that level with low velocities. Note that before the wavelet treatment none correlation peak was obtained. This is a promising result because these low elevations correspond to a sublayer of the sheet flow layer where the sediments are picked-up from the bed and, usually, measurements of the grains' velocity profile are difficultly detected. Although low velocities should be expected in this sublayer, as high concentrations occur, a substantial part of the sediment transport can take place here.

Figure 3.47 shows the sediment grain velocities for five experimental conditions for the full flow cycle at different elevations (z = -3, 0, 3 and 6 mm). The flow velocity (phase-average) captured by the EMF at z =300 mm is given for reference. Above $z = 0$, velocities were measured for almost the full flow cycle and the results seem consistent in their overall magnitude. The differences between the velocity shapes of the different conditions are found to be in accordance with those at higher elevations i.e., the

asymmetries that generated those kind of flows above the wave boundary layer appear to be reflected in the sheet flow layer. For example, at lower levels the velocity skewness is still present. Still, for phases near the flow reversal, where the velocities are low and the sheet flow layer is very thin, the correlation peaks are more difficult to obtain. The methodology itself has a limitation to measure velocities below 0.12 m/s, which depend on the space between the probes (11 mm) and the maximum time lag considered in the cross-correlation technique (90 ms). Nevertheless, this technique seems promising and can add to the capacity to measure particle velocities in the sheet flow. Moreover, it helped to verify the ability of the ADVP to penetrate into the highly concentrated sheet flow layer.

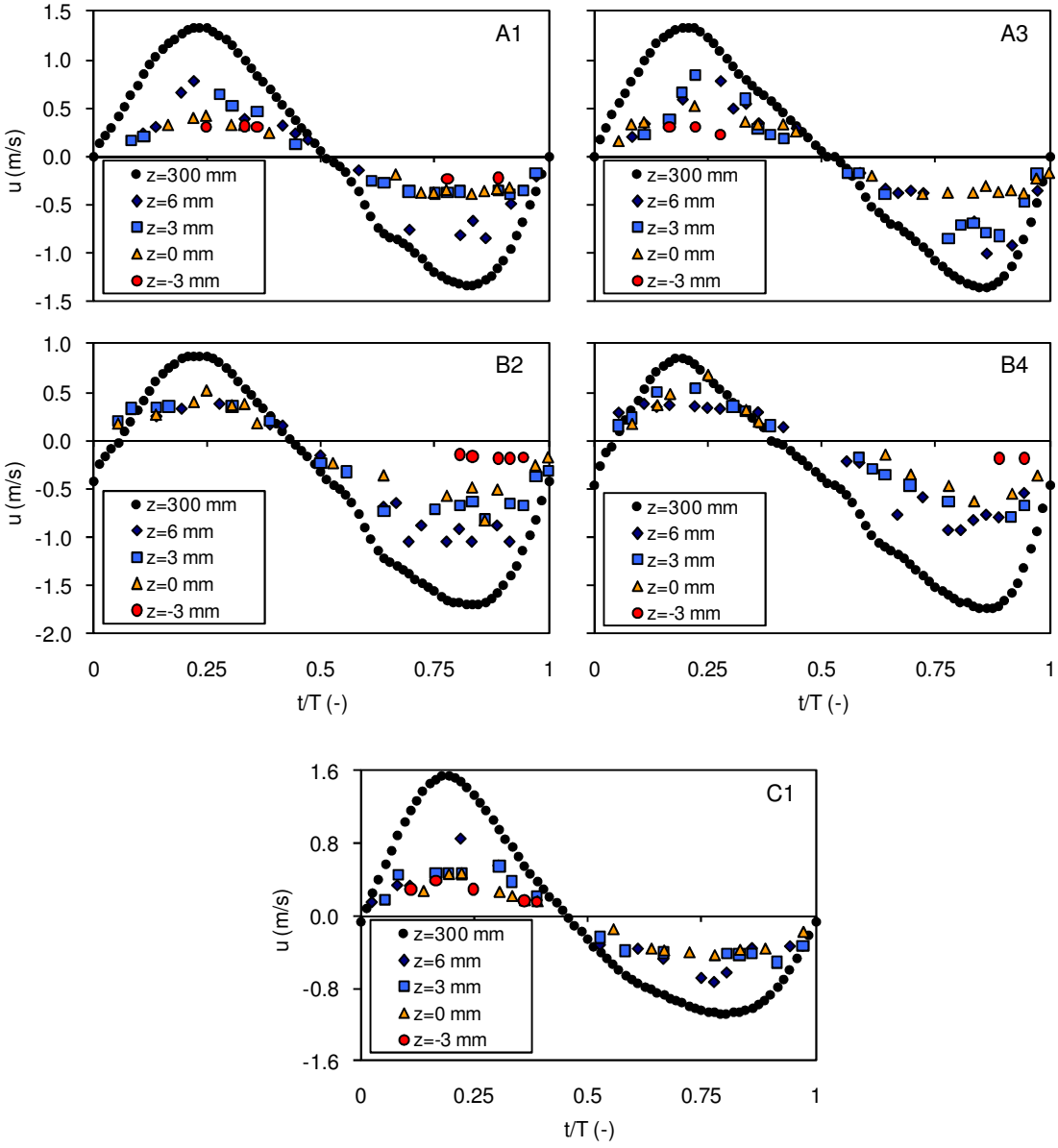

Figure 3.47 – Grain velocities obtained through the wavelet technique for A1, A3, B2, B4 and C1 at z = -3, 0, 3 and 6 mm. The flow velocity (phase-average) captured by the EMF at z =300 mm is given for reference.

3.7 Sediment fluxes within the sheet flow layer

3.7.1 Methodologies

The computations of the sediment fluxes within the sheet flow layer require the knowledge of sediment concentrations and flow velocities in that region. The instantaneous horizontal sediment flux, $\phi_f(z,t)$, is obtained from the product of the instantaneous flow velocity and sediment concentration:

$$\phi_f(z,t) = u(z,t)\,c(z,t). \tag{3.40}$$

For the bin-averaged sediment flux, it immediately follows:

$$\hat{\phi}_f(z,t) = \frac{1}{N_p}\sum_{n=1}^{N_p}\phi_f\left(z,t+(n-1)T\right),\ 0 \le t < T\ . \tag{3.41}$$

Though the combination of the cross-correlation techniques described by McLean et al. (2001) with wavelet multilevel decomposition (Mallat, 1999; and Franca and Lemmin, 2006) is capable to determine sediment grain velocities within the sheet flow layer (see also, Abreu et al., 2009), the methodology itself has a limitation to measure velocities below a certain value depending on the space between the probes and the maximum time lag considered in the cross-correlation technique. Therefore, the ADVP was combined with the CCM data to compute the sediment fluxes. It is noted that the instruments were not collocated during the experiments but, since the flow is horizontally uniform in the tunnel, the impact in the sediment flux estimates is expected to be minimum. In addition, the measurements of the two devices are not of the same sampling volume.

ADVP velocity data was processed in order to obtain velocities within the SFL ($d_e \le z \le d_t$) with a 0.5 mm vertical bin size to match the available concentration time series. For the upper sheet flow layer ($0 \le z \le d_t$), the velocities were interpolated using the ADVP data recorded at z = 0, 3 and 6 mm. For the pick-up layer ($d_e \le z \le 0$), a linear velocity profile was assumed between $z = 0$ and the instantaneous erosion depth, following O'Donoghue and Wright (2004b) and van der A et al. (2009). Because the pick-up layer presents large vertical gradients in sediment concentration, small uncertainties in the velocities or at the location of the erosion depth might cause large differences in flux computations.

Integrating the instantaneous horizontal sediment flux over the flow period, the time-averaged fluxes $\phi_t(z)$ are obtained:

$$\phi_t(z) = \frac{1}{T}\int_0^T \phi_f(z,t)\,dt\,. \tag{3.42}$$

Moreover, it is possible to evaluate the time-averaged oscillatory flux, $\tilde{\phi}_t(z)$, and current-related flux, $\bar{\phi}_t(z)$, according to:

$$\tilde{\phi}_t(z) = \frac{1}{T}\int_0^T \tilde{u}(z,t)\tilde{c}(z,t)\,dt\,, \tag{3.43}$$

$$\bar{\phi}_t(z) = \bar{u}(z)\bar{c}(z)\,. \tag{3.44}$$

3.7.2 Results

From Figure 3.48 to Figure 3.52 the sediment flux computations within the sheet flow are presented for tests A1, A3, C1, B2 and B4, accordingly. Panel (a) presents the instantaneous horizontal sediment flux, $\phi_f(z,t)$, within the sheet flow layer. The lower and upper limits of the SFL are indicated over $\phi_f(z,t)$ through continuous lines. Above the panel (a), the free-stream velocity is given for reference, indicating selected phases for which the instantaneous flux profiles are shown in (c-j). These phases refer to flow reversal, maximum free-stream velocities, accelerating and decelerating phases of the flow. Panel (b) shows the vertical profiles of the time-averaged $\phi_t(z)$ (dots) fluxes and the corresponding oscillatory $\tilde{\phi}_t$ (circles) and current-related $\bar{\phi}_t$ (pluses) components. Moreover, panels (c-j) show for each select phase the value of the erosion depth d_e and the upper sheet flow position d_t represented by the long-dashed and short-dashed horizontal lines.

The five figures demonstrate that the instantaneous fluxes in the sheet flow layer vary practically in phase with the free-stream velocity. The highest values of ϕ_t are obtained at $z \approx 0$ or bellow and occur at times of high flow velocity (panels (e) and (i)). Somewhat surprisingly, the largest magnitudes of ϕ_t are obtained for the pure accelerated skewed flows, A1 and A3. For instance, panels (e) and (i) reveal that ϕ_t reaches 600 kg/m^2/s for A1. The addition of velocity skewness in test C1, compared to A1, results in large discrepancies in magnitude between the positive and negative flow cycles at $z = 0$. Under the maximum positive velocity the value is 490 kg/m^2/s, while under the maximum negative velocity it reaches 230 kg/m^2/s. The tests with counter currents (B2 and B4) present lower magnitudes of ϕ_t. For example, B2 shows 240 and -410 kg/m^2/s in panels (e) and (i) at $z = 0$.

At flow reversal the influence of the accelerated skewed flows in the sediment fluxes is obvious. The comparison between panels (c) and (g) allows the confirmation of the aforementioned phase-lag effects, suggested by the visual observations of sand motion in the tunnel runs and detailed analysis of the CCM measurements. With the exception of test C1 that possess velocity skewness, panels (c) at

maximum flow acceleration, reveal that part of the sediment particles that are mobilized during the negative velocity phase have not settled completely at the negative-to-positive flow reversal and are still available to be transported by the positive velocities in the next half-cycle. Probably, this occurs because the time between maximum negative flow and the negative-to-positive flow reversal is small compared to the time needed for sand to settle. In contrast, the positive-to-negative flow reversal shown through panels (g), at maximum negative flow acceleration, show that sediment particles have practically settled, now because the time between the maximum positive flow and the positive-to-negative flow reversal is larger due to the wave asymmetry.

This existence of phase-lag effects also contributes to onshore net transport. Thus, the increase in q_s in Figure 3.21a,b with β is likely not due to more skewed bed shear stress alone, but also to phase lag effects at the negative-to-positive flow reversal. Note that with an increase in β, the time for sand to settle between maximum negative flow and the subsequent flow reversal reduces.

The time-averaged fluxes ϕ_t and the corresponding oscillatory $\tilde{\phi}_t$, and current-related $\overline{\phi}_t$ fluxes present interesting patterns for the five flow conditions. The magnitude of time-averaged fluxes, ϕ_t, are at least one order of magnitude lower than the instantaneous fluxes, ϕ_f. That is not surprising, since they are the result of the difference between positive and negative similar large quantities.

The tests without a counter current (A1, A3 and C1) generally present positive values of ϕ_t throughout the entire sheet flow layer thickness. This behaviour is due to the current-related $\overline{\phi}_t$ flux contribution resulting from a residual positive flow near the bottom, which balances the oscillatory negative flux $\tilde{\phi}_t$. Test C1 shows that in the upper sheet flow layer the time-averaged oscillatory sediment flux becomes positive as the current-related flux. However, for the three tests $\tilde{\phi}_t$ is consistently negative in the pick-up layer. As explained by Ruessink et al. (2011) this difference of sign is justified when, at a certain elevation, lower concentrations occur during the positive flow phase or, equivalently, higher concentrations take place during the negative flow phase. As the pick-up layer is characterised by a decrease in the concentrations due to an increase of the free-stream velocity, and that this decrease is accentuated under the positive half cycle, it is expected to obtain the opposite sign in $\tilde{\phi}_t$ within that region.

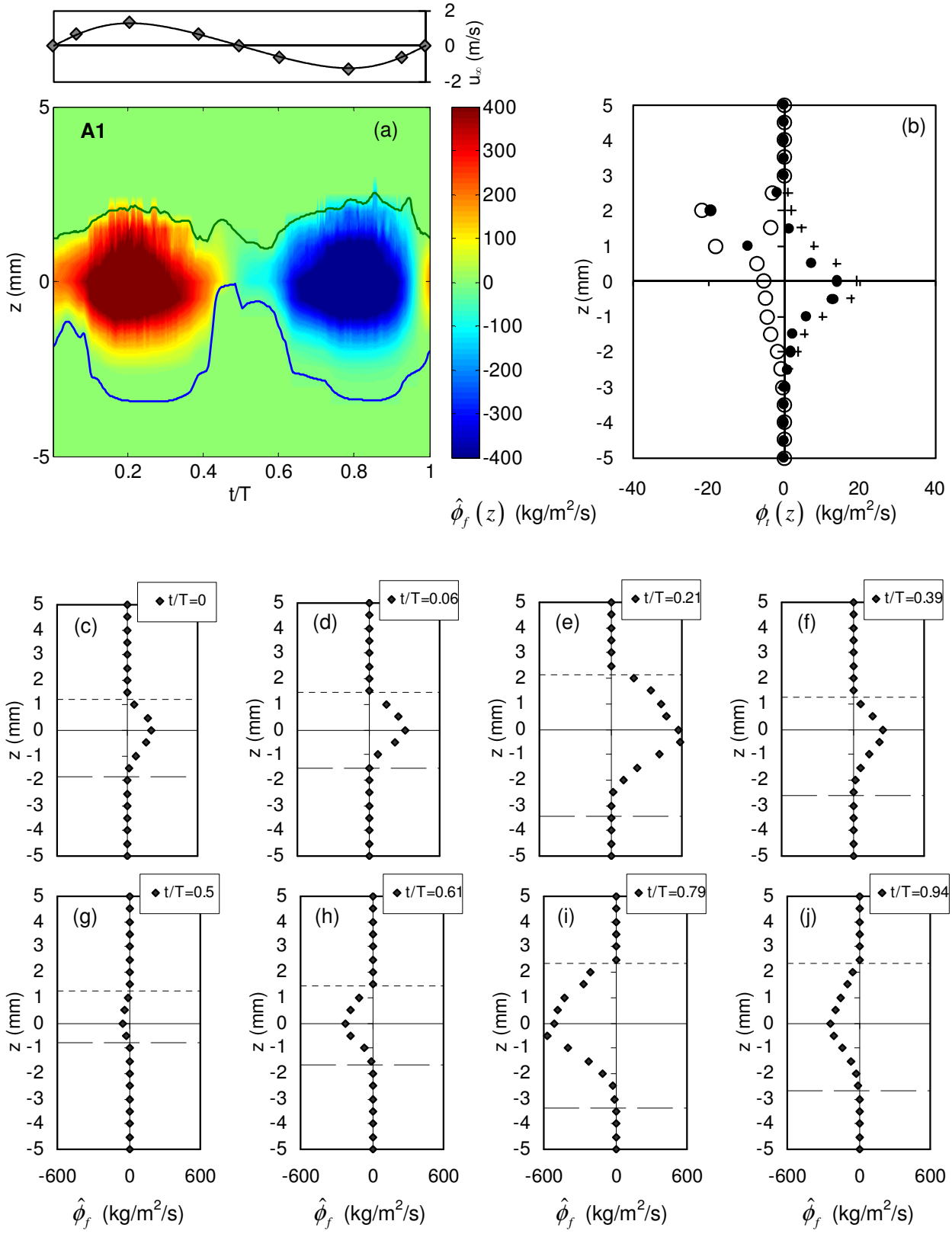

Figure 3.48 – Sediment fluxes for A1. (a) Bin-averaged sediment flux, $\hat{\phi}_f(z,t)$. (b) Vertical profiles of oscillatory $\tilde{\phi}_t$ (circles), current-related $\overline{\phi}_t$ (pluses) and time-averaged $\phi_t(z)$ (dots) flux. (c-j) Bin-averaged sediment fluxes at the phases indicated in the free-stream velocity panel above (a).

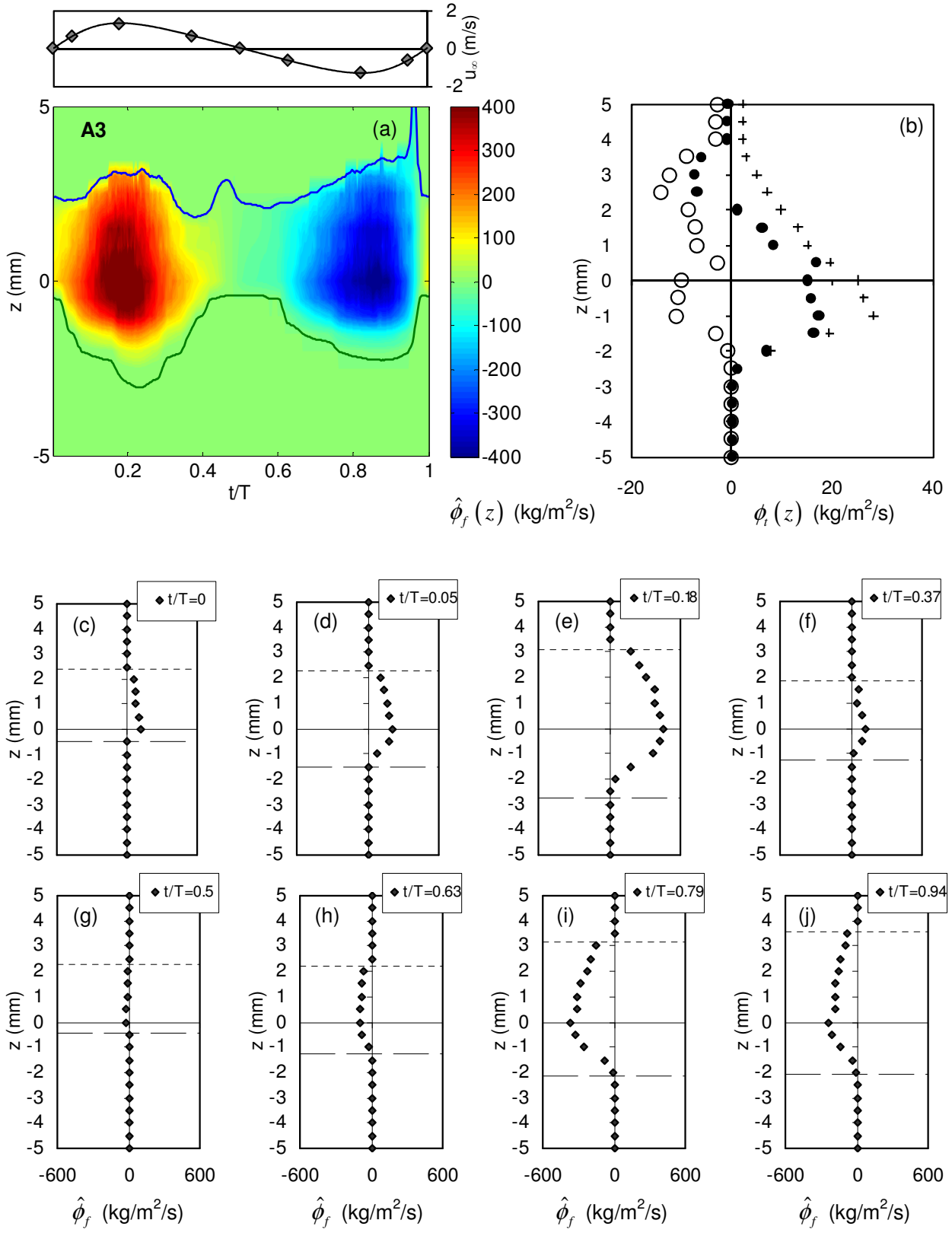

Figure 3.49 – Sediment fluxes for A3. (a) Bin-averaged sediment flux, $\hat{\phi}_f(z,t)$. (b) Vertical profiles of oscillatory $\tilde{\phi}_t$ (circles), current-related $\overline{\phi}_t$ (pluses) and time-averaged $\phi_t(z)$ (dots) flux. (c-j) Bin-averaged sediment fluxes at the phases indicated in the free-stream velocity panel above (a).

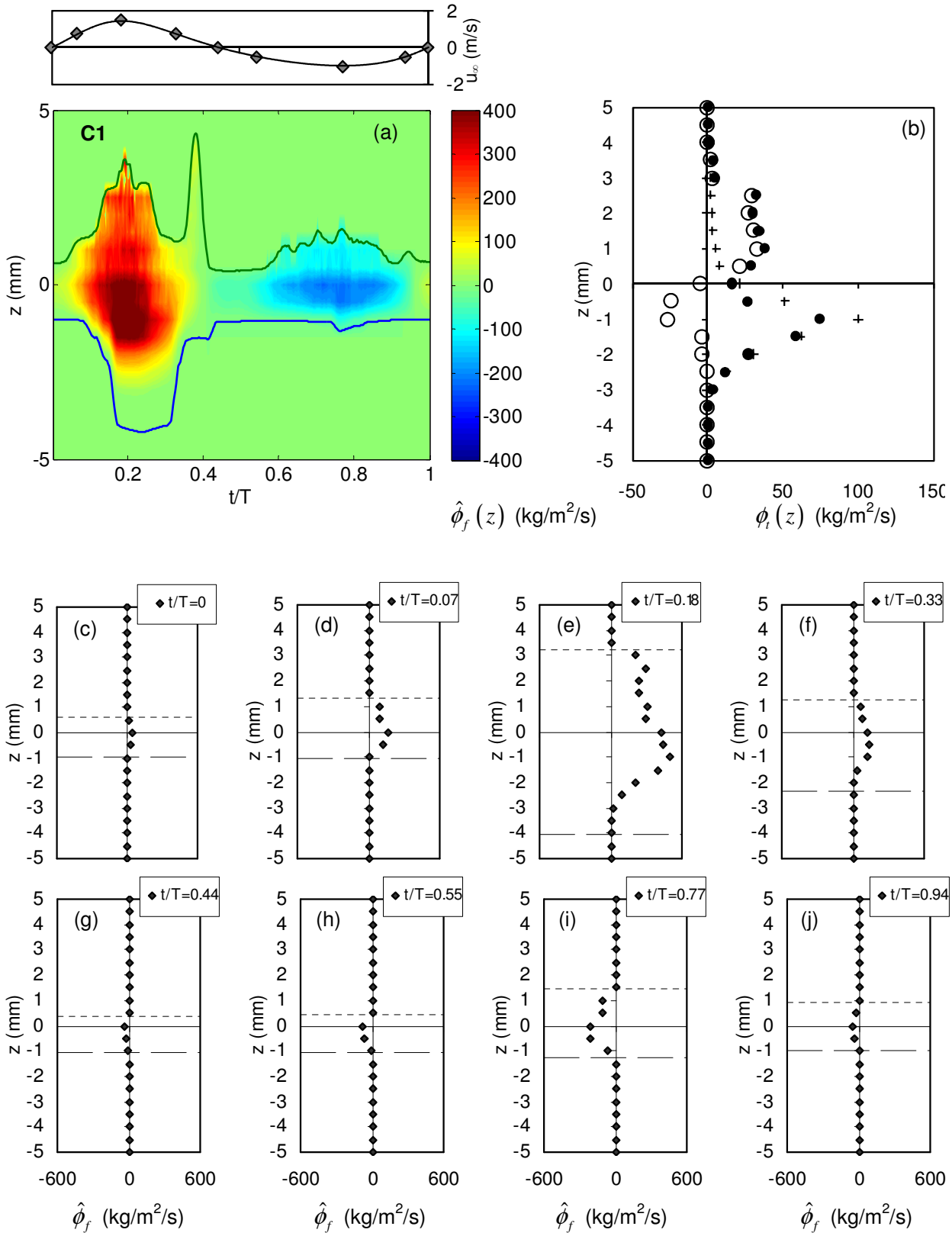

Figure 3.50 – Sediment fluxes for C1. (a) Bin-averaged sediment flux, $\hat{\phi}_f(z,t)$. (b) Vertical profiles of oscillatory $\tilde{\phi}_t$ (circles), current-related $\overline{\phi_t}$ (pluses) and time-averaged $\phi_t(z)$ (dots) flux. (c-j) Bin-averaged sediment fluxes at the phases indicated in the free-stream velocity panel above (a).

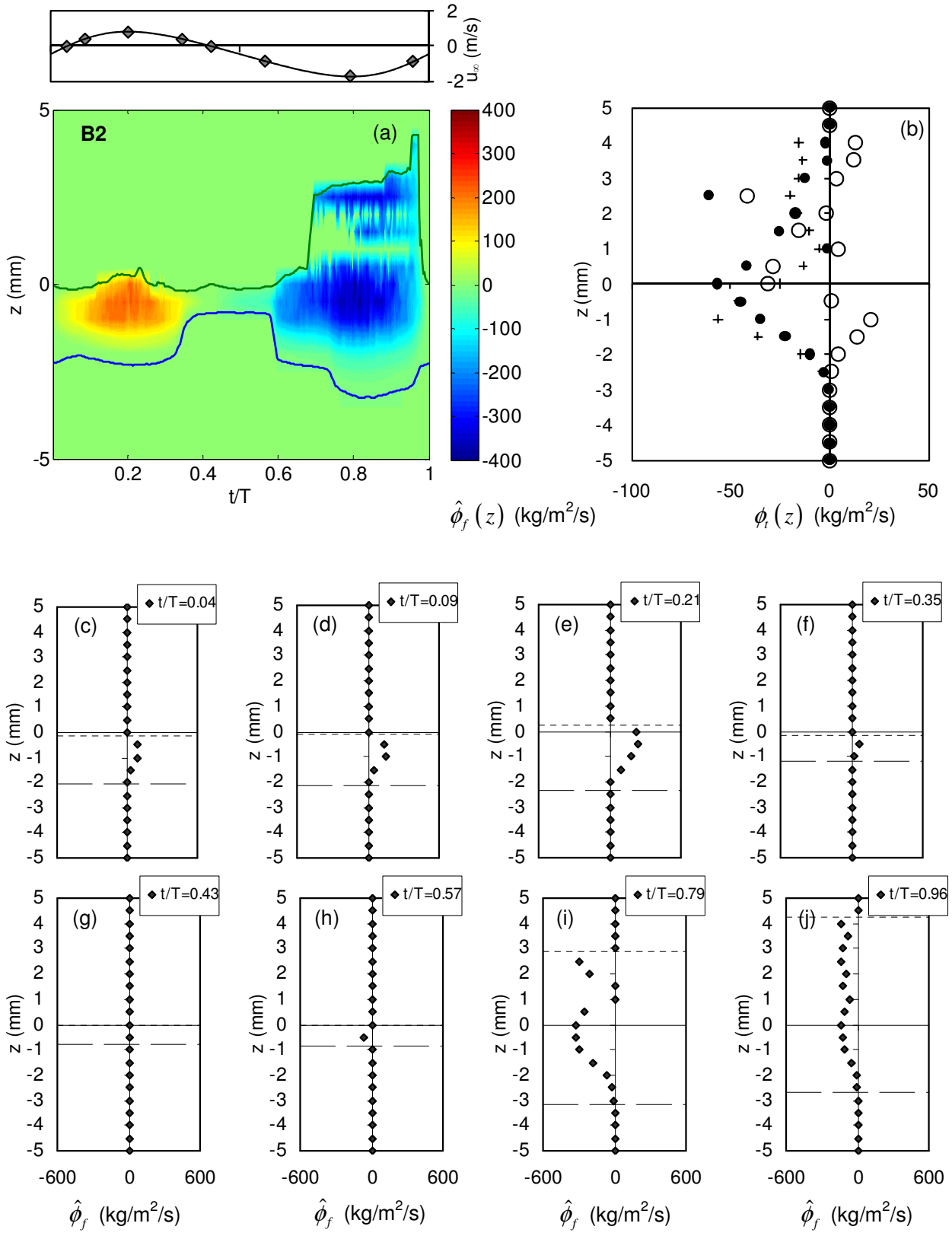

Figure 3.51 – Sediment fluxes for B2. (a) Bin-averaged sediment flux, $\hat{\phi}_f(z,t)$. (b) Vertical profiles of oscillatory $\tilde{\phi}_t$ (circles), current-related $\overline{\phi}_t$ (pluses) and time-averaged $\phi_t(z)$ (dots) flux. (c-j) Bin-averaged sediment fluxes at the phases indicated in the free-stream velocity panel above (a).

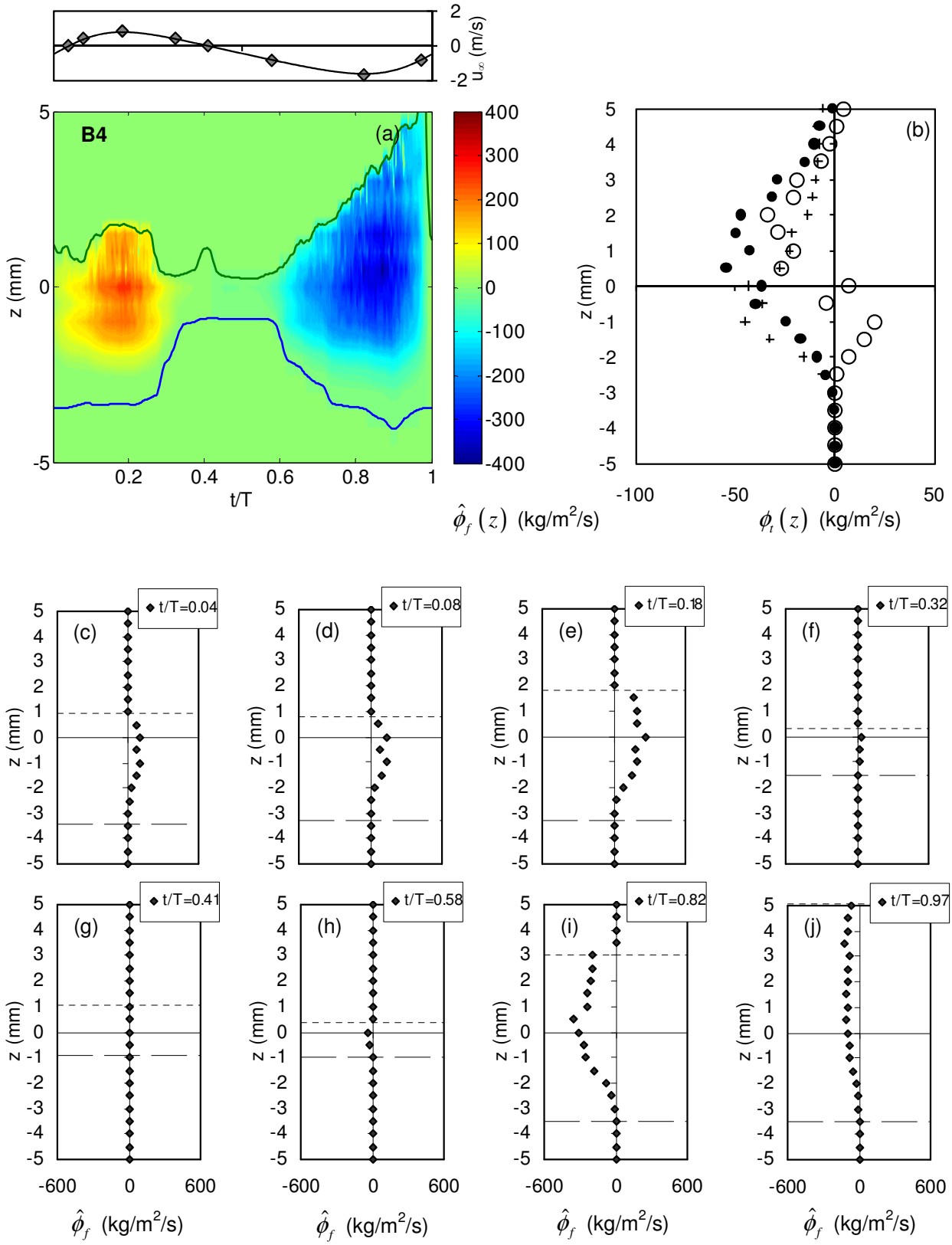

Figure 3.52 – Sediment fluxes for B4. (a) Bin-averaged sediment flux, $\hat{\phi}_f(z,t)$. (b) Vertical profiles of oscillatory $\tilde{\phi}_t$ (circles), current-related $\overline{\phi}_t$ (pluses) and time-averaged $\phi_t(z)$ (dots) flux. (c-j) Bin-averaged sediment fluxes at the phases indicated in the free-stream velocity panel above (a).

The tests with a counter current (B2 and B4) present always negative values of ϕ_t throughout the entire sheet flow layer thickness. Again, the oscillatory flux $\tilde{\phi}_t$ presents opposite signs to the current-related $\overline{\phi}_t$ flux in the pick-up layer. In this case, lower concentrations are found during the negative flow phase than during the other half cycle. Still, in that region, $\overline{\phi}_t$ is generally higher than $\tilde{\phi}_t$ due to the counter current effect, dominating the values of ϕ_t. Above z > 0, $\tilde{\phi}_t$ becomes negative for both tests, resulting from higher concentrations during the negative flow phase than during the other half cycle. Moreover, the magnitude of the values of $\tilde{\phi}_t$ approximately equals those of $\overline{\phi}_t$, contributing both components for the negative values of ϕ_t.

Table 3.3 – Net transport rates.

Condition	q_{on} (kg/m/s)	q_{off} (kg/m/s)	$q_{on} + q_{off}$ (kg/m/s)	q_{sc} (kg/m/s)
A1	0.883	-0.857	0.026	0.0539
A3	0.756	-0.673	0.083	0.1137
B2	0.099	-0.445	-0.356	-0.3826
B4	0.255	-0.683	-0.428	-0.2241
C1	0.589	-0.197	0.391	0.1845

By integrating the instantaneous horizontal sediment fluxes between d_e and d_t, the depth-integrated fluxes in the sheet flow, $\phi_d(t)$, can be estimated:

$$\phi_d(t) = \int_{d_e(t)}^{d_t(t)} \phi_f(z,t)\, dz \,. \tag{3.45}$$

Figure 3.53 shows the results of Eq. (3.45), confirming that ϕ_d vary approximately in phase with u_∞. The advantage to obtain instantaneous values of ϕ_d relies in the possibility to evaluate the contribution of the net fluxes during the positive and negative flow phases.

It illustrates that the net transport rate for the cases without a counter current is the result of a close balance between the positive (onshore) and negative (offshore) fluxes. Such differences can be quantified by integrating the positive and negative flux regions:

$$q_{on} = \int_{d_e(t)}^{d_t(t)} \phi_t^+(z)\, dz \,, \tag{3.46}$$

$$q_{off} = \int_{d_e(t)}^{d_t(t)} \phi_t^-(z)\, dz \,. \tag{3.47}$$

where q_{on} and q_{off} represent the positive (onshore) and negative (offshore) transport rates in the sheet flow layer.

The results of Eq.s (3.45) and (3.46) and the balance between both estimations are listed in Table 3.3. The values of q_{sc} given in Table 3.2 are also included for reference. Here, the objective is to highlight the influence of the velocity and acceleration skewness on the transport rates. For A1, A3 and C1, Table 3.3 indicates that the increase of β and R lead to a noticeable reduction of q_{off} compared to q_{on}. For A1 and A3, the increase of acceleration skewness leads to a shorter duration between the maximum negative flow velocity and the following flow reversal and, hence, to a lower value of q_{off}. For C1, the increase of velocity skewness clearly reflects the reduction of the values during the negative half cycle, which is a consequence of both lower velocities and sediment concentrations (see Figure 3.28 and Figure 3.37). For B2 and B4, the increase of β leads to larger values of q_{on} in proportion to q_{off}. This balance results in lower negative net transport rates when the acceleration skewness arise.

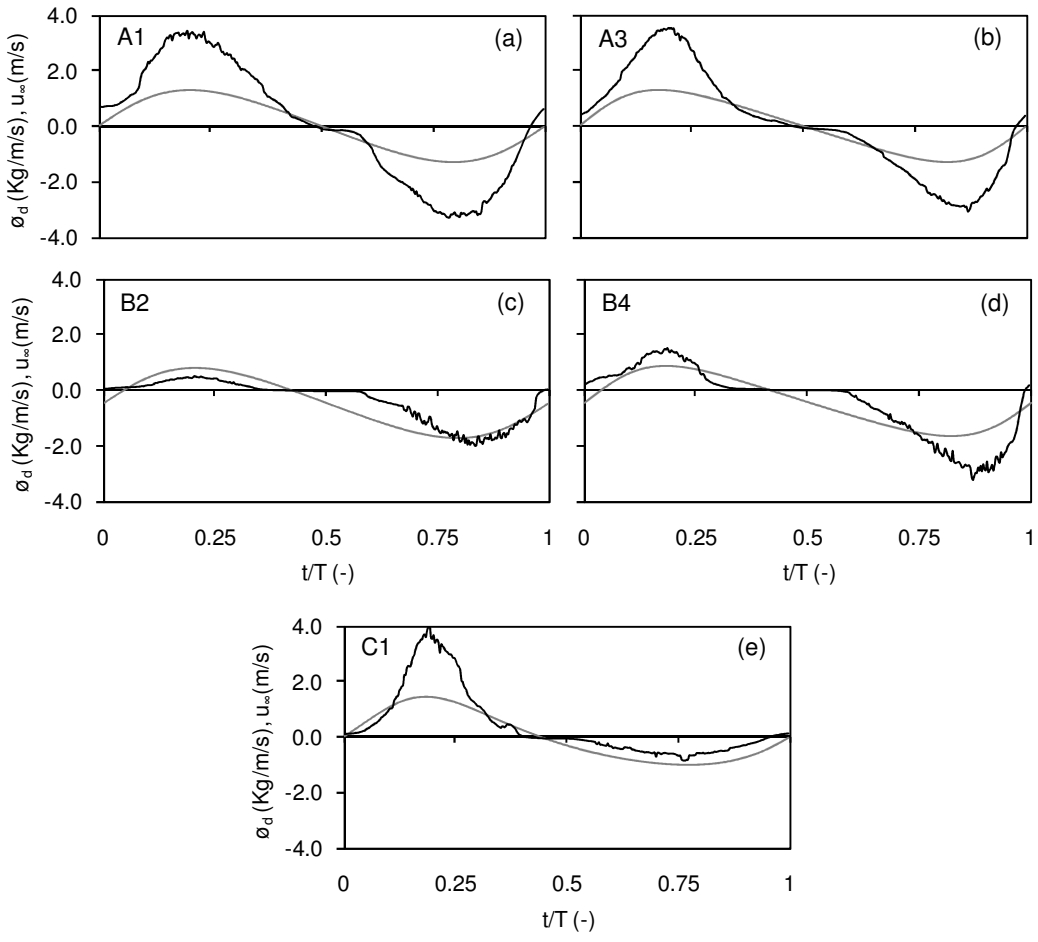

Figure 3.53 – Depth-integrated flux ϕ_d (black line) and free-stream velocity (gray line) *versus* nondimensional time t/T for: (a) A1, (b) A3, (c) B2, (d) B4 and (e) C1.

Nevertheless, the results in Table 3.3 and Figure 3.53 confirm that there is a delicate balance between positive and negative flow phases and the results are sensitive to changes in acceleration skewness, particularly for tests A1 and A3, and B2 and B4.

Ruessink et al. (2011) combined the ADVP with both CCM and ABS data and evaluated the importance of the contribution of the sheet flow layer and the suspension layer to the overall flux. By computing cumulative sand transport rate distributions Ruessink et al. concluded that the sheet flow layer contributes with 60-70% to the total net transport rate.

3.8 Bed shear stresses

3.8.1 Methodologies

Accurate measurements of the local shear stress under oscillatory flows are difficult to attain, particularly in mobile sand bed situations (e.g., Dyer and Soulsby, 1988). As an alternative, several methods that rely on different assumptions have been developed and are usually employed to infer the bed shear (e.g., Soulsby and Wainwright, 1987). Recently, van der A et al. (subm.) compared three methodologies (the Log-fit, the momentum-integral equation and the Reynolds stress methods) for fixed, rough bed experiments, under sinusoidal and acceleration-skewed oscillatory flows. The results of van der A et al. provide a good physical insight about the influence of velocity-asymmetric flows in the bed shear stresses and a general good agreement between the three approaches was confirmed. All the methodologies agreed about the effect of the acceleration skewness of the oscillatory motion: under the rapidly accelerated half cycle, larger (absolute) bed shear stresses were observed.

A partial objective of this work is to study the bed shear stress forced by velocity and acceleration skewed waves of mobile sand beds as typically found in the shoaling and surf zone of sandy beaches. This objective is pursued using two methodologies to estimate the bed shear stresses: the Log-fit method and the momentum integral method.

Momentum-integral method

Assuming that in the LOWT the free-stream oscillating flow is uniform and parallel to the bed ($\partial u/\partial x \approx 0$) and that the pressure is horizontally constant across the thin bottom boundary layer, it is possible to apply the momentum-integral method to compute the shear stress at a certain elevation $z = z'$ for the case of pure oscillatory flow with no superimposed current (e.g., Nielsen, 1992; Fredsøe and Deigaard, 1992). This corresponds to the integration of Eq. (2.15), yielding:

$$\tau(z',t) = \rho \int_{z'}^{\infty} \frac{\partial}{\partial t}(u_\infty - u)\, dz\,. \tag{3.48}$$

In the particular case of mobile sand beds, Eq. (3.48) should also consider the density of the sediment/fluid mixture, ρ_m, resulting in (e.g., Dick and Sleath, 1991):

$$\tau(z',t) = \int_{z'}^{\infty} \frac{\partial}{\partial t}(\rho u_\infty - \rho_m u)\, dz \tag{3.49}$$

with

$$\rho_m = (1 - C_v)\,\rho + C_v \rho_s \tag{3.50}$$

in which C_v is the volumetric sediment concentration.

From Eq. (3.49) it is clear that the value for the "**bed**" shear stress will depend on the lower limit of integration. In the case of a rigid bottom, the lower limit of integration, z', corresponds to the level of the bed. However, in the case of movable beds, a sheet flow layer develops during the flow cycle in which there is mobilization of fluid and sand particles below $z = 0$. Since the sand moves below the initial bed level this reference level is not constant and is thus ill-defined. In the present experiments, to obtain the bed shear stress estimation through Eq. (3.49), the undisturbed bed level is defined as the initial bed level at the beginning of an experiment, prior to flow action ($z' = 0$). Moreover, to avoid errors in the integration arising from the difference between large and similar quantities at the higher levels, it is recommended to use an upper limit of integration (Dick and Sleath, 1991). It was chosen $z = 30$ mm because the test conditions without collinear currents had very low suspended sediment concentrations around flow reversal, particularly, for $z > 30$ mm (Ruessink et al., 2011). Further calculations, using an even lower value of 21 mm resulted in very similar bed shear stress values, confirming the validity of using 30 mm for the upper limit of integration. To suppress part of the noise resulting from the velocity time derivatives, a 2 Hz low-pass filter was applied to the ADVP measured velocity time-series.

At higher levels the concentrations are relatively small (Ruessink et al., 2011) and within the interval $0 < z < 30$ mm the sediments do not significantly affect the fluid density ($\rho_m \approx \rho$). This implies that the results obtained through Eq. (3.49) are practically identical to those of Eq. (3.48).

The application of the momentum-integral method for combined wave-current motions is not strictly valid, since the Eq. (3.49) does not provide a mean component of τ. Nevertheless, in such cases, Eq.

(3.49) can assess the shape of the oscillatory component of τ and it is therefore useful for comparison with other methods.

Momentum-integral method and velocity-defect law

The temporal shear stress distributions obtained from Eq. (3.48) is strongly linked to the free-stream acceleration and the defect function $D_1(z)$ (Eq. (3.16)). Introducing Eq. (3.14) into Eq. (3.48), the shear stress can be rewritten as:

$$\tau(z',t) = \rho\int_{z'}^{\infty}\frac{\partial}{\partial t}\left(D_1(z)u_\infty(t)\right)dz$$

$$\Leftrightarrow \tau(z',t) = \rho a_\infty(t)\int_{z'}^{\infty}D_1(z)dz \qquad (3.51)$$

Eq. (3.51) is consonant with Dick and Sleath (1991) observations in the way that the shear stress calculated from this methodology is mainly determined by the free-stream pressure gradient:

$$\tau \sim \rho\int_{z}^{\infty}\frac{\partial u_\infty}{\partial t}dz \Leftrightarrow \tau \sim \rho\int_{z}^{\infty}a_\infty dz \Leftrightarrow \tau \sim \rho a_\infty \Delta z\,. \qquad (3.52)$$

Nonetheless, Dick and Sleath noticed in their experiments that there was a phase difference between the shear stress and the acceleration over the sheet flow layer. These results can be justified by Eq. (3.51) since $D_1(z)$ is a complex function.

Log-fit method

The Log-fit method assumes that, in the case of a hydraulically rough bed, the velocity vertical profile can be approximated by a logarithmic function over the lower part of the bottom boundary layer. This results from the assumption that the shear stress is vertically constant in this layer:

$$\tau = \rho u_*^2\,, \qquad (3.53)$$

where u_* represents the shear velocity.

For a two-dimensional horizontal flow, the velocity profile can be written according to the *law-of-the-wall*:

$$u(z) = \frac{u_*}{\kappa}\ln\left(\frac{z}{z_0}\right) \qquad (3.54)$$

where u is the horizontal velocity, κ is the von Kármán's constant, which is assumed equal to 0.4, and z_0 is the zero-intercept level of the log-velocity profile. Eq. (3.54) can be written as:

$$\ln(z) = \frac{\kappa}{u_*} u(z) + \ln(z_0) \tag{3.55}$$

From Eq. (3.55) follows that if one plots the velocity profiles logarithmically, a straight line between $ln(z)$ and u is expected. The slope of that line is equal to κ/u_* from which the bed shear stress may be obtained.

The *law-of-the-wall*, Eq. (3.54), was established for steady flows. Its validity for turbulent oscillatory boundary layers, for both smooth and rough beds, was demonstrated, for example, in the experiments performed by Jensen et al. (1989). When applying this methodology to oscillatory flows one should remind that the unsteady inherent behaviour can cause slight deviations from the logarithmic shape, particularly for small flow periods and around flow reversal.

Recently, Dixen et al. (2008) presented a step-by-step methodology to compute the bed shear stresses under the logarithmic law. According to that work, the logarithmic layer lies within the interval $0.2k_s \le z \le (0.2-0.3)\delta$, where δ represents the boundary layer thickness. The upper edge of δ is located above the *overshoot velocity* and is defined as the level where the velocity amplitude reaches its minimum (Figure 3.54). The upper limit of the interval ensures that the levels lie in the constant stress layer, while the lower limit ensures that the velocity profiles are not directly influenced by the boundary roughness. For the present experiments, the interval $3 \le z \le 21$ mm satisfies these conditions. Figure 3.55 shows the phase-averaged velocity profiles for the five test conditions for several flow phases. The data reasonably follow the log-linear trend for $z < 21$ mm, except for phases close to flow reversal (especially for $t/T = 0.1$ and 0.5).

The Log-fit method also assumes that the velocities are measured relative to a reference level. In the case of a rigid bed, this level is fixed and constant in time. In mobile beds there is the development of a sheet flow layer structure along the wave cycle in which there is mobilization of fluid and particles bellow $z = 0$. Therefore, the reference level is not constant and thus is ill-defined. As the shear stress computations require the exact knowledge of the bottom elevations where the velocity measurements were gathered, different values could be attained if a translation of z is performed. For the present analysis, it was assumed that $z = 0$ corresponds to the bed level at the beginning of the experiments, prior to wave action. It is pointed that a translation of the vertical axis of $\Delta z = \pm 1.5$ mm, relative to the initial reference level $z = 0$, produce differences in the magnitude of the bed shear stress of 50%.

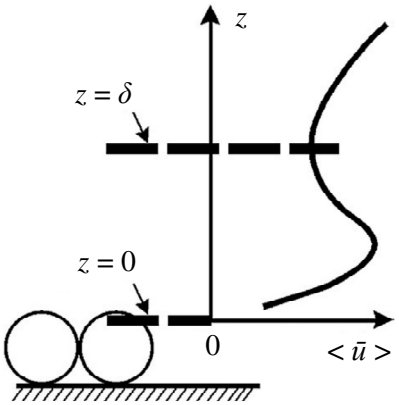

Figure 3.54 – Definition sketch for the momentum-integral method (adapted from Dixen et al., 2008).

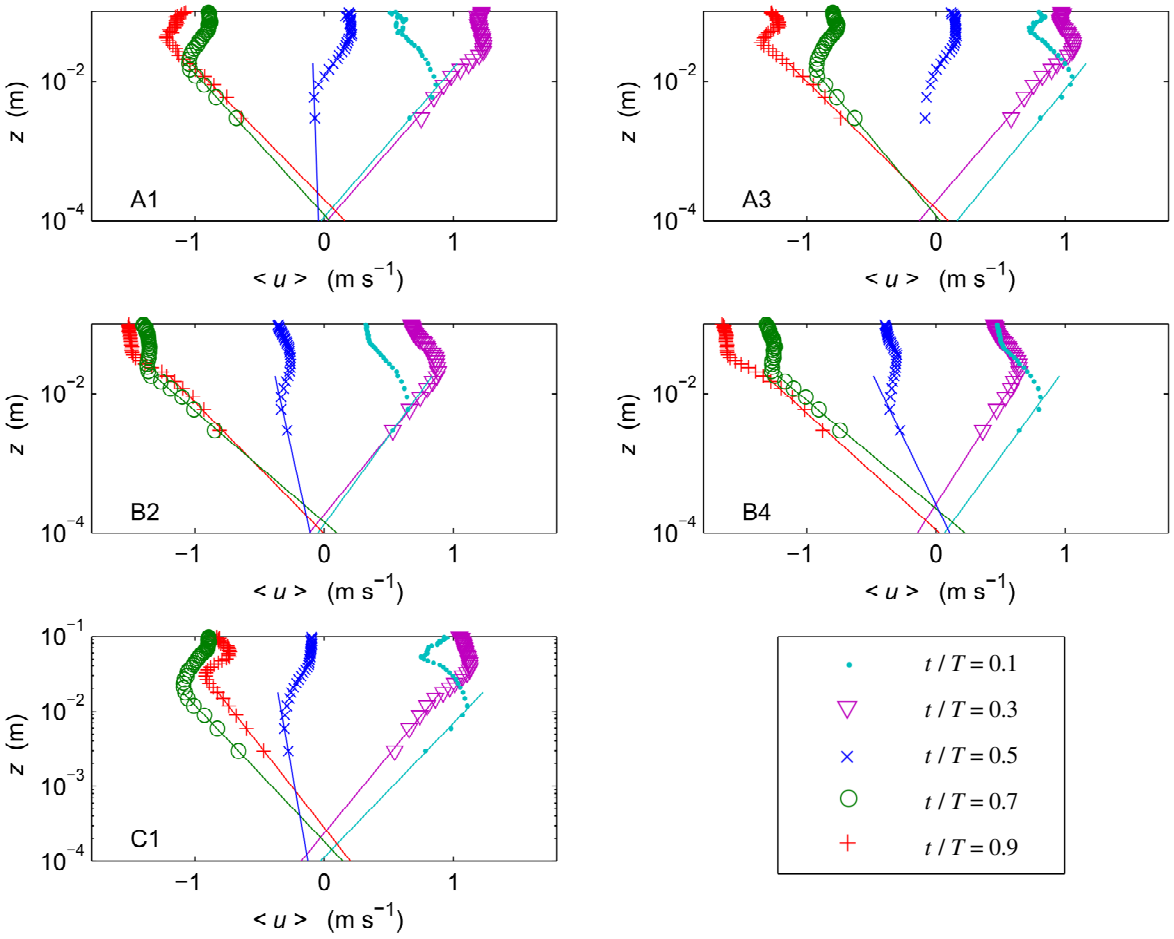

Figure 3.55 – Vertical profiles of phase-average horizontal velocities for tests A1, A3, B2, B4 and C1 measured at several phases: *t/T*=0 (crosses), 0.2 (circles), 0.4 (pluses), 0.6 (dots) and 0.8 (triangles).

To complement this study, a parameterisation linking z_0 with the shear velocity is introduced in Eq. (3.55). The roughness length z_0 in the log-law profile corresponds to the extrapolated level where the velocity would be zero. The values of z_0, which are often solely related to the diameter of the grains or of the bed forms, under intense sediment transport (like in sheet flow) have a transport contribution

that should be taken into account (Soulsby, 1997). According to this, several investigators have proposed the computation of the roughness from the knowledge of the Shields parameter and the sediment grain diameter (e.g., Ribberink, 1998; Herrmann and Madsen, 2007). In this work the expression of Herrmann and Madsen's (2007) is considered:

$$z_0 = \frac{\left[4.5(\theta - 0.05) + 1.7\right]1.1}{30} d_{50}. \tag{3.56}$$

Hereafter, Eq. (3.56) will be identified as HM07. The substitution of Eq. (3.56) in Eq. (3.55) gives an expression that can be solved implicitly for u_*, requiring some iterations to get the solution. Note that after the introduction of HM07, Eq. (3.55) requires the velocity at one level only. This avoids the definition of a reference level in movable bed experiments. In the computations the level z = 15 mm was chosen. Though not shown, the velocities in the range $6 \leq z \leq 18$ mm gave very similar results, being consistent that in the lower part of the flow the shear stress remains constant.

3.8.2 Results

Figure 3.56 presents the bed shear stresses obtained for the five test conditions (A1, A3, C1, B2 and B4) from the aforementioned methodologies. The left column shows the results relying on Eq.s (3.49) and (3.51) of the momentum-integral, while the right column shows the results obtained from the Log-fit (Eq. (3.55)). The free-stream velocity is also given for reference.

Focusing on the left column, one observes that the first harmonic analysis, used in Eq. (3.51), gave similar trends in the temporal evolution of the shear stress obtained from Eq. (3.49). There are some differences mainly caused by oscillations in the acceleration time series obtained from the ADVP. Despite this disagreement, it is obvious that, whenever the assumption that the velocity data follows Eq. (3.16) is valid, the shear stress computations obtained from the momentum-integral method will strongly rely on the free-stream acceleration.

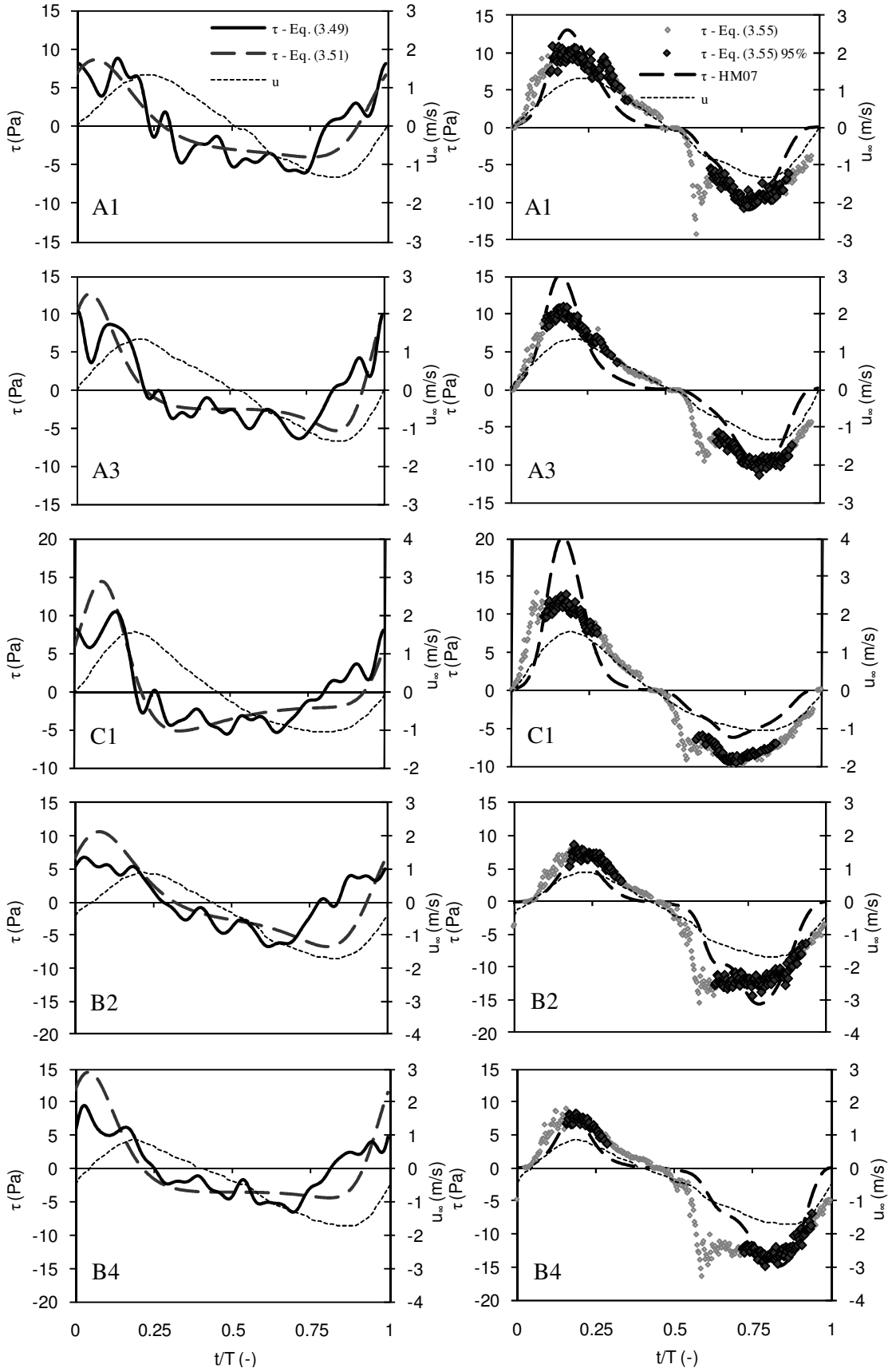

Figure 3.56 –Time series of τ estimated with the momentum-integral (Eq.s (3.49) and (3.51)) and Log-fit (Eq. (3.55) and HM07) for tests A1, A3, C1, B2 and B4. The thick dots correspond to squared correlation coefficients larger than 0.95 and the thinner dots to lower values. The dotted lines represent the free-stream velocity.

The right column shows the deduced bed shear stress obtained from Eq. (3.55). The thick dots correspond to squared correlation coefficients larger than 0.95 and the thinner dots to lower values. The thicker dots reveal that the *law-of-the-wall* follows reasonably well the measured velocity variations during a wide part of the oscillatory flow. Like in Dixen et al. (2008), the logarithmic layer for the present experiments started to appear only after a certain period after the flow reversal. Yet, if one assumes lower correlations (thinner dots), the layer remains well established in a quite substantial portion of the orbital motion cycle. The dashed line corresponds to the introduction of HM07 in Eq. (3.55), which provides a continuous time variation of the bed shear stress. It is noted that the HM07 solution gave results of the same order of magnitude than the other results.

Table 3.4 – TRANSKEW experimental conditions (target values).

Condition	$\lvert\tau_{max} / \tau_{min}\rvert$ (-)				φ (º)			
	Momentum-integral		Log-fit		Momentum-integral		Log-fit	
	Eq. (3.49)	Eq. (3.51)	Eq. (3.55)	HM07	Eq. (3.49)	Eq. (3.51)	Eq. (3.55)	HM07
A1	1.4	2.1	1.0	1.2	29	55	29	10
A3	1.6	2.4	1.0	1.5	71	57	10	13
C1	1.9	2.8	1.3	3.2	25	41	9	12
B2	1.0	1.6	0.6	0.4	74	58	15	10
B4	1.4	3.3	0.6	0.5	62	57	4	5

General conclusions can be extracted regarding the differences between the absolute values of the shear stress computations and the phase differences between the maximum values of the shear stresses and the corresponding of the free-stream velocities, φ. Table 3.4 summarizes that information, indicating the ratio of maximum and minimum bed shear stress $\lvert\tau_{max} / \tau_{min}\rvert$ and the values of φ found in Figure 3.26. Moreover, the definition for φ presented by Fredsøe and Deigaard (1992; figure 2.12) is adopted, where a positive value means that the shear stress is in advance to the free-stream velocity.

The Log-fit method presents two major differences in comparison with the momentum-integral method. First, the bed shear stress for the Log-fit method is practically in phase with the free-stream velocity ($\varphi \leq 29º$), contrasting with larger values obtained with the momentum-integral method ($\varphi \geq 29º$). In the latter, particularly with Eq. (3.49), some fluctuations resulting from the velocity time derivatives do not allow a precise determination of the phase lead and maxima in τ. The same occurs using the Log-fit method through Eq. (3.55) where small dispersions exist in the results, afecting the conclusions. The results of Eq. (3.51) and HM07 provide smoother curves, allowing a better identification of the maxima of τ and, consequently, of φ.

The lack of agreement in the values of φ between both methodologies was not observed in van der A et al. (2011) fixed bed experiments, but it can be explained to a certain extent for mobile beds. The major problem lies in the definition of the elevation where the bed shear stress should be evaluated for mobile beds and in the physical processes that are implied in the different methods. This question was recently addressed by Guard and Nielsen (2008) through the analysis of the sheet flow experimental data of O'Donoghue and Wright (2004b). The authors computed the bed shear stress at different elevations according to the momentum-integral and Nielsen's (1985) method and reported phase-leads that asymptotically increase to 90° further into the sheet flow layer. They show that the magnitude and phase lead of the total shear stress depends on the chosen elevation within the sheet flow layer which makes it difficult to define a particular phase lead under mobile sand beds.

The second main difference is the disagreement in the prediction of the magnitudes of τ. One observes that, with the exception of HM07, the *law-of-the-wall* leads to $|\tau_{max}| \approx |\tau_{min}|$ for tests A1, A3 and C1. This clearly contrasts with the momentum-integral method where larger bed shear-stresses (in absolute value) are obtained under the rapidly accelerating half cycle, when the velocity changes from the offshore negative maximum to an onshore positive maximum ($|\tau_{max} / \tau_{min}| > 1$). Interestingly, though the solution of HM07 is obtained with the *law-of-the-wall* (Eq. (3.55)), the results corroborate the tendencies observed for the momentum-integral, denoting similar asymmetries in the shear stress maxima between both half cycles. For the pure accelerated skewed flows it is possible to observe that the increase of β leads to increased ratios of $|\tau_{max} / \tau_{min}|$ (compare A1 with A3). This increase of $|\tau_{max} / \tau_{min}|$ for acceleration-skewed flows was recently observed over fixed rough bed experiments (van der A et al., 2011). Comparable observations can be made for tests B2 and B4 for the momentum-integral method, since the methodology assesses the shape of the oscillatory component of τ. The log-law also indicates that a negative mean component of the shear stress does exist, where the opposing net current leads to shear stresses significantly larger under the negative flow phase. However, its value cannot be obtained since the method does not provide a continuous time series of the shear stress. For test C1, where both velocity and acceleration skewness coexist, the introduction of the velocity skewness enhances the shear stress under the positive flow phase. The results are corroborated by all shear stress solutions, indicating that a velocity skewed flow induces more differences between τ_{max} and τ_{min} than an acceleration skewed flow.

The ratio $|\tau_{max} / \tau_{min}|$ reflects the skewness of the bed shear stress and can be considered an important parameter for sediment transport rate predictions. The mechanism that causes a net transport in the wave direction in sawtooth waves was first pointed out by Nielsen (1992) due to an enhancement of the bed shear stress, τ, when the flow evolves rapidly from the maximum negative velocity to the

maximum positive velocity and therefore has a limited time available for the bottom boundary layer to develop. Since the present data illustrates the asymmetry in τ, between the half cycles, Figure 3.57 shows q_s values as a function of the bed shear stress skewness, β_τ (defined as in Eq. (2.7) but for τ) computed with the momentum-integral method for the conditions A1 and A3. The result for C1 condition is also displayed, although the bed shear-stress skewness in this case is also determined by the velocity skewness. The results of τ considered in the computation of β_τ refer to Eq. (3.49) and it is seen that the net transport rates are well correlated with β_τ. Similar trends are attained with the values of τ resulting from Eq. (3.51) and HM07.

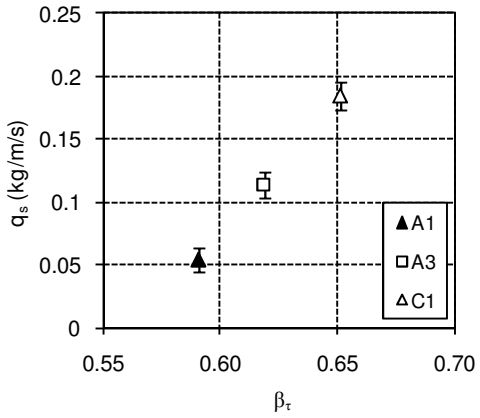

Figure 3.57 – Measured net transport rates for conditions A1, A3 and C1 as a function of β_τ. The error bars correspond to the standard deviation.

Another different question arises regarding the choice of the hydraulic roughness. From the Log-fit method, Eq. (3.55), it is also possible to deduce the roughness height, z_0. Figure 3.58 presents the results of z_0 for all five conditions. When the squared correlation coefficient between the data and the straight line is over 95% (thicker dots), the roughness height z_0 is of the order of 0.1 mm, corresponding to a roughness k_s (using $k_s = 30\, z_0$) of the order of 15 times d_{50}. Considering also lower correlations, one notes that z_0 reaches unrealistic large values close to flow reversal and varies along the flow cycle, as previously shown by many authors (e.g., Cox et al., 1996; Wilson, 1989; Wilson et al., 1995; Ribberink, 1998; Herrman and Madsen, 2007). The intermediate value $15d_{50}$ is far from the classical value ($2.5d_{50}$) of rough rigid bottoms and corresponds to a length scale characteristic of the sheet flow (e.g. Madsen, 1993).

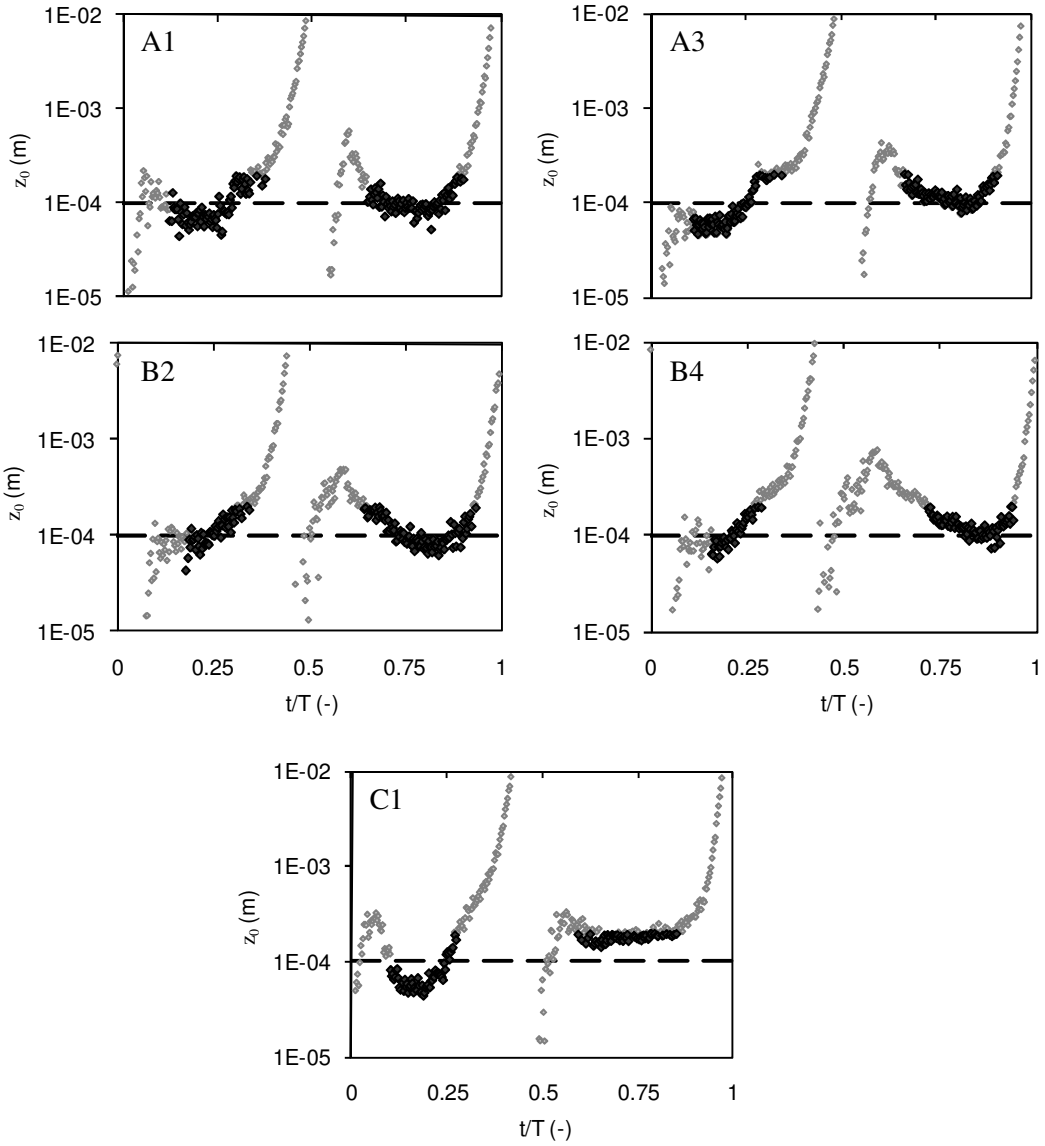

Figure 3.58 – Results obtained for the roughness height from the Log-fit method. The thick dots correspond to correlation coefficients larger than 0.95 and the thinner dots to lower values. The horizontal long-dashed line marks $z_0 = 1\times10^{-4}$, i.e., $k_s = 15d_{50}$.

3.9 Chapter closure

A reliable dataset under sheet flow conditions of net sand transport rates, detailed hydrodynamics and sediment concentrations, generated by full-scale, regular, acceleration- and velocity-skewed oscillatory flows combined with opposing net currents, was obtained. This data base allows analyzing the effect of velocity and acceleration skewness and of a net current, typical of shoaling and surf zones waves, on the sediment transport processes. The data base also contributes to the validation and further development of predictive sand transport models including verification of intra-wave bottom boundary layer models.

The obtained net transport rate measurements are consistent with earlier experimental data sets (Watanabe and Sato, 2004; van der A et al., 2010) but extend the hydrodynamic conditions, particularly considering longer wave periods (T = 7, 10 s), a net current representative of the undertow, and the combined effect of acceleration and velocity skewness. The results for purely acceleration-skewed oscillatory flows are consistent with the previous studies: acceleration skewed oscillatory flows produce a net sand transport in the direction of the largest acceleration (onshore) and the net transport rates increase with increasing acceleration skewness. The added effect of velocity skewness increases the net transport rates. The addition of an opposing net current to the acceleration-skewed oscillatory flow results for all cases in a negative (seaward) net transport rate, but for increasing values of β the magnitude of q_s decreases.

Moreover, an innovative methodology is applied, which combines cross-correlation techniques described by McLean et al. (2001) with wavelet multilevel decomposition (Mallat, 1999; and Franca and Lemmin, 2006), to determine sediment grain velocities within the sheet flow layer. The application of wavelet transforms to the signals of the two conductivity probes allows the use of scale-conditioned cross-correlation techniques, yielding clearer cross-correlation peaks and allowing a better estimation of particle velocities. The results are consistent and appear to reproduce the grain velocity variations through the flow cycle, at different bed level elevations, inside the sheet flow layer quite well. Still, for the wave phases near the flow reversal, where the velocities are near zero and the sheet flow layer is very thin, the correlation peaks are more difficult to obtain. Also, the methodology itself has some limitations due to the space between the probes and the maximum time lag considered in the cross-correlation technique. Additionally, the results seem to confirm that the ADVP is able to penetrate inside the dense mobile sediment layer.

Detailed measurements of time-dependent flow velocities obtained with the ADVP allowed the development, application and validation of the defect law, enhancing features of the flow within the

boundary layer (including the SFL). Furthermore, the zero-velocity values obtained by the defect law practically coincide with the lower limit of the SFL obtained from detailed measurements of sediment concentrations.

The SFL thickness was assessed along the flow cycle through the characterization of the upper and lower limits obtained from time-dependent sediment concentration measurements. Net sediment fluxes were computed within the SFL, revealing that net transport rates are the result of a delicate balance between positive and negative flow phases, with the acceleration skewness contributing to phase-lag effects.

Bed shear stresses were estimated using two standard methodologies: Log-fit and momentum-integral methods. It is noticed that both methodologies brought out different results, contrasting with previous fixed bed experiments. The shear stress from the Log-fit method is practically in phase with the free-stream velocity, whereas the momentum-integral method predicts larger phase-lags. Moreover, the Log-fit method leads to $|\tau_{max}| \approx |\tau_{min}|$, unlike the results of the momentum-integral method that lead to skewed shear stresses.

In summary, for the present experiments, two mechanisms are invoked to play a key role in the sediment transport in acceleration skewness flows: the skewed bed shear-stress and the phase lag effects between the sediment concentration and flow velocity observed at flow reversal, when the flow acceleration attains its maximum value. These mechanisms were confirmed due to detailed measurements of time-dependent sediment concentrations and flow velocities performed for five of the experiments through the computation of sediment fluxes and bed shear stresses. The results confirm that both phase lag effects and the skewed shear stresses drive a positive net transport, i.e, in the (implied) wave propagation direction.

Chapter 4

ANALYTICAL MODELLING

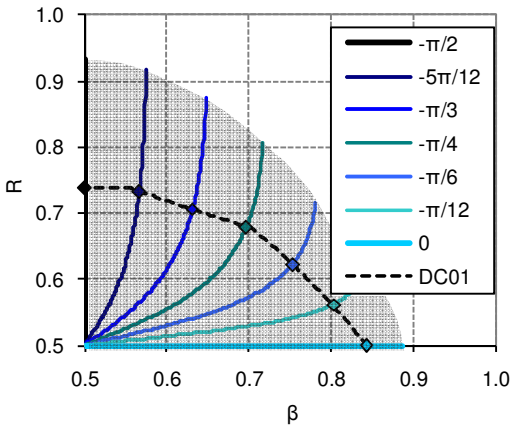

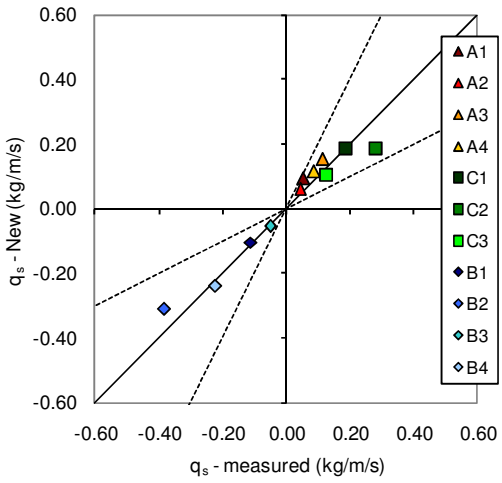

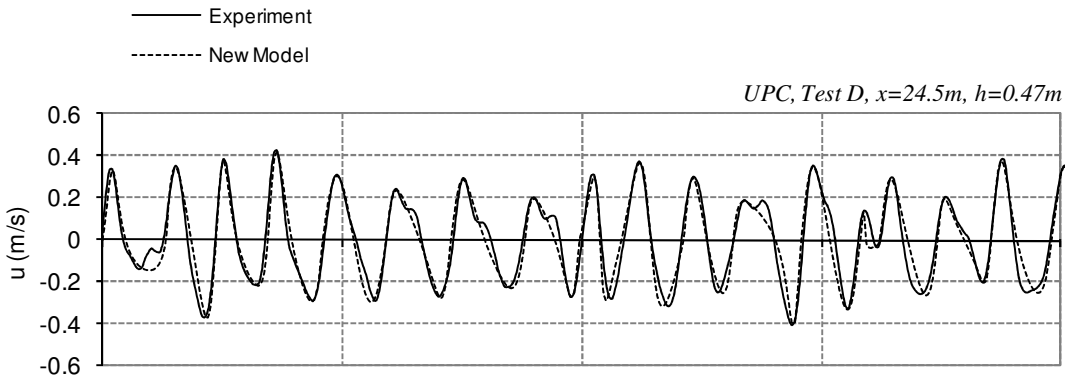

4. ANALYTICAL MODELLING

4.1 Introduction

Improved knowledge and description of the hydrodynamics and sediment transport in the nearshore zone is crucial to beach evolution predictions. The asymmetries of the wave shape and the induced near-bed flow are related to sediment transport as shown in the previous chapter. Also, the knowledge of such wave motion in water is required for several practical sediment transport formulae (e.g., Bailard, 1981; Hoefel and Elgar, 2003; Soulsby and Damgaard, 2005; Silva et al., 2006; Nielsen, 2006). Moreover, Hsu and Hanes (2004) concluded that the sediment transport process may strongly depend on the wave shape and cannot be fully described solely by the magnitude of the free-stream velocity. Finally, the importance of wave asymmetries in morphodynamics, like sandbar migrations, has also been recognized (Elgar et al., 2001).

The following section of this chapter is dedicated to the presentation of a new analytical function that reproduces wave shapes for any combination of velocity and acceleration skewness within the ranges found in nature. The expression is compared to existing different theoretical wave formulations given in the literature and is afterwards validated with two experimental conditions: a large-scale experiment (Sancho et al., 2001) and a field campaign (Birkemeier and Thornton, 1994).

The second section compares the performance of several bottom shear stresses parameterisations found in the literature for non-linear waves. A new bed shear stress predictor for net sand transport rate predictions under non-linear waves is presented, using the same parameters proposed in the analytical expression for the fluid velocity under skewed-asymmetric waves. The parameterisation extends the work of Nielsen (1992, 2002), Nielsen and Callaghan (2003) and Terrile et al. (2009) and can be considered in the instantaneous shear stress computations, bringing in more physics.

The last section compares predictions of five sediment transport models to the TRANSKEW measured net transport rates. Also, the inclusion of the new bed shear stress predictor in practical sediment transport formulae is tested, enabling the transport to be computed directly as a function of the velocity and acceleration skewness parameters. Moreover, its ability to compute sediment transport rates is extended to other experimental data.

4.2 Wave hydrodynamics

4.2.1 Introduction

Wave motion in water is one of the most fascinating physical phenomena in nature. The wave dynamics in shallow water has long been pursued by mathematicians, physicists and engineering scientists, leading to the development of different nonlinear mathematical theories and equations (e.g., Boussinesq and Korteweg-de Vries equations).

Based on a large number of field measurements at the nearshore zone, Elfrink et al. (2006) have determined that the range of the nonlinear parameters were within $0.51 \le R \le 0.66$ and $0.22 \le \alpha \le 0.54$. These findings confirm, thus, the importance of wave asymmetries in the nearshore.

All these nonlinear wave effects can be obtained from detailed wave models (e.g., Boussinesq models, RANS models) that describe the transformation of waves as they approach the shore. However, these models can be computationally demanding and for practical engineering purposes a representation of the wave based on simple analytic theories (linear and nonlinear theories) is often considered.

The main purpose of the present section is to propose a new simple analytical expression that can replicate both velocity and acceleration asymmetries similar to those found in shallow water waves (Abreu et al., 2010b). The new expression is compared with previous ones developed by Isobe and Horikawa (1982), Drake and Calantoni (2001) and Elfrink et al. (2006), which turn out to be particular cases of the present more general formula. The simplicity inherent in the new formulation allows the generation and reproduction in wave flumes, or water tunnels, of shallow-water waves with several nonlinear shapes, as found in nature. The formula contains four free parameters, two related to the orbital velocity amplitude and wave period and two related to the velocity and acceleration asymmetries, R and α. In the literature it is possible to find several publications that provide (R,α) as a function of commonly used parameters such as wave height, wave period, local water depth and local bottom slope (e.g., Dibajnia et al., 2001; Tajima and Madsen, 2002; Tajima, 2004; Elfrink et al., 2006; and Mariño-Tapia et al., 2007b) therefore enabling the practical application of this formulation. The acceleration-skewed waves performed in the LOWT used this new expression. The proposed wave form can also be used for the wave-generating boundary conditions in detailed wave-propagation models (e.g., Ruessink et al., 2009) and in sediment transport parameterisations.

The following subsection starts with a description and analysis of the new formulation. It is followed in the third section by an examination of the relations between the macro wave-form parameters

presented earlier (R, α, β), and the direct input parameters of the new formula. Afterwards, the new expression is tested against different theoretical wave formulations found in the literature. Next, the new wave form is applied to reproduce the time series of measured near bed velocities, of both a field and a laboratory experiment.

4.2.2 Analytical description of nonlinear waves

Because natural waves in the nearshore often present both velocity and acceleration skewnesses, a simple analytical formulation for the near-bed orbital velocity that accounts for both asymmetries is developed. The expression intends to reproduce the horizontal velocity above the wave boundary layer which is generally only a small fraction of the water depth, of the order of a few centimetres in thickness (Nielsen, 1992).

The new formula is based on the work of Drake and Calantoni (2001), who considered a near-bed orbital velocity representative of a wide range of shoaling and broken waves proportional to:

$$u(t) = U_w \sum_{j=0}^{4} \frac{1}{n^j} \sin\left[(j+1)\omega t + j\phi \right] \tag{4.1}$$

where j represents an integer value and ϕ is a waveform parameter. In their work, Drake and Calantoni (2001) considered only the case for $n = 2$ and presented three particular cases of ϕ: (i) $\phi = 0$, resulting in an accelerated skewed wave (sawtooth wave profile); (ii) $\phi = -\pi/2$, approaching the case of a velocity-skewed wave (with a velocity shape similar to that of a 1st order cnoidal wave); and (iii) $\phi = -\pi/4$, corresponding to a wave with both velocity and acceleration skewnesses.

One can generalize Eq. (4.1) and admit that the velocity is given by:

$$u(t) = U_w \sum_{j=0}^{\infty} \frac{1}{n^j} \sin\left[(j+1)\omega t + j\phi \right] \tag{4.2}$$

where n is a parameter that allows changing the wave acceleration and velocity skewness. In the formulation of Drake and Calantoni (2001) $n = 2$, which corresponds to fixed values of R and β for each ϕ, as described in Section 4.2.4.

Eq. (4.2) is equivalent to:

$$u(t) = U_w \, \mathrm{Im}\left[\sum_{j=0}^{\infty} \frac{1}{n^j} \exp\left(i\left[(j+1)\omega t + j\phi \right] \right) \right]. \tag{4.3}$$

Assuming

$$x = \left(\frac{1}{n}\right)\exp\left[i\left(\omega t + \phi\right)\right], \tag{4.4}$$

Eq. (4.3) can be written as:

$$u(t) = U_w \,\mathrm{Im}\left[\sum_{j=0}^{\infty} x^j \exp\left(i\omega t\right)\right]. \tag{4.5}$$

The sum of such Taylor series can be exactly computed within the case of analytical functions with complex variables:

$$u(t) = U_w \,\mathrm{Im}\left[\left(\frac{1}{1-x}\right)\exp\left(i\omega t\right)\right]. \tag{4.6}$$

with

$$\mathrm{Im}\left[\left(\frac{1}{1-x}\right)\exp\left(i\omega t\right)\right] = n\frac{\left(n\sin\left(\omega t\right)+\sin\phi\right)}{\left(1+n^2-2n\cos\left(\omega t+\phi\right)\right)}. \tag{4.7}$$

Thus, Eq. (4.2) can be exactly computed, yielding the solution previously presented as Eq. (3.1):

$$u(t) = U_w f \frac{\left[\sin(\omega t) + \dfrac{r\sin\phi}{1+\sqrt{1-r^2}}\right]}{\left[1-r\cos(\omega t+\phi)\right]} \tag{4.8}$$

where $r = 2n/\left(1+n^2\right)$ and the dimensionless factor $f = \sqrt{1-r^2}$.

There is no simple relation between *r* and the skewness parameters proposed, *R* and β. As described further in this subsection, an analytical approximate formulation can be found, relating both parameters for some particular cases of ϕ. Also, a procedure to determine *r* and ϕ from the knowledge of *R* and α is devised in subsection 4.2.3.

The corresponding acceleration time series of Eq. (4.8) is given by

$$a(t) = U_w \omega f \frac{\cos(\omega t) - r\cos\phi - \dfrac{r^2}{1+\sqrt{1-r^2}}\sin\phi\sin(\omega t+\phi)}{\left[1-r\cos(\omega t+\phi)\right]^2} \tag{4.9}$$

Figure 4.1 and Figure 4.2 show examples of the shape of time varying orbital velocities and accelerations calculated from Eq. (4.8) and (4.9), respectively, for a number of values in the *r* and ϕ domain ($r = [0, 0.25, 0.5, 0.75]$, $\phi = [0, -\pi/4, -\pi/2]$). Clearly, it is possible to deduce that, independently of ϕ values, Eq. (4.8) matches to the sinusoidal wave for $r = 0$. However, when *r* increases, the nonlinear behaviour is evidenced. The particular cases of $\phi = -\pi/2$ and $\phi = 0$ correspond to two wave formulations, respectively, the skewed wave forcing, with the shape of a 1st order cnoidal wave, and the sawtooth profile described by Drake and Calantoni (2001).

Case ϕ = -π/2

For $\phi = -\pi/2$, Eq. (4.8) reduces to the following equation:

$$u(t) = U_w f \frac{\left[\sin(\omega t) - \dfrac{r}{1+\sqrt{1-r^2}}\right]}{\left[1 - r\sin(\omega t)\right]}, \tag{4.10}$$

with the corresponding acceleration time series

$$a(t) = U_w \omega f \frac{\cos(\omega t) - \dfrac{r^2}{1+\sqrt{1-r^2}}\cos(\omega t)}{\left[1 - r\sin(\omega t)\right]^2}. \tag{4.11}$$

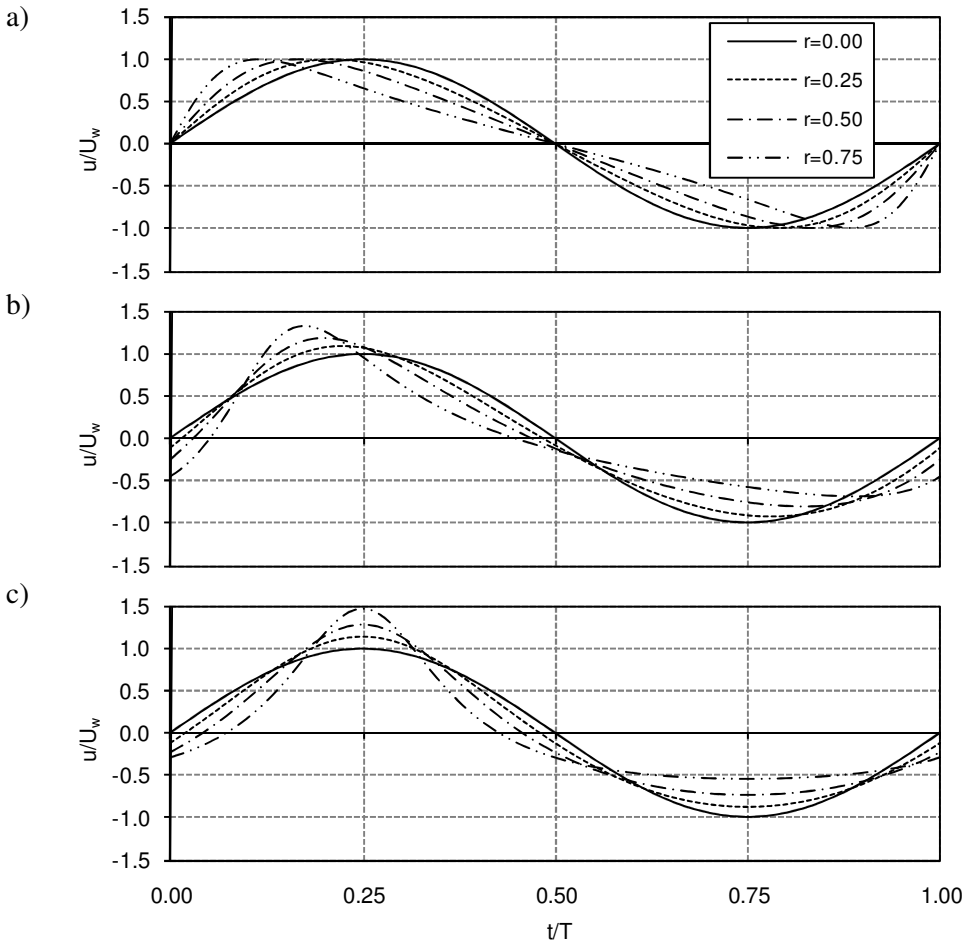

Figure 4.1 – Time varying orbital horizontal velocity for different values of index of skewness r and ϕ: a) ϕ=0; a) ϕ=-π/4; c) ϕ=-π/2.

Eq. (4.10) gives a velocity time series with a shape similar to that of a 1st-order cnoidal wave (Figure 4.1c) in a way that only accounts for the velocity skewness. Given the definition of $R\ \left(=u_{\max}/\left(u_{\max}-u_{\min}\right)\right)$, it is possible from Eq. (4.10) to obtain a relation between R and r, yielding:

$$R=\frac{(1+r)\left(1-r+\sqrt{1-r^2}\right)}{2\left(1-r^2+\sqrt{1-r^2}\right)} \tag{4.12}$$

A similar calculation of $\beta\ \left(=a_{\max}/\left(a_{\max}-a_{\min}\right)\right)$ and Eq. (4.11) results in $\beta=0.5$ for this particular case ($\phi=-\pi/2$).

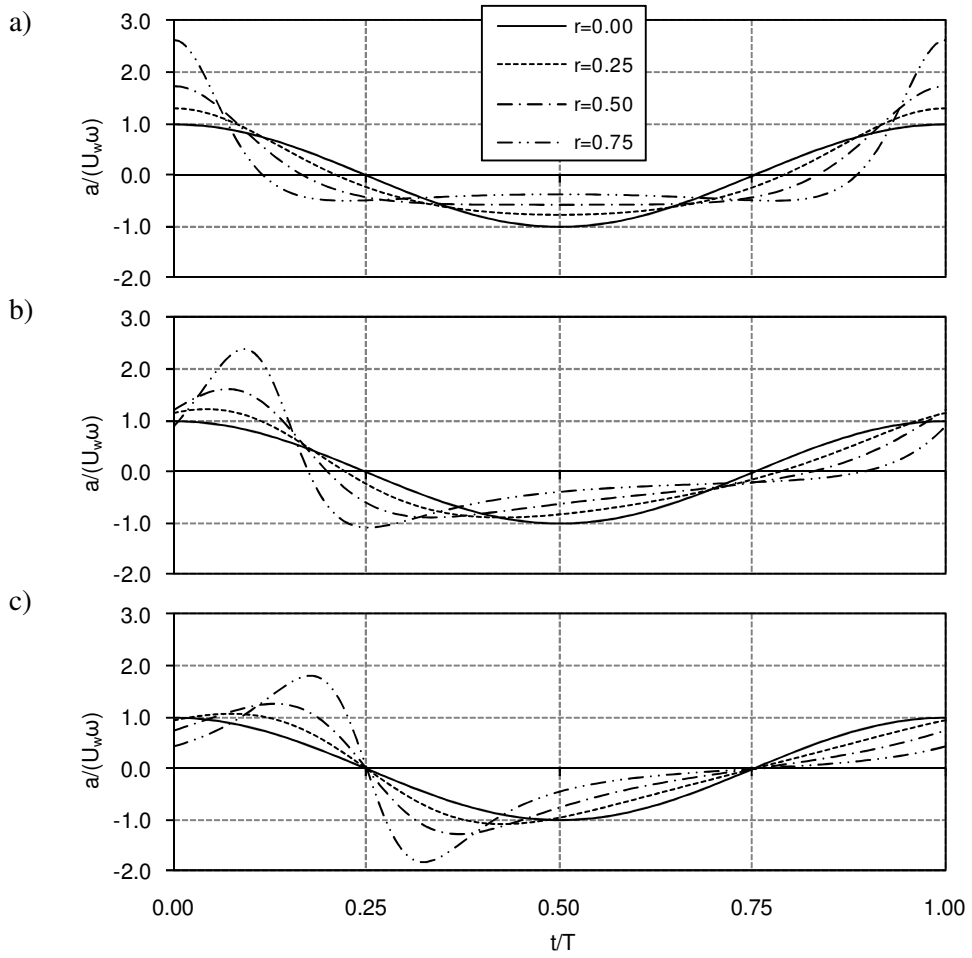

Figure 4.2 – Time varying orbital horizontal acceleration for different values of index of skewness r and ϕ: a) ϕ=0; a) ϕ=-π/4; c) ϕ=-π/2.

Elfrink et al. (2006) further pointed out that the shape of the velocity distribution between the wave crest and the zero down-crossing is usually concave and not convex. The present function clearly shows this behaviour for the $r > 0.25$ (Figure 4.1c).

Case $\phi = 0$

For $\phi = 0$, Eq. (4.8) reduces to the following equation with $f = \sqrt{1-r^2}$:

$$u(t) = \frac{U_w \sqrt{1-r^2}\,\sin(\omega t)}{\left[1 - r\cos(\omega t)\right]} \tag{4.13}$$

For this wave, the orbital velocity is symmetric with respect to the horizontal axis (velocity skewness is zero: R=0.5) but is asymmetric with respect to the vertical axis within each half cycle, which gives rise to skewed accelerations ($\beta \neq 0.5$) (Figure 4.1a). Following Drake and Calantoni (2001), this wave is characteristic of surf zone bores.

The previous wave form (Eq. (4.13)) was already proposed by Silva et al. (2007), apart the coefficient $f=\sqrt{1-r^2}$, assuming that the sawtooth wave acceleration time series is similar to the velocity profile of a 1st-order cnoidal wave. The acceleration corresponding to Eq. (4.13) is given by:

$$a(t)=\frac{U_w\omega\sqrt{1-r^2}\left[\cos(\omega t)-r\right]}{\left[1-r\cos(\omega t)\right]^2} \tag{4.14}$$

From Eq. (4.14) it is possible to obtain a relation between β and r, yielding:

$$\beta=\begin{cases}(1+r)/2 & ,r\le 0.5\\ 4r(1+r)/(1+2r)^2 & ,r>0.5\end{cases} \tag{4.15}$$

For completeness, we compare in Figure 4.3 the results from the above formulae (Eq. (4.10) and Eq. (4.14)) with those from 1st-order cnoidal wave theory (from Svendsen, 2006, pp. 396-406). In detail, the left panel shows the results from Eq. (4.10), for various r values ($0 \le r \le 0.8$), against the cnoidal wave solution for various Ursell numbers ($0.05 \le U_r \le 120$). No match in the nonlinear parameters was pursued between these solutions, although according to Eq. (4.12) the results from Eq. (4.10) correspond to the range $0.5 \le R \le 0.75$, and those from the 1st order cnoidal wave theory correspond to $0.55 \le R \le 0.75$. For the lower values of r, the present solution is a good approximation of a cnoidal wave shape, whereas for $r > 0.6$ it exhibits a form deviating significantly from the cnoidal wave.

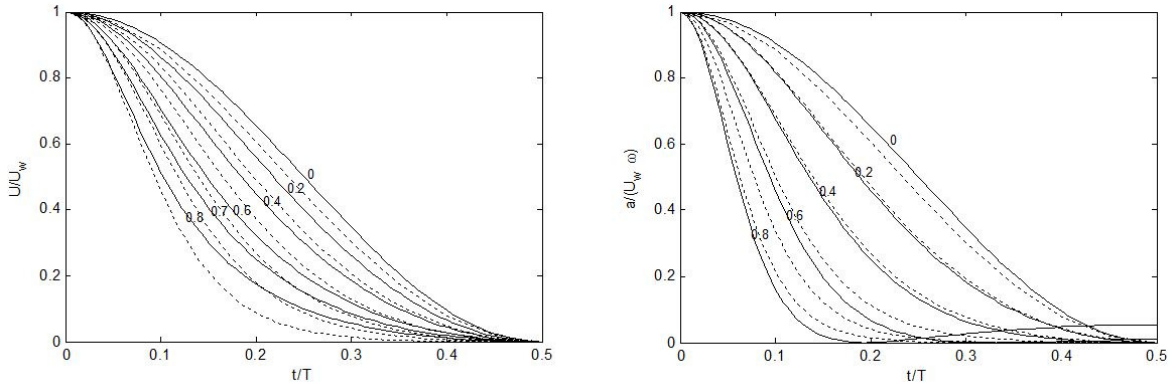

Figure 4.3 – Half-period time variation of present approximate functions (—), for $0 \le r \le 0.8$ (see labels in Figure), and exact cnoidal wave (---) for various Ursell numbers ($0.05 \le U_r \le 120$). Left: velocity given by Eq. (4.10); Right: acceleration given by Eq. (4.14).

In the right panel of Figure 4.3 one observes a comparison between the non-dimensional acceleration time series as given by Eq. (4.14), for the same range of r values, and the exact cnoidal wave solution ($0.005 < U_r < 265$). Note that the same range of r values ($0 < r < 0.8$) for the velocity and acceleration

given by Eq. (4.10) and Eq. (4.14) , respectively, corresponds visually to a wider range of Ursell numbers for the latter. In general, this solution, which is the particular case of Eq. (4.9) for $\phi = 0$, compares favourably with the exact solution for low values of *r*. For values of $r > 0.6$ a second local maximum at $t = 0.5T$ is apparent in the results from the approximated function, leading to a convex-curve shape at the wave trough, instead of the expected concave shape. It may be therefore recommended, if one aims at reproducing a cnoidal wave shape, to restrict the use of expression (4.8) to values $-0.6 < r < 0.6$, keeping in mind that negative values of *r* cause a sharp trough and a flat crest.

For values of ϕ between $\phi = 0$ and $\phi = -\pi/2$, expression (4.8) yields a wave form with both velocity and acceleration skewnesses ($R \neq 0.5$ and $\beta \neq 0.5$), (see Figure 4.1b and Figure 4.2b).

Figure 4.1 and Figure 4.2 show that the velocity skewness increases while the acceleration skewness decreases for increasing values of $|\phi|$. Thus, the waveform parameter ϕ expresses the relative importance of both skewnesses. Negative values of *r* or positive values of ϕ lead to temporal shifts and reversals to the asymmetric wave shape as shown and clarified in Figure 4.4. In the upper panel, the influence of *r* is presented. The negative value of *r* caused a reflected image in relation to the horizontal axis and a phase shift of $t/T = 0.5$. In the lower panel, the influence of ϕ is presented and it is perceptible that a positive value of ϕ reproduces a wave profile that is reflected both horizontally and vertically. Hence, in the following we restrict to the positive domain of *r*, that is, $0 < r < 1$, and the negative domain of ϕ, $-\pi/2 < \phi < 0$, covering the majority of the nonlinear wave forms found in nature.

Finally, the new function fulfils the requirement of zero mean velocity and was already used in numerical modelling (Ruessink et al., 2009).

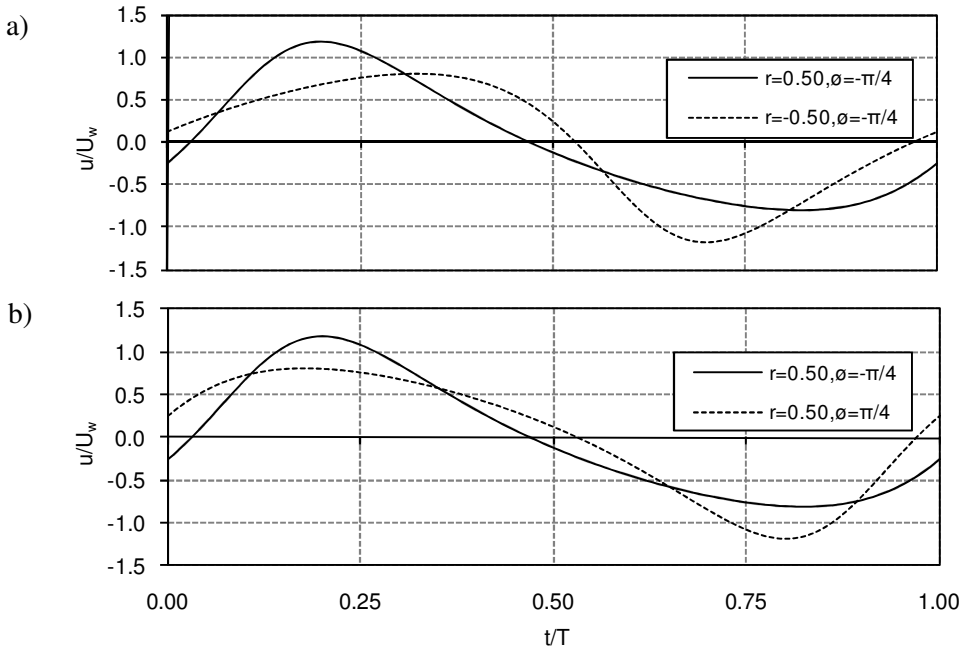

Figure 4.4 – Time varying orbital velocities for ϕ = -π/4 and r = 0.5 showing the influence of r negative values or ϕ positive values.

4.2.3 Parameterisations of input parameters

The new formulation presented above allows the representation of several nonlinear wave profiles through the introduction of two parameters: ϕ and r. For the particular cases $\phi = 0$ and $\phi = -\pi/2$ it has been shown that one can relate analytically the nonlinear index r with the usual macroscopic wave skewness parameters R and β (see Eq. (4.12) and (4.15)). A similar analysis could be performed for other intermediate values of ϕ, but the results would become forbiddingly unmanageable, justifying the use of simple parameterisations. Therefore, this section presents general parameterisations of R and β as functions of r, for values of ϕ within a certain range. The analysis was also extended to the commonly used "wave skewness parameter", α. The expressions concern the principal range of application of those parameters presented earlier (Elfrink et al., 2006), i.e., for $R \geq 0.5$, $\beta \geq 0.5$ and $\alpha \leq 0.5$.

Regarding Eq. (4.8), the relations between r and R, β and α are constructed by varying ϕ, as presented in Figure 4.5.

Focusing on r *versus* R, for $\phi = 0$ the outcome is $R = 0.5$ for all values of r (velocity under the crest equal to the velocity under the trough). For the other values of ϕ it is possible to see that the relation between the two parameters is almost linear for $r \leq 0.5$ but increasingly non-linear for $r > 0.5$.

Concerning the curves $\beta(r)$, a similar approach may be taken. The cnoidal wave shape is obtained for $\phi = -\pi/2$, corresponding to the horizontal axis where $\beta = 0.5$ ($a_{max} = a_{min}$). For the other values of ϕ, the figure shows that β is proportional to *r*, in the range $-\pi/2 < \phi < 0$.

For *r versus* α, Figure 4.5 shows that α decreases (non-linearly) with increasing values of *r* and the waveform parameter ϕ. Note that the particular case of $\phi = 0$ verifies the simple relation between α and *r*:

$$r = \cos(\pi \cdot \alpha). \tag{4.16}$$

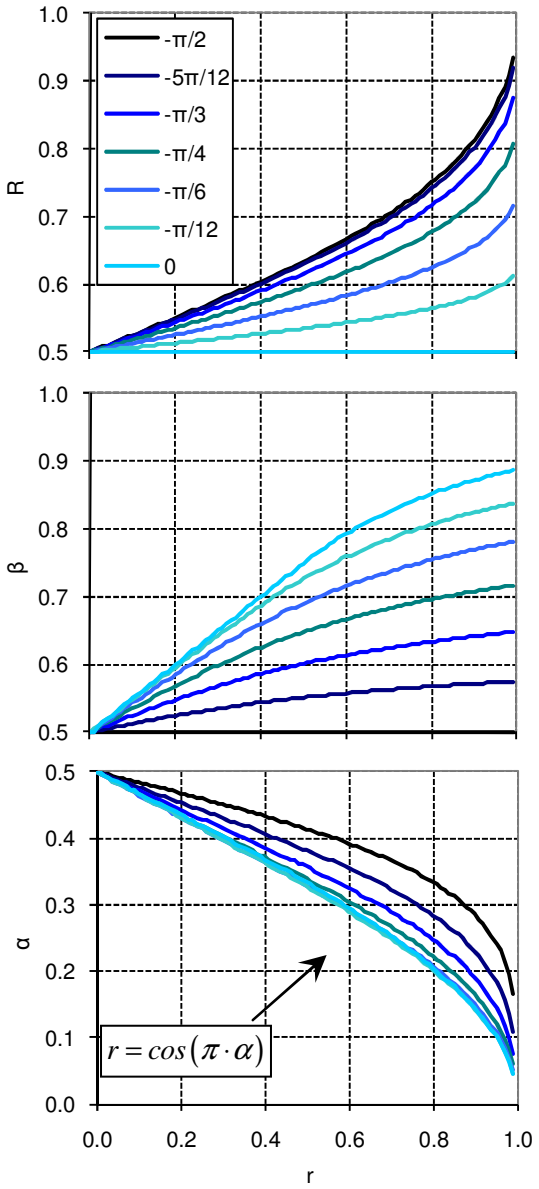

Figure 4.5 – *r versus* R, β and α for $-\pi/2 \le \phi \le 0$.

Each curve in Figure 4.5 can be accurately parameterised by rational functions of 3rd order polynomials, of the form:

$$R \approx \frac{a_1 + b_1 \cdot r + r^3}{c_1 - d_1 \cdot r + e_1 \cdot r^2 + r^3}, \tag{4.17}$$

$$\beta \approx \frac{a_2 + b_2 \cdot r + r^3}{c_2 - d_2 \cdot r + e_2 \cdot r^2 + r^3}, \tag{4.18}$$

$$\alpha \approx \frac{a_3 + b_3 \cdot r + r^3}{c_3 - d_3 \cdot r + e_3 \cdot r^2 + r^3}. \tag{4.19}$$

where a_i, b_i, c_i, d_i and e_i are fitting coefficients for each ϕ (i=1, 2, 3). The best values of those constants are presented in Table 4.1, Table 4.2 and Table 4.3 for Eqs. (4.17), (4.18) and (4.19), respectively. The root-mean-square absolute errors (e_{rms}) of the parameterised curves are presented in the last row of each table. The low e_{rms} values found clearly show that the adopted functions (4.17) to (4.19), with the fitting coefficients given in Table 4.1 to Table 4.3, represent quite well the exact curves of Eq. (4.8) for the studied domain. The above set of rational 3rd order polynomials provided much closer agreement to the desired relationships than that obtained from other simpler functions (e.g., exponentials), that the observation of the curves in Figure 4.5 may suggest.

Table 4.1 – Fitting coefficients for Eq. (4.17).

ϕ	-π/12	-π/6	-π/4	-π/3	-5π/12	-π/2
a_1	6.883	6.489	7.699	7.775	7.793	7.702
b_1	-6.964	-7.197	-8.528	-8.687	-8.726	-8.645
c_1	13.798	12.975	15.315	15.375	15.321	15.115
d_1	16.030	17.557	21.672	22.539	22.815	22.655
e_1	2.728	3.983	5.560	6.259	6.562	6.596
e_{rms}	4.06E-05	4.87E-06	1.00E-04	4.66E-04	9.50E-04	1.19E-03

Table 4.2 – Fitting coefficients for Eq. (4.18).

ϕ	-π/12	-π/6	-π/4	-π/3	-5π/12	-π/2
a_2	0.195	0.072	0.122	0.383	1.169	2.179
b_2	0.182	0.090	0.006	-0.019	0.007	-1.607
c_2	0.391	0.144	0.245	0.767	2.341	4.363
d_2	0.028	-0.014	0.230	0.623	1.242	4.432
e_2	0.188	0.227	0.426	0.755	1.255	1.795
e_{rms}	1.10E-04	2.81E-05	1.64E-05	4.53E-06	1.83E-06	1.10E-05

Table 4.3 – Fitting coefficients for Eq. (4.19).

ϕ	-π/12	-π/6	-π/4	-π/3	-5π/12	-π/2
a_3	3.499	3.782	4.227	4.675	5.126	5.158
b_3	-4.481	-4.760	-5.199	-5.640	-6.078	-6.103
c_3	6.999	7.572	8.464	9.365	10.279	10.348
d_3	4.172	4.314	4.930	6.072	7.773	9.403
e_3	-3.230	-3.587	-3.797	-3.590	-2.893	-1.526
e_{rms}	3.00E-05	1.95E-05	2.30E-05	3.57E-05	5.47E-05	6.78E-05

For the practical use of the proposed wave form, Eq. (4.8), it is desirable to find a relation between the independent variables (r, ϕ) and (R, β), or (R, α), that is, inverting the pairs of Eqs. (4.17)- (4.18), or Eqs. (4.17) and (4.19). The advantage to use such parameterisations is that, given a set of desired values of R and β (or α), these expressions can be used to compute r and ϕ. For this purpose, we rewrite each Eq. (4.17) to (4.19) as a cubic polynomial of r, whose roots are computed directly via Cardano's method (e.g., Anglin and Lambek, 1995). Combining the solutions of r resulting from the associations (R, β) or (R, α), it is possible to deduce the corresponding range of ϕ that simulates those asymmetries. Then, one can finally interpolate the values of r and ϕ to use directly as input in Eq. (4.8). In Appendix A.1, a step-by-step guide, explaining the previous methodology, is illustrated through a numerical example.

Also, the dependence between α and both velocity and acceleration parameters (R and β, respectively) has been obtained by changing ϕ (Figure 4.6). Figure 4.6 evidences the nonlinear relations between those parameters. For the "sawtooth" wave ($\phi = 0$), α changes while R remains constant (R=0.5, i.e., velocity under the crest equal to the velocity under the trough). For a constant ϕ, α decreases almost linearly with increasing values of R. Concerning α *versus* β (Figure 4.6, lower panel), for $\phi = -\pi/2$ the corresponding line between the two parameters coincides with the vertical axis, where $\beta = 0.5$ ($a_{max} = a_{min}$). For a fixed ϕ, the (α, β) relation shows a stronger nonlinearity than the (α, R) relation, with α inversely proportional to β.

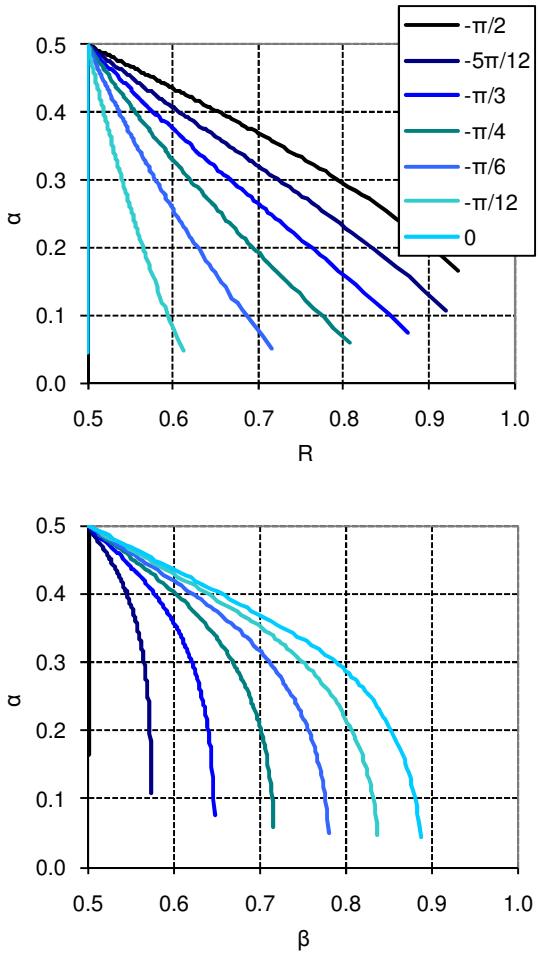

Figure 4.6 – α *versus* R and β for $-\pi/2 \le \phi \le 0$.

4.2.4 Comparison with other formulations

In this section, three different theoretical wave formulations given in the literature are tested against Eq. (4.8). The results suggest that the new expression can accurately reproduce those wave shapes, which turn out to be particular cases of it for most conditions.

Isobe and Horikawa (1982)

Isobe and Horikawa (1982) developed a hybrid wave theory which combines fifth-order Stokes wave theory with third-order cnoidal wave theory to compute the wave orbital motion, and it can be used in a wide range of wave conditions. Hereafter, the method will be referred as IH82. This theory is able to yield skewed and asymmetric wave forms, and will thus be compared with the present formulation.

The expressions of IH82 can be used to generate representative waves in terms of R and α and, following Dibajnia et al. (2001), the method is as follows:

$$u(t) = R \cdot 2U_w \cdot \sin\left(\frac{\pi t}{\alpha T}\right),\ -\Theta_2 T \le t \le (\alpha - \Theta_2)T \tag{4.20}$$

$$u(t) = (1-R) \cdot 2U_w \cdot \sin\left(\frac{\pi\left[t - T(1+\Theta_1)\right]}{T - \alpha T}\right),\ (\alpha - \Theta_2)T < t \le (1-\Theta_2)T \tag{4.21}$$

with

$$\Theta_1 = \frac{1-\alpha}{\pi}\arcsin\sqrt{\frac{\mu_u^2\mu_T^2 - 1}{\mu_u^2(\mu_T^2 - 1)}} - \Theta_2, \tag{4.22}$$

$$\Theta_2 = \frac{\alpha}{\pi}\arcsin\sqrt{\frac{\mu_u^2\mu_T^2 - 1}{\mu_T^2 - 1}}, \tag{4.23}$$

$$\mu_u = \frac{1-R}{R}, \tag{4.24}$$

$$\mu_T = \frac{1-\alpha}{\alpha}. \tag{4.25}$$

The analysis of the expressions revealed discontinuities in the acceleration time series for $R \neq 0.5$, which are related with the boundary values of t in Eqs. (4.20) and (4.21). Because β relies on the extreme values of the fluid acceleration and the discontinuities are reflected in its calculation, it is recommended to reproduce the same kind of wave with Eq. (4.8) through the "wave skewness parameter" α.

The upper panel of Figure 4.7 shows the orbital velocities from the IH82 method, for $R = 0.65$ and $\alpha = 0.30$, and the curve computed through Eq. (4.8). The wave represented has both velocity and acceleration skewness, corresponding to a value of ϕ in Eq. (4.8) between 0 and $-\pi/2$. The values for ϕ and r in Eq. (4.8) were obtained through interpolation of the parameterisations presented in Section 4.2.3, leading to $\phi = -0.31\pi$ and $r = 0.652$. Also, to have a comparable trend between the curves, a certain time lag, Δt, needs to be considered in the new formulation ($t' = t + \Delta t$), because for IH82 $t = 0$ corresponds to a null velocity. This time lag corresponds to the zero up-crossing of the velocity time series of Eq. (4.8) and can be calculated as follows:

$$\Delta t = \frac{T\arcsin\left(\dfrac{-\sin\phi + \sqrt{1-r^2}\sin\phi}{r}\right)}{2\pi} \tag{4.26}$$

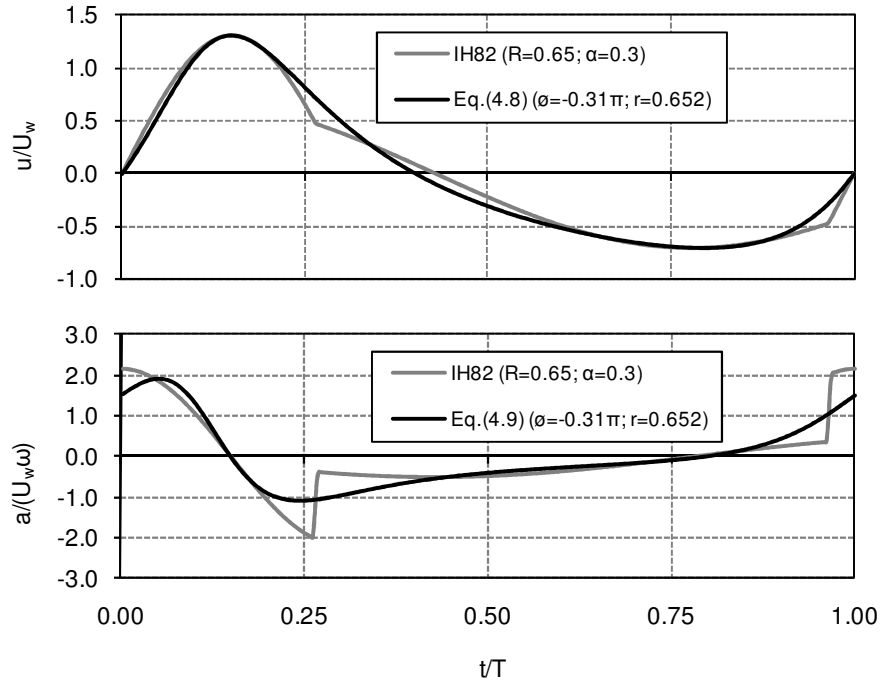

Figure 4.7 – Time varying orbital velocities and accelerations: comparison between IH82 formulation with $R = 0.65$ and $\alpha = 0.30$ *versus* Eq. (4.8) with $\phi = -0.31\pi$ and $r = 0.652$.

The lower panel of Figure 4.7 contains the corresponding time series of the acceleration and clearly shows the two discontinuities associated with the time limits of Eqs. (4.20) and (4.21). Consequently, the new formulation seems more adequate as representative of both velocity and acceleration time series.

For the particular cases of sawtooth-shaped waves, some differences in the orbital velocity time series were found between the two formulations (Figure 4.8). The corresponding indexes of skewness r used in Eq. (4.8) are presented in Figure 4.8 and were computed according to Eq. (4.16). Although both formulations match at the instants of maximum and minimum values, the concavities of the curves differ between the wave crest and the wave trough for the lowest value of α (larger *r*). In that case, the present solution provides a sharper (velocity) wave profile, with somewhat unrealistic curvatures immediately past the wave crest and prior to the wave trough. On the contrary, for larger values of α, the results are very consistent, e.g. for $\alpha = 0.45$, corresponding to a nearly sinusoidal wave, one can observe an almost perfect match between both curves. For the intermediate α value ($\alpha = 0.3$ and r = 0.588), the curves match considerably and it is difficult to assert which analytical curve is more representative of a real wave shape. The fact that the present approach does not fully represent the more theoretical formulation of Isobe and Horikawa (1982) is not a matter of concern, once the development of the new equation aims at providing a realistic non-linear skewed wave shape, but not necessarily in perfect agreement with other non-linear wave theory.

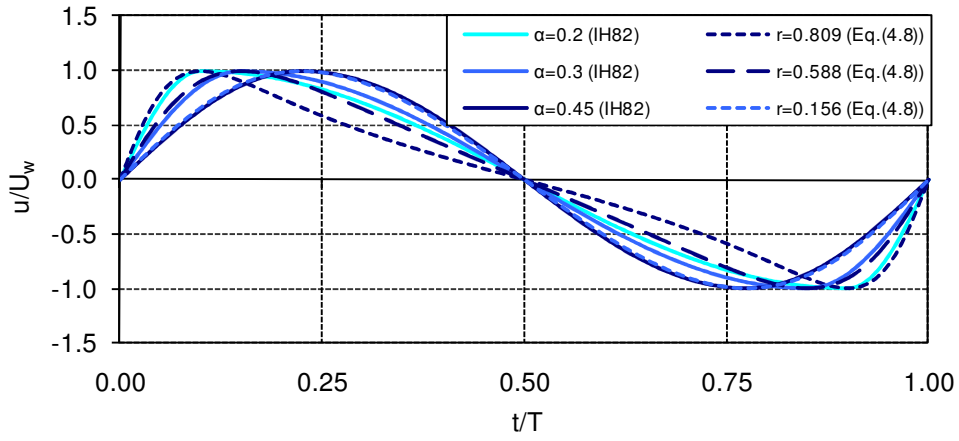

Figure 4.8 – Time varying orbital velocities: comparison between IH82 theory (—) and present formulation (---) for the sawtooth wave velocity profile ($\phi = 0$) and three values of the skewness index *r*.

Drake and Calantoni (2001)

In order to investigate the effect of the fluid acceleration on bedload transport, in nearshore marine environments, Drake and Calantoni (2001) considered a near-bed orbital velocity representative of a wide range of shoaling and broken waves as described in Eq. (4.1) with $n = 2$. Hereafter, the method of Drake and Calantoni (2001) will be referred to as DC01.

The upper panel of Figure 4.9 represents the dimensionless values of $u(t)$ (also shifted in time) obtained from DC01 and Eq. (4.8), for different values of the waveform parameter (ϕ=0, -π/4 and -π/2). The corresponding dimensionless values of $a(t)$ are shown in the lower panel of Figure 4.9. The solutions for $u(t)$ with values of ϕ between the limits represented in the figure characterize a wide qualitative range of shoaling and broken waves. However, the values of the velocity and acceleration skewness parameters obtained for each ϕ following DC01 are fixed because the corresponding value of *n* in Eq. (4.8) is equal to 2. Table 4.4 presents these values for different values of ϕ. For the comparison, Eqs. (4.17), (4.18) and the values of *R* and β corresponding to ϕ=0, -π/4 and -π/2 in Table 4.4 were used to find the best approximation for the input parameter r in Eq. (4.8) ($r = 0.766$, $r = 0.805$ and $r = 0.772$, respectively). It is further possible to distinguish that small fluctuations appear in the acceleration time series of DC01 solution, caused by the truncated five terms of the sum in Eq. (4.1). However, with the new formulation, those fluctuations disappear completely.

Table 4.4 – Values of R and β for different ϕ values in Drake and Calantoni (2001) formulation.

ϕ	0	-π/12	-π/6	-π/4	-π/3	-5π/12	-π/2
R	0.500	0.561	0.623	0.680	0.706	0.733	0.738
β	0.844	0.803	0.753	0.697	0.631	0.567	0.500

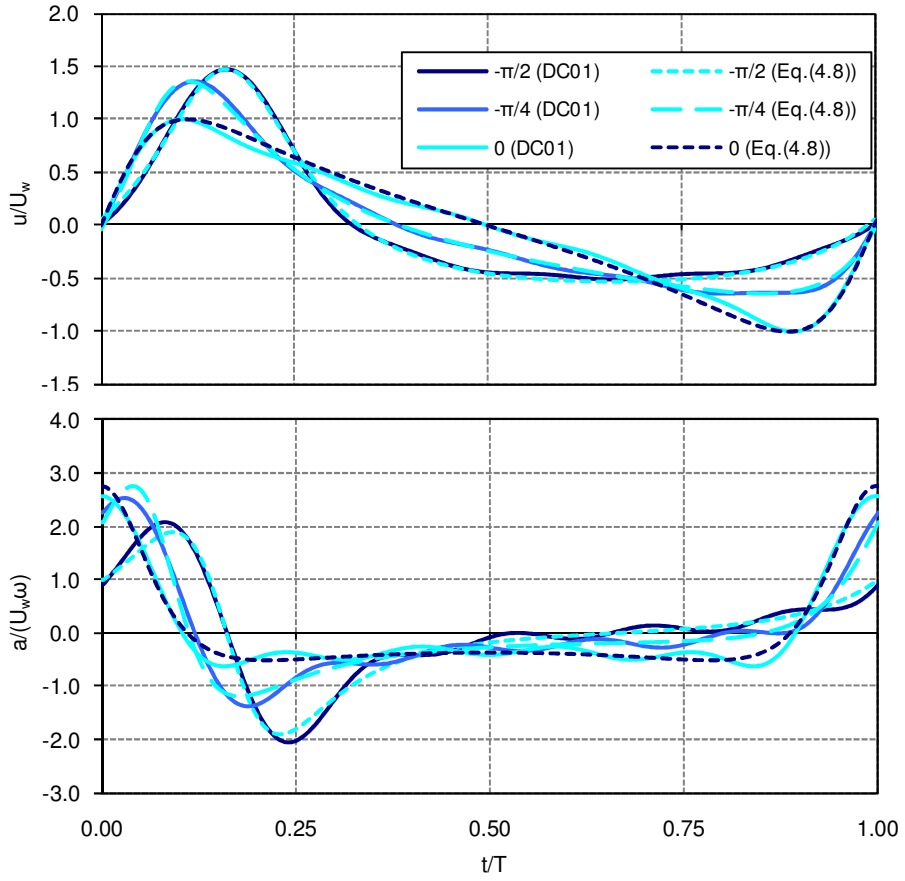

Figure 4.9 –Time varying orbital velocity and acceleration: comparison between DC01 theory (—) and Eq. (4.8) (---) for different ϕ values.

Figure 4.10 further evidences that Drake and Calantoni's solution (dashed line) can be assumed as a particular solution of Eq. (4.8), given the unique relation of R and β corresponding to their solution, and contained by the field of solutions of the present formulae (shaded region).

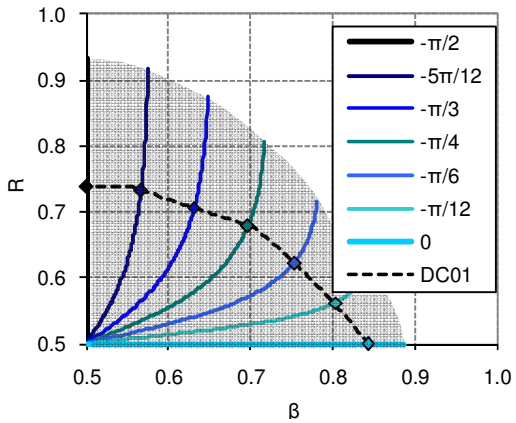

Figure 4.10 – Domain of solutions (β, R) for Eq. (4.8) (shaded area) and for DC01 (dashed line).

Elfrink et al. (2006)

Recently, Elfrink et al. (2006) analyzed a broad range of hydrodynamic conditions, corresponding to a large number of field data. In their work, a set of empirical formulations, describing important wave properties in shallow water, were derived using data mining techniques (evolutionary algorithms). Based on their proposed expressions, the continuous near-bed orbital velocity was expressed as:

$$u(t') = U_c \cdot \sin\left[1/2\,\pi t'/T_1\right],\ 0 < t' < T_1 \tag{4.27}$$

$$u(t') = U_c \cdot \cos\left[1/2\,\pi\left(t'-T_1\right)/\left(T_0-T_1\right)\right] - U_{zc}\sin\left[\pi\left(t-T_1\right)/\left(T_0-T_1\right)\right],\ T_1 < t' < T_0 \tag{4.28}$$

$$u(t') = -U_t \cdot \sin\left[1/2\,\pi\left(t-T_0\right)/\left(T_2-T_0\right)\right],\ T_0 < t' < T_2 \tag{4.29}$$

$$u(t') = -U_t \cdot sin\left[1/2\,\pi\left(t-T_2\right)/\left(1-T_2\right)\right],\ T_2 < t' < 1 \tag{4.30}$$

where t' is defined as $t' = t/T$; U_c, U_t, U_{zc} are velocity amplitudes and T_0, T_1 and T_2 are dimensionless instants associated to the time at maximum velocities and zero crossings. All these parameters are functions of the normalized wave height $\left(H/h\right)$, normalized wave length $\left(L/h\right)$ and the surf similarity parameter ξ ($= \tan\beta_s / \left(H/L_0\right)^{1/2}$), where β_s represents the local bed slope and L_0 the wave length offshore ($L_0 = \left(g/2\pi\right)T^2$). Hereafter, the method of Elfrink et al. (2006) is referred to as BE06.

The proposed expressions of BE06 for the time varying velocity result in discontinuous and non-smooth acceleration time series as already pointed out for the IH82 formulation. This is evidenced in Figure 4.11 where BE06 solutions are compared against the new formulation (Eqs. (4.8) and (4.9)), for varying L/h. These figures reproduce some of the cases given in Figure 9 of Elfrink et al. (2006), for two waves with different lengths (L/h=15, 20) in a water depth of 2 m, H/h=0.4 and the bed slope equals 1:40. From Eq. (4.27) to (4.30) the corresponding values of R and α are, respectively, $R = 0.66$ and $\alpha = 0.28$ for L/h=15, and $R = 0.63$ and $\alpha = 0.22$ for L/h=20. Through the parameterisations presented in the previous section, one reached the values of $\phi = -0.29\pi$ and $r = 0.699$ for L/h=15, and $\phi = -0.19\pi$ and $r = 0.784$ for L/h=20. Figure 4.11 shows a good match of both velocity time series, but differences are clear in the corresponding accelerations time series. The BE06 method presents discontinuities in the acceleration associated with the limits of Eqs. (4.27)-(4.30). The largest discrepancies are observed at the zero up-crossing of $u(t)$.

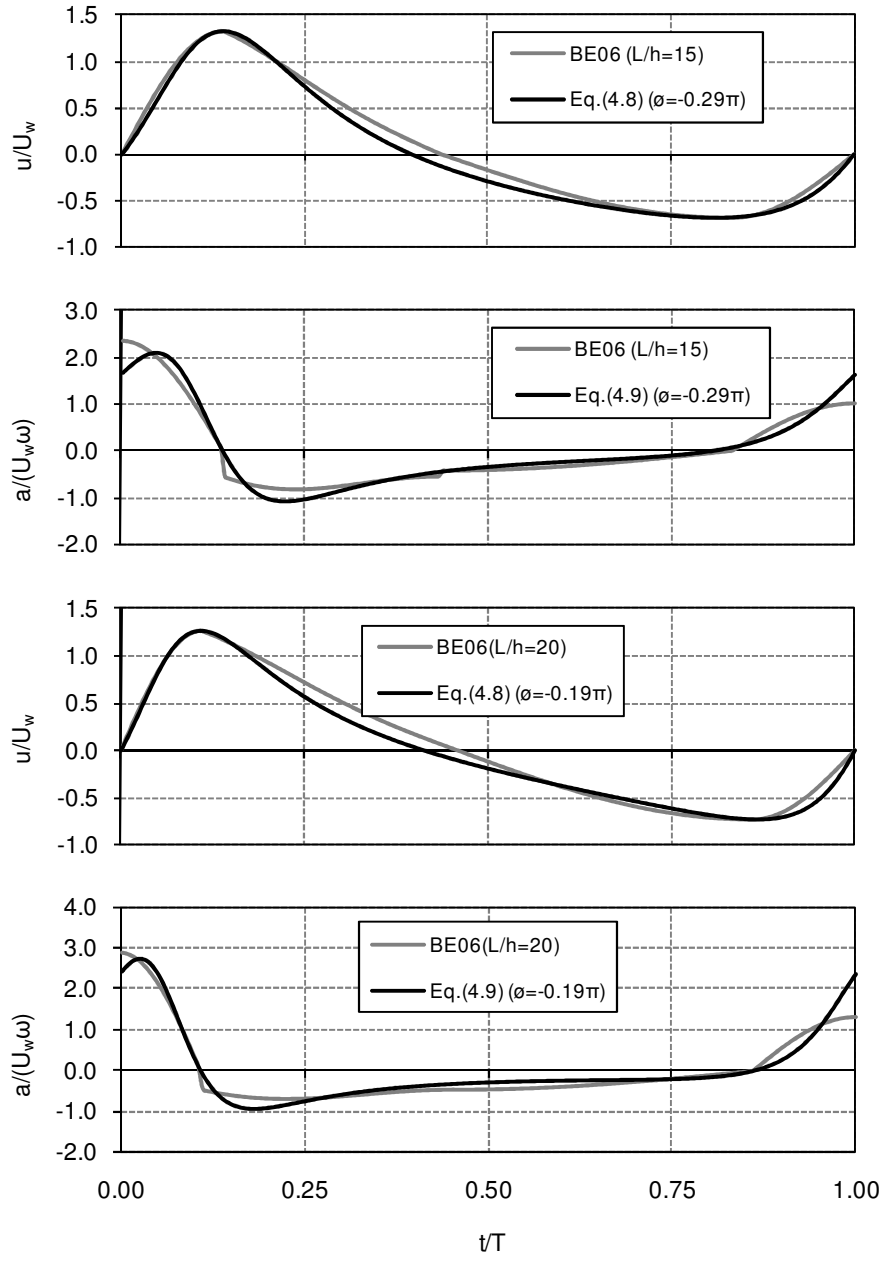

Figure 4.11 – Comparison of orbital velocity and acceleration time series computed from Eq. (4.8) and (4.9), and BE06 with *H/h*=0.4, *h*=2m, slope 1:40, and varying L/h. The reproduction with Eq. (4.8) and (4.9) are accomplished with $\phi = -0.29\pi$ and *r*=0.699, and $\phi = -0.19\pi$ and *r*=0.784.

4.2.5 Simulation of measured velocity time series

In this section, we simulate measured near-bed velocity time series by means of Eq. (4.8). The analysis reflects a number of situations in shallow water with significant velocity and acceleration asymmetries. The simulated time series concern positions prior to, over and past a breaker-bar (Figure

4.12) for two experimental conditions, one in a large-scale experiment (Sancho et al., 2001) and another in the field (DUCK94 campaign, Birkemeier and Thornton, 1994).

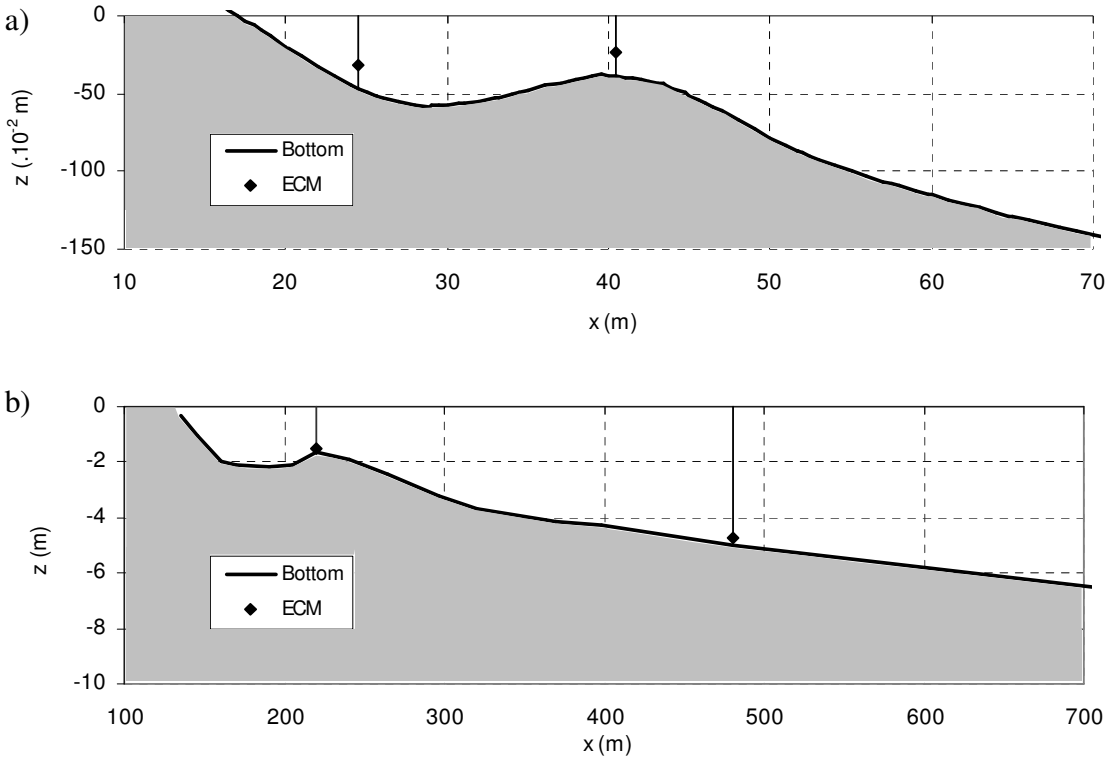

Figure 4.12 – Cross-shore bottom profiles (—) and positions of electromagnetic current meters (ECM) (◆) used in the data analysis: a) UPC experiment; b) DUCK94 experiment (October, 1st).

For the present purpose, the selected velocity records were transformed into a set of individual waves, delimited by two successive zero up-crossings. Each wave is associated with a value of U_w, ($U_w = (u_{max} - u_{min})/2$), and of the asymmetry coefficients R and α. The input parameters r and ϕ used in Eq. (4.8) were calculated for each wave considering the combinations (R,α) through the methodology described in subsection 4.2.3 and Appendix A.1. We further remark that the use of the input parameters (R,α) is preferable to using the combination (R,β) because the latter implies differentiating the velocity records in order to compute β, whereas the former can easily be computed directly from the time series analysis of $u(t)$.

The first data set is reported in Sancho et al. (2001), and concerns the velocity records measured in the large-scale wave flume of the Polytechnic University of Catalonia (UPC), aimed at studying the wave-induced turbulence and undertow over a fixed-bed, barred beach. Several instruments were deployed at several positions along the wave flume but, for the present analysis, we focus solely on the records provided by the electromagnetic current meters (ECM) in the 0.30 m layer above the bottom and at

$x = 24.5m$ and $x = 40.5m$. The data were gathered at 8 Hz sampling frequency. The experiments considered four types of wave conditions (3 monochromatic and 1 irregular sea state).

The second data set corresponds to the DUCK94 nearshore field experiment (Birkemeier and Thornton, 1994), performed by the Coastal and Hydraulics Laboratory of the U.S. Army Corps of Engineers at its Field Research Facility located in Duck, North Carolina (U.S.A.). This experiment provided high quality real data, aimed at understanding the complex phenomena associated with sand transport under waves and currents, and beach morphological evolution. In this study, we analyse the data of the SPUVT array (http://dksrv.usace.army.mil/jg/dk94dir) for the near-bottom (less than 30 cm) cross-shore velocities at two positions, x=220.23 m and x=480.34 m (lower panel of Figure 4.12). The velocities were sampled at 2 Hz.

Figure 4.13 illustrates the observed pairs (r,ϕ) for both experiments. The results evidence that a combination of both velocity and acceleration skewness is usually present and that the majority of the data lies within $0 < r < 1$ and $-\pi/2 \le \phi \le 0$.

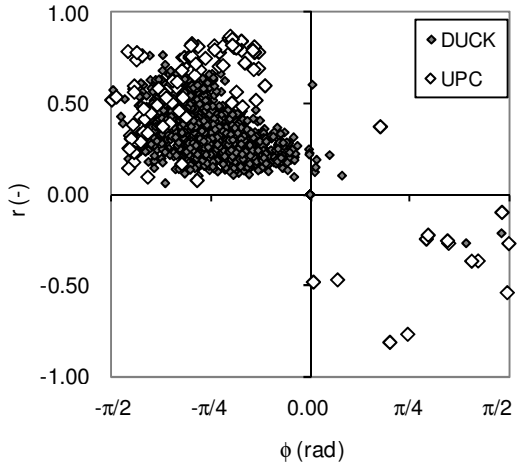

Figure 4.13 – Scatterplot of observed pairs (r, ϕ) for DUCK and UPC experiments.

For the following analysis, the velocities from both data sets were high-pass filtered in order to remove low-frequency motions, since the present formulation aims at reproducing the wave-form of single waves, with zero net current. Accounting for low-frequency oscillations in the velocity records would enhance deviations from that requirement, and hence such oscillations were filtered out. The high-pass frequency cut-off was set at approximately half of the peak frequency, namely, at 0.25 Hz for the UPC data and at 0.05 Hz for the DUCK experiment. For the UPC velocity data, higher-frequency oscillations (> 2 Hz) were further removed in order to avoid spurious oscillations in the velocity time series, mainly associated with surf zone turbulence.

An example comparison between the experimental UPC results and the simulated time series by means of Eq. (4.8) is given in Figure 4.14. It corresponds to an irregular sea state described by a Jonswap spectrum (test D), with a peak enhancement factor equal to 3.3, a root-mean-square wave height (H_{rms}) of 0.21 m and a wave peak period (T_p) equalling 2.5 s in front of the wave maker (where h = 2.05 m). An overall quite satisfactory agreement is evident. Most wave forms are well reproduced, both over the bar-crest (panel b), where mostly broken waves propagate (Sancho, 2002), and past the bar-trough, where non-broken waves have reformed (panel a). Part of the discrepancies in some waves is due to the high-frequency fluctuations, with frequencies lower than 2 Hz, discernible in the measured velocities. Because the new formulation re-creates an equivalent wave with the same R and α values, such high-frequency fluctuations within the principal wave are not possible to be reproduced with the new expression.

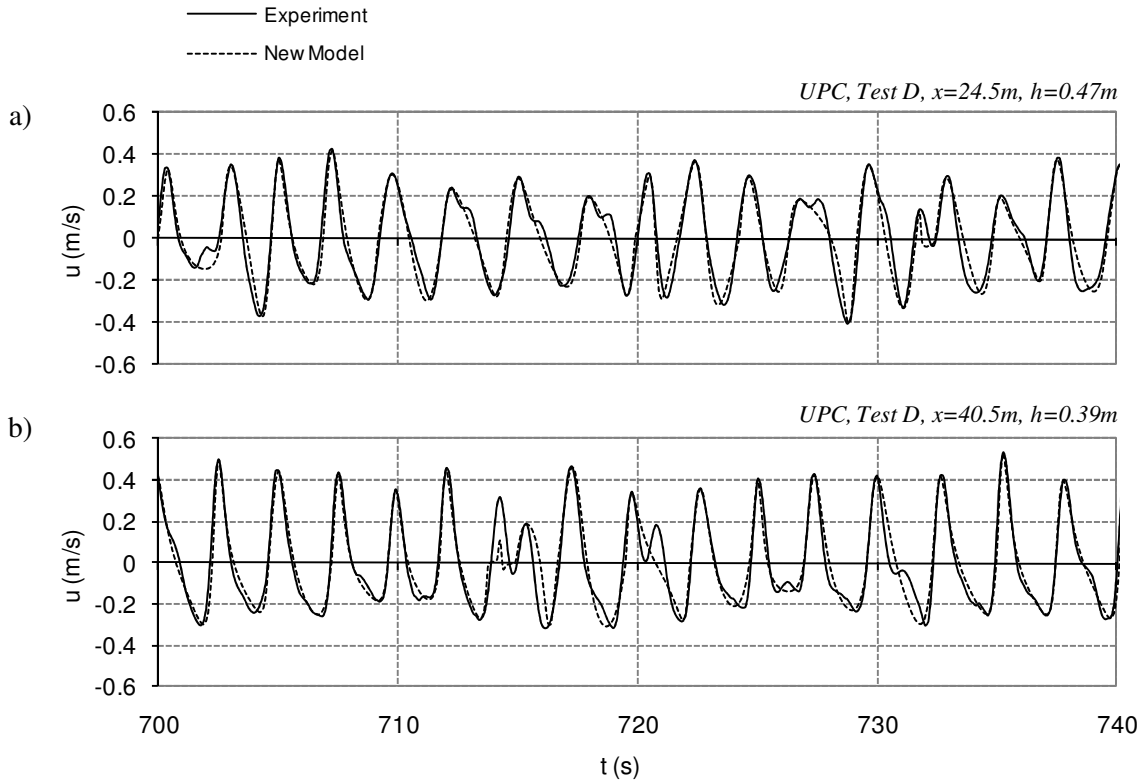

Figure 4.14 – Velocity time series: present model (---) and UPC experiment (—). (Refer to x-positions in Figure 4.12a).

Concerning the DUCK94 time series model-data comparison (Figure 4.15), one perceives a non-negligible number of mismatches. These occur mainly for individual waves in which the velocity magnitude at the crest is smaller than at the trough, corresponding to conditions when $R < 0.5$. Indeed, our parameterisations were validated in the region $R > 0.5$, and thus, one could not expect a good agreement for the waves with such small values of R. Other mismatches occur in cases where the

average measured velocity differs considerably from zero and our parameterisations consider a null averaged value. Nevertheless, there is a general good agreement between measurements and model predictions.

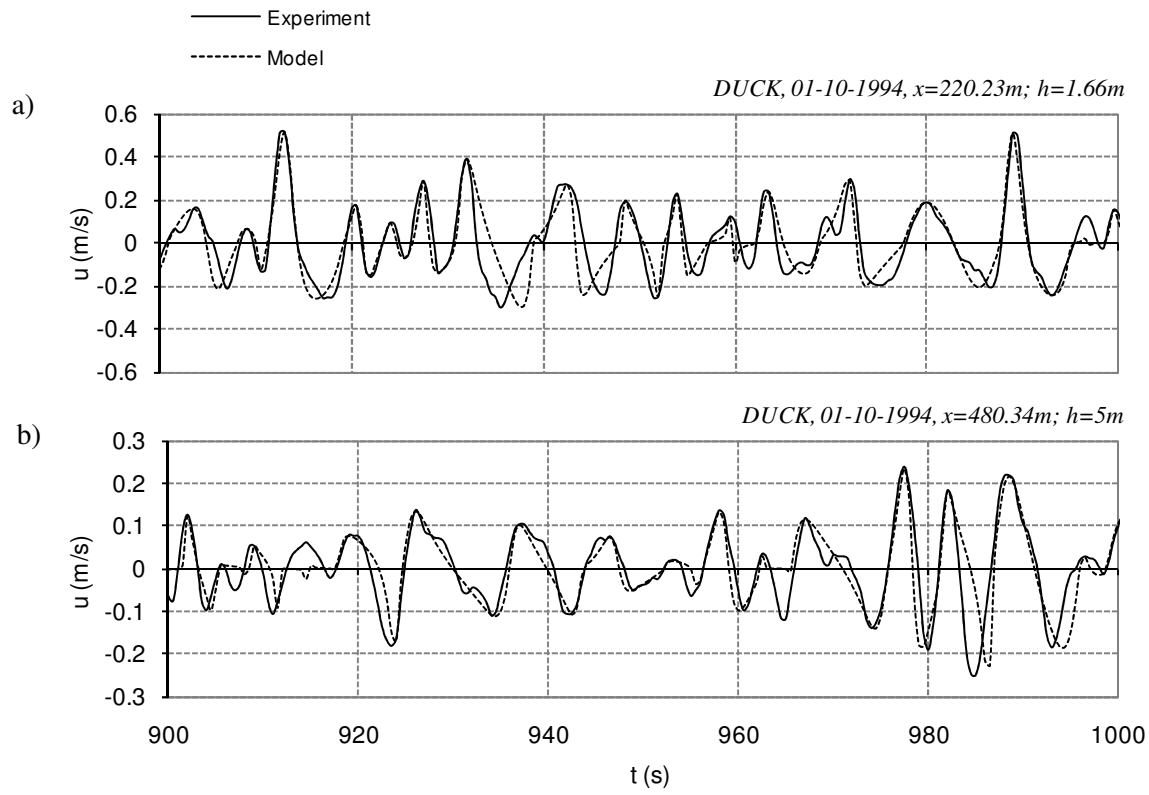

Figure 4.15 – Velocity time series: present model (---) and DUCK94 experiment (—). (Refer to x-positions in Figure 4.12b).

4.2.6 Partial conclusions

A new analytical approximate formulation for the wave form in the coastal zone is presented. The expression is very concise and requires the input of 4 parameters: amplitude of the orbital velocity, U_w; the angular frequency ω; an index of skewness r; and a waveform parameter ϕ. The new function can be used to describe the evolution of wave nonlinearities quite well and it fulfils the requirement of zero mean velocity. The equation is mathematically straightforward and, when compared with other existing formulations in the literature, it surpasses some of their limitations and extends their conditions of applicability. The new function has the advantage that it reproduces wave shapes for any combination of velocity and acceleration skewness parameters, generalizing the DC01 formulation and, moreover, it provides a continuous acceleration time series surpassing the mismatches of IH82 and BE06 formulations.

For practical applications several parameterisations of macro-scale wave velocity and acceleration asymmetry indexes, (R, α and β), have been proposed. These are all similar polynomial functions (Eqs. (4.17) to (4.19)) of the input parameters r and ϕ, that provide an excellent fit to the mathematically unmanageable theoretical relations. For reproducing a wave with the velocity or the acceleration time series close to the shape of a 1st-order cnoidal wave, one should observe the restriction to the limit $r < 0.6$.

The expression has been validated against field and laboratory experiments, revealing that the function can represent with reasonable accuracy the time varying near-bed orbital velocities, measured in the nearshore region, under breaking and non-breaking waves.

The equation is sufficiently general to be applied to a wide variety of nonlinear waves and it can be used for several practical engineering purposes; for example it can provide the wave forcing in experimental facilities (e.g., Silva et al., 2008) or in numerical modelling (e.g., Ruessink et al., 2009). Also, the inclusion of this formula in practical sediment transport formulae (e.g., Silva et al., 2006; Nielsen, 2006) enables the transport to be computed directly as a function of the velocity and acceleration skewness parameters.

As a final note, an expression has been proposed here for the near-bed horizontal orbital velocity, and the corresponding horizontal acceleration. It is envisaged that one may derive a corresponding equation for the free-surface displacement, based on an adequate description of the vertical variation of U_w and the wave celerity.

4.3 Bed shear stress

4.3.1 Introduction

There are several approaches that relate the frictional force that the fluid exerts on the bed to the mass of sediment moved. In particular, many sand transport models evaluate directly the sediment transport rates as a function of the time-dependent bed shear stress or the orbital velocity just above the wave boundary layer, assuming some kind of proportionality among these quantities (e.g., Meyer-Peter and Müller, 1948; van Rijn, 1984; Madsen, 1991; Nielsen, 1992; Wang, 2007). In the latter case the velocities are used to compute the bed shear stress or the equivalent bed shear velocity (e.g., Ribberink and Al-Salem, 1994; Ribberink, 1998, Nielsen and Callaghan, 2003; Nielsen, 2006). This approach is applicable as long as the bedload is the dominant transport mode, as in the sheet flow plane-bed regime (e.g., Horikawa et al., 1982; Ribberink, 1998; Dohmen-Janssen and Hanes, 2002; Hsu and Hanes, 2004). When non-steady processes, resulting, for example, from the phase-lag between the sediments' concentration and the flow velocities, are not negligible, as in rippled beds and fine grain sizes (e.g., Watanabe and Isobe, 1990; Dibajnia and Watanabe, 1992; Dohmen-Janssen et al., 2002; O'Donoghue and Wright, 2004a), they must also be accounted for predicting accurately sediment transport rates (Ruessink et al., 2009). In more complex bottom boundary layer models, including sediment suspension and phase-lag effects (e.g., Thanh et al., 1994; Ruessink et al., 2009), the bed shear stress determines the reference concentration (e.g., Zyserman and Fredsøe, 1994). Therefore, independently of the grain size/dominant transport mode, the bed shear stress is always related with the mobilization of sediments.

This section concentrates on the bottom shear stresses parameterisations caused by non-linear, skewed, surface waves in shallow water. For the present analysis, it suffices to consider only the effect that the bottom boundary layer has on the flow above, namely, to generate a bottom shear stress. Some of the formulations used herewith do not resolve the details of the boundary flow. They have a strong empirical character and rely on physical insights in combination with data collected in laboratory and field campaigns. In general, the selected formulations may incorporate both velocity- and acceleration-related terms all at once, or may include a time-varying friction factor and phase-lag (e.g., Gonzalez-Rodriguez and Madsen, 2007, Suntoyo et al., 2008).

The overall objective of this section is to evaluate several bottom shear stress formulations that can be combined with existing practical sediment transport formulae and to provide a new simple analytical instantaneous bed shear stress parameterisation for arbitrary nonlinear oscillatory flows (Abreu et al.,

2011). The effects of velocity and acceleration skewness on the new expression are incorporated in the time-varying bed shear stress using the two parameters proposed in the previous section: the index of skewness or nonlinearity, r, and the waveform parameter, ϕ. The new formulation extends the work of Nielsen (1992, 2002), Nielsen and Callaghan (2003) and Terrile et al. (2009) and shows that, beside acceleration effects, the shape of the wave described through r and ϕ needs to be considered in the instantaneous shear stress estimations.

The following subsection starts with a description of the existing bottom shear stress parameterisations. The formulae are applied to the TRANSKEW laboratory data set in order to gain insight by considering the influence of the several intervenient parameters. That analysis is followed by the presentation of the new formula. Afterwards, the expression is tested against bed shear stress measurements by van der A et al. (2011) in the Aberdeen Oscillatory Flow Tunnel for acceleration-skewed flows over fixed rough beds. The main conclusions are presented at the end.

4.3.2 Existing parameterisations

Here, bottom shear stress parameterisations found in the literature for non-linear waves are presented. Most of them can be used as an input to sediment transport models because, when the bedload is dominated, sediment fluxes can be accurately parameterised in terms of the seabed shear stress (Hsu and Hanes, 2004).

Usually, it is used a wave friction factor, f_w, to link the bed shear stress to the free-stream velocity (e.g. Soulsby, 1997). In the oscillatory wave motion, the dimensionless friction factor f_w is given as

$$\tau_{max} = \frac{1}{2}\rho f_w U_w^2 \tag{4.31}$$

where τ_{max} represents the maximum bed shear stress. From dimensional analysis one can conclude that f_w depends on the Reynolds number (Re) and on the amplitude/roughness ratio (A/k_s). Attending to the different flow regimes and that the most common occurring in nature is the rough turbulent flow, several formulae depend only on the parameter A/k_s, i.e., $f_w = f_w\left(A/k_s\right)$ (e.g., Jonsson, 1966, Swart, 1974, Tanaka and Thu, 1994).

Furthermore, it is often assumed that the instantaneous bed shear stress within a basic harmonic wave-cycle is given by the generalization of Eq. (4.31) to arbitrary time:

$$\tau(t) = \frac{1}{2}\rho f_w \left|u(t)\right| u(t)\,. \tag{4.32}$$

However, this basic conceptual model, known as quasi-steady approach does not account for nonlinear effects because it assumes that the instantaneous bottom shear stress can be estimated directly from $u(t)$ under the hypothesis that the bottom stress is in phase with the free-stream velocity. For example, for a sawtooth wave, where $|u_{max}| = |u_{min}|$, Equation (4.32) implies $|\tau_{max}| = |\tau_{min}|$ in contrast to the observations of the previous chapter.

Thus, the quasi-steady approach can lead to considerable errors when applied to sediment transport estimations under nonlinear waves (e.g., Drake and Calantoni, 2001; Nielsen and Callaghan, 2003). Nonetheless, this method is the basic conceptual model that motivated several authors to adapt Equation (4.32) to account for nonlinear effects. Some modifications incorporate both velocity and acceleration terms or include time-varying friction factors and time-varying phase differences (e.g., Nielsen, 1992, 2002; Antunes do Carmo et al., 2003; Tanaka and Samad, 2006; Gonzalez-Rodriguez and Madsen, 2007; Suntoyo et al., 2008; Terrile et al., 2009).

Nielsen, 1992, 2002 – N02

In contrast with the previous approach, Nielsen (1992, 2002) included the effect of the fluid acceleration acting on the sediment particles on the bottom shear stress. The parameterisation is formed in terms of the instantaneous wave friction velocity, $u_*(t)$, and is based on harmonic boundary layer theory:

$$u_*(t) = \sqrt{\frac{f_w}{2}}\left(cos(\varphi)\ u(t) + \frac{sin(\varphi)}{\omega}\frac{\partial u(t)}{\partial t} \right), \tag{4.33}$$

$$\tau(t) = \rho u_*(t)\left|u_*(t)\right| . \tag{4.34}$$

where the angle φ roughly represents the phase lead of bed shear stress over the free-stream velocity.

Because Nielsen's (1992, 2002) parameterisation incorporates both velocity- and acceleration-related terms, Nielsen and Callaghan (2003) suggested that the model might represent both pressure gradient and boundary layer thickness effects. The inertial (pressure) forces add the drag forces, contributing to the total horizontal forces acting on the sediment particles. The effect of the pressure gradient to the overall horizontal sediment momentum budget, particularly for asymmetric flows, has been recognized by several investigators (e.g., Drake and Calantoni, 2001; Hsu and Hanes, 2004; Calantoni and Puleo, 2006).

Tanaka and Samad, 2006 – TS06

To account for the asymmetry of the bottom shear stresses in non-linear wave boundary layers, Tanaka and Samad (2006) proposed the introduction of a phase difference between the free-stream velocity and the bottom shear stress, φ. This originates the following equation:

$$\tau(t) = \frac{1}{2}\rho f_w u\left(t + \frac{\varphi}{\omega}\right)\left|u\left(t + \frac{\varphi}{\omega}\right)\right| . \tag{4.35}$$

In addition to the introduction of the phase difference φ, Antunes do Carmo et al. (2003) proposed a parameterisation including a time-varying friction factor, $f_w(t)$. However, since the subsequent methodology also follows a similar idea, the expression of Antunes do Carmo et al. (2003) was not employed here.

Gonzalez-Rodriguez and Madsen, 2007 – GRM07

Gonzalez-Rodriguez and Madsen (2007) presented a simple conceptual model to compute bottom shear stresses under asymmetric and skewed waves. Their formulation uses a time-varying friction factor, $f_w(t)$, in addition to the time-varying phase lead, $\varphi(t)$, of Tanaka and Samad (2006) that accounts for the variability in the wave shape. They justify the use of a variable friction factor over the wave period by examining the physics of the boundary layer. The values are calculated at the wave crest and at the wave trough, and are then assumed to be linearly interpolated for the rest of the wave phases:

$$\tau(t) = \frac{1}{2}\rho f_w(t) u\left(t + \frac{\varphi(t)}{\omega}\right)\left|u\left(t + \frac{\varphi(t)}{\omega}\right)\right| . \tag{4.36}$$

Suntoyo et al., 2008 – S08

Suntoyo et al. (2008) proposed slight changes to Nielsen (1992, 2002) formulation, developing a new acceleration coefficient under sawtooth-shaped waves. This parameterisation is formed in terms of the instantaneous wave friction velocity, $u_*(t)$, including a new acceleration coefficient, a_c, determined empirically. The instantaneous wave friction velocity is thus expressed as:

$$u_*(t) = \sqrt{\frac{f_w}{2}}\left[u\left(t + \frac{\varphi}{\omega}\right) + \frac{a_c}{\omega}\frac{\partial u(t)}{\partial t}\right] \tag{4.37}$$

and the bottom shear stress is given by Eq. (4.34).

The acceleration coefficient a_c provided for pure accelerated-skewed flows by Suntoyo et al. (2008) follows:

$$a_c = -0.36\,ln(\alpha) - 0.249\,. \tag{4.38}$$

Eq. (4.38) was not derived for flows that possess both velocity and acceleration skewnesses. Still, Suntoyo et al. (2006) provide an instantaneous wave friction velocity for pure velocity skewed flows similar to Equation (4.37) with:

$$a_c = 0.592\,ln(R) + 0.411\,. \tag{4.39}$$

In such case the acceleration coefficient a_c is function of R instead of α.

Figure 4.16 presents the results of Eq.s (4.38) and (4.39), revealing that a_c is zero if $R = 0.5$ or $\alpha = 0.5$ as for the sinusoidal form. Furthermore, both formulas predict an increase of the acceleration coefficient a_c with the increase of the velocity or acceleration skewness, i.e., $R > 0.5$ or $\alpha < 0.5$.

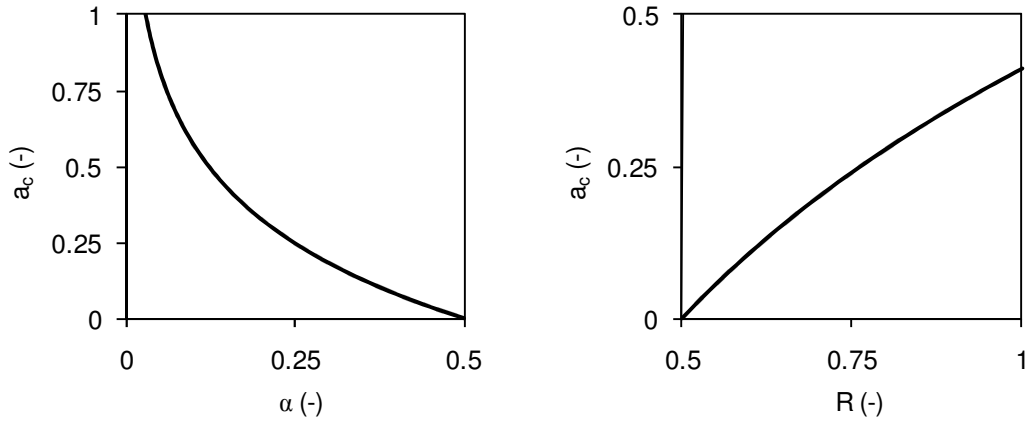

Figure 4.16 – Values of a_c using Eq.s (4.38) and (4.39).

Terrile et al., 2009 – T09

Recently, the parameterisation of Nielsen (1992, 2002) was extended by Terrile et al. (2009), with the purpose of generalizing the formulation to an arbitrary wave shape. They argued that Eq. (4.33) was developed for the case of a simple harmonic motion and introduced a new expression representative of a wide range of shoaling and broken waves, considering the influence of a waveform parameter ϕ' (Elgar and Guza, 1985). Their formulation reads:

$$u_*(t)=\sqrt{\frac{f_w}{2}}\left(cos(\varphi)\ u(t)+\frac{sin(\varphi)}{\omega}\left[\frac{\partial u(t)}{\partial t}-S(t,\phi')\right]\right). \tag{4.40}$$

where the function $S(t,\phi')$ allows for nonlinear near-bed orbital velocities like Drake and Calantoni's (2001) and is defined as follows:

$$S(t,\phi')=-A_{rms}\omega^2\sum_{j=0}^{N}\frac{j}{2^j}sin\left[(j+1)\omega t+j\phi'\right]. \tag{4.41}$$

The waveform parameter ϕ' can be related with ϕ of (4.8) through a simple relation: $\phi'=\phi+\pi/2$. Equation (4.40) was validated with Terrile et al. (2006) laboratory observations.

4.3.3 Comparison between formulations

To establish the comparison of the different methodologies presented before, some remarks are pointed out. The implicit wave friction factor proposed by Tanaka and Thu (1994) was used in all the methods:

$$f_w=exp\left(8.07\left(\frac{A}{z_0}\right)^{-0.100}-7.53\right). \tag{4.42}$$

Therefore, the magnitudes of bed shear stress are compromised by the solutions of Equation (4.42). In Appendix B several frictional coefficient formulae are presented showing that large differences can be expected if another formula is used. For the choice of the phase shift between the bed shear stress and the free-stream velocity, φ, two options were considered for this comparison. First, the methodology presented in Suntoyo et al. (2008) for the rough turbulent regime was assumed. Their approach is based in the formula proposed by Tanaka and Thu (1994) for the sinusoidal case, φ_s, and, to account for the wave nonlinearities, a correction factor depending on α is added:

$$\varphi=2\alpha\varphi_s, \tag{4.43}$$

$$\varphi_s=42.4C_f^{\,0.53}\frac{1+0.00279C_f^{\,-0.357}}{1+0.127C_f^{\,0.563}}, \tag{4.44}$$

where, for rough flows,

$$C_f=\frac{0.111}{\kappa\sqrt{\frac{f_w}{2}}\frac{A}{z_0}}\ . \tag{4.45}$$

The consideration of Eq. (4.43) provides, for the majority of the TRANSKEW experiments, values of φ between 8.7º and 13.2º.

Secondly, the phase-lead of $\varphi = 51°$ proposed by Nielsen (2006) was also used. Nielsen (2006) found this calibrated value by applying his shear stress approach to a quasi-steady Meyer-Peter and Müller type bedload formula and optimizing the net transport predictions to Watanabe and Sato's (2004) measurements for acceleration-skewed flows.

It is remarked that the calculation of the acceleration coefficient, a_c, proposed by Suntoyo et al. (2008) concerns only sawtooth waves with the velocity skewness $R = 0.5$, i.e., the velocity under the crest is equal to the velocity under the trough. Consequently, the proposed expression is based only on the acceleration skewness α. However, in the case of TRANSKEW Series C (C1 to C3), in addition to different degrees of acceleration skewness, several degrees of velocity skewness are found. In the present study the same expression (Equation (4.38)) was extended to Series C, but it might be advisable, in further studies, to find a more generic expression between Equations (4.38) and (4.39) that accounts for the combination of both asymmetries in the coefficient a_c.

Figure 4.17 and Figure 4.18 synthesise the time-variation of the bottom shear stresses, computed with the methods described above, for Series A and C, considering both φ obtained from Eq. (4.43) and $\varphi = 51º$. Also, because the ratio of the shear stress maxima $|\tau_{max}/\tau_{min}|$ can be considered as a proxy for sediment transport rate predictions, its values are listed in Table 4.5 per method. Moreover, this ratio is unaffected by the choice of f_w. Note the differences in scales from Figure 4.17 to Figure 4.18.

Table 4.5 – Ratio of maximum positive and maximum negative bed shear stress $|\tau_{max}/\tau_{min}|$ for TRANSKEW tests without current.

Test	N02		TS06		GRM07		S08		T09	
	Eq.(4.43)	51°	Eq.(4.43)	51°	Eq.(4.43)	51°	Eq.(4.43)	51°	Eq.(4.43)	51°
A1	1.01	1.70	1.00	1.00	1.10	1.07	1.01	1.09	1.38	2.70
A2	0.93	1.48	0.92	0.92	0.99	0.96	0.93	0.96	1.27	2.45
A3	1.01	2.36	1.00	1.00	1.14	1.11	1.03	1.22	1.43	3.23
A4	0.93	2.16	0.92	0.92	1.04	1.01	0.94	1.09	1.33	3.06
C1	2.16	4.55	2.07	2.07	2.16	2.15	2.20	2.38	2.82	3.59
C2	2.16	4.35	2.07	2.06	2.14	2.12	2.17	2.31	2.78	3.40
C3	2.18	3.11	2.07	2.07	2.03	2.03	2.11	2.16	2.58	2.22

With the exception of T09, the left columns of Figure 4.17 and Figure 4.18 show that the small values of φ obtained from Eq. (4.43) yield very similar results between the methods and it is possible to observe an overlapping between some curves. The differences arise with the assumption of $\varphi = 51º$ (right columns of Figure 4.17 and Figure 4.18). Regarding the ratio $|\tau_{max}/\tau_{min}|$, Table 4.5 reveals that the

method of TS06 is almost insensitive to φ. Indeed, Equation (4.35) presents some limitations to predict a ratio $|\tau_{max}/\tau_{min}|$ like the quasi-steady approach. For example, for pure acceleration-skewed flows ($R = 0.5$ and $\beta \neq 0.5$), the ratio approaches 1 ($\tau_{max} = \tau_{min}$). The difference to the quasi-steady approach is that the introduction of the phase lead φ in Equation (4.35) induces a mean bed shear stress different from zero. Consequently, when integrated in a sediment transport formula like Meyer-Peter and Müller, it provides non null values even for a pure acceleration-skewed flow. Looking to GRM07 results, it becomes also clear that the ratio $|\tau_{max}/\tau_{min}|$ doesn't change significantly for different values of φ. The differences with TS06 is that the asymmetries between τ_{max} and τ_{min} are a direct outcome of Eq. (4.36) due to the use of a time-varying friction factor, $f_w(t)$, and a time-varying phase lead, $\varphi(t)$. The methods of N02, S08 and T09 contain a second term of the instantaneous wave friction velocity, $u_*(t)$, which is linked to the acceleration and assumes a larger relative magnitude when compared to the first velocity-related term (Eq.s (4.33), (4.37) and (4.40)). As consequence, higher values of φ will enhance the acceleration skewness in the bed shear stresses, leading to higher shear stresses at the crest compared to those at the trough.

Regardless the value of φ and focusing on Series A (Figure 4.17), it is noticed, for the same wave period (conditions A1 and A3 correspond to $T = 7$ s, while A2 and A4 correspond to $T = 10$ s), that all the methods (except TS06) predict an increase in the asymmetry of bottom shear stress ($|\tau_{max}/\tau_{min}|$) with the increase of the acceleration skewness β. The method which accentuates more the differences between τ_{max} and τ_{min} is T09, where the asymmetry is much more pronounced, originating the time-varying shear stress to detach clearly from the others predictions.

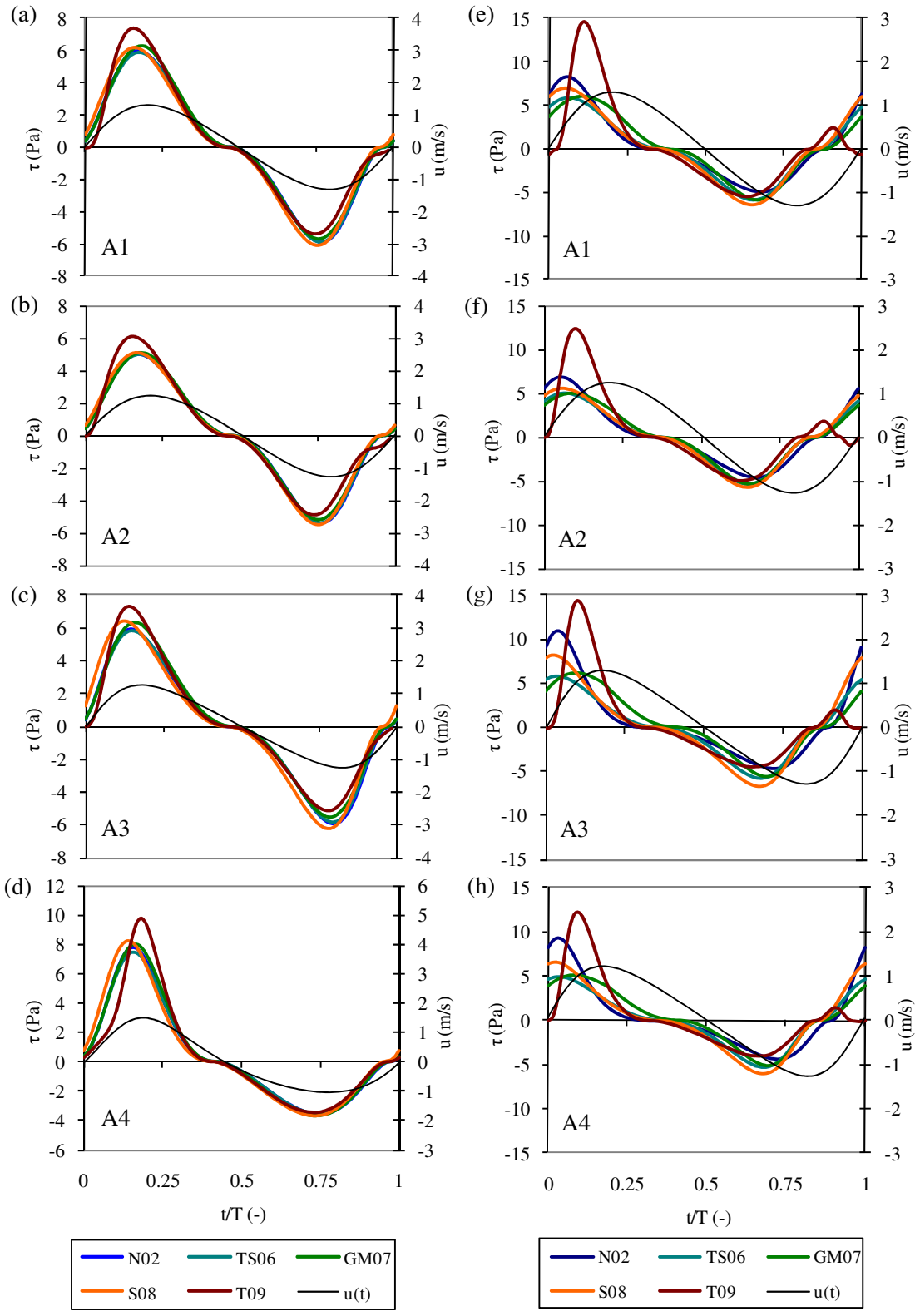

Figure 4.17 – Comparison between the results of different bottom shear stress methodologies for Series A with φ from Eq. (4.43) (left column) and $\varphi = 51°$ (right column).

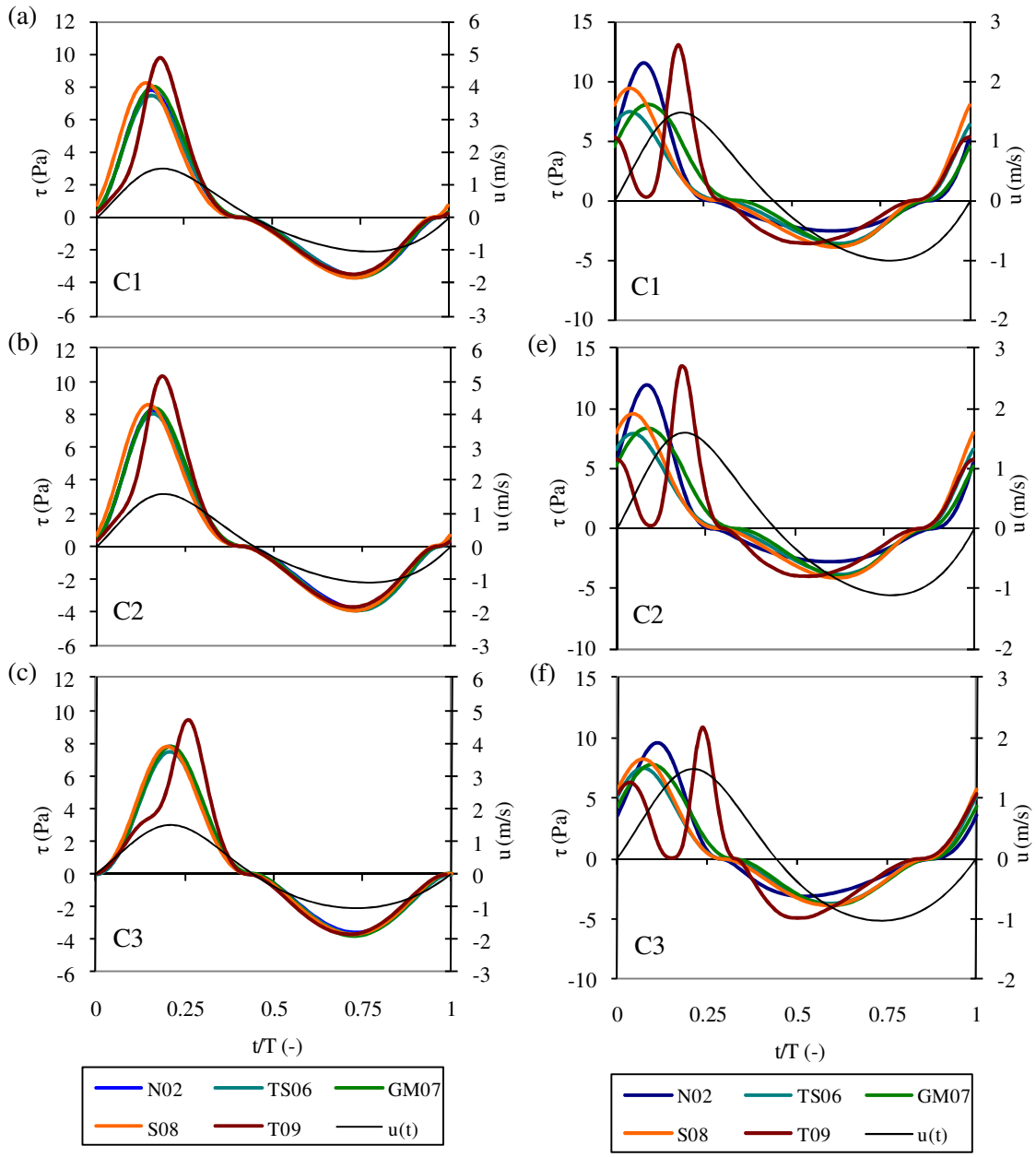

Figure 4.18 – Comparison between the results of different bottom shear stress methodologies for Series C with φ from Eq. (4.43) (left column) and $\varphi = 51°$ (right column).

Analysing the influence of the wave period for the same acceleration skewness, i.e., comparing conditions A1 with A2 and A3 with A4, all methods present a slight reduction in the magnitudes of the shear stresses with an increase in the wave period. That pattern is straightforwardly understandable since increasing values of the wave period cause decreasing values of the wave friction factor (Tanaka and Thu, 1994). Also, the ratio $|\tau_{max}/\tau_{min}|$ decreases with an increase in the wave period. This

observation is also comprehensible since the boundary layer has more time to grow, reducing the differences between the shear stress under both half cycles (Nielsen, 1992).

Focusing on Series C, it is seen that the peak magnitudes resulting from T09 are somewhat larger than those from the other methods. For small values of φ (Figure 4.18, left column) the other methods present almost identical results. The one obtained with S08 presents some small differences, but it should be kept in mind that the acceleration coefficient, a_c, applied was developed for pure sawtooth waves. For $\varphi = 51°$ (Figure 4.18, right column) the larger ratios $|\tau_{max}/\tau_{min}|$ are obtained for N02 and are generally greater than for the other methods. It is followed by T09, S08, GRM07 and TS06. However, it can be seen that T09 leads to two distinct peaks in the positive direction. That was already perceivable in the right column of Figure 4.17 but with lower magnitudes. That is a direct outcome of the introduction of the function $S(t,\phi')$ in Eq. (4.33) because Eq. (4.41) was developed using Drake and Calantoni's (2001) free-stream velocity. As such solution corresponds to $r = 0.8$ in Equation (4.8) it means that their solution is not appropriate for different values of r like TRANSKEW test conditions. In the next subsection (4.3.4) a new analytical parameterisation is devised correcting such limitation.

It is possible to detect, through the comparison of Series A with Series C, that the velocity skewness has a much greater interference on the time-mean shear stress than the acceleration skewness. Comparing condition C1 with A1 we see that the velocity skewness induced a considerable reduction of the peak values of the bottom shear stress under the trough, when compared with the peak values under the crest.

4.3.4 New parameterisation

The previous analysis revealed the performance of several parameterisations found in the literature that attempt to account for nonlinear effects. It was seen that Terrile's et al. (2009) formulation has some limitations for higher values of φ. Here, an improvement of Equation (4.40) is presented through the addition of the index of skewness r used in (4.8). The new generalization follows the procedure given in subsection 4.2.2, where the extension of Drake and Calantoni's (2001) formulation resulted in a simple analytical expression that reproduces any skewed, nonlinear near-bed wave orbital velocity with any kind of skewness or asymmetry degrees.

Therefore, as shown in subsection 4.2.2, but defining $u(t)$ as the real part of

$$u(t) = U_w \, Re\left[\sum_{j=0}^{\infty} \frac{1}{n^j} exp\left(i\left[(j+1)\omega t + j\phi'\right]\right)\right]. \tag{4.46}$$

and noting that $\phi' = \phi + \pi/2$, one obtains

$$u(t) = U_w f \frac{\left[cos(\omega t) - \frac{r\cos\phi'}{1+f}\right]}{\left[1 - r\cos(\omega t + \phi')\right]}. \tag{4.47}$$

Eq. (4.47) is an extension of the expression originally presented by Terrile et al. (2009).

Abreu, 2011 – A11

Thus, one proposes to extend Equation (4.40) by introducing $S(t,\phi,r)$ instead of $S(t,\phi')$ and replacing the number 2 in the denominator of Eq. (4.41) by *n* and, consequently, through $r = 2n/\left(1+n^2\right)$ (see subsection 4.2.2). This results in

$$u_*(t) = \sqrt{\frac{f_w}{2}}\left(cos(\varphi)\; u(t) + \frac{sin(\varphi)}{\omega}\left[\frac{\partial u(t)}{\partial t} - S(t,\phi,r)\right]\right), \tag{4.48}$$

with

$$S(t,\phi,r) = A_{rms}\omega^2 \sum_{j=0}^{+\infty} \frac{r^j j}{\left(1+\sqrt{1-r^2}\right)^j} cos\left[(j+1)\omega t + j\phi\right]. \tag{4.49}$$

Here, the representative near bed semi-excursion A_{rms} is given by

$$A_{rms} = \frac{U_{rms}}{\omega} \cdot \frac{2\sqrt{1-r^2+\sqrt{1-r^2}}}{1+\sqrt{1-r^2}}. \tag{4.50}$$

This definition of A_{rms} accounts for the different harmonics in the velocity variance of an arbitrary periodical wave shape. The sinusoidal wave case ($r = 0$) results in the usual $A_{rms} = \sqrt{2}\sigma_u/\omega$, while, in the case of $r = 0.8$ (corresponding to Drake and Calantoni's solution), A_{rms} equals $\sqrt{3/2}\sigma_u/\omega$.

The summation in Equation (4.49) can be computed exactly within the framework of analytical functions of complex variables, yielding:

$$S(t,\phi,r) = \omega \cdot f \cdot U_w \frac{r\left[-(-1+f)\cos\phi - 2r\cos(\omega t) + (1+f)\cos(2\omega t + \phi)\right]}{2(1+f)\left[-1+r\cos(\omega t)\right]^2}. \tag{4.51}$$

Hence, the effects of velocity and acceleration skewness are incorporated in the time-varying bed shear stress (Equations (4.34), (4.48) and (4.51)) using the two above parameters r and ϕ. The sinusoidal wave leads to $S = 0$ which corresponds to Nielsen's (1992, 2002) instantaneous wave friction velocity (Eq. (4.33), while the particular case of $r = 0.8$ corresponds to Terrile et al.'s (2009) instantaneous wave friction velocity (Eq. (4.40)).

4.3.5 Comparison with previous formulations

Figure 4.19 presents the improvements of the instantaneous bottom shear stress for the tests with different shapes (A1, A3, C1 and C3) using the new expression (Eq.(4.48)) with $\varphi = 51°$. The results are superimposed with the preceding formulations of Nielsen (1992, 2002) and Terrile et al. (2009). The Figure shows that the positive secondary peaks observed for T09 completely disappear with the new formulation. Moreover the ratio $|\tau_{max}/\tau_{min}|$ is reduced to 1.56, 2.07, 2.43 and 1.77 for tests A1, A3, C1 and C3, correspondingly. Such reduction is attributed to the term $S(t,\phi,r)$ which corrects the instantaneous accelerations in Eq. (4.48).

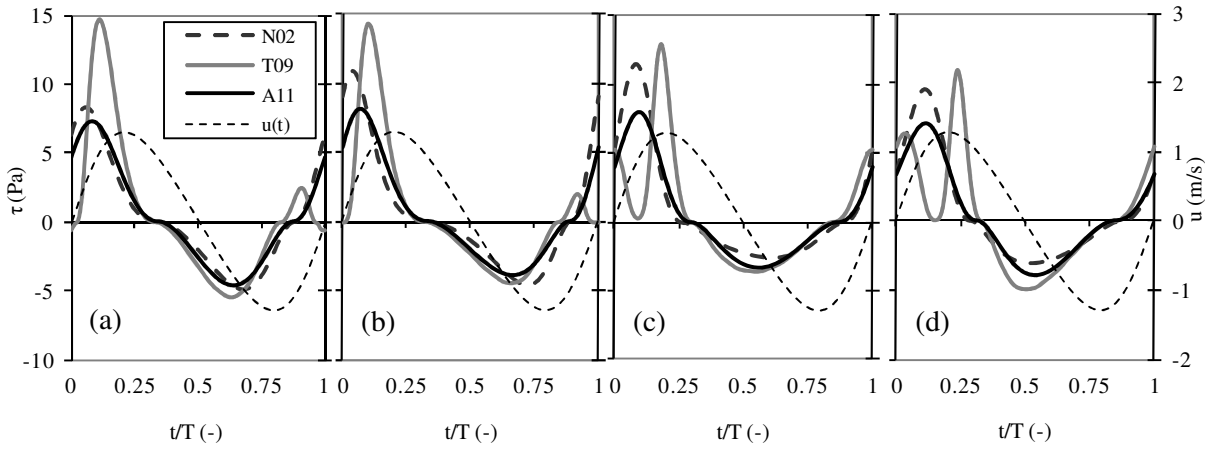

Figure 4.19 – Comparison between the results of different bottom shear stress methodologies for N02 (Eq. (4.33), T09 (Eq. (4.40)) and A11 (Eq.(4.48)) using $\varphi = 51°$ for Tests: (a) A1, (b) A3, (c) C1 and (d) C3.

The magnitude of $S(t,\phi,r)$ relative to the acceleration is shown in Figure 4.20. As tests A1, C1 and C3 are representative of $\phi = 0$, $\phi \approx -\pi/4$ and $\phi \approx -\pi/2$ it is possible to attain an idea of $S(t,\phi,r)$ with the evolution of the waveform parameter ϕ.

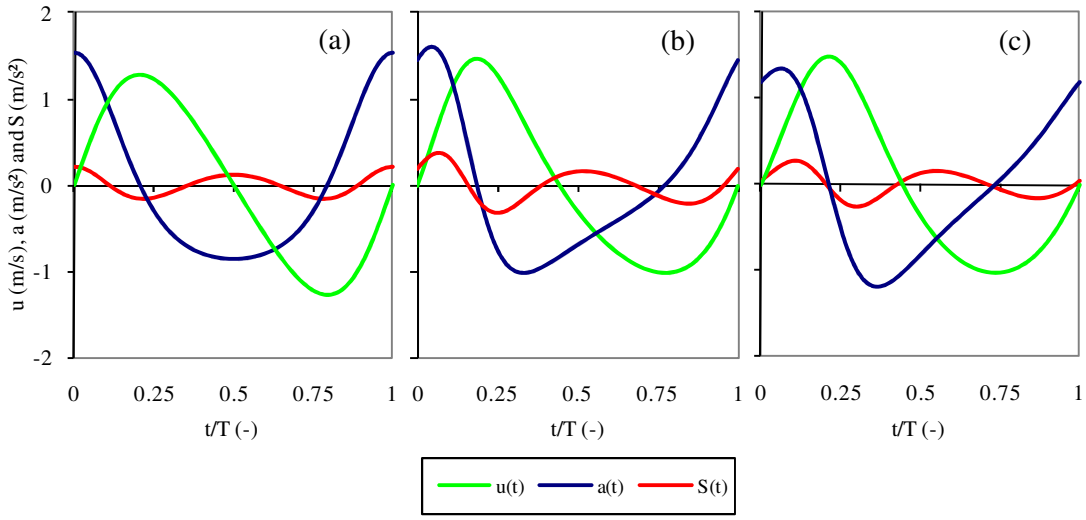

Figure 4.20 – Instantaneous velocity, acceleration and *S* for: (a) A1, (b) C1 and (c) C3.

Hereafter, the performance of the new formulation is tested comparing the predictions of bed shear stress under acceleration-skewed oscillatory flows with bed shear stress measurements over fixed rough beds (van der A et al., 2011) and over mobile beds (TRANSKEW data).

4.3.6 Validation to acceleration-skewed oscillatory flows over fixed rough beds

In a recent experimental study in the Aberdeen Oscillatory Flow Tunnel (AOFT), van der A et al. (2011) measured the instantaneous velocity profiles in the boundary layer for a range of acceleration-skewed oscillatory flows over fixed rough beds. The test conditions had flow periods of T = 5s and 7s, with U_w = 0.9 or 1.1m/s. The bed roughness consisted of sand (with Nikuradse roughness k_s = 1.1mm) or gravel (k_s = 13.8mm) glued to the fixed bed. The free-stream oscillatory flow was dominated by acceleration skewness. Bed shear stress was estimated for large parts of the oscillatory flow cycle by applying *the law-of-the-wall* (Eq. (3.54), Section 3.8.1) to the measured instantaneous velocity profiles. The present comparison focus on the results of the gravel bed experiments, for which all the flow conditions were in the rough turbulent regime.

Figure 4.21 shows an example comparison of measured bed shear stress with the predicted bed shear stress using the new predictor (Equation (4.48)) and using Nielsen's (1992, 2002) method (i.e., S = 0). To compute the wave friction factor, one assumes Nielsen (1992) formulation:

$$f_w = exp\left[5.5\left(\frac{k_s}{A_{rms}}\right)^{0.2} - 6.3\right] \tag{4.52}$$

Figure 4.21a compares the measured and predicted (Eq. (4.8)) free-stream velocity time-series, the latter is used as input to both bed shear stress predictors. Bed shear stress is shown for two scenario's: Figure 4.21b shows the results using Nielsen's (1992, 2002) optimized phase-lead value of φ = 51°, while in Figure 4.21c the results are shown using the measured (first harmonic) phase-lead, which is approximately $\varphi = 26°$ for this condition. It is shown that using $\varphi = 51°$ Nielsen's (1992, 2002) approach largely overestimates the maximum shear stress, while much better agreement is obtained with the new method which includes the additional term to adjust the acceleration contribution.

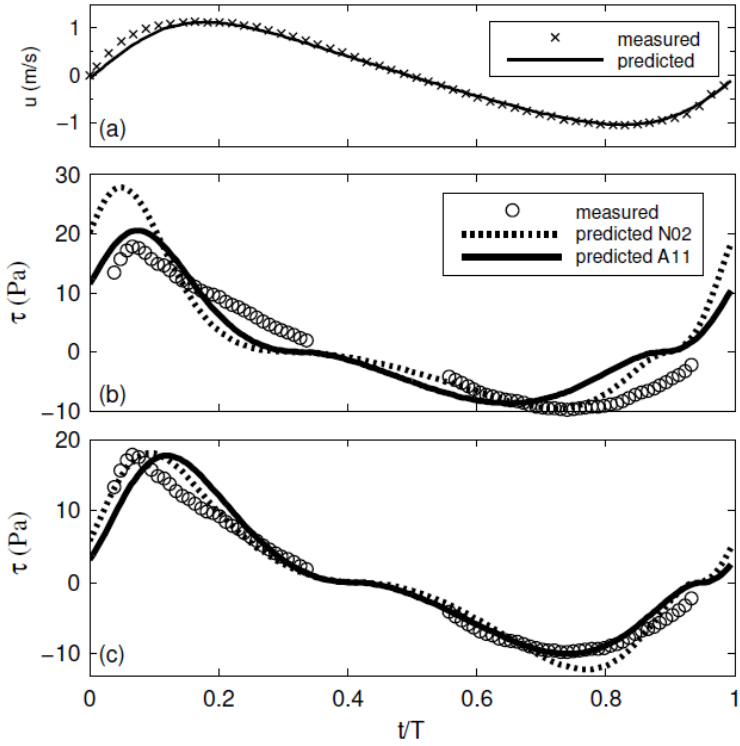

Figure 4.21 – (a) Measured and predicted free-stream velocity; (b) measured and predicted bed shear stress using φ =51°; (c) idem using φ =26° Flow condition: T = 7s, U_w = 1.1m/s, r = 0.451, ϕ = 0.161, k_s = 13.8mm.

Table 4.6 – Ratio of maximum positive and maximum negative bed shear stress $|\tau_{bmax}/\tau_{bmin}|$. Test conditions were dominated by acceleration skewness (i.e. waveform parameter $\phi \approx 0$)

Test conditions	measured	φ = 51°		φ measured	
		N06	Eq. (4.48)	N06	Eq. (4.48)
T=5s,Uw=0.9m/s, r=0.22	1.0	1.4	1.4	1.0	1.2
T=5s,Uw=0.9m/s, r =0.25	1.3	1.4	1.4	1.0	1.2
T=5s,Uw=0.9m/s, r =0.62	1.7	3.4	1.7	1.5	1.8
T=7s,Uw=1.1m/s, r =0.16	1.0	1.3	1.3	1.0	1.1
T=7s,Uw=1.1m/s, r =0.31	1.2	1.9	1.7	1.2	1.4
T=7s,Uw=1.1m/s, r =0.45	1.8	2.9	2.4	1.5	1.8

On the other hand, both predicted maxima in the negative direction agree quite well with the measurements. The measured and predicted values of the ratio $|\tau_{max}/\tau_{min}|$ are listed in Table 4.6 for the whole set of experimental tests. It is shown that using $\varphi = 51°$ both methods generally overestimate the measured ratio. Figure 4.21c shows that using the measured phase-lead values significantly improves the predictions of bed shear stress maxima, except in the negative direction for Nielsen (1992, 2002) which now overestimates the measurements somewhat. The last two columns in Table 4.6 show that both methods present an overall much better agreement when the measured phase-lead is considered (for the measurements $26° \leq \varphi \leq 30°$). However, there is, not a predictor that is superior to the other: Nielsen (1992, 2002) represents better the lower ratio of $|\tau_{max}/\tau_{min}|$ and the new method tends to represent better the high measured ratios.

4.3.7 Validation to mobile beds - TRANSKEW data

This section presents a comparison between the new parameterisation and the results obtained in the previous chapter with the momentum-integral method and the Log-fit approach. As in Nielsen's method (Eq. (4.33)), the new parameterisation requires the knowledge of the phase-lead φ of the bed shear stress over the free-stream velocity. Since the TRANSKEW experiments involved accelerated-skewed flows under sheet flow conditions similar to Watanabe and Sato's (2004) experiments, it seems reasonable to use the same calibrated phase-lead parameter φ in Eq. (4.48), that is, $\varphi = 51°$. To compute the wave friction factor f_w one considers $k_s = 15d_{50}$ in Eq. (4.52) as suggested by the Log-fit approach (Figure 3.58).

Figure 4.22 shows the bed shear stresses for tests A1, A3, B2, B4 and C1. The dots are obtained with Log-fit approach and concern large values of the squared correlation coefficient $\left(cor^2 \geq 0.95\right)$. The new parameterisation generally agrees quite well with the momentum-integral method, differing from the Log-fit method. The bed shear stress for the Log-fit method is practically in phase with the free-stream velocity ($\varphi < 15°$) in contrast to the 51° used in the new parameterisation and roughly confirmed by the momentum-integral. For tests B2 and B4, despite the lack of a mean component of τ in the momentum-integral method, the shape of the bed shear stress agrees fairly well with the new parameterisation. Thus, the "optimal" value of 51° found by Nielsen (2006) and used in the new parameterisation has two contributions: one from the usual drag force component acting in sediment particles (corresponding to $\varphi = 0°$) and the other from the pressure gradient/free-stream acceleration (corresponding to $\varphi = 90°$). This agrees with the momentum-integral approach and is in agreement with Dick and Sleath's (1991) observations that the shear stress calculated from this methodology is mainly determined by the free-stream pressure gradient.

Another difference of the Log-fit method with the other approaches is the mismatch in the prediction of the magnitudes of τ, in particular, for the largest negative values. One observes that, similarly to the momentum-integral method, as discussed in Section 3.8.2, the new parameterisation leads to an increase of the ratio $\left|\tau_{max}/\tau_{min}\right|$. Figure 4.23 shows this ratio, using the new parameterisation (Eq. (4.48)) and that of Nielsen (Eq. (4.33)), as function of φ for pure sawtooth waves ($\phi = 0$). Two different values of r (0.3 and 0.5) are considered that correspond to acceleration skewness β of 0.65 and 0.75, close to those used in the TRANSKEW tests (A1 and A3). The two extreme values of φ, 0º and 90º, correspond to drag dominated sediment transport and to pressure gradient dominated scenarios like plug flows (Sleath, 1999). In analogy to Guard and Nielsen (2008), the increase of φ can be interpreted as a way to look further into the sheet flow layer. Figure 4.23 reveals that both parameterisations produce an increase of the ratio $|\tau_{max} / \tau_{min}|$ with increasing φ. This agrees with the log-law where small values of φ leads to $|\tau_{max}| \approx |\tau_{min}|$ and with the momentum-integral approach where higher values of φ result in $|\tau_{max}| > |\tau_{min}|$. The parameterisations also show that the increase of acceleration skewness β enhances the ratio $|\tau_{max} / \tau_{min}|$, in agreement with van der A et al.'s (2011) fixed bed experiments. Still, there are some differences between the results of Eq. (4.33) and Eq. (4.48): the concavity of the curves is different, producing very strong ratios of $|\tau_{max} / \tau_{min}|$ for Nielsen's approach with large values of φ. This would result in significant differences whenever the formulations are extended to sediment transport predictions, particularly, for large phase-leads φ.

Moreover, the skewness of τ was also evaluated according to:

$$\mu_{3,\tau} = \frac{1}{T}\int_0^T \frac{(\tau - \overline{\tau})^3}{\sigma_\tau^3}\, dt\,, \tag{4.53}$$

where $\overline{\tau}$ and σ_τ represent, respectively, the mean component and standard deviation of τ. Eq. (4.53) enters with the time series of τ, allowing a more complete comparison between the momentum-integral and the new bed shear stress parameterisation.

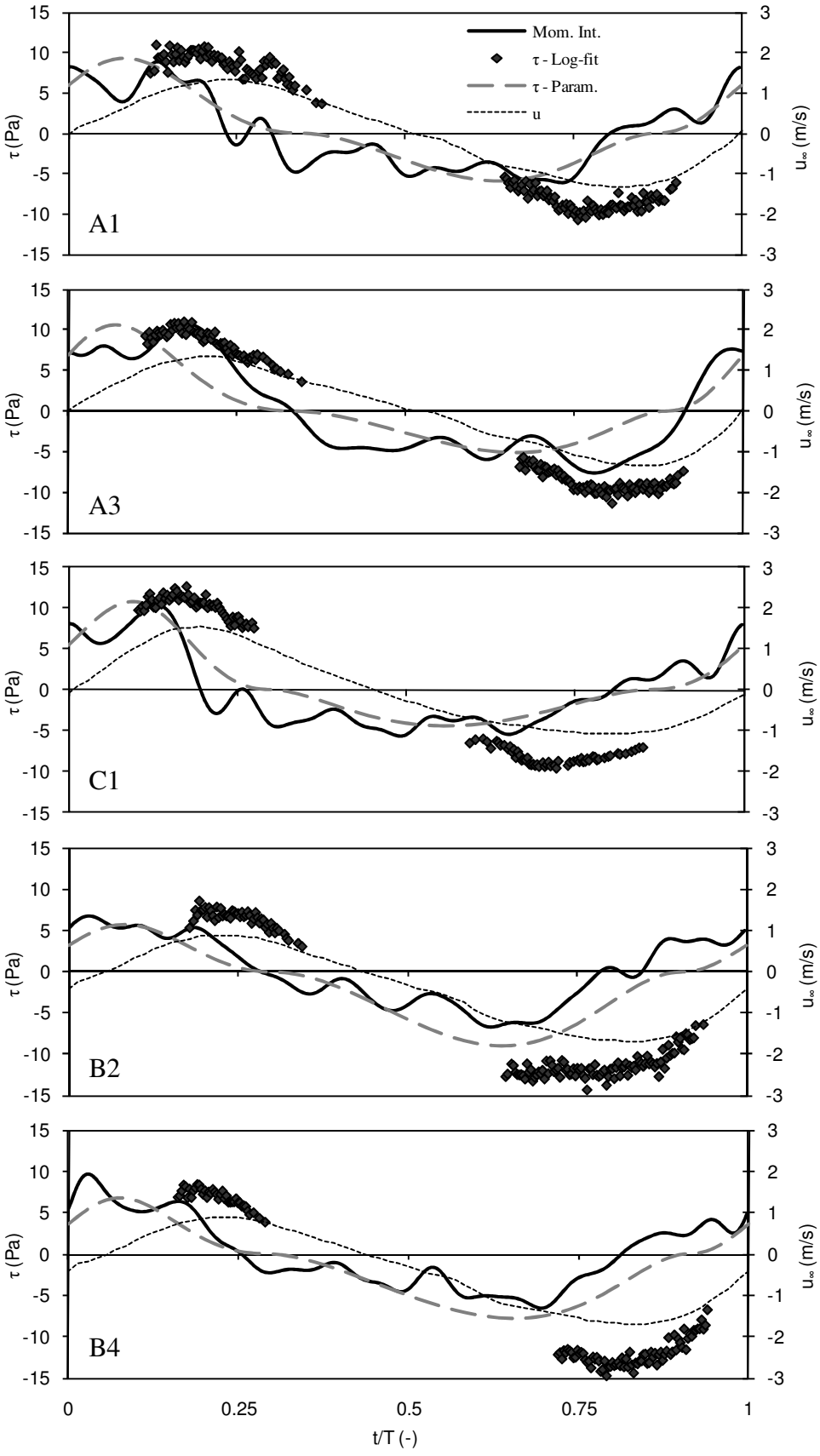

Figure 4.22 – Time series of the bed shear stress computed with the Log-fit method (dots), momentum-integral (solid line) and the new parameterisation (dashed line) for tests A1, A3, C1, B2 and B4.

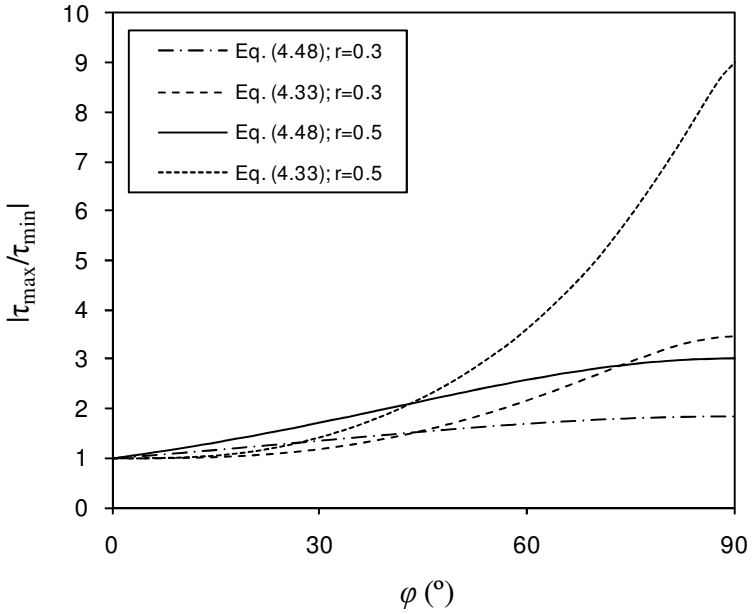

Figure 4.23 – Ratio $|\tau_{max}/\tau_{min}|$, using Eq. (4.48) and Eq. (4.33) as function of φ. The results are obtained for pure sawtooth waves ($\phi = 0$) using $r = 0.3$ and 0.5.

Figure 4.24 shows the results for the five test conditions obtained with the momentum-integral approach and with the new formulation (Eq. (4.48)) using two values of φ: $\varphi = 15º$ (blank symbols) and $\varphi = 51º$ (filled symbols). The introduction of $\varphi = 15º$ in Eq. (4.48) results in a poor performance of the new parameterisation to obtain estimates of $\mu_{3,\tau}$. Undoubtedly, the "optimal" value of $\varphi = 51º$ confirms better estimates of $\mu_{3,\tau}$ for all five conditions. With the exception of tests B2 and B4, the points practically lie over the line of perfect agreement. The differences obtained for these two tests are to be expected because the mean component of τ is not reproduced with the momentum-integral method. Therefore, the results confirm that the calibration value of 51º seems adequate to be used and that Eq. (4.48) provides a good characterisation of the bed shear stress skewness for the present mobile bed experiments.

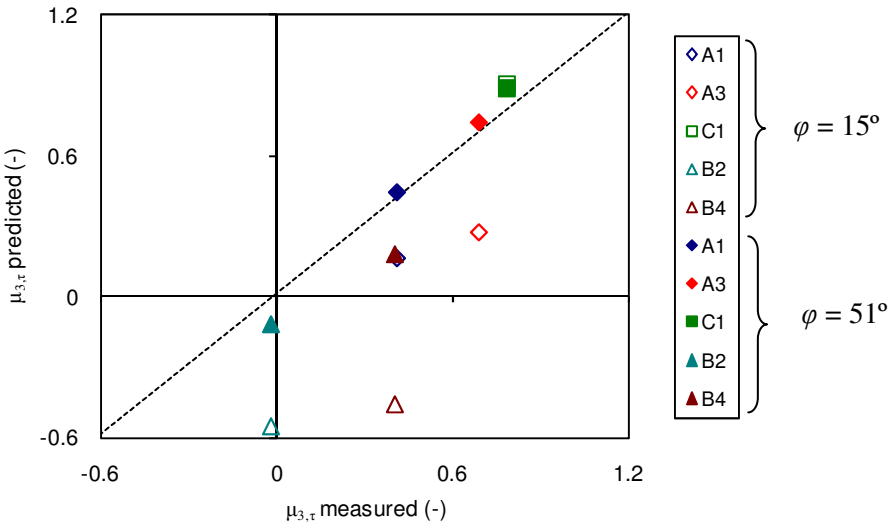

Figure 4.24 – Skewness of τ ("measured" means with momentum integral, "predicted" is the new formulation Eq. (4.48): blank symbols are for φ = 15° while filled symbols are for φ = 51°).

4.3.8 Partial conclusions

In this section, several simple bottom shear stresses parameterisations found in the literature are investigated and applied to the TRANSKEW data set. The methods proposed by Nielsen (1992, 2002), Tanaka and Samad (2006), Gonzalez-Rodriguez and Madsen (2007), Suntoyo et al. (2008) and Terrile et al. (2009) are employed. For small values of the phase-lag, φ, an overall good agreement between each other was found with the exception of Terrile et al. (2009). Larger values of φ enhance the discrepancies between the methods, reflecting the differences introduced by the incorporation of both velocity and acceleration terms, the inclusion of time-varying friction factors or time-varying phase differences.

For the accelerated skewed waves (Series A), all the methods predict an increase in the asymmetry of bottom shear stress with the acceleration skewness parameter in accordance to Chapter 3 and van der A et al. (2011). This is reflected in the ratio $|\tau_{max}/\tau_{min}|$ that arises for larger values of φ with the exception of Tanaka and Samad's (2006) method. This kind of asymmetry can cause net sediment transport rates and, as suggested by Nielsen (1992, p. 128), it may be that the bedload transport lags slightly behind the bed shear stress. Thus, for sediment transport purposes, it can be reasonable to introduce large values of φ.

Furthermore, slight reductions in the magnitudes of the shear stresses are noticed when increasing the wave period. Also, the differences between the shear stress under both half cycles decrease with an increase in the wave period.

For the oscillatory flows with both velocity- and acceleration- skewness (Series C), the methods show that the velocity skewness parameter has a much greater interference on the time-mean shear stress than the acceleration skewness. In addition, the velocity skewness parameter induces a considerable reduction of the peak values under the trough in detriment with the peak values under the crest. The ratio $|\tau_{max}/\tau_{min}|$ is higher for the parameterisations of Nielsen (1992, 2002) and Terrile et al. (2009), but the last method leads to secondary peaks in the positive direction. This limitation is corrected with the new formulation, revealing a small decrease of the ratio $|\tau_{max}/\tau_{min}|$ when compared to its preceding formulas.

This new formulation generalises Terrile et al. (2009) work for more general oscillatory flow conditions. The parameterisation shows that, beside acceleration effects, the shape of the wave, described through the two parameters (r, ϕ), can be considered in the instantaneous shear stress computations, bringing in more physics.

The new expression together with Nielsen's (1992, 2002) original approach are also compared to bed shear stress measurements for acceleration-skewed flows over fixed rough beds and mobile beds. The fixed bed experiment was performed by van der A et al. (2011) and concerns a recent experimental study in the Aberdeen Oscillatory Flow Tunnel (AOFT). It is shown that using the phase-lead between the shear stress and the corresponding free-stream velocity $\varphi = 51°$, as recommended by Nielsen (1992, 2002), gives a better agreement for the new formulation. However, both methods generally overestimate the measured ratio of $|\tau_{max}/\tau_{min}|$. Using the measured phase-lead values (26º), the predictions of bed shear stress maxima are significantly improved for both formulations. However, based solely on the ratio of $|\tau_{max}/\tau_{min}|$ there is not a predictor that is overall superior to the other.

For the mobile bed experiment (TRANSKEW), it is shown that using the roughness $k_s = 15d_{50}$ and using the default value of the phase lead of bed shear stress over the free-stream velocity, $\varphi = 51°$, the new formulation is in good agreement with the momentum-integral approach. A sensitivity analysis illustrates that different values of φ produce differences in the ratio $|\tau_{max}/\tau_{min}|$. Under accelerated-skewed waves, small values of φ indicate $|\tau_{max}| \approx |\tau_{min}|$ in accordance to the Log-law and higher values of φ show $|\tau_{max}| > |\tau_{min}|$ in accordance to the momentum-integral approach. These observations are linked to the weightings of the drag forces and pressure gradients introduced by φ in the new parameterisation and suggest that the differences found between the log-fit and momentum-integral approach might be due to the fact that the "bed" shear stress estimates are referenced to different elevations.

The present results suggest that most of the existent formulations predict adequately the bed shear stress for rigid bottoms. In such cases, the drag forces are usually associated to flow velocities. However, for mobile beds, the factors that contribute for bottom shear stress present new components, especially within the mixture of sand and water, where pressure gradients also become important. First steps are being done to understand these processes and the bed shear stress formulations are being developed for this purpose. The one developed here represents a step to achieve this goal.

Moreover, expressing the bed-shear stresses in terms of the wave shape is of particular interest for modelling the sediment transport induced by shoaling waves. In the next section the new parameterisation is combined with sediment transport formulae and applied to different data sets. In the future, the formula can be useful for the implementation in process-based 2D and 3D near shore sediment transport models.

4.4 Sediment Transport

4.4.1 Introduction

The recognition of the importance of wave asymmetry to nearshore sediment transport has also motivated the development of practical sand transport models including this process (Drake and Calantoni, 2001; Hoefel and Elgar, 2003; Nielsen, 2006; Silva et al., 2006; Gonzalez-Rodriguez and Madsen, 2007; van Rijn, 2007) and numerical studies with detailed bottom boundary layer models (Drake and Calantoni, 2001; Hsu and Hanes, 2004; Ruessink et al., 2009). The practical models are extensions of well-known previous formulations (e.g., Meyer-Peter and Müller, 1948) and describe the effect of wave asymmetry in sediment transport by either considering an increase of bed shear-stress induced by the large flow accelerations, as suggested by Nielsen (1992), or through the inclusion of the free-stream acceleration directly. The more sophisticated process-based models allow examining in more detail the physical mechanisms underlying the effect of wave shape on sediment transport.

Sediment transport models based on the statistical moments of the free-stream orbital velocity, u, (e.g. Bailard, 1981) are unable to simulate adequately the observations of net transport rates in asymmetric waves (e.g., Silva et al., 2006). The previous section suggests that in order to reproduce accurately the net transport rates in acceleration-skewed oscillatory flows, the transport models should be able, at least, to account for the skewed bed shear-stress. This section compares predictions of 5 models to the TRANSKEW measured net transport rates. The comparison contains four recent practical models and a more complex model resolving the bottom boundary layer hydrodynamics. The practical models are based on existing modelling concepts (Meyer-Peter Müller, 1948; Bailard, 1981; Dibajnia and Watanabe, 1992), but are each modified to account for acceleration skewness in a different way. These formulations are briefly described in the following. The input of these models is the free-stream velocity time-series synthesized using Equation (4.8) and the parameters listed in Table 3.1.

In addition, the new bed shear stress predictor presented in Section 4.3 is incorporated in the quasi-steady bed load formulation of Nielsen (2006), providing a new transport rate model, and the transport rate predictions are compared with measurements in other oscillating water tunnels.

4.4.2 Existing sediment transport models

Drake and Calantoni (2001) – DC01; Hoefel and Elgar (2003) – HE03

Drake and Calantoni (2001) have suggested a modification of the classical formulations of the energetics-type sediment transport models (Bailard, 1981), suitable for application to field measurements of nearshore fluid motion, through the inclusion of an additional term, q_{ba}, representing acceleration effects. According to Drake and Calantoni, the bed load is given by:

$$q_b = k_b \left\langle \left| u(t) \right|^3 \right\rangle + q_{ba} \tag{4.54}$$

$$q_{ba} = \begin{cases} K_a \left(a_{spike} - a_{cr} \right) & , a_{spike} > a_{cr} \\ 0 & , a_{spike} < a_{cr} \end{cases} \tag{4.55}$$

In Equation (4.54) $a_{spike} = \left\langle a^3 \right\rangle / \left\langle a^2 \right\rangle$, and a_{cr} is the critical value of a_{spike} that must be exceeded before acceleration enhances transport. The parameter k_b represents all constants in the Bailard (1981) equation with standard values including the friction coefficient. The values of K_a and a_{cr} were determined by fitting the computed sediment transport rates with the ones obtained with a discrete-particle model simulations in sheet flow, yielding: $K_a = 2.64 \times 10^{-5}$ ms and $a_{cr} = 1$ m/s^2.

Hoefel and Elgar (2003) have extended Equation (4.54) to account for random waves and take into account the sign of a_{cr}. Through the comparison of model results with field observations of sandbar migration (Duck94 field data) they have determined the optimal values of $K_a = 1.4 \times 10^{-4}$ ms and the critical threshold $a_{cr} = 0.2$ m/s^2. As shown in Silva et al. (2007) and van der A et al. (2010) the DC01 net transport results are systematically lower than HE03; due to the similarity between the two formulations and because the HE03 model has previously shown a good fit to the present experimental results (Abreu et al., 2008) only the HE03 results are presented. The suspended load, q_{ss}, was also computed according to Bailard (1981)

$$q_{ss} = k_{ss} \left\langle \left| u(t) \right|^3 u(t) \right\rangle \tag{4.56}$$

and added to Equation (4.54) to give the total transport. The parameter k_{ss} represents all constants in the Bailard (1981) equation with standard values, also including the friction coefficient.

Silva et al. (2006) – S06

Silva et al. (2006), based in the work of Dibajnia and Watanabe (1992), developed a semi-unsteady, practical model, to predict the total sediment transport rates in wave or combined wave-current flows. The predicted non-dimensional transport rates, Φ, are computed from:

$$\Phi = \frac{q_s}{\sqrt{(s-1)gd_{50}^{\ 3}}} = \upsilon \left|\Gamma\right|^{\gamma} \frac{\Gamma}{\left|\Gamma\right|} \tag{4.57}$$

with

$$\Gamma = \frac{u_c T_c (\Omega_c^3 + \Omega_t'^3) - u_t T_t (\Omega_t^3 + \Omega_c'^3)}{2(u_c T_c + u_t T_t)}. \tag{4.58}$$

In these equations ρ and ρ_s are the water and sediment density, respectively, $s = \rho_s/\rho$, g is the gravitational acceleration, T_c and T_t are the time duration of the positive and negative half cycle of the near bed velocity, respectively, with equivalent velocities u_c and u_t (the subscript c stands for crest and t for trough). The quantities Ω_i and Ω_i' (i = c, t) represent the amount of sediment that is entrained, transported and settled in the i half cycle, and the amount of sediment still in suspension from the i half cycle that will be transported in the next half cycle, respectively. The values of Ω_i and Ω_i' are computed from the bed shear-stress:

$$\Omega_i = (\theta_i - \theta_{cr}) \min\left(1; \frac{\omega_{cr}}{\omega_i}\right), \tag{4.59}$$

$$\Omega'_i = (\theta_i - \theta_{cr}) \max\left(0; 1 - \frac{\omega_{cr}}{\omega_i}\right). \tag{4.60}$$

where the parameter ω_i depends on the ratio between the settling time of the sediment particles and the duration of each half cycle and θ_i represents the shields parameter at each half cycle. If ω_i exceeds a threshold limiting value, ω_{cr}, part of the sediment that is entrained during the i half cycle remains in suspension and is carried into the opposite direction by the velocity of the succeeding cycle.

The friction factor is determined from Swart (1974) formula at each half-cycle considering that the wave period in the semi-orbital excursion is equal to four times the time of peak velocities. This results in an enhanced bed shear stress in the positive half-cycle of u(t) and a decrease during the negative half-cycle. A total bed roughness with the grain related and sediment transport component is considered in the computations as described in Silva et al. (2006). The phase-lag effects are taken into account through the exchange of sediment fluxes between the two half cycles (Ω_i' quantities). υ and γ

are two empirical constants; their best values were determined by fitting the predictions to a large data set of measured transport rates, yielding υ = 3.2 and γ = 0.55.

Nielsen (2006) – N06

The instantaneous sheet flow sediment transport rate is estimated through an adapted Meyer-Peter Müller type formula:

$$\Phi(t) = 12\left[\theta(t) - \theta_{cr}\right]\sqrt{\theta(t)}\,\frac{u_*}{|u_*|},\ \theta > \theta_{cr} \tag{4.61}$$

with θ_{cr}=0.05. The Shields parameter, $\theta(t) = u_*^2(t)/\left((s-1)\,gd_{50}\right)$, is computed with the sediment mobilization velocity, u_*(t), corresponding to Equation (4.33).

Gonzalez- Rodriguez and Madsen (2007) – GRM07

Gonzalez-Rodriguez and Madsen (2007) proposed a conceptual model to compute bed load transport rates in asymmetric and skewed waves. The formulation, used for waves without superimposed net currents, computes bed shear stresses using a time-varying friction factor, $f_w(t)$, and a time-varying phase lead, $\varphi(t)$, that accounts for the variability in the wave shape. The use of a variable friction factor over the wave period is justified by examining the physics of the boundary layer. The values of f_w are calculated at the wave crest and at the wave trough following S06, and are then assumed to be linearly interpolated for the rest of the wave phases.

Following Madsen (1993), the non-dimensional transport rate is computed from:

$$\Phi(t) = \frac{8}{\cos\beta_s\,(\tan\phi_m + \tan\beta_s)}\max\left(0, \theta(t) - \theta_{cr}\right)\left[\theta(t)^{1/2} - \alpha_{\beta_s}\theta_{cr}^{1/2}\right]\frac{u_*}{|u_*|} \tag{4.62}$$

with

$$\alpha_{\beta_s} = \sqrt{\frac{\tan\phi_m + \tan\beta_s}{\tan\phi_s + \tan\beta_s}}\,. \tag{4.63}$$

The parameter β_s represents the bottom slope and ϕ_s and ϕ_m are, correspondingly, the values of the angles of static and moving friction. Recently, Gonzalez-Rodriguez (2009) referred to the fact that the bottom roughness, k_s, used in the wave friction factor, significantly affects the magnitude of the predicted values, assuming that $k_s = d_{50}$ provide good results for the predictions in velocity-skewed oscillatory flows. However, in the cases of acceleration skewed oscillatory flows the results become

severely under predicted. In this case, it is suggested to calculate the total sheet flow roughness through Herrmann and Madsen's (2007) formula (Eq. (3.56)).

1DV model – R09[2]

In addition to the practical sand transport models above, the predictions of a 1DV process-based model are compared to the data. This will highlight whether a more complicated model does indeed outperform the practical models.

The 1DV model applied here is described in detail in Uittenbogaard et al. (1999), Ruessink et al. (2009) and Hassan and Ribberink (2010). It is based on the linearized Reynolds-averaged momentum equation to simulate time-dependent vertical profiles of horizontal flow u(z):

$$\frac{\partial u}{\partial t} = -\frac{1}{\rho}\frac{\partial p}{\partial x} + \frac{\partial}{\partial z}\left\{(\nu + \nu_T)\frac{\partial u}{\partial z}\right\}. \tag{4.64}$$

Here, ν_T represents the eddy viscosity defined as $\nu_T = 0.09k^2/\varepsilon$, where k stands for turbulent kinetic energy and ε for its dissipation. A k-ε model for turbulence closure was applied (Rodi, 1987), containing sediment-flow interaction by the time-varying suppression of turbulence by gradients in suspended sediment concentration.

The advection-diffusion equation is used to predict concentration profiles c(z):

$$\frac{\partial c}{\partial t} = \frac{\partial}{\partial z}\left(w_s c + \varepsilon_s \frac{\partial c}{\partial z}\right), \tag{4.65}$$

where ε_s is the sediment diffusivity defined as ν_T / σ_T, being σ_T the Prandtl-Schmidt number. The sediment fall velocity w_s is parameterised as proposed by Van Rijn (1993), with a correction for hindered sediment settling in large sediment concentrations following Richardson and Zaki (1954).

The sediment boundary condition is computed from a pick-up formulation

$$w_s c_b + \varepsilon_s \left.\frac{\partial c}{\partial z}\right|_{z=z_a} = 0 \tag{4.66}$$

[2] The results obtained with this model were made available by B.G. Ruessink.

that includes the reference concentration, c_b, of Zyserman and Fredsøe (1994) at a reference height z_a ($z_a = 2d_{50}$).

The model contains two free parameters: (1) the Prandtl-Schmidt number σ_T, which is the ratio of the eddy viscosity to the sediment diffusivity, and (2) the roughness length z_0. In the simulations presented here, the default values of $\sigma_T = 0.7$ and $z_0 = 2.5d_{50}/30$ were used.

The 1DV model was run in the same configuration as in Ruessink et al. (2009). In all cases this implies that the model contained 100 (u,c) cells, with an exponential increase in thickness (or spacing) with increasing distance from the bed. For series A and C, the free-stream velocity was described at the top of the flow domain (= 0.15 m above the bed) with the condition of no depth-averaged mean flow (i.e., continuity) in the entire domain. This condition was imposed to ensure an accurate description of the vertical structure of the mean flow, see Ruessink et al. (2009) for details. For series B, the measured free-stream velocity was used as upper velocity boundary condition. The model was initialized with small positive values for turbulence and flow quantities and then run for 91 regular waves, by which time the effect of the initial values had well disappeared from the model output. The instantaneous sediment flux profiles of the last wave were depth-averaged and time-integrated to yield the net sediment transport rate for each simulation.

4.4.3 Comparison of existing models with TRANSKEW data

The predicted net sediment transport rates from the models described earlier are compared in Figure 4.25 against the TRANSKEW experimental data. The dashed lines in Figure 4.25 define a region where the predicted transport is within 50 and 200% of the measured transport. The presented GRM07 solution considers Herrmann and Madsen's (2007) formula to compute the total roughness for Series A, $k_s = d_{50}$ for C3, while for C1 and C2 test conditions the bed roughness was computed from the two above hypothesis, corresponding to the pair of solutions in Figure 4.25d.

To analyse the performance of each model, the skill defined as the ratio between the mean standard deviation between the computed, q_s, and the measured values, q_{sc}, and the root mean square value of q_{sc} was evaluated:

$$S_q = 1 - \sqrt{\frac{\sum_{k=1}^{M}\left(q_{s,k} - q_{sc,k}\right)^2}{\sum_{k=1}^{M} {q_{sc,k}}^2}}, \tag{4.67}$$

where M corresponds to the number of conditions. The results of S_q are presented in Table 4.7 separately for the oscillatory data in Series A and C and for combined wave-current condition in Series B. Model skill is maximum and equal to 1 when there is a perfect agreement between the computations and the observations. If $S_q = 0$, the error is as large as the root-mean-square of q_{sc}.

Table 4.7 – Model skill

Condition	HE03	S06	N06	GRM07	R09
A1 – A4; C1 – C3	0.82	0.95	0.93	0.25/0.69	0.98
B1 – B4	0.88	0.48	0.68	-	0.95

The models are generally able to predict the net transport rates within a factor of 2 in almost 100% of the observations with the exception of GRM07 (see Figure 4.25). The comparison shows that the 1DV model performs generally better (see Table 4.7). It is followed by S06 and N06 models which also give very good results. The model of HE03 appears to slightly overestimate the measured transport rates. The GRM07 results illustrate the dependence of this formulation on the bed roughness coefficient specified. For the acceleration-skewed oscillatory flow data A1-A4, and C3 test the predictions are similar to the observations (see Figure 4.25d), whereas in the combined velocity and acceleration skewness conditions, C1 and C2, none of the bed roughness values considered leads to satisfactory results, either under-predicting ($k_s = d_{50}$) or over-predicting (k_s given by Eq. (3.56)) the observations. The corresponding values of S_q given in Table 4.7 are, respectively, 0.69 and 0.25.

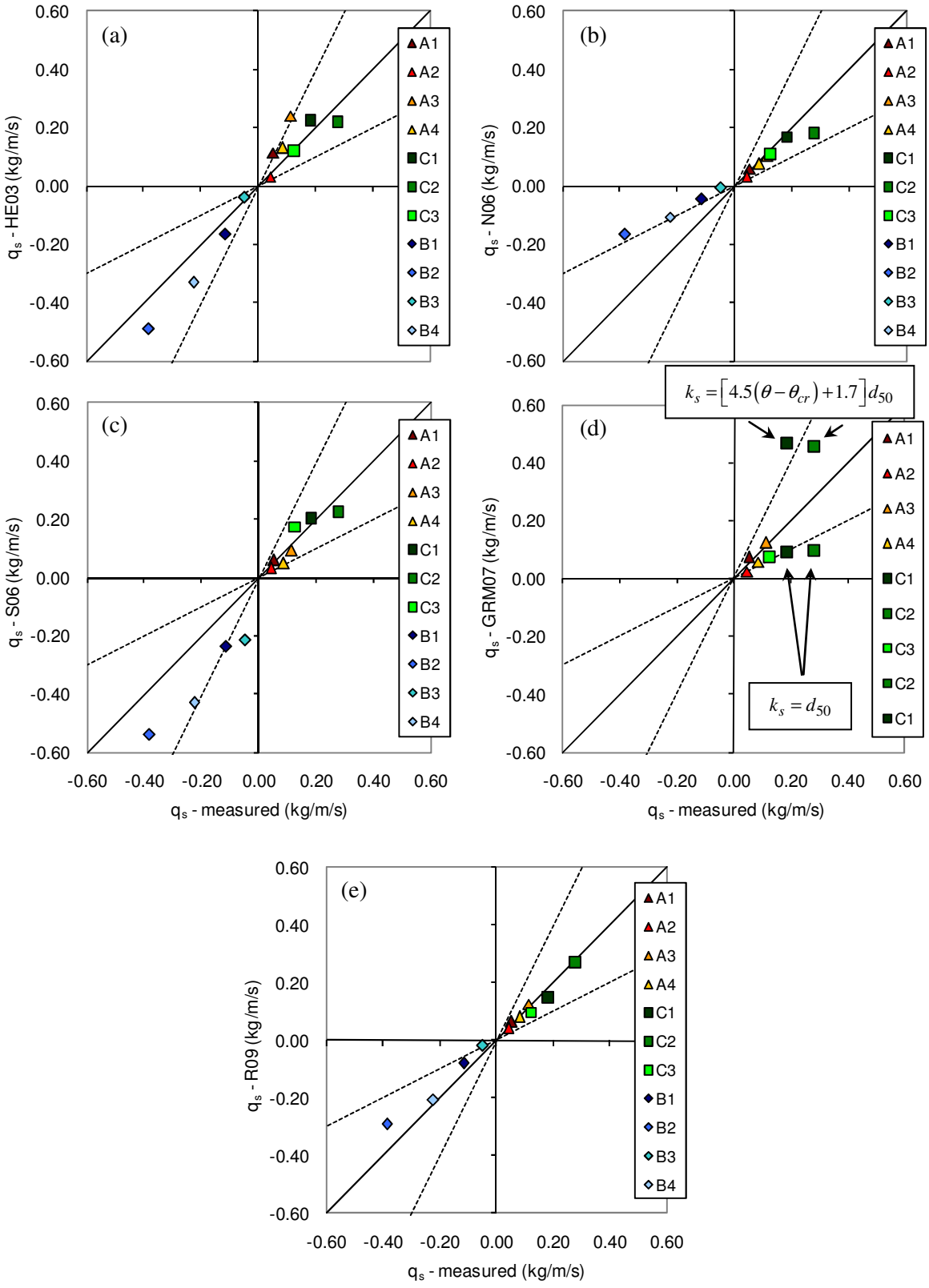

Figure 4.25 – Comparison between predicted and measured net transport rates: (a) HE03; (b) N06; (c) S06; (d) GRM07 and (e) R09.

Further, the predicted net transport rates are showed as a function of β, R, and U_0 in Figure 4.26 (for the conditions with $T = 7$ s). In Figure 4.26b, for the GRM07 solution, only the one corresponding to $k_s = d_{50}$ is presented.

For the oscillatory flow conditions (Series A and C) the trends of the experimental data in terms of β, R and T described in Section 3 are well reproduced by the models. As depicted in Figure 4.26a,b all the models predict an increase of q_s with β and R . However, for the C1 condition, with both velocity and acceleration skewness, the predictions are less accurate than for the other experimental conditions.

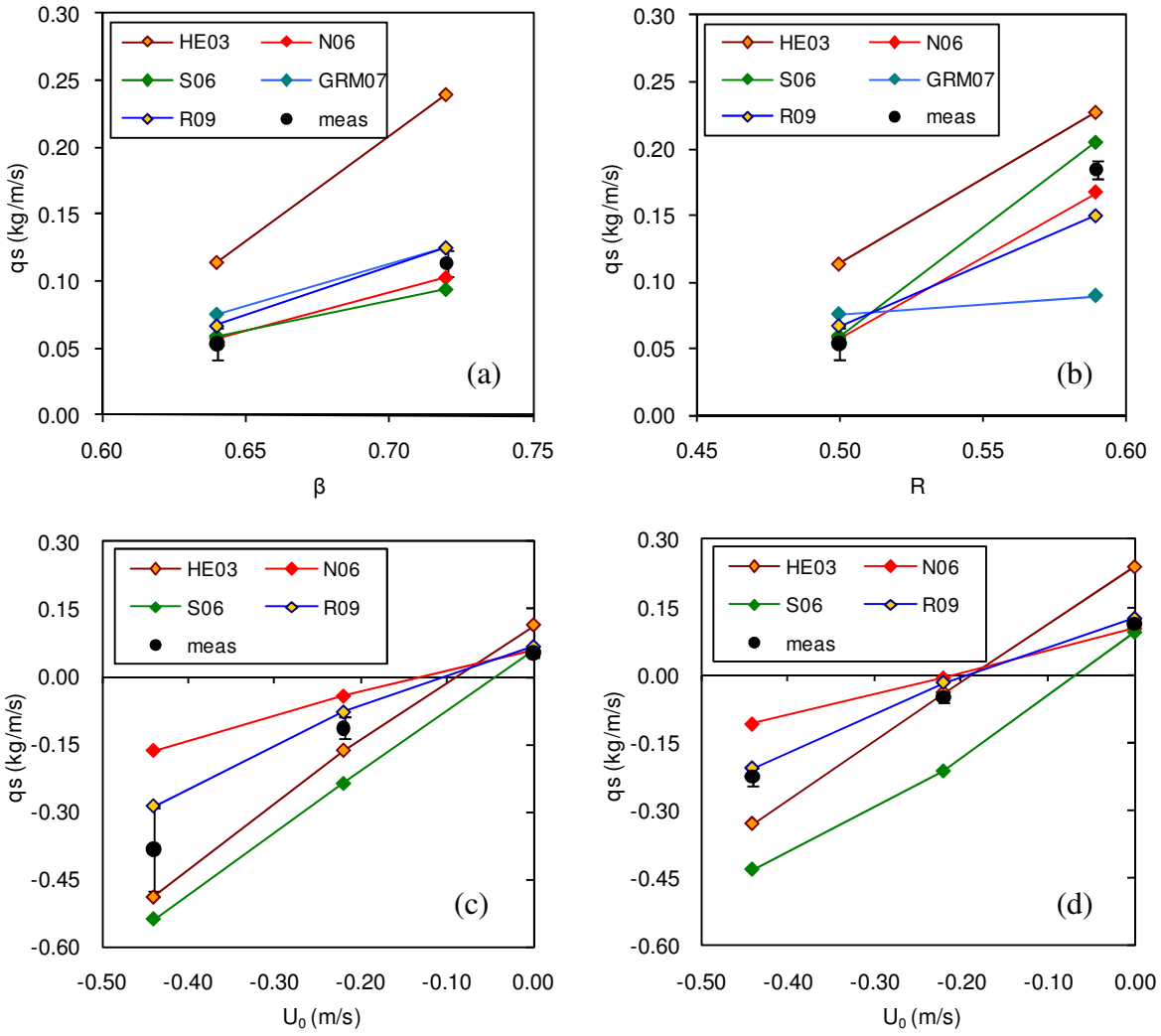

Figure 4.26 – Predicted and measured net transport rates for $T = 7$s as a function of (a) β (A1, A3); (b) R (A1, C1) ;(c) U_0 (A1, B1, B2 -$\beta = 0.64$) and (d) U_0 (A3, B3, B4 - $\beta = 0.71$).

The Brier Skill Score computed by van der A el al. (2010) for different sediment transport formulations for the AOFT experiments with fine sand (0.15 mm) agrees with the present results for the S06 and N06 models. However, different results are obtained here for HE03 and GRM07. The

differences in GRM07 results can be explained because the calculations of van der A el al. (2010) were made with $k_s = d_{50}$, based on the Gonzalez-Rodriguez and Madsen (2007), while one has considered the total roughness given by Herrmann and Madsen's (2007) as described in Gonzalez-Rodriguez (2009). The overall poor performance of the HE03 formulation as described in van der A et al. (2010) is not found here, although in their application the HE03 formulation also over-predicts the observations. The good agreement for HE03 might, at least to some extent, be the result of the empirical parameters K_a and a_{cr} in Eq. (4.55), which were calibrated for field data collected in the inner and outer surf zone, where net currents against the wave direction (undertow) are present.

In the presence of a net current (Series B) all the models predict a negative transport, i.e., in the net current direction, and reproduce the observed tendency of q_s becoming more positive for increasing values of β. Most models show some shortcomings: they either systematically under predict (N06 and 1DV) or over predict (HE03 and S06) the magnitude of the measured transport rates. Note also that it was pointed in the previous chapter that the accuracy of the measurements is lower for B1-B3. The 1DV and HE03 models have higher skills and, as depicted in Figure 4.25a,e, their predictions are close to the experimental results. The largest discrepancies are found for B3, but note that the observed net transport is quite small. The fact that the N06 predictions are smaller than the measurements is most likely related to the absence of the suspend load contribution in Equation (4.61), which may be more important for the combined oscillatory flow-current conditions. Similar behaviour was found by Nielsen (2006) for the Watanabe and Sato (2004) data (U_0 = -0.2 m/s tests for which the net transport is negative). However, a comparison with Watanabe and Sato (2004) data is not straightforward as the small flow periods of T = 3 s will probably induce larger phase lag effects at flow reversal. As for the S06, the numerical results over-predict the observed transport rates. Silva et al. (2006) also showed that their formulation does not perform as well in the combined oscillatory flow-current tests of Watanabe and Sato (2004) compared to oscillatory flow data.

Among the sediment transport models considered here, only the 1DV model describes explicitly the phase lag effects between the sediment concentration and flow velocity at flow reversal, while S06 takes this process into account but indirectly. For the present tests of sawtooth waves, Ruessink et al. (2009) numerical results with d_{50} = 0.2 mm (Figure 5 in their paper) indicate that the net transport rates are not only related to the skewness of the bed shear-stress but also that phase lag effects contribute to the net positive transport rate, albeit marginally for $d_{50} > 0.2$ mm. For the present tests, the S06 model predicts that the phase lag effects lead to a positive increment in q_s of 17% for A3, B3 and B4 tests and a small contribution of 5% in B2. For the Series A data, this minor phase-lag contribution is qualitatively consistent with the results in Ruessink et al. (2009) and explains the good performance

obtained here with the quasi-steady N06 model. For Series B, the phase lag effects become more important as suggested by S06, and therefore the models of N06 and HE03 are not expected to behave as well as the R09 and S06 models. This is partly verified here, as the R09 models attains a higher skill than the other models, but for the S06 model, although the phase lag effects contribute to a positive q_s, their importance appear to be larger than suggested from the S06 model. Van der A et al. (2010) indicated that phase lag effects in the S06 model are invoked to a limited extend for fine sands, despite their data suggesting otherwise. They note that increasing the overall importance of the phase lag contribution to the net transport rate leads to better overall agreement, which also follows from the present results.

4.4.4 Improved model

The improvement of the bed shear-stress parameterisations in nonlinear flows is thought to improve further the predictive skill of the practical models. Thus, the new bed shear stress predictor (Eq.s (4.48) and (4.51)) is incorporated in the bed load formulation of Nielsen (2006) (Eq. (4.61)), using Nielsen's (1992) formulation to compute the wave friction factor (Eq. (4.52)). This formula is alternative to Swart's (1974) one, used in S06, and to Tanaka and Thu's (1994) (Eq. (4.42)).

Comparison with TRANSKEW data

To compute the wave friction factor two different equivalent roughnesses are assumed in Eq. (4.52): $k_s = 15d_{50}$ and $k_s = 2.5d_{50}$. The latter equivalent roughness is commonly used in sediment transport computations and was shown to produce good results in Nielsen's (2006) formula, whereas the former might be related to sheet flows as discussed above. A constant value for the phase-lead parameter of $\varphi = 51°$ is employed in both transport rates estimates.

Figure 4.27 shows a comparison between predicted and measured net transport rates inserting Eq. (4.33) and Eq. (4.48) to compute $u_*(t)$. The results are referred to as N06 and New, respectively. The panels (a) and (b) use $k_s = 2.5d_{50}$ for the roughness and the panels (c) and (d) use $k_s = 15d_{50}$. Focusing on panel (a) one observes that N06 predictions reproduce well the measurements for the pure oscillatory flows (conditions A and C). However, the results of the combined oscillatory flow-current conditions are under predicted. Panel (b) shows a good linear trend for the overall data, but the small roughness leads to results under predicted by a factor of 2. Introducing the roughness $k_s = 15d_{50}$ improves N06 predictions for the combined oscillatory flow-current conditions (panel (c)), but leads to over-predict the transport for the pure oscillatory flow conditions. Finally, the best agreement between

measured and predicted transports is obtained with the new parameterisation for $k_s = 15d_{50}$ (Figure 4.27d).

Apparently there are not major improvements using the new bed shear stress estimator (Eq. (4.48)) when compared to the original method of Nielsen (2006). The tests without currents (Series A and C) are now under predicted by a factor of 2, whereas, in Figure 4.25b, most of the points lie over the line of perfect agreement. Nonetheless, the results in Figure 4.27d show a better linear trend also to Series B. It seems that a simple rotation of the predicted q_s would yield good results for the overall data. The corresponding values of S_q are equal to 0.91 for the tests without currents (A1 – A4; C1 – C3) and 0.97 for the tests with currents (B1-B4).

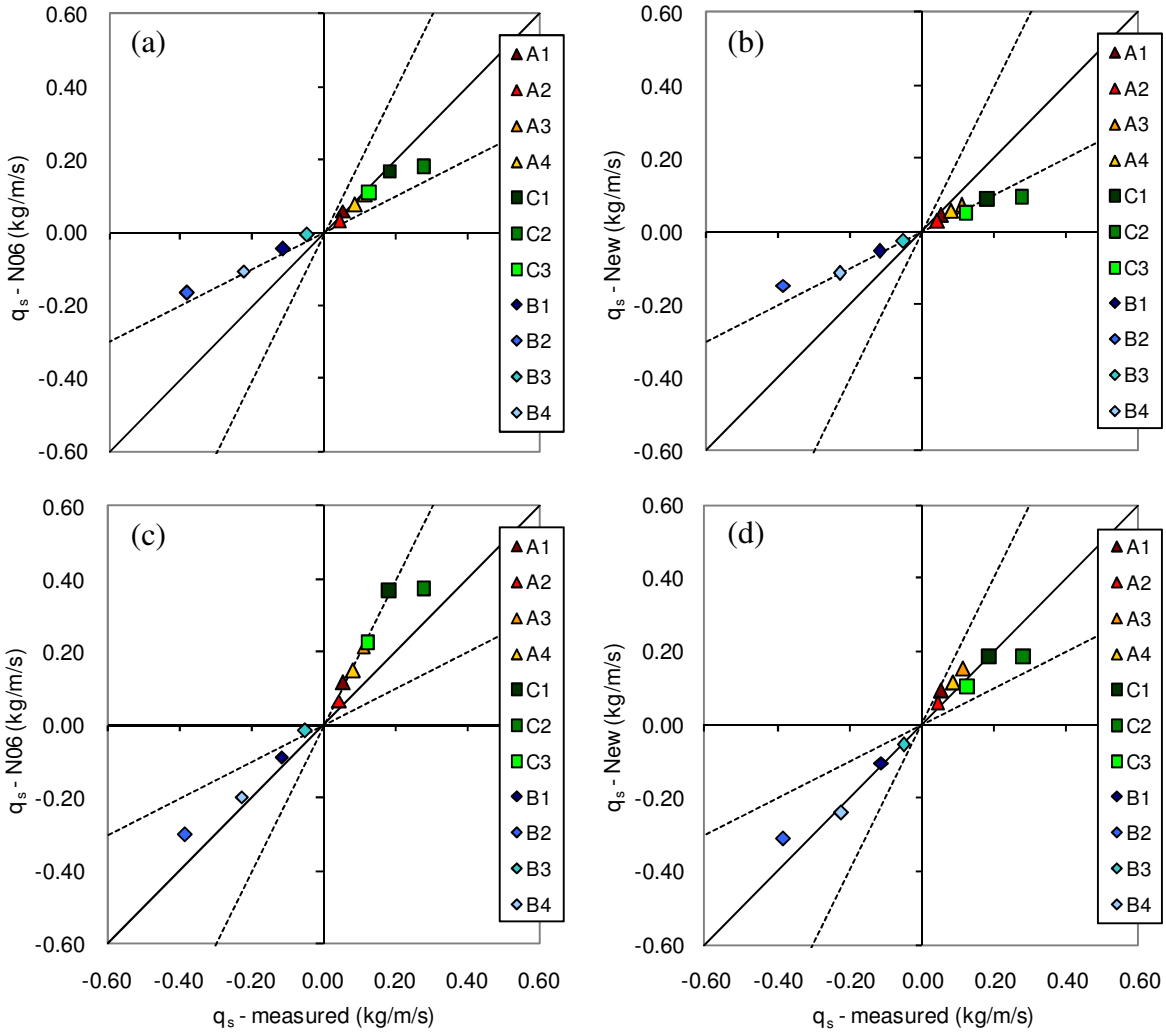

Figure 4.27 – Comparison between predicted and measured net transport rates assuming for $u_*(t)$: (a) N06 - Eq. (4.33) with $k_s = 2.5d_{50}$; (b) Eq. (4.48) with $k_s = 2.5d_{50}$; (c) N06 - Eq. (4.33) with $k_s = 15d_{50}$ and (d) Eq. (4.48) with $k_s = 15d_{50}$, using $\varphi = 51°$.

Comparison with other data

Watanabe and Sato (2004) performed experiments with two different median grain sizes (d_{50} = 0.20 and 0.46 mm). However, the coarse grain data of Watanabe and Sato (2004) was discarded for this analysis because it presents inconsistencies (Gonzalez-Rodriguez and Madsen, 2007).

Van der A et al. (2010) experiments involved three different median grain sizes (d_{50} = 0.15, 0.27 and 0.46 mm). Their oscillatory flows also contained a small degree of velocity skewness, which was taken into account in the new formulation through r and ϕ.

Accordingly, Figure 4.28 and Figure 4.29 show the results of the predicted q_s using Nielsen's bed shear stress model (left panel) and the new bed shear stress predictor (right panel) for Watanabe and Sato (2004) and van der A et al. (2010) data with $k_s = 2.5d_{50}$. Regarding the estimates of the net transport rates, the results clearly confirm that the introduction of $S(t,\phi,r)$ given by Equation (4.49) in Equation (4.48) results in accurate trends. The improvement of predictions seems to be related to the sediment size, but some disagreement in the magnitude of the transport rates. As shown in Figure 4.28, the Watanabe and Sato's data for d_{50} = 0.20 mm resulted in the same under predicted values by a factor of 2. Again, the use of $k_s = 15d_{50}$ would increase the magnitude of the transport rates, approaching the line of perfect agreement. Van der A et al.'s data show that the medium and coarse sands are generally within a factor of about 2, while the fine sands are under-estimated by a greater factor. It is not entirely surprising that the finer sand are under-estimated since it was shown by van der A et al. (2010) that these transport rates are subject to significant phase lag effects, which are of course not captured in the present quasi-steady approach.

It is further remarked that, to allow for comparison with Nielsen (2006), in the present approach the roughness is taken proportional to the grain size, but the results suggest that if other values are taken the magnitude of the transport rates would be better predicted. Much better agreement between predicted and measured transport rates can also be obtained if f_w is calibrated separately for the different sand sizes. For example, Figure 4.30 shows that using $k_s = 25d_{50}$, 15 d_{50}, 2.5 d_{50} and d_{50}, for d_{50} = 0.15, 0.20, 0.27 and 0.46 mm, respectively, most of the results lie over the line of perfect agreement. Essentially this means that a smaller grain size implies a proportionally larger roughness and, consequently, friction factor. This can translate that the bed roughness is approximately equal to the grain size for medium sands, but for fine sands it has to be enhanced in relation to sand size, in order to account for the sediment transport component.

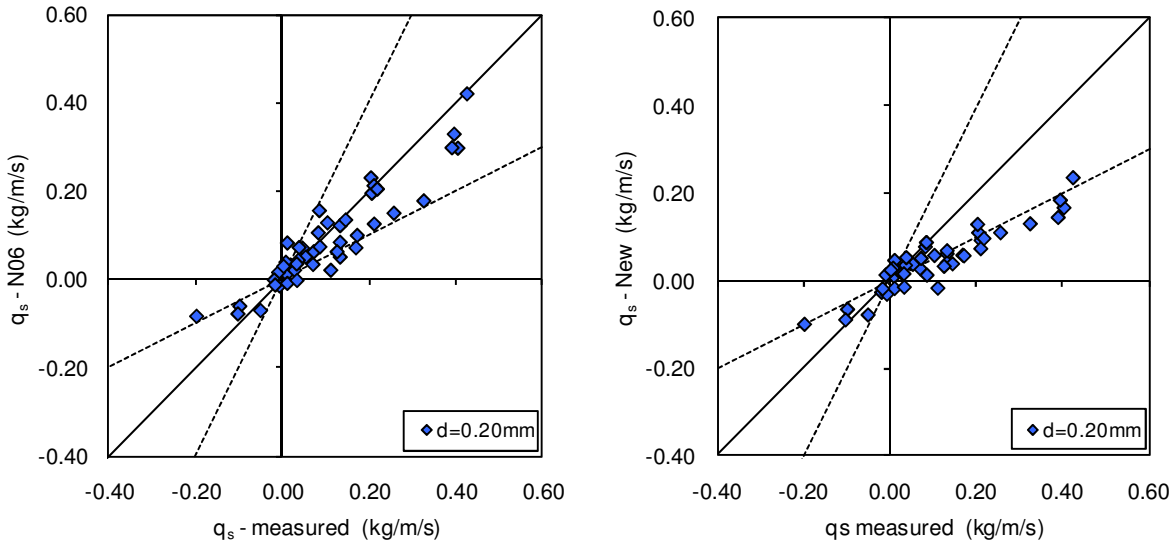

Figure 4.28 – Watanabe and Sato (2004) measured net transport rates versus predicted on (a) Nielsen's (2006) bed shear stress approach; (b) new method to compute bed shear stress (Eq. (4.48)). $\varphi = 51°$.

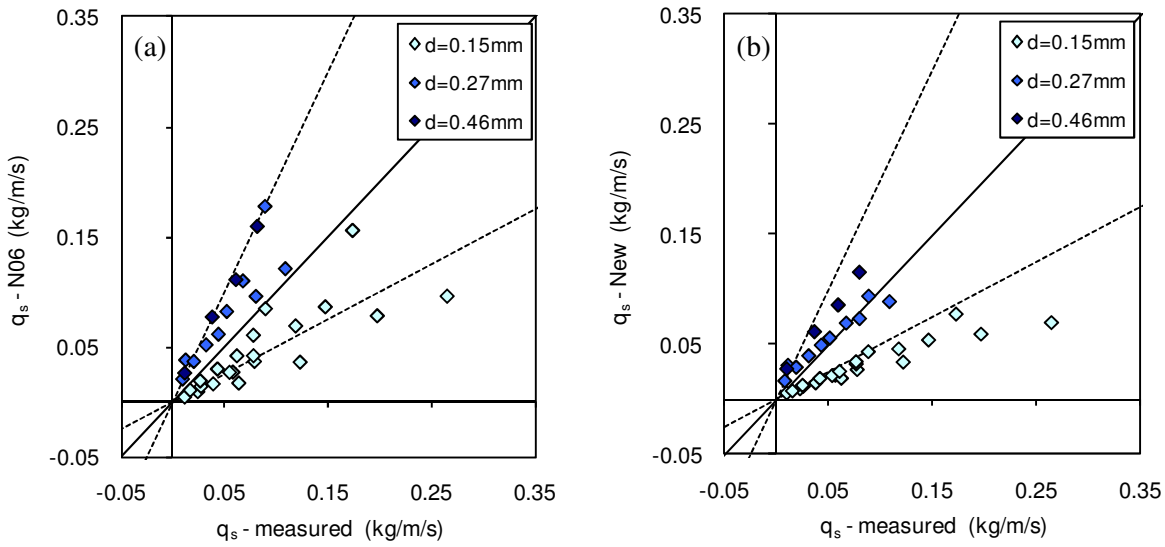

Figure 4.29 – Van der A et al. (2010) measured net transport rates versus predicted on (a) Nielsen's (2006) bed shear stress approach; (b) new method to compute bed shear stress (Eq. (4.48)). $\varphi = 51°$.

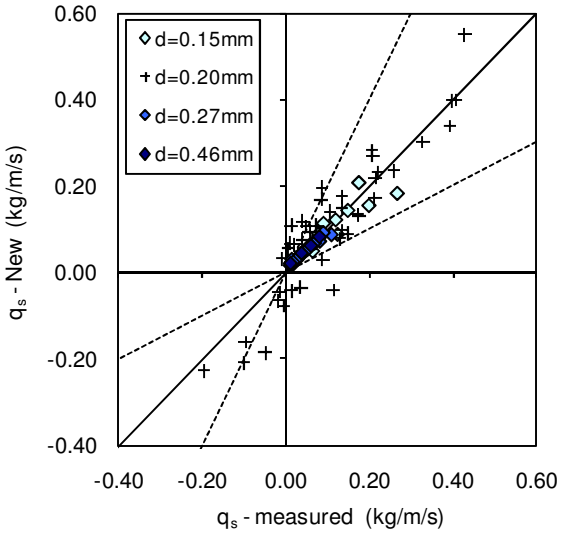

Figure 4.30 – Watanabe and Sato (2004) and van der A et al. (2010) measured net transport rates versus predicted with the new method to compute bed shear stress (Eq. (4.48)), using $k_s = 25d_{50}$, 15 d_{50}, 2.5 d_{50} and d_{50} for d_{50} = 0.15, 0.20, 0.27 and 0.46 mm, respectively. $\varphi = 51°$.

Rather than predicting the exact magnitude of the transport rates, it was focused the prediction of the correct trends in the transport rates which seems improved by the new formulation. This is illustrated in Figure 4.31 which shows the value of the squared correlation coefficient, cor^2, between the measured and predicted transport rates for each sediment size as a function of φ. The case of d_{50} = 0.20 mm was obtained using both TRANSKEW and Watanabe and Sato's data. The two extreme values of φ, 0º and 90º, correspond to drag dominated sediment transport and to pressure gradient dominated scenarios like plug flows (Sleath, 1999).

These results show that for almost any φ other than 0, the new formulation improves the correlation compared to Nielsen's (2006) original approach. Note that the absolute differences in cor^2 for the different sand sizes results from the different number of conditions. The optimal correlations are found with φ = 57º, 58º, 73º and 42º for d_{50} = 0.15, 0.20, 0.27 and 0.46 mm, respectively. These values are significantly larger than the phase-lead values resulting from the bed shear stress comparisons for fixed beds within the range of 20° - 30° for accelerated skewed flows (van der A et al., 2011). The reason for these large φ values, most even in excess of the 45° for laminar flows, is not entirely clear. However, such values do not necessarily disagree with the measurements for mobile bed sheet flows. For example, Guard and Nielsen (2008) reported phase-leads that asymptotically increase to 90° when one looks further into the sheet flow layer. They show that the magnitude and phase lead of the total shear stress depends on the chosen elevation within the sheet flow layer which makes it difficult to define a particular phase lead under mobile sand beds. These results are also in agreement with the present findings, reported in Chapter 3.

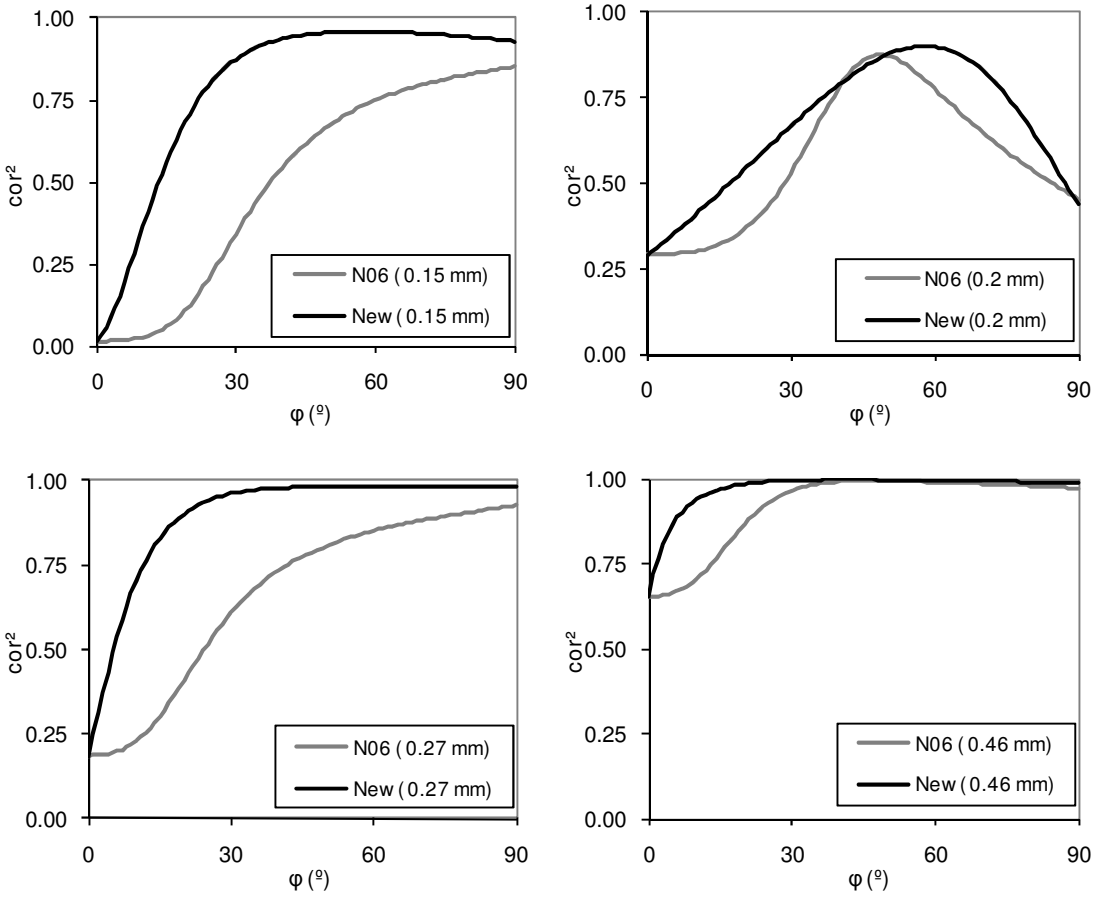

Figure 4.31 – Correlation between measured and predicted transport rates using Nielsen's (2006) bed shear stress approach (N06) and the new approach (Eq. (4.48)), as a function of the phase-lead φ.

4.4.5 Partial conclusions

At the beginning of this section, five different sediment transport models were tested to replicate the hydraulic conditions of the TRANSKEW experiments. All of them predicted a non-zero net transport rate for the acceleration- skewed oscillatory flows and reproduced well the trends observed in the data for Series A and Series C as a function of β, R and T. However, for the combined wave-current conditions (Series B) the predicted transport rates, especially those of the practical models, exhibited some mismatches with the experimental data, revealing a lower ability of these relatively simple models to replicate the detailed processes involved (e.g., phase lag effects and the suspended load), compared to a more advanced 1DV oscillatory bottom boundary model.

The proposed bed shear stress predictor was incorporated in the quasi-steady bed load formula (Nielsen, 2006) and its performance was tested against the measured net transport rates of TRANSKEW, Watanabe and Sato (2004) and van der A et al. (2010) experiments. All of these data sets concerned accelerated skewed flows under sheet flow conditions. Using the default value $\varphi = 51°$,

the new bed shear stress approach lead to better estimates of the net transport rates when compared to Nielsen's original approach. A sensitivity analysis for φ also illustrated that the new approach resulted in better correlations with measurements. Maximum correlation was obtained for φ between 42º and 73°, which are much larger than the optimum values found for the fixed bed measurements of van der A et al. (2011), in the range of 20°-30°.

The new formulation provides further insights in sediment transport predictions, accounting for the effect of nonlinear wave shapes, and can be useful in several engineering applications, in particular for morphological models.

4.5 Chapter closure

This chapter concerns the mathematical modelling of nonlinear wave motions and their interaction with sediments. The main purpose was to provide simple analytical expressions that give useful predictions without substantial computational expense.

It starts with the presentation of a new analytical function that reproduces wave shapes for any combination of velocity and acceleration skewness within the ranges found in nature. The formula contains four free parameters: two related to the orbital velocity amplitude and wave period and two related to the velocity and acceleration skewnesses, namely, an index of skewness, r, and a waveform parameter, ϕ. It is shown that the consideration of these two parameters can simulate a wide range of nonlinear wave shapes, overcoming some limitations of previous models.

Then, a comparison of several bottom shear stress parameterisations for non-linear waves is made. A new predictor is presented by considering the same parameters (r, ϕ) proposed in the analytical expression for the fluid velocity under skewed-asymmetric waves. This expression extends previous works. It is shown that, beside acceleration effects, the shape of the wave, described through r and ϕ, can be considered in the instantaneous shear stress computations, bringing in more physics. The results show that the new formulation and the momentum-integral method are in a good agreement.

The last section compares predictions of five models to the TRANSKEW measured net transport rates. When compared to a more advanced 1DV oscillatory bottom boundary model, the practical models show a lower ability to replicate the detailed processes involved, particularly for the combined wave-current conditions. The inclusion of the new bed shear stress predictor in a quasi-steady bed load formula is tested, resulting in the improvement of net transport rates estimations.

Chapter 5

APPLICATION TO A LARGE-SCALE DUNE EROSION EXPERIMENT

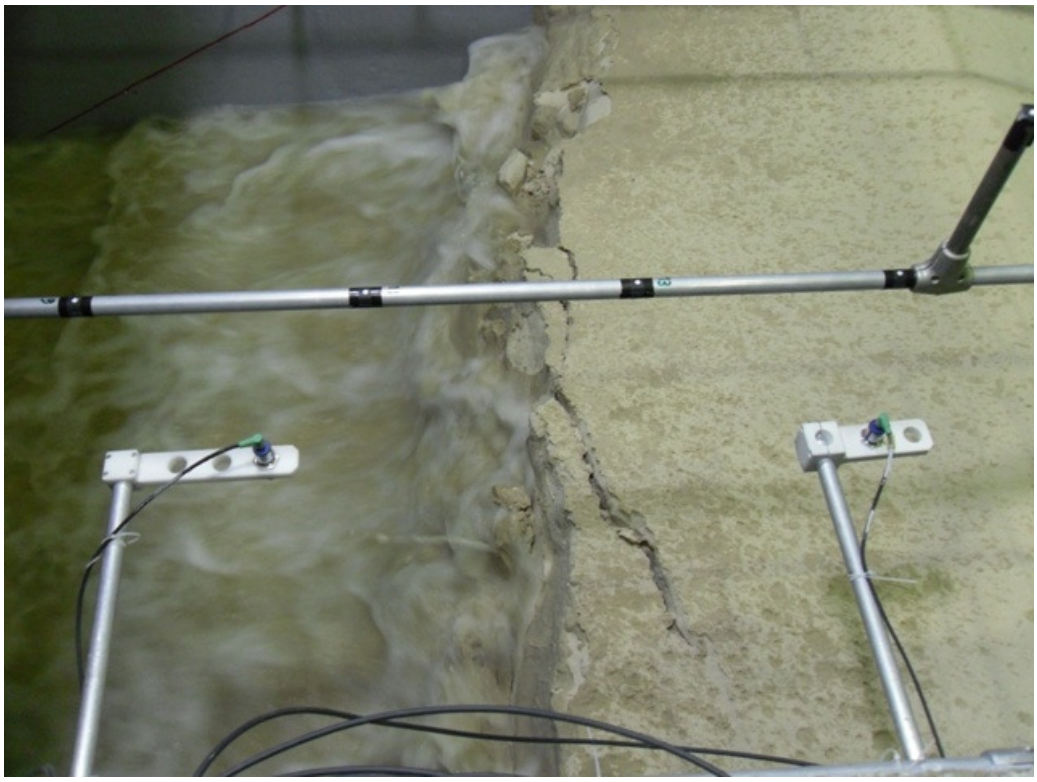

5. APPLICATION TO A LARGE-SCALE DUNE EROSION EXPERIMENT

5.1 Introduction

Dunes and beaches are effective natural coastal defences, due to their ability to adapt to the forcing agents (waves, tides, currents, wind). However, in sediment-starved coastal sectors, they often become out of balance with the forcing agents, and erosion takes place, pushing the coastline inland and causing dune destruction. Particularly, under storm-driven surges, wind and waves can cause severe dune erosion with rapid large-scale morphological changes, and possibly damage to hinterland infrastructure and loss of human lives. It is thus crucial to better understand the hydrodynamics and sediment dynamics of such systems (beaches and coastal dunes) under such extreme conditions, in order to better establish efficient coastal protection schemes (e.g., dune rehabilitation and dike construction, amongst others).

It is common to define four regimes of storm attack on a beach/dune system (Sallenger et al., 2003):

(1) swash regime with wave run-up confined to the foreshore;

(2) collision regime with swash and run-up to the dune face;

(3) overwash regime with wave run-up overtopping the dune crest;

(4) breaching and inundation regime.

In the case of the collision regime, the incoming storm waves break frequently at the toe of the dune, resulting in large water fluxes running up the dune face, but seldom overtopping it (Figure 5.1). Sand is carried down the slope by the down-rush, causing erosion of the upper beach and dune. Part of the dune face collapses, becoming nearly vertical, and lumps of sediment slide downwards to form a bar/step.

Since gathering detailed field information under storm surges and intense wave action becomes a challenging, costly and risky proposition, it has been studied under controlled conditions in wave flumes. Experiments on dune erosion using scaled models, in almost any kind of regime, have been performed in the past (e.g., Vellinga, 1986; Dette et al., 1998). Most of the these experiments have focused on the analysis of the bulk profile topographical variations and their relationship with the incoming wave field, and few have looked closely at the hydrodynamic actions and their relations with the sediment transport, with exception to the recent work of van Thiel de Vries et al. (2008).

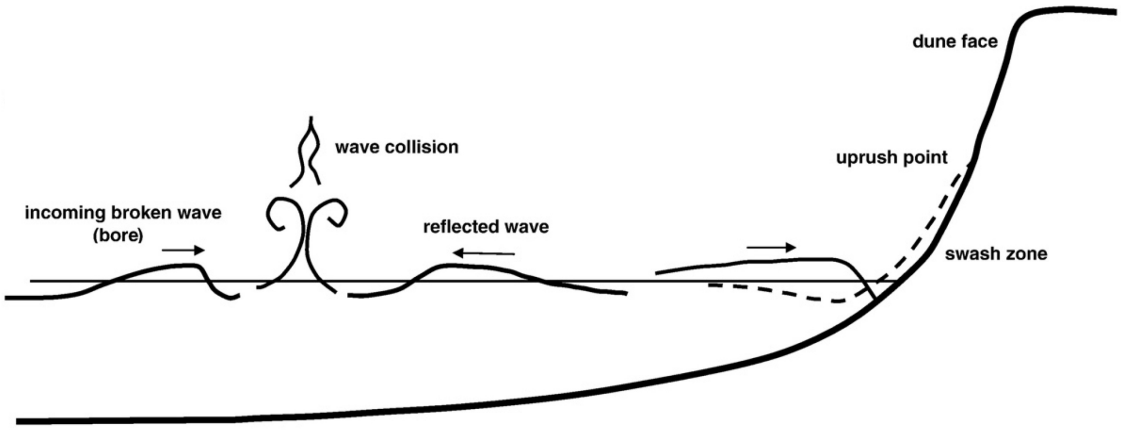

Figure 5.1 - Wave processes in the shallow surf zone in front of the dune (adapted from van Rijn, 2009).

The present chapter provides further insight in the knowledge of the hydrodynamics in front of a collapsing dune performed at a large-scale wave flume by Tomasicchio et al. (2010, 2011). It starts with a brief description of the experiments and it is followed by an analysis of the nonlinearities of the short-wave component in the surf region (see also Sancho et al., 2011). Finally, the ability of the analytical formulations presented in the previous chapter to reproduce nonlinear orbital motions and to make predictions of cross-shore evolutions is evaluated against this new dataset.

5.2 BOB experiment

A carefully designed set of experiments, designated as "BOB – Beach Overwashing and Breaching", was conducted at the large-scale wave flume of the *Laboratori d'Enginyeria Marìtima* (LIM) at UPC, from October to December 2009 (Tomasicchio et al., 2010, 2011). The dimensions of the wave flume (100 m long, 3 m wide and 5 m deep) allowed to perform near prototype-scale tests with a movable bed beach. The initial cross-shore beach and dune profile is shown in Figure 5.2 together with the instrumentation set-up. The dune front and back faces had equal slopes (1:2.30). The beach was formed of a quite homogeneous sand, with median diameter, d_{50}, equal to 0.246 mm, and fall velocity, w_s, of 34 mm/s.

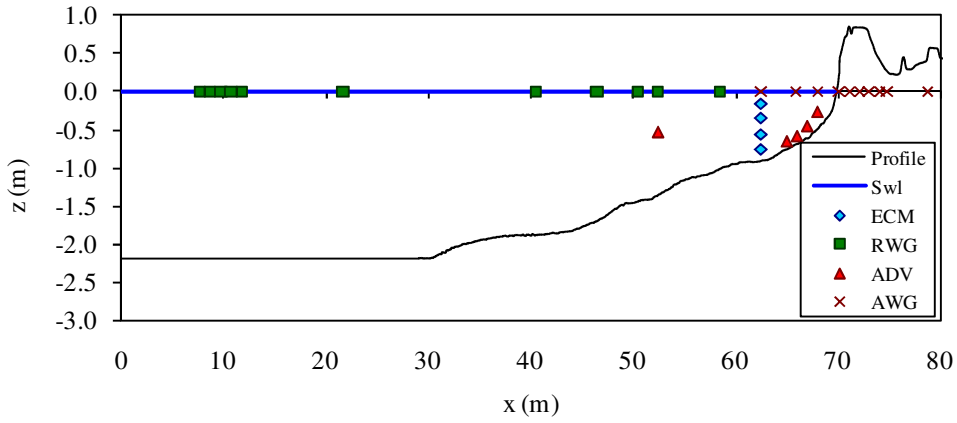

Figure 5.2 - Initial cross-shore profile and instruments locations.

Two different off-shore water depths, h_0, have been considered in the flume: the lower value, $h_0 = 2.35$ m, was raised up to 2.50 m to simulate the storm surge. Eleven different combinations of wave and water depth were performed (Tomasicchio et al., 2011). Practically all the tests exhibit similar nonlinear cross-shore evolutions of the near-bed velocities in the surf region and, for that reason, the following analysis focuses only on Test E, for which $h_0 = 2.35$ m. The corresponding significant wave height in front of the wave maker equalled 0.33 m, and the wave peak period equalled 3.0 s. Five experiments (runs) were conducted until total dune collapse. The duration of a single experiment was divided into five different wave attacks composed by 250, 250, 250, 500 and 1000 waves, respectively. The wave time series were forced following a given Jonswap spectrum with a peak enhancement factor equal to 3.3.

Measurements of water surface elevation, flow velocities and sediment concentration along the flume were carried out during each test with several instruments. Figure 5.2 shows the location of the Resistance Wave Gauges (RWG), Acoustic Wave Gauges (AWG), Electromagnetic Current Meters

(ECM), Acoustic Doppler Velocity meters (ADV) and the initial measured profile. Bed profile measurements were conducted using a mechanical profiler, together with detailed photogrammetric surveys at the emerged part of the dune. The profiles were measured at the beginning/ending of each time series. Overtopping and overwashing fluxes over the dune crest were measured by means of acoustic wave gauges, pressure sensors and an overtopping/overwashing collection tank. More details on the experimental setting is given in Tomasicchio et al. (2010, 2011).

5.3 Data analysis and methodologies

The present analysis concentrates on the hydrodynamics in the surf region, in front of the dune face. Point-velocity measurements, gathered with four high-resolution ADV located within the wave collision/breaking region and slightly above the bed surface are analysed (Figure 5.3). They were placed along different cross-shore locations, 1 m apart (x = 65.06, 66.06, 67.06 and 68.06 m), see Figure 5.2. The vertical distance of the ADV probes to the bed altered during the experiments due to morphological changes but, in general, the distance was seen to be around 10 to 30 cm. The vertical positions of the ADV were checked between tests and in certain occasions the devices were readjusted to higher levels whenever the probes become buried during the experiments.

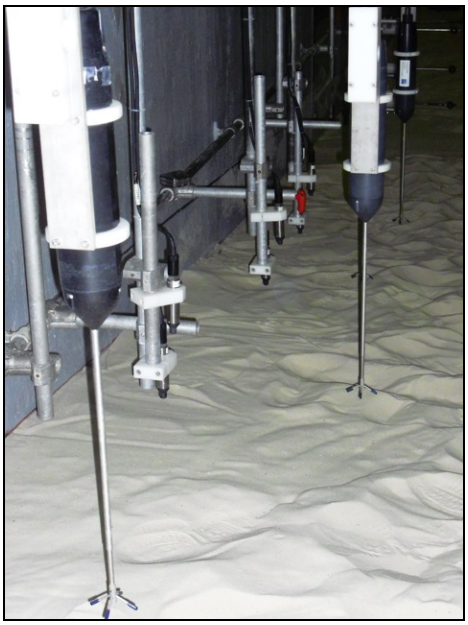

Figure 5.3 – ADV deployed in front of the dune face.

Due to the fact the instruments were placed in the wave breaking/surging region, the ADV velocity signals contain some spikes (noisy data) associated to air bubbles that entered in the flow. The spike noise looks similar to turbulent components in the velocity data and several despiking algorithms have been proposed to eliminate it (e.g., Goring and Nikora, 2002). To remove them, all the ADV velocity

data was pre-processed according to the 3D phase space method given by Mori et al. (2007). The noisy data-points were replaced through cubic interpolation, representing, in general, less than 5% of all data. Also, the levels of the auto-correlation and of the signal-to-noise ratio levels were assessed: whenever the correlation was less than 70% or the signal-to-noise ratio was low, the data points were excluded from the present analysis. The total discarded data represented a small portion of the measurements, suggesting a good quality of the velocity data.

To assess the horizontal velocity changes along the beach profile, a spectral analysis was firstly performed. The main purpose concerns only short waves characteristics. Figure 5.4 presents the velocity power spectrum of the horizontal velocity, u, for Test E (third run) plotted in both linear and logarithmic scales. The velocities correspond to measurements performed at $x = 65.06$ and 68.06 m, respectively. The left panel shows that the energy is concentrated around 0.33 Hz, corresponding to the incident wave spectrum ($T_p = 3$ s). However, closer to the shore line ($x = 68.06$ m), the energy in the low-frequency range (< 0.15 Hz) is not negligible. Hence, in the subsequent analysis, and because only the most energetic frequency-range is of interest, the low frequencies were filtered from the de-spiked velocity signals, using a high-pass filter with a cut-off frequency of 0.125Hz. In the right panel of Figure 5.4, the power spectrum plotted in a log-log scale contains a straight line with a -5/3 slope. That slope represents Kolmogorov's 5/3 law and helps the identification of the inertial subrange of the energy spectrum where the turbulence dominates. The data shows that frequencies higher than 2 Hz follow fairly well that spectral slope. Similar patterns were found for the other test conditions. To remove these high-frequency oscillations associated to turbulence, a low-pass filter with a cut-off frequency of 2Hz was also applied.

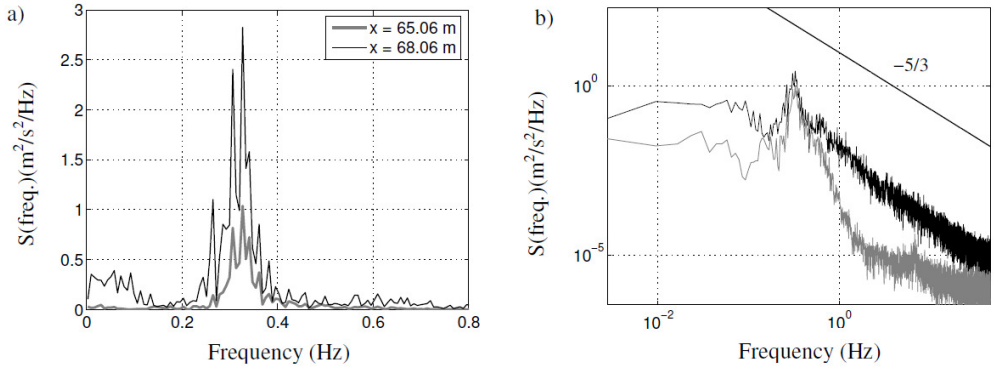

Figure 5.4 – Computed Power Spectrum for Test E at x= 65.06 and 68.06 m.: (a) linear scales, (b) logarithmic scales.

The following definitions are used to analyse the filtered time series of u. Some statistical moments like the mean, $\bar{u}$, standard deviation, σ_u, and skewness, $\mu_{3,u}$, were computed to assess their cross-shore evolution. Their definitions follow:

$$\bar{u} = \frac{\sum u}{N_p}, \tag{5.1}$$

$$\sigma_u = \sqrt{\frac{1}{T}\int_0^T (u-\bar{u})^2 \, dt} \approx \sqrt{\frac{\sum_{i=1}^{N_p}(u-\bar{u})^2}{N_p}}, \tag{5.2}$$

$$\mu_{3,u} = \frac{1}{T}\int_0^T \frac{(u-\bar{u})^3}{\sigma_u^3} \, dt \approx \frac{\sum_{i=1}^{N_p}(u-\bar{u})^3}{N_p \, \sigma_u^3}, \tag{5.3}$$

where N_p is the total number of data points in the time series.

The mean value, $\bar{u}$, estimates the time-averaged currents measured near the shoreline; the standard deviation, σ_u, is related to the intensity of the velocities; and $\mu_{3,u}$ is a measure of the non-linearity of the wave. The skewness $\mu_{3,u}$ is zero for a linear wave and a linear Gaussian wave field. Since we are analysing data within the wave breaking/surging/collision region one expects to obtain non-zero values, indicating strong nonlinearities.

Furthermore, the velocity skewness coefficient, R, and the wave skewness parameter, α, were also computed and transformed in pairs of r and ϕ, using the methodology proposed in Chapter 4. These parameters complement the statistical analysis, helping to characterise the main characteristics of nonlinear motion at each ADV location. For this purpose, the instantaneous measured near-bed velocity time series were transformed into a set of individual waves, delimited by two successive zero up-crossings. Each wave is associated with a value of T, U_w, R and α and, each combination of (R,α) was transformed in pairs of (r,ϕ). As shown in the previous chapter, beside the reproduction of wave orbital velocities, this allows, in principle, to estimate bed shear stresses and, consequently, transport rates under arbitrary nonlinear, skewed and asymmetric oscillatory flows.

The ability of the new bed shear stress estimator inserted in Nielsen's (2006) bedload formula to predict sediment transport rates can be seen against the bathymetric changes recorded with the mechanical profiler. Since the physical model contains non negligible slopes, the bedload transport needs to account for bed slope effects.

Different ways can be found in the literature that enter with the local bed slope, β_s (e.g., Antunes do Carmo, 1995; Damgaard et al., 1997; Lesser et al., 2004). Antunes do Carmo (1995) modified Meyer-Peter and Müller (1948) formula, replacing the critical value of Shields, θ_{cr}, by an equivalent one that enters with β_s:

$$\theta_{cr,slope} = \theta_{cr}\left(\cos\beta_s \cos\beta_t \sqrt{1-\frac{\tan^2\beta_t}{\tan^2\phi_i}} + \frac{\sin\beta_s}{\tan\phi_i}\right). \tag{5.4}$$

where ϕ_i is the internal angle of friction of bed material, $\tan\beta_t = \cos\beta_s \tan\beta_s$ and the value of θ_{cr} is obtained by Eq. (2.27). For most sands, ϕ_i can be assumed approximately equal to 33º (Bagnold, 1966).

In the following, the bedload formula of Nielsen (2006) was modified to consider the value of $\theta_{cr,\,slope}$:

$$q_s(t) = 12\sqrt{(s-1)gd_{50}^{\,3}}\left[\theta(t)-\theta_{cr,slope}\right]\sqrt{\theta(t)}\,\frac{u_*}{|u_*|},\ \theta > \theta_{cr,slope}. \tag{5.5}$$

Eq. (5.5) requires the ADV velocity time-series for $\theta(t)$ predictions. It is noted that the values of r and ϕ of $u(t)$ were obtained from a wave-by-wave analysis of the short-wave component only.

Attending the good agreements of the previous chapter to compute q_s with $k_s = 15d_{50}$ and $2.5d_{50}$ for $d_{50} = 0.2$ and 0.27 mm, using φ = 51º, it seems reasonable to use an intermediate value for $d_{50} = 0.246$ mm. Thus, the value of $k_s = 6d_{50}$ was adopted for bedload predictions.

The cross-shore gradients in the sediment flux are correlated with the morphological changes through the mass conservation equation:

$$\frac{dh}{dt} = \frac{1}{1-\varepsilon_0}\frac{dq_s}{dx}. \tag{5.6}$$

As the sand porosity ε_0 was not measured during BOB experiment, two representative values were considered: 0.4 and 0.3 (e.g., Thornton et al., 1996).

For a constant spacing of the ADV probes (Δx = 1 m), the cross-shore gradients in the sediment flux can be computed using the Method of Equal Grid Spacings (Plant et al., 2004) through a central-difference scheme at the instrument locations or at the mid-points of these sensors (x = 65.55, 66.55, and 67.55 m).

Thus, for the instrument locations the sediment flux gradients yield:

$$\frac{dq_{s,x_i}}{dx} = \frac{q_{s,x_{i+1}} - q_{s,x_{i-1}}}{2\Delta x}, \tag{5.7}$$

and for the mid-points the central difference method yields:

$$\frac{dq_{s,x_{i+\frac{1}{2}}}}{dx} = \frac{q_{s,x_{i+1}} - q_{s,x_i}}{\Delta x}. \tag{5.8}$$

The error associated to this method at the instrument locations is $O(\Delta x)^2$ and at the mid-points of the sensors is $O(\Delta x/2)^2$, suggesting that at the mid-points the prediction accuracy should be better.

5.4 Results

The computed cross-shore variations of $\bar{u}$, σ_u, $\mu_{3,u}$, R, α, ϕ and r are shown in Figure 5.5 for Test E (similar trends could be observed for the other conditions). The error bars in Figure 5.5 correspond to the standard deviation obtained for each parameter, obtained from the measurements during the repeated experiments (where the beach profile evolved significantly). It is pointed out that the data acquisition does not refer to constant water depths since the experiments were performed over a movable bed. In general, the errors bars arise near the shoreline except for R and ϕ, where the opposite is found. Still, one perceives smooth trends around the average values with rather small error bars.

The present results are from the measured total flow, after noise reduction and band-pass filtering. However, the average of u is computed before band-pass filtering. The flow is due to incoming waves, to dune-reflected waves and to waves generated by the collapsing of the dunes (Figure 5.6). Thus, one expects the flow not to observe the properties of a purely propagating wave.

Focusing in the statistical moments, it is observed that the values of $\bar{u}$ are negative and their magnitude increases as the distance to the shoreline decreases. It means that the devices are capturing the undertow which returns seaward the Stokes-drift wave flux carried onshore. The values of σ_u also increase for lower water depths. This means that the magnitude of the oscillatory motion near the bottom is increasing, which is linked to the shoaling process of the waves, the reduction of the water depth, and the increase in the vertical position of the sensor. The spatial variation of $\mu_{3,u}$ shows that, at the deepest position (x = 65.06 m), the velocities present already non-linear effects that increase at around x = 66.06 m. Further onshore, the value of $\mu_{3,u}$ drops almost to zero for the other cross-shore positions. That doesn't mean that close to the shore line, where the waves break, the velocity u becomes sinusoidal.

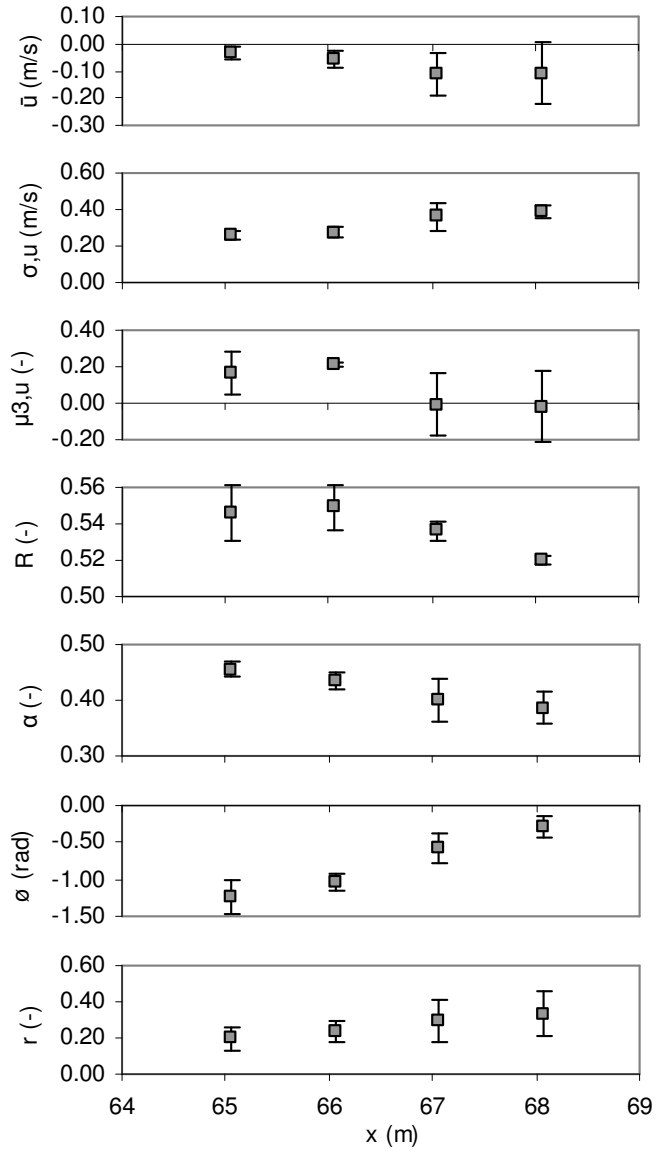

Figure 5.5 – Cross-shore variations of $\bar{u}$, σ_u, $\mu_{3,u}$, R, α, ϕ and r for Test E. The error bars signalize the standard deviation obtained of each parameter.

Looking to the cross-shore variation of R, α, ϕ and r, a better insight on the phenomena can be provided. Figure 5.5 shows values of $R > 0.5$ for all the positions, but with the lowest values at the lowest depths, pointing towards a reduction of the velocity skewness, thus confirming the $\mu_{3,u}$ trend. However, the values of α are also decreasing bellow 0.5, which is the representative value of a linear (sinusoidal) motion. This means that, for the onshore positions, the wave is pitching forward (sawtooth shape) and the acceleration skewness is, now, playing an important role. This wave transformation from velocity-skewed in the shoaling zone, to acceleration-skewed in the inner surf and swash zone can also be observed in natural beaches (e.g., Elfrink et al., 2006; Ruessink et al., 2009), with significantly lower wave reflection rates. The values of the parameters r and ϕ corroborate those observations. The growth of the values of r with the shoreline proximity evidences that the

nonlinearities are increasing. Moreover, the increase of ϕ from $\phi \sim -\pi/2$ to ~ 0 shows that the orbital motion is changing from a near first order cnoidal shape ($\phi = -\pi/2$, i.e., preponderance of short, high crests) to a near sawtooth wave shape ($\phi = 0$).

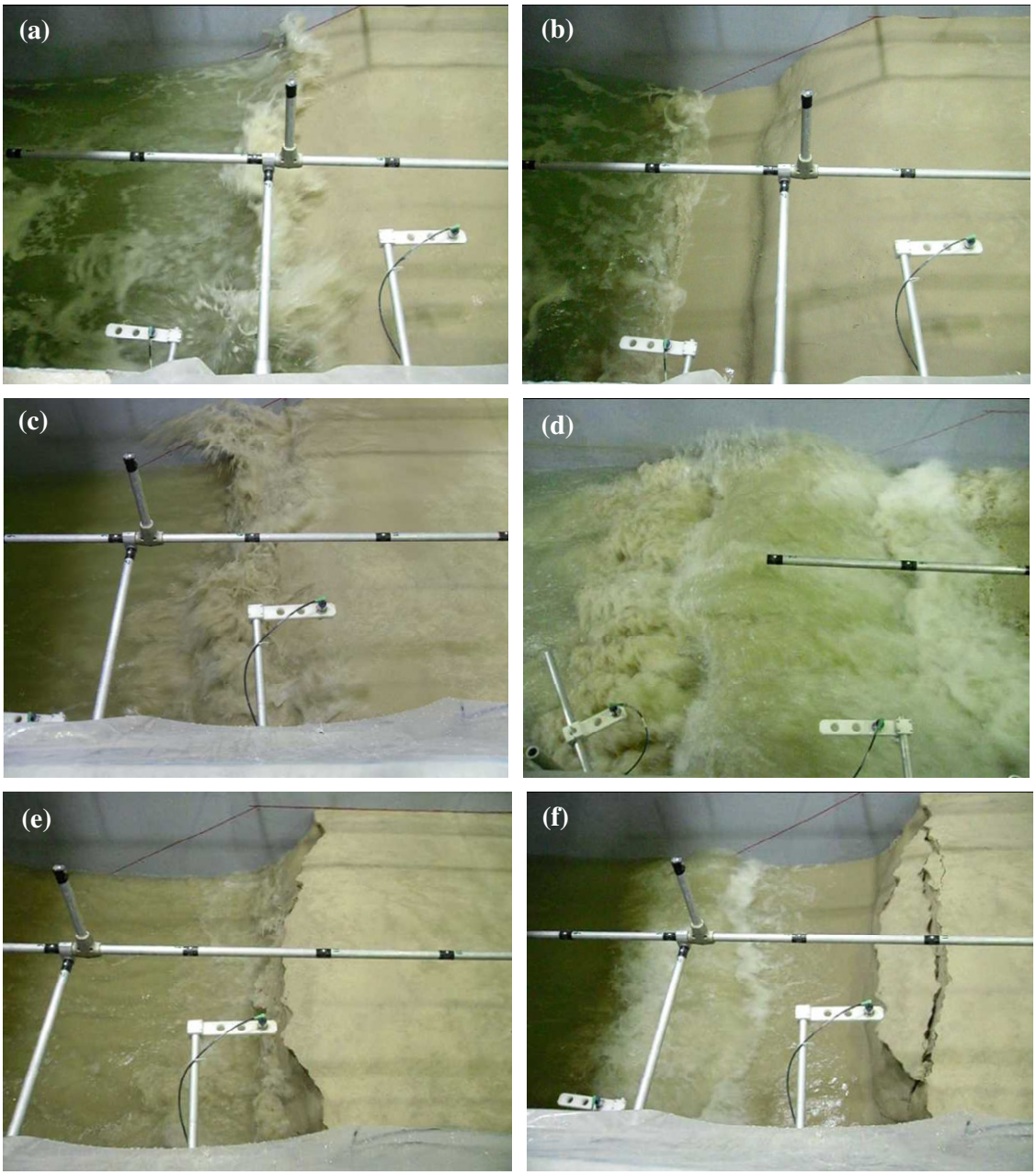

Figure 5.6 – The observed collision regime for Test E: a) limited wave overtopping and sediment overwash; b) formation of scarping at the toe of the dune; c) and d) wave collision in front of the collapsed dune (to the right); e) undermining of the dune toe; f) slumping of the dune face. (Tomasicchio et al., 2011)

Figure 5.7 shows the comparison between the measured filtered horizontal velocity and the simulated time series, using Eq. (4.8). A very good agreement is perceived, as the majority of the wave forms are well reproduced. One observes small discrepancies for some waves due to the high-frequency fluctuations within the principal wave, with $f < 2$ Hz. These oscillations are not possible to be

reproduced with Eq. (4.8), but the general trends put in evidence that this formulation successfully re-creates an equivalent wave shape.

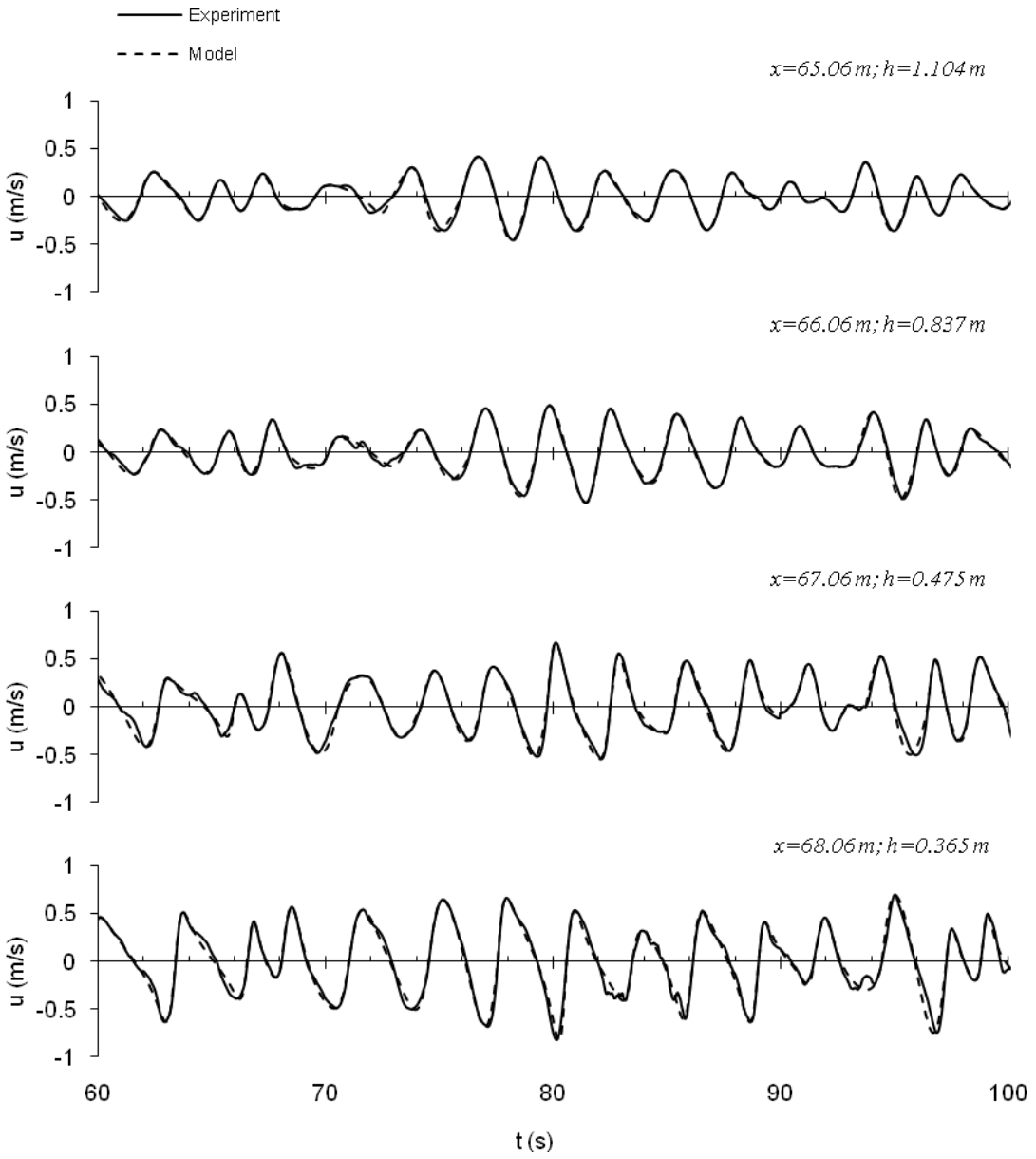

Figure 5.7 – Velocity time series for Test E: measured values (gray line) *versus* Eq. (4.8) (black line). Refer to *x*-coordinates in Figure 5.2.

Undoubtedly, the results show that nonlinearities are present in the data. This information can be useful to make predictions for sediment transport rates. However, strong cross-shore bathymetric changes suggest that other physical mechanisms than nonlinear oscillatory motions associated to mean currents are present. Figure 5.8 exemplifies the bed level evolution during Test E. The results show that the wave attack caused the collapse of part of the dune face and that lumps of sediment slide downwards. Consequently, two of the ADV sensors became buried at the end of the experiment.

Similar behaviour was found in most tests of BOB experiments, indicating that the processes are associated to dune erosion driving sediment offshore.

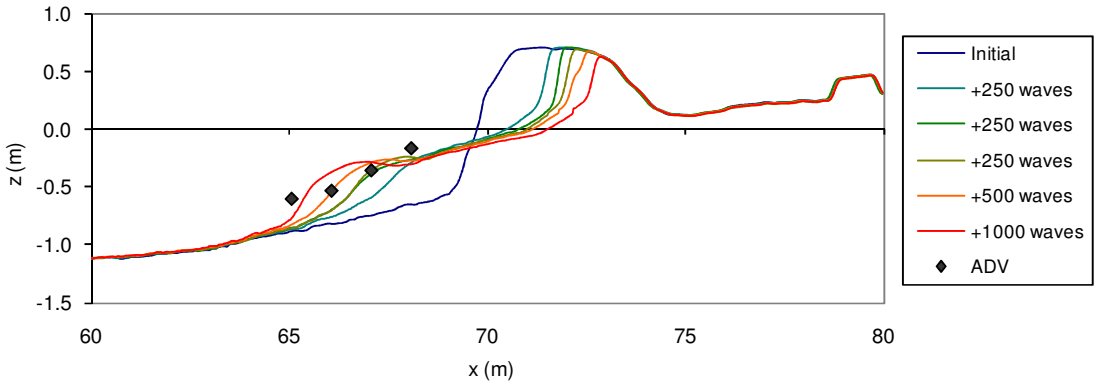

Figure 5.8 – Profiles measured during Test E after different wave attacks composed by 250, 250, 250, 500 and 1000 waves, respectively.

Larson et al. (2004) provide an extensive overview of existing empirical models to estimate dune erosion. Nevertheless, since such mechanism is not accounted with the new transport formulation and is beyond the scope of this thesis, the analysis was restricted to specific runs where the morphological changes in the dune are small. In such cases, one might expect that cross-shore bathymetric changes are mostly due to nonlinear effects of the oscillatory motion associated with mean currents. It is noted that the present data does not fall in sheet flow conditions since, generally, $\theta < 0.6$ (see Figure 2.8). Moreover, the bathymetric surveys do not indicate any presence of ripples.

Figure 5.9 shows the measured profiles for the third run of test B where small morphological changes are observed, compared to the majority of the experiments. The final profile was obtained after 250 wave attacks, corresponding to a duration of approximately 530 s. The measured and estimated bathymetric changes obtained on a wave-by-wave basis through Eq. (5.6) are synthesised in Table 5.1. Moreover, the transport rates at the instrument locations used in Eq.s (5.7) and (5.8) are also added. It is emphasized that this transport corresponds to the succession of waves, where the velocities enter with mean, short-wave and low-frequency components.

Table 5.1 indicates that the final beach profile survey reveals generalised accretion in the region of the ADV. Particularly, near the most onshore location, the bed level changes indicate large amounts of sediment deposition that are impossible to obtain through the bedload formulation. At $x = 66.56$ and 67.06 m the bed level changes obtained through Eq. (5.6) even predict erosion as evidenced by the negative values of dh. Only near the furthest offshore locations of the ADV there is a reasonable agreement between measured and predicted dh. The change of the porosity ε_0 between 0.3 and 0.4

does not introduce major differences in the predicted bed level changes and, consequently, the incertitude of this value is not the main cause responsible by the differences observed.

Table 5.1 – Measured and predicted bed level changes, *dh*, according to Eq. (5.6).

x (m)	Measured *dh* (mm)	Predicted q_s (mm^2/s)	Predicted *dh* with ε_0 =0.3 (mm)	Predicted *dh* with ε_0 =0.4 (mm)
68.06	56	2.38	-	-
67.56	77	-	1.9	2.2
67.06	46	4.90	-0.7	-0.9
66.56	15	-	-3.4	-4.0
66.06	11	0.41	1.1	1.3
65.56	7	-	5.6	6.5
65.06	5	7.80	-	-

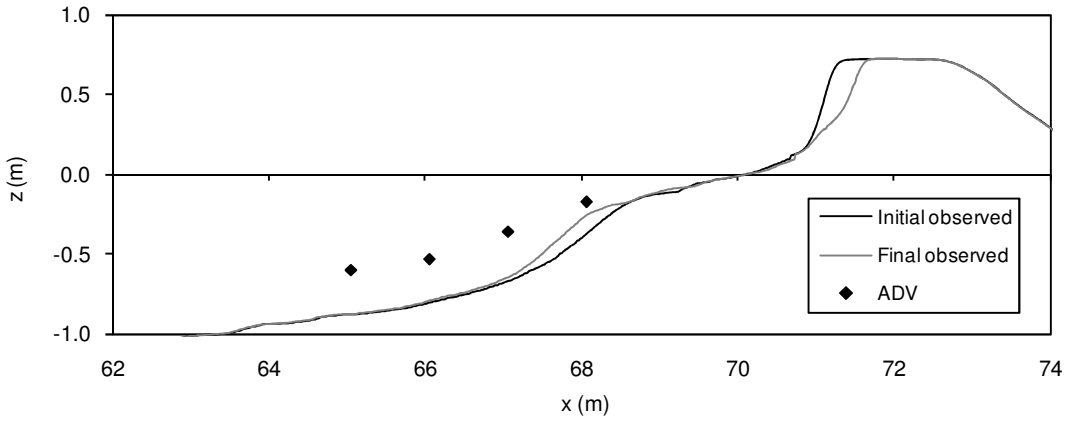

Figure 5.9 – Measured profiles for Test B at the beginning and end of the third run.

The significant accretion observed near the most onshore location can be attributed to a partial dune collapse where lumps of sediment slide downwards. The erosion of the dune drives sediment offshore, but this process is not represented by the present bedload formula. In addition, the sediment transport formula does not account for suspended load and, since the ADV sensors are located in a breaking wave zone, large amounts of suspended sediments could be expected in that area. It is noticed that the good experimental transport rate predictions observed in the previous chapter are associated to U-tube flows under non-breaking waves. There is ample evidence from laboratory and field that sand suspension under breaking waves may no longer be governed by bed-generated turbulence (bed shear stress), but by breaking-induced surface-generated turbulence (e.g., Butt et al., 2004; Aagaard and Hughes, 2010; Grasso and Ruessink, 2011). Indeed, part of the breaking-wave induced turbulence penetrates into the water column and might reach the seabed, stirring sand (e.g., Nadaoka et al., 1988;

Scott et al., 2009; Chassagneux, 2011). Since the simplified dynamics contained in the bedload formulation do not include a full understanding of the physical processes involved, this approach cannot predict correctly the morphological changes associated with the underlying predicted fluxes.

5.5 Chapter closure

In this chapter the hydrodynamics of the surf region in front of collapsing coastal dunes is investigated. The data was gathered during the HYDRALAB-III funded Transnational Access experiment performed at the CIEM large-scale wave flume (Tomasicchio et al., 2011). The ADV velocity data, collected in the wave breaking/surging region, was pre-processed and the cross-shore variation of seven flow parameters, $\bar{u}$, σ_u, $\mu_{3,u}$, R, α, ϕ and r were computed, reflecting linear and nonlinear wave properties.

The hydrodynamic results concern only those from test E. Other tests (not shown) follow similar trends. Interestingly, despite the strong wave reflection off the dune, the wave transformation in front of the dune exhibits analogous behaviour as observed in non-dune and wider beaches: the wave orbital motion evolves from velocity-skewed in the shoaling zone, to acceleration-skewed in the inner surf and swash zone. The parameters R and α clearly capture the waveform transformation, which is not so well represented by the "classical" wave skewness $\mu_{3,u}$.

The application of the analytical formulations presented in the previous chapter is seen against this new data set. The velocity time series are accurately replicated by the new expression (Eq. 4.8). However, the nonlinear effects incorporated in the new bed shear stress estimator inserted in Nielsen's bedload formula are not able to reproduce the observed morphological changes. In these dune erosion experiments, there are other intervenient processes which are not included in the sediment transport formula, reducing severely its predictive capacity.

Chapter 6

CONCLUSIONS AND FUTURE RESEARCH

Beach of São João, Costa da Caparica, Portugal (2007-01-22)

6. CONCLUSIONS AND FUTURE RESEARCH

6.1 Conclusions

A proper understanding of sediment transport processes is of vital importance to the coastal community, since morphological changes result from the movement of sediments. This thesis contributes for the understanding of cross-shore sediment transport processes under combined nonlinear waves and currents. A new dataset of detailed flow and sand transport processes under flat-bed/sheet flow conditions, in the presence of velocity and acceleration skewnesses and of a net current, was presented. This insight was used for the development, implementation and application of analytical models that permit an efficient replication of nonlinear orbital motions and corresponding bed shear stresses. This resulted in the improvement of a sediment transport model for sheet flow conditions under currents and waves of arbitrary shape.

The developed research is summarised below, together with the following main conclusions, which synthesize the partial ones previously presented at each chapter:

I.i) New experiments were conducted in the Large Oscillating Water Tunnel of Deltares (formerly, WL|Delft Hydraulics), allowing to obtain a reliable dataset of detailed flow and sand transport processes under flat-bed/sheet flow conditions. The experiments were performed with well-sorted, medium-sized sand (d_{50} = 0.2 mm) and the hydraulic conditions consisted of a repetition of regular oscillatory flows with different degrees of acceleration skewness (with or without a net current) as well as an oscillatory flow with both velocity and acceleration skewnesses.

I.ii) Net transport rates were evaluated and show that (a) the acceleration skewness in an oscillatory flow produces a net sediment transport in the direction of the highest acceleration (onshore); (b) the net transport in the presence of an opposing current is negative, against the direction of the highest acceleration, and reduces with an increase in flow acceleration; and, (c) the velocity skewness increases the values of the net onshore transport rates, and in greater importance than the acceleration skewness.

I.iii) Detailed velocity measurements within the boundary layer in accelerated-skewed flows indicate positive residual flows in the entire vertical, particularly relevant very close to the bed. Moreover, the increase of acceleration skewness seems to enhance this streaming, contrasting with previous observations for fixed-bed experiments under acceleration-skewed

flows, where the increase of acceleration skewness lead to an increase in magnitude of negative near-bed streamings.

I.iv) An analysis of the signal's first harmonic was performed for the velocity measurements along the boundary layer. The analysis confirmed that the dimensionless velocity defect function $D_1(z)$ can be described satisfactorily by two parameters proposed by Nielsen (1985, 1992). This is particularly useful for the reconstruction/prediction of velocity vertical profiles and bed shear stress estimations. It is evidenced that, similar to smooth laminar flows, the identity between ln $|D_1|$ and Arg $\{D_1\}$ is verified almost all the way to the bed. It only fails very near the bottom where a reduction of the phase lead ϕ_u closer to the bed is observed. Furthermore, the zero-velocity values obtained by the defect law practically coincide with the lower limit of the sheet flow layer obtained from detailed measurements of sediment concentrations.

I.v) Time-dependent sediment concentration measurements allowed to assess the sheet flow layer thickness along the flow cycle. For the accelerated-skewed flows, the sheet flow layer thickness remains thicker under the largest acceleration than at the opposite positive-to-negative flow reversal (on-offshore), where much smaller flow accelerations are found. As a consequence, the sand that is stirred in the negative flow phase has short time to settle back to the bed during the negative-to-positive flow cycle, suggesting that the acceleration skewness is responsible for the existence of phase-lag effects between the sediment particles and the flow. This is also evidenced during sediment flux computations performed within the sheet flow layer, particularly at flow reversal phases. The overall results show that the sheet flow layer thickness and the erosion depth are nearly in phase with the free-stream oscillatory flow, evidencing therefore a quick response of the bed. Both the acceleration and velocity skewnesses increase the erosion depth, mobilizing more sediment from the bed, and the sheet flow layer thickness, at the maximum positive flow (implied wave crest).

I.vi) An innovative methodology is applied for the first time to determine sediment grain velocities within the sheet flow layer. It combines cross-correlation techniques described by McLean et al. (2001) with wavelet multilevel decomposition (Mallat, 1999; and Franca and Lemmin, 2006). The application of wavelet transforms to the signals of the two conductivity probes (CCM) allowed the use of scale-conditioned cross-correlation techniques, yielding clearer cross-correlation peaks and a better estimation of particle velocities. Despite some limitations of the methodology, the results obtained were consistent and allowed to estimate reasonably well the grain velocities through the flow cycle, at different bed level elevations,

inside the sheet flow layer. Additionally, they seem to confirm that the Acoustic Doppler Velocity Profiler (ADVP) is able to penetrate inside the dense mobile sediment layer.

I.vii) Sediment fluxes computations within the sheet flow were computed by combining the ADVP with the CCM data. They are shown to be nearly in phase with the free-stream velocity. Time-averaged fluxes are at least one order of magnitude lower than the instantaneous fluxes. The tests without a counter current generally present positive values of time-averaged sediment flux throughout the entire sheet flow layer thickness. This behaviour is due to the current-related flux contribution resulting from a residual positive flow near the bottom, which balances the oscillatory negative time-averaged sediment flux. The tests with counter current present always negative values of the time-averaged sediment flux throughout the entire sheet flow layer thickness.

I.viii) Bed shear stresses were estimated using two standard methodologies: Log-fit and momentum-integral methods. Both methodologies brought out different results concerning the phase-lead between the shear stress and the free-stream velocity and the ratio of maximum to (absolute) minimum bed shear stress. The shear stress from the Log-fit method is practically in phase with the free-stream velocity, contrasting with the larger phase-lags between those quantities obtained with the momentum-integral method. Moreover, the Log-fit method provides an estimate of the bed roughness (about 15 times the sand median diameter) that corresponds to a length scale characteristic of the sheet flow (Madsen, 1993) but leads to $|\tau_{max}| \approx |\tau_{min}|$, unlike the results of the momentum-integral method that lead to skewed shear stresses. However, if a parameterisation linking z_0 with the shear velocity is introduced in the *law-of-the-wall* the method provided the same kind of skewnesses of τ. The combination of the dimensionless velocity defect function $D_1(z)$ with the momentum-integral method showed that the temporal shear stress distributions are strongly linked to the free-stream acceleration.

II.i) A simple analytical formulation that reproduces a skewed, nonlinear near-bed wave orbital velocity was presented. It contains four free parameters, where two are solely related to the velocity and acceleration skewnesses, namely, an index of skewness, r, and a waveform parameter, ϕ. The equation was compared with other models and validated against field and laboratory data. The results revealed that the new model can simulate a wide range of nonlinear wave shapes, reproducing satisfactorily the measured nonlinear wave particle velocity. Also, it overcame some limitations of the other models and extends their conditions of applicability. The new formulation is therefore capable of being used in many engineering

applications that require the use of representative wave forms. For example, it can provide the wave forcing in experimental facilities or in numerical modelling.

II.ii) Several simple bottom shear stresses parameterisations found in the literature, under nonlinear waves, were analysed. The effects of the wave shape on the bottom shear stress estimates were investigated by analysing the new set of experimental data. The results indicated a good agreement between all the formulations for small values of the phase difference between bed shear stress and the free-stream velocity, φ. However, the discrepancies between the methods were greater for larger values of φ.

II.iii) A new bed shear stress estimator was developed improving some limitations of the previous formulae. The parameterisation showed that, beside acceleration effects, the shape of the wave, described through the two parameters (r,ϕ), can be considered in the instantaneous shear stress computations. Results from the new model were compared with estimates from two different data sets: a fixed bed experiment performed in the Aberdeen Oscillatory Flow Tunnel (van der A et al., 2011) and the present new mobile bed experiment. The results for the fixed bed experiment showed that using the phase-lead between the shear stress and the free-stream velocity, $\varphi = 51°$, as recommended by Nielsen (2006), the new formulation satisfactorily reproduces the measured ratios $|\tau_{max}/\tau_{min}|$. For the mobile bed experiments, the use of $\varphi = 51°$ with an equivalent roughness $k_s = 15d_{50}$ (obtained from Log-fit method) provided a very good agreement between the new formulation and estimates from the momentum-integral method.

II.iv) The measured transport rates of the new data set have been used to evaluate the performance of different existing sediment transport models that take into account wave nonlinearities: these consisted of four practical engineering models and one detailed 1DV bottom boundary layer model. All of them reproduced generally well the trends observed in the net transport rates as a function of β, R and T but, for the combined wave-current conditions, the predicted transport rates, especially those of the practical models, showed some differences with the measurements. The results highlighted the lower ability of these relatively simple models to replicate the detailed processes involved, in comparison with the detailed 1D model.

II.v) The new bed shear stress estimator was incorporated in Nielsen's (2006) quasi-steady bed load formula, and reproduced accurately the transport rates with and without an opposing current by using $\varphi = 51°$ and $k_s = 15d_{50}$. This resulted on an improvement of the predictions of the practical models. The new expression was validated with data from other flow-tunnel

experiments under accelerated skewed flows, confirming the ability to predict net sand transport rates under nonlinear, non-breaking waves. Moreover, a sensitivity analysis for the phase-lead between the bed shear stress and the outer flow indicated that the new expression provides the best trends between predicted and measured transport rates for large values of φ, as 51°. This reflects the importance between drag and pressure gradients forces acting on sediments in asymmetric flows. Furthermore, the results indicated that the bed roughness that leads to correct magnitudes of the transport rates depends on the grain sizes. Good estimations demonstrated that the bed roughness is approximately equal to the grain size for medium sands, but needs to be enhanced in relation to sand size for fine sands.

III.i) The hydrodynamics of the surf region in front of collapsing coastal dunes was investigated. The data was gathered at the CIEM large-scale wave flume, where velocity data was collected in the wave breaking/surging region. The velocities were pre-processed in order to compute the cross-shore variation of several flow parameters, reflecting linear and nonlinear wave properties. Despite the strong wave reflection off the dune, the data reveals that, similar to observed in non-dune and wider beaches, the wave orbital motion evolves from velocity-skewed in the shoaling zone, to acceleration-skewed in the inner surf and swash zone. It was seen that the velocity time series were accurately replicated by the new analytical formulation, but the new bed shear stress estimator together with Nielsen's bedload formula were not able to reproduce the observed cross-shore sediment fluxes and bathymetric changes. Beside nonlinear oscillatory motions and mean currents, other physical mechanisms were involved in the experiments, reducing the predictive capacity of the bedload formula to replicate the observed morphological changes.

6.2 Future Research

The work presented in this thesis provides further insights in the understanding and correct prediction of cross-shore sediment transport processes, accounting for the effect of nonlinear wave shapes. The database provided by the TRANSKEW experiments is certainly useful to perform studies evaluating the performance of alternative sediment transport models, developed by different research groups. However, several new developments and more full-scale experiments are still needed to improve our understanding and modelling capacity of the complex physics associated with sediment transport processes. Therefore, some research topics in line with the developed work are presented in the following paragraphs.

- The collection of additional experimental data, comprising different sediment grain sizes in similar hydraulic conditions comparable to those found in the field, involving undertow, wave skewness and wave asymmetry will contribute to enlarge the already existing data base and allow for further development of more accurate predictive sediment transport models.

- The new experiments present some contrasting results between mobile and fixed beds. It is worthwhile to confirm the effects of the sheet flow layer dynamics on the near-bed streaming, phase-lead and bottom roughness with additional data.

- The first harmonic analysis obtained from the velocity measurements, provided good insights about the oscillatory boundary layer structure. It was shown that combining the free-stream velocity with two simple parameters (z_1, p_1) a good insight of the wave boundary layer flow could be obtained. Therefore, it would be interesting to investigate relations for z_1 and p_1 in different flow regimes, and their relation with the grain size.

- Further work is needed for the validation with data from other experiments of the application of the Log-fit method to predict the bed shear stress, by the appropriate setting/estimate of the no motion bed level, which turned out to be crucial to obtain the correct order of magnitude of that property.

- The combination of cross-correlation techniques described by McLean et al. (2001) with wavelet multilevel decomposition (Mallat, 1999; and Franca and Lemmin, 2006) allowed to determine sediment grain velocities within the sheet flow layer. The methodology yielded clearer cross-correlation peaks, allowing a better estimation of particle velocities by considering two resolution levels. It would be interesting to investigate if better results could be provided by testing different combinations (in number and order) of resolution levels and/or by attributing different weights to each resolution level.

- In addition, this work did not consider experiments involving heterogeneous mixture of cohesionless grains as found in nature (Guillén and Hoekstra, 1997). The number of experiments involving different size fractions is still very limited and, consequently there is a lack of basic knowledge about sediment transport processes of graded sediments in wave-dominated conditions. There are some experiments (e.g., Hassan and Ribberink, 2005) and numerical simulations (e.g., Calantoni and Thaxton, 2008) that consider bimodal size mixtures of sediment and contribute for that understanding. However, further research is needed in this area. This is an important research topic since, for example, the design of

effective beach nourishments usually involves different (dredged) materials, requiring such knowledge.

- An expression has been proposed here for the near-bed horizontal orbital velocity, and the corresponding horizontal acceleration. It is envisaged that one may derive a corresponding equation for the free-surface displacement, based on an adequate description of the vertical variation of the velocity amplitude, U_w, and the wave celerity.

- The new bed shear stress estimator and its application to sediment transport computations suggest that simple models can give useful predictions by incorporating some of the important physical processes. Its simplicity can be useful in several practical engineering purposes, in particular for morphodynamic models. Further work is needed to evaluate its performance for a wider number of experiments, including other facilities like wave flumes, which include additional processes in comparison with U-tube flows (e.g., Ribberink et al., 2000, Schretlen et al., 2009), and for a broader range of bed regimes.

- It is noted that the good estimations of the sediment transport rates in this work correspond to experimental observations associated to U-tube oscillatory flows, alike those under non-breaking waves. The last chapter shows that there is a predominant inability of the new model to reproduce the observed cross-shore bathymetric changes in the inner surf zone in front of collapsing coastal dunes. It may be explained because the new formulation does not include effects on wave-breaking induced turbulence on sand suspension. Though some significant efforts have been done regarding this subject (e.g., Scott et al., 2009; Aagaard and Hughes, 2010; Grasso and Ruessink, 2011), this issue remains a challenge to researchers.

7. REFERENCES

Aagaard, T. and Hughes, M.G., 2010. Breaker turbulence and sediment suspension in the surf zone. Marine Geology, 271(3-4): 250-259.

Abreu, T., Franca, M.J., Silva, P.A. and Sancho, F., 2009. Estimation of sediment particle velocities in sheet flow: cross-correlation and wavelet analysis. In: Vionnet C.A. et al. (Editor), 6th River Coastal and Estuarine Morphodynamics 2009. Taylor & Francis, Santa Fe, Argentina, pp. 1051-1056.

Abreu, T., Michallet, H., Silva, P.A., Sancho, F. and Nielsen, P., 2010a. 32nd International Conference on Coastal Engineering, Poster Paper ICCE2010, Shangai, China.

Abreu, T., Silva, P.A. and Sancho, F., 2008. Comparison of sediment transport formulae regarding accelerated skewed waves. In: J.M. Smith (Editor), 31st International Conference on Coastal Engineering, Poster Proc. 1703-1714, Hamburg, Germany, pp. 145-155.

Abreu, T., Silva, P.A., Sancho, F. and Temperville, A., 2010b. Analytical approximate wave form for asymmetric waves. Coastal Engineering, 57(7): 656-667.

Abreu, T., van der A, D.A., Silva, P.A., Sancho, F. and Michallet, H., 2011. New bed shear stress estimator for net sand transport rate predictions under non-linear waves. Journal of Coastal Research, SI 64: 2007-2011.

Airy, G.B., 1841. Tides and waves. Encyclopaedia Metropolitana, 396 pp.

Andrade, C., Pires, H.O., Silva, P., Taborda, R. and Freitas, M.C., 2006. Alterações Climáticas em Portugal. Cenários, Impactos e Medidas de Adaptação - Projecto SIAM II. In: F.D.S.e.P. Miranda (Editor), Zonas Costeiras. Gradiva, pp. 169-208.

Anglin, W.S. and Lambek, J., 1995. Mathematics in the Renaissance, Ch. 24. Springers.

Antunes do Carmo, J.S., 1995. Contribuição para o estudo dos processos morfodinâmicos em regiões costeiras e estuarinas. PhD thesis, University of Coimbra, Coimbra, Portugal, 225 pp.

Antunes do Carmo, J.S., Temperville, A. and Seabra-Santos, F.J., 2003. Bottom friction and time-dependent shear stress for wave-current interaction. Journal of Hydraulic Research, 41(1): 27 - 37.

Bagnold, R.A., 1966. An approach to the sediment transport problem from general physics. US Geological Survey Washington, USA.

Bailard, J.A., 1981. An energetics total load sediment transport model for a plane sloping beach. Journal of Geophysical Research, 86(C11): 10938–10954.

Battjes, J.A., 2006. Developments in coastal engineering research. Coastal Engineering, 53(2-3): 121-132.

Birkemeier, W.A. and Thornton, E.B., 1994. The DUCK94 nearshore field experiment, Coastal Dynamics '94. ASCE, pp. 815-821.

Bosman, J.J., van der Velden, E.T.J.M. and Hulsbergen, C.H., 1987. Sediment concentration measurement by transverse suction. Coastal Engineering, 11(4): 353-370.

Butt, T., Russell, P., Puleo, J., Miles, J. and Masselink, G., 2004. The influence of bore turbulence on sediment transport in the swash and inner surf zones. Continental Shelf Research, 24(7-8): 757-771.

Calantoni, J. and Puleo, J.A., 2006. Role of pressure gradients in sheet flow of coarse sediments under sawtooth waves. Journal of Geophysical Research, 111(C1): C01010.

Calantoni, J. and Thaxton, C.S., 2008. Simple power law for transport ratio with bimodal distributions of coarse sediments under waves. Journal of Geophysical Research, 113(C3): C03003.

Chassagneux, F.-X., 2011. Etude expérimentale des processus hydro-sédimentaires sous le déferlement de vagues irrégulières. PhD thesis, University of Grenoble, Grenoble, France, 219 pp.

Coastal Wiki, 2011. Accessed: April 6, 2011. Available online at: http://www.coastalwiki.org/coastalwiki/Human_causes_of_coastal_erosion

Cox, D.T., Kobayashi, N. and Okayasu, A., 1996. Bottom shear stress in the surf zone. Journal of Geophysical Research, 101(C6): 14337-14348.

Damgaard, J.S., Whitehouse, R.J.S. and Soulsby, R.L., 1997. Bed-load sediment transport on steep longitudinal slopes. Journal of Hydraulic Engineering, 123(12): 1130-1138.

Daubechies, I., 1988. Orthonormal Bases of Compactly Supported Wavelets. Communications on Pure and Applied Mathematics, 41(7): 909-996.

Davies, A.G. and Li, Z., 1997. Modelling sediment transport beneath regular symmetrical and asymmetrical waves above a plane bed. Continental Shelf Research, 17(5): 555-582.

Davies, A.G., van der A, D.A., O'Donoghue, T. and Ribberink, J.S., 2008. Modeling and observation of acceleration-skewed oscillatory flow over fixed beds. In: A.J.S.A. Lane (Editor), PECS08 - Physics of Estuaries and Coastal Seas, Liverpool, UK, pp. 115-118.

Davies, A.G. and Villaret, C., 1997. Oscillatory flow over rippled beds: Boundary layer structure and wave-induced Eulerian drift. In: J.N. Hunt (Editor), Gravity Waves in Water of Finite Depth (Advances in Fluid Mechanics). WIT Press / Computational Mechanics, pp. 215–254.

Dean, R.G. and Dalrymple, R.A., 1991. Water wave mechanics for engineers and scientists. Advanced Series on Ocean Engineering, 2. World Scientific, 353 pp.

Dette, H.H., Peters, K. and Newe, J., 1998. Large wave flume experiments '96/97, experiments on beach and dune stability, Leichtweiss Institute, Braunschweig University of Technology, Braunschweig, Germany.

Dibajnia, M., Moriya, T. and Watanabe, A., 2001. A representative wave model for estimation of nearshore local transport rate. Coastal Engineering Journal, 43(1): 1-38.

Dibajnia, M. and Watanabe, A., 1992. Sheet flow under nonlinear wavesand currents. In: B.L. Edge (Editor), 23rd International Conference on Coastal Engineering. ASCE, Venice, Italy, pp. 2015– 2028.

Dibajnia, M. and Watanabe, A., 1998. Transport rate under irregular sheet flow conditions. Coastal Engineering, 35(3): 167-183.

Dick, J.E. and Sleath, J.F.A., 1991. Velocities and concentrations in oscillatory flow over beds of sediment. Journal of Fluid Mechanics, 233: 165-196.

Dick, J.E. and Sleath, J.F.A., 1992. Sediment Transport in Oscillatory Sheet Flow. Journal of Geophysical Research, 97(C4): 5745-5758.

Dixen, M., Hatipoglu, F., Sumer, B.M. and Fredsøe, J., 2008. Wave boundary layer over a stone-covered bed. Coastal Engineering, 55(1): 1-20.

Doering, J.C. and Bowen, A.J., 1995. Parametrization of orbital velocity asymmetries of shoaling and breaking waves using bispectral analysis. Coastal Engineering, 26(1-2): 15-33.

Dohmen-Janssen, C.M., 1999. Grain size influence on sediment transport in oscillatory sheet flow. PhD thesis, Delft University of Technology, Delft, The Netherlands.

Dohmen-Janssen, C.M. and Hanes, D.M., 2002. Sheet flow dynamics under monochromatic nonbreaking waves. Journal of Geophysical Research, 107(C10): 3149.

Dohmen-Janssen, C.M. and Hanes, D.M., 2005. Sheet flow and suspended sediment due to wave groups in a large wave flume. Continental Shelf Research, 25(3): 333-347.

Dohmen-Janssen, C.M., Kroekenstoel, D.F., Hassan, W.N. and Ribberink, J.S., 2002. Phase lags in oscillatory sheet flow: experiments and bed load modelling. Coastal Engineering, 46(1): 61-87.

Dong, P. and Zhang, K., 2002. Intense near-bed sediment motions in waves and currents. Coastal Engineering, 45(2): 75-87.

Drake, T.G. and Calantoni, J., 2001. Discrete particle model for sheet flow sediment transport in the nearshore. Journal of Geophysical Research, 106(C9): 19859-19868.

Dyer, K.R. and Soulsby, R.L., 1988. Sand Transport on the Continental Shelf. Annual Review of Fluid Mechanics, 20(1): 295-324.

Elfrink, B., Hanes, D.M. and Ruessink, B.G., 2006. Parameterization and simulation of near bed orbital velocities under irregular waves in shallow water. Coastal Engineering, 53(11): 915-927.

Elgar, S., 1987. Relationships involving third moments and bispectra of a harmonic process. IEEE Acoustics, Speech and Signal Processing, 35(12): 1725-1726.

Elgar, S., Gallagher, E.L. and Guza, R.T., 2001. Nearshore sandbar migration. Journal of Geophysical Research, 106(C6): 11623-11627.

Elgar, S. and Guza, R.T., 1985. Observations of bispectra of shoaling surface gravity waves. Journal of Fluid Mechanics, 161: 425-448.

Elgar, S., Guza, R.T. and Freilich, M.H., 1988. Eulerian Measurements of Horizontal Accelerations in Shoaling Gravity Waves. Journal of Geophysical Research, 93(C8): 9261-9269.

Flores, N.Z. and Sleath, J.F.A., 1998. Mobile layer in oscillatory sheet flow. Journal of Geophysical Research, 103(C6): 12783-12793.

Foster, D.L., Bowen, A.J., Holman, R.A. and Natoo, P., 2006. Field evidence of pressure gradient induced incipient motion. Journal of Geophysical Research, 111(C5): C05004.

Franca, M.J. and Lemmin, U., 2006. Detection and reconstruction of coherent structures based on wavelet multiresolution analysis. In: E.C.T.L.A. Rui M.L. Ferreira, Joao G.A.B. Leal, Antonio H. Cardoso (Editor), River Flow 2006 – International Conference on Fluvial Hydraulics. Taylor & Francis, Lisbon (Portugal).

Fredsøe, J. and Deigaard, R., 1992. Mechanics of coastal sediment transport. Advanced Series on Ocean Engineering, 3. World Scientific, 470 pp.

Gonzalez-Rodriguez, D., 2009. Wave Boundary layer hydrodynamics and cross-shore sediment transport in the surf zone. PhD thesis, Massachussets Institute of Technology, Cambridge, MA, 171 pp.

Gonzalez-Rodriguez, D. and Madsen, O.S., 2007. Seabed shear stress and bedload transport due to asymmetric and skewed waves. Coastal Engineering, 54(12): 914-929.

Goring, D.G. and Nikora, V.I., 2002. Despiking Acoustic Doppler Velocimeter Data. Journal of Hydraulic Engineering, 128(1): 117-126.

Grasso, F. and Ruessink, B.G., 2011. Vertical structure of the turbulence dissipation rate in the surf zone. Journal of Coastal Research, SI 64: 90-94.

Guard, P.A. and Nielsen, P., 2008. Unsteady flow effects on bed shear stress and sheet flow sediment transport. In: J.M. Smith (Editor), 31st International Conference on Coastal Engineering. Singapore: World scientific publishing co., Hamburg, Germany, pp. 1521–1532.

Guillén, J. and Hoekstra, P., 1997. Sediment Distribution in the Nearshore Zone: Grain Size Evolution in Response to Shoreface Nourishment (Island of Terschelling, The Netherlands). Estuarine, Coastal and Shelf Science, 45(5): 639-652.

Hamm, L., Dohmen-Janssen, C.M., Ribberink, J.S., Samothrakis, P., Cloin, B., Savioli, J. C., Chatelus, Y., Bosboom, J., Nicholson, J. and Hein, R., 1998. Grain size, gradation and density effects on sediment transport processes in oscillatory flow conditions, WL|Delft Hydraulics, Delft, The Netherlands.

Hassan, W.N. and Ribberink, J.S., 2005. Transport processes of uniform and mixed sands in oscillatory sheet flow. Coastal Engineering, 52(9): 745-770.

Hassan, W.N.M. and Ribberink, J.S., 2010. Modelling of sand transport under wave-generated sheet flows with a RANS diffusion model. Coastal Engineering, 57(1): 19-29.

Herrmann, M.J. and Madsen, O.S., 2007. Effect of stratification due to suspended sand on velocity and concentration distribution in unidirectional flows. Journal of Geophysical Research, 112(C2): C02006.

Hoefel, F. and Elgar, S., 2003. Wave-Induced Sediment Transport and Sandbar Migration. Science, 299(5614): 1885-1887.

Horikawa, K., Watanabe, A. and Katori, S., 1982. Sediment transport under sheet flow condition, 18th International Conference on Coastal Engineering. ASCE, Cape Town, pp. 1335–1352.

Hsu, T.-J. and Hanes, D.M., 2004. Effects of wave shape on sheet flow sediment transport. Journal of Geophysical Research, 109(C5): C05025.

Hurther, D. and Lemmin, U., 2001. A Correction Method for Turbulence Measurements with a 3D Acoustic Doppler Velocity Profiler. Journal of Atmospheric and Oceanic Technology, 18(3): 446-458.

Isobe, M. and Horikawa, K., 1982. Study on water particle velocities of shoaling and breaking waves. Coastal Engineering Japan 25: 109-123.

Jensen, B.L., Sumer, B.M., Freds, oslash and e, J., 1989. Turbulent oscillatory boundary layers at high Reynolds numbers. Journal of Fluid Mechanics, 206: 265-297.

Jonsson, I.G., 1966. Wave boundary layers and friction factors, 10th International Conference on Coastal Engineering, Tokyo, pp. 127–148.

Jonsson, I.G., 1980. A new approach to oscillatory rough turbulent boundary layers. Ocean Engineering, 7(1): 109-152.

Jonsson, I.G., 1996. Wave boundary layers and friction factors, 10th International Conference on Coastal Engineering. ASCE, Tokyo, Japan, pp. 127–148.

Jonsson, I.G. and Carlsen, N.A., 1976. Experimental and theoretical investigations in an oscillatory turbulent boundary layer. Journal of Hydraulic Research, 14(1): 45 - 60.

Kajiura, K., 1968. A model of the bottom boundary layer in water waves. Bull. Earthquake Res. Inst., 46: 75–123.

Kamphuis, J.W., 1975. Friction factors under oscillatory waves. J. Waterway, Harbours and Coastal and Ocean Eng. Div., ASCE, 101 (WW2): 135–144.

King, D.B., 1991. Studies in oscillatory flow bed load sediment transport. PhD thesis, University of California, San Diego, USA, 183 pp.

Kleinhans, M., 2005. Phase diagram of bed states in steady, unsteady, oscillatory and mixed flows. In: L. Van Rijn, Soulsby, R., Hoekstra, P., Davies, A. (Editor), SANDPIT: Sand Transport and Morphology of Offshore Sand Mining Pits. Aqua Publications, The Netherlands (Chapter Q).

Koelewijn, H. and Ribberink, J.S., 1994. Sediment transport under sheet flow conditions, Delft University of Technology, WL|Delft Hydraulics, Delft, The Netherlands.

Larson, M., Erikson, L. and Hanson, H., 2004. An analytical model to predict dune erosion due to wave impact. Coastal Engineering, 51(8-9): 675-696.

Le Méhauté, B., 1976. An Introduction to Hydrodynamics and Water Waves. Springer, 315 pp.

Lesser, G.R., Roelvink, J.A., van Kester, J.A.T.M. and Stelling, G.S., 2004. Development and validation of a three-dimensional morphological model. Coastal Engineering, 51(8-9): 883-915.

Leykin, I.A., Donelan, M.A., Mellen, R.H. and McLaughlin, D.J., 1995. Asymmetry of wind waves studied in a laboratory tank. Nonlinear Processes in Geophysics, 2(3/4): 280-289.

Madsen, O.S., 1991. Mechanics of cohesionless sediment transport in coastalwaters. In: K.J.G. N. C. Kraus, and D. L. Kriebel (Editor), Coastal Sediements '91. ASCE, Seattle, pp. 15– 27.

Madsen, O.S., 1993. Sediment transport outside the surf zone. Waterways Experiment Station, U.S. Army Corps of Engineer, Vicksburg, Mississippi, USA.

Madsen, O.S., 1994. Spectral wave-current bottom boundary layer flows. 24th International Conference on Coastal Engineering, Kobe, Japan, pp. 384-398.

Malarkey, J., Pan, S., Li, M., O'Donoghue, T., Davies, A.G. and O'Connor, B.A., 2009. Modelling and observation of oscillatory sheet-flow sediment transport. Ocean Engineering, 36(11): 873-890.

Mallat, S., 1999. A Wavelet Tour of Signal Processing. Academic Press, San Diego (USA), 620 pp.

Mariño-Tapia, I.J., O'Hare, T.J., Russell, P.E., Davidson, M.A. and Huntley, D.A., 2007a. Cross-shore sediment transport on natural beaches and its relation to sandbar migration patterns: 2. Application of the field transport parameterization. Journal of Geophysical Research, 112(C3): C03002.

Mariño-Tapia, I.J., Russell, P.E., O'Hare, T.J., Davidson, M.A. and Huntley, D.A., 2007b. Cross-shore sediment transport on natural beaches and its relation to sandbar migration patterns: 1. Field observations and derivation of a transport parameterization. Journal of Geophysical Research, 112(C3): C03001.

Masselink, G., 2004. Formation and evolution of multiple intertidal bars on macrotidal beaches: application of a morphodynamic model. Coastal Engineering, 51(8-9): 713-730.

Masselink, G. and Black, K.P., 1995. Magnitude and cross-shore distribution of bed return flow measured on natural beaches. Coastal Engineering, 25(3-4): 165-190.

McLean, S.R., Ribberink, J.S., Dohmen-Janssen, C.M. and Hassan, W.N.M., 2001. Sand Transport in Oscillatory Sheet Flow with Mean Current. Journal of Waterway, Port, Coastal and Ocean Engineering, 127(3): 141-151.

Meyer-Peter, E. and Müller, R., 1948. Formulas for bed-load transport, IAHR, 2nd Meeting of the International Association for Hydraulic Structures Research, Stockholm, Sweden, pp. 39-64.

Mori, N., Suzuki, T. and Kakuno, S., 2007. Noise of Acoustic Doppler Velocimeter Data in Bubbly Flows. Journal of Engineering Mechanics, 133(1): 122-125.

Myrhaug, D. and Holmedal, L.E., 2007. Mobile layer thickness in sheet flow beneath random waves. Coastal Engineering, 54(8): 577-585.

Myrhaug, D., Holmedal, L.E., Simons, R.R. and MacIver, R.D., 2001. Bottom friction in random waves plus current flow. Coastal Engineering, 43(2): 75-92.

Nadaoka, K., Ueno, S. and Igarashi, T., 1988. Sediment suspension due to large scale eddies in the surf zone. In: B.L. Edge (Editor), 21st International Conference on Coastal Engineering. ASCE, New York, Coata del Sol-Malaga, Spain, pp. 1646–1660.

Nielsen, P., 1985. On the structure of oscillatory boundary layers. Coastal Engineering, 9(3): 261-276.

Nielsen, P., 1992. Coastal Bottom Boundary Layers and Sediment Transport. Advanced Series on Ocean Engineering, 4. World Scientific, 324 pp.

Nielsen, P., 2002. Shear stress and sediment transport calculations for swash zone modelling. Coastal Engineering, 45(1): 53-60.

Nielsen, P., 2006. Sheet flow sediment transport under waves with acceleration skewness and boundary layer streaming. Coastal Engineering, 53(9): 749-758.

Nielsen, P., 2009. Coastal and Estuarine Processes. Advanced Series on Ocean Engineering, 29. World Scientific, 360 pp.

Nielsen, P. and Callaghan, D.P., 2003. Shear stress and sediment transport calculations for sheet flow under waves. Coastal Engineering, 47(3): 347-354.

Nikuradse, J., 1932. Gesetzmäßigkeiten der turbulenten Strömung in glatten Rohren. VDI-Forschungsheft, 356.

O'Donoghue, T., Doucette, J.S., van der Werf, J.J. and Ribberink, J.S., 2006. The dimensions of sand ripples in full-scale oscillatory flows. Coastal Engineering, 53(12): 997-1012.

O'Donoghue, T. and Wright, S., 2004a. Concentrations in oscillatory sheet flow for well sorted and graded sands. Coastal Engineering, 50(3): 117-138.

O'Donoghue, T. and Wright, S., 2004b. Flow tunnel measurements of velocities and sand flux in oscillatory sheet flow for well-sorted and graded sands. Coastal Engineering, 51(11-12): 1163-1184.

Plant, N.G., Holland, K.T., Puleo, J.A. and Gallagher, E.L., 2004. Prediction skill of nearshore profile evolution models. Journal of Geophysical Research, 109(C1): C01006.

Pugh, F.J. and Wilson, K.C., 1999. Velocity and concentration distributions in sheet flow above plane beds. Journal of Hydraulic Engineering, 125(2): 117-125.

Reniers, A.J.H.M., Roelvink, J.A. and Thornton, E.B., 2004a. Morphodynamic modeling of an embayed beach under wave group forcing. Journal of Geophysical Research, 109(C1): C01030.

Reniers, A.J.H.M., Thornton, E.B., Stanton, T.P. and Roelvink, J.A., 2004b. Vertical flow structure during Sandy Duck: observations and modeling. Coastal Engineering, 51(3): 237-260.

Ribberink, J.S., 1998. Bed-load transport for steady flows and unsteady oscillatory flows. Coastal Engineering, 34(1-2): 59-82.

Ribberink, J.S. and Al-Salem, A.A., 1994. Sediment transport in oscillatory boundary layers in cases of rippled beds and sheet flow. Journal of Geophysical Research, 99(C6): 12707-12727.

Ribberink, J.S. and Al-Salem, A.A., 1995. Sheet flow and suspension of sand in oscillatory boundary layers. Coastal Engineering, 25(3-4): 205-225.

Ribberink, J.S., Dohmen-Janssen, C.M., Hanes, D.M., McLean, S.R. and Vincent, C., 2000. Nearbed sand transport mechanisms under waves, 27th International Conference on Coastal Engineering. ASCE, Sydney, Australia, pp. 3263-3276.

Ribberink, J.S., van der Werf, J.J., O'Donoghue, T. and Hassan, W.N.M., 2008. Sand motion induced by oscillatory flows: Sheet flow and vortex ripples. Journal of Turbulence, 9: N20.

Richardson, J.F. and Zaki, W.N., 1954. Sedimentation and fluidization. Trans. Inst. Chem. Eng., 32: 35–53.

Rodi, W., 1987. Examples of calculation methods for flow and mixing in stratified fluids. Journal of Geophysical Research, 92(C5): 5305-5328.

Ruessink, B.G., Michallet, H., Abreu, T., Sancho, F., van der A, D.A., van der Werf, J.J. and Silva, P.A., 2011. Observations of velocities, sand concentrations, and fluxes under velocity-asymmetric oscillatory flows. Journal of Geophysical Research, 116(C3): C03004.

Ruessink, B.G., van den Berg, T.J.J. and van Rijn, L.C., 2009. Modeling sediment transport beneath skewed asymmetric waves above a plane bed. Journal of Geophysical Research, 114(C11): C11021.

Sallenger, A.H., Howd, P., Stockdon, H., Guy, K. and Morgan, K.L.M., 2003. On predicting storm induced coastal change, Coastal Sediments. World Scientific Publishing Corp. and East Meets West Productions, Clearwater Beach, Florida, USA, CD-ROM.

Sancho, F., 2002. Surface wave statistics past a barred beach. Proceedings of 6th Congress of the Italian Society for Applied and Industrial Mathematics (SIMAI), Chia Laguna, Italy.

Sancho, F., Abreu, T., D'Alessandro, F., Tomasicchio, G.R. and Silva, P.A., 2011. Surf hydrodynamics in front of collapsing coastal dunes. Journal of Coastal Research, SI 64: 144-148.

Sancho, F., Mendes, P.A., Antunes do Carmo, José S., Neves, M.G., Tomasicchio, G.R., Archetti, R., Damiani, L., Mossa, M., Rinaldi, A., Gironella, X. and Arcilla, A.S., 2001. Wave hydrodynamics over a barred beach, International Symposium on Ocean Wave Measurement and Analysis - "Waves 2001". ASCE, S. Francisco.

Schretlen, J.J.L.M., Ribberink, J.S. and O'Donoghue, T., 2009. Sand transport under full-scale surface waves, 6th International Conference on Coastal Dynamic, paper no. 123. World Scientific, Tokyo, Japan.

Scott, N.V., Hsu, T.-J. and Cox, D., 2009. Steep wave, turbulence, and sediment concentration statistics beneath a breaking wave field and their implications for sediment transport. Continental Shelf Research, 29(20): 2303-2317.

Shields, A., 1936. Anwendung der Aehnlichkeitsmechanik und der Turbulenz Forschung auf die Geschiebebewegung, Mitt. der Preussische Versuchanstalt für Wasserbau und Schiffbau, Berlin, Germany.

Silva, P.A., Abreu, T., Freire, P., Kikkert, G., Michallet, H.,O'Donoghue, T., Plecha, S., Ribberink, J.S., Ruessink, B.G., Sancho, F., Steenhauer, K., Temperville, A., van der A, D. and van der Werf, J.J., 2008. Sand transport induced by acceleration-skewed waves and currents – The TRANSKEW project. In: A.J.S.A. Lane (Editor), PECS08 – Physics of Estuaries and Coastal Seas, Liverpool, UK, pp. 163-166.

Silva, P.A., Abreu, T., Michallet, H., Hurther, D. and Sancho, F., 2009. Sheet flow layer structure under oscillatory flows. In: Vionnet C.A. et al. (Editor), 6th River Coastal and Estuarine Morphodynamics 2009. Taylor & Francis, Santa Fe, Argentina, pp. 1057-1062.

Silva, P.A., Abreu, T., Sancho, F. and Temperville, A., 2007. A sensitivity study of sediment transport rates in accelerated skewed waves. In: M.D.-J.a.S. Hulscher (Editor), 5th IAHR Symposium on River, Coastal and Estuarine Morphodynamics, Enschede, The Netherlands, pp. 337-343.

Silva, P.A., Abreu, T., van der A, D.A., Sancho, F., Ruessink, B.G., van der Werf, J.J. and Ribberink, J.S., 2011. Sediment transport in non-linear skewed oscillatory flows: Transkew experiments. Journal of Hydraulic Research, 49, sup1 : 72-80.

Silva, P.A., Temperville, A. and Seabra Santos, F., 2006. Sand transport under combined current and wave conditions: A semi-unsteady, practical model. Coastal Engineering, 53(11): 897-913.

Simons, R.R., Myrhaug, D., Thais, L., Holmedal, L.E. and Maciver, R.D., 2000. Bed friction in combined wave-current flows, 27th International Conference on Coastal Engineering. ASCE, Sydney, Australia, pp. 216-226.

Sleath, J.F.A., 1987. Turbulent oscillatory flow over rough beds. Journal of Fluid Mechanics, 182: 369-409.

Sleath, J.F.A., 1993. Bedload transport in oscillatory flow. In: M. Belorgey, Rajoana, R. D., and Sleath, J.F.A. (Editor), Sediment transport mechanisms in coastal environments and rivers. Euromech. World Scientific, pp. 93-106.

Sleath, J.F.A., 1999. Conditions for plug formation in oscillatory flow. Continental Shelf Research, 19(13): 1643-1664.

Soulsby, R.L., 1997. Dynamics of marine sands. Thomas Telford Ltd, London, 272 pp.

Soulsby, R.L. and Damgaard, J.S., 2005. Bedload sediment transport in coastal waters. Coastal Engineering, 52(8): 673-689.

Soulsby, R.L. and Wainwright, B.L.S.A., 1987. A criterion for the effect of suspended sediment on near-bottom velocity profiles. Journal of Hydraulic Research, 25(3): 341 - 356.

Soulsby, R.L. and Whitehouse, R.J.S., 1997. Threshold of sediment motion in coastal environments, Pacific Coasts and Ports Conference. University of Canterbury, Christchurch, New Zealand, pp. 149–154.

Stokes, G.G., 1847. On the theory of oscillatory waves, 8. Pitt Press, Cambridge, 15 pp.

Suntoyo, Tanaka, H. and Sana, A., 2006. Shear stress and sediment transport rate calculations for non-linear waves. 30th International Conference on Coastal Engineering, San Diego, California, USA, pp. 2308-2317.

Suntoyo, Tanaka, H. and Sana, A., 2008. Characteristics of turbulent boundary layers over a rough bed under saw-tooth waves and its application to sediment transport. Coastal Engineering, 55(12): 1102-1112.

Svendsen, I.A., 2006. Introduction to nearshore hydrodynamics, 24. World Scientific, 722 pp.

Svendsen, I.A., Madsen, P.A. and Hansen, J.B., 1978. Wave characteristics in the surf zone, 16th International Conference on Coastal Engineering, pp. 520-539.

Swart, D.H., 1974. Offshore sediment transport and equilibrium beach profiles, 131. Publication / Delft Hydraulics Laboratory, Delft, The Netherlands, 302 pp.

Tajima, Y., 2004. Waves, Currents, and Sediment Transport in the Surf Zone along Long. PhD thesis, Straight Beaches, Massachusetts Institute of Technology, Cambridge, MA.

Tajima, Y. and Madsen, O.S., 2002. Shoaling, breaking and broken wave characteristics, 28th International Conference on Coastal Engineering. World Scientific, pp. 222–234.

Tanaka, H. and Samad, M.A., 2006. Prediction of instantaneous bottom shear stress for smooth turbulent bottom boundary layers under irregular waves. Journal of Hydraulic Research, 44(1): 94 - 106.

Tanaka, H. and Thu, A., 1994. Full-range equation of friction coefficient and phase difference in a wave-current boundary layer. Coastal Engineering, 22(3-4): 237-254.

Tanaka, H. and Van To, D., 1995. Initial motion of sediment under waves and wave-current combined motions. Coastal Engineering, 25(3-4): 153-163.

Terrile, E., Reniers, A.J.H.M. and Stive, M.J.F., 2009. Acceleration and Skewness Effects on the Instantaneous Bed-Shear Stresses in Shoaling Waves. Journal of Waterway, Port, Coastal, and Ocean Engineering, 135(5): 228-234.

Terrile, E., Reniers, A.J.H.M., Stive, M.J.F., Tromp, M. and Verhagen, H.J., 2006. Incipient motion of coarse particles under regular shoaling waves. Coastal Engineering, 53(1): 81-92.

Thanh, S.H., Thu, T.T. and Temperville, A., 1994. A numerical model for suspended sediment in combined currents and waves, Euromech 310. World Scientific.

Thorne, P.D. and Hanes, D.M., 2002. A review of acoustic measurement of small-scale sediment processes. Continental Shelf Research, 22(4): 603-632.

Thornton, E.B., Humiston, R.T. and Birkemeier, W., 1996. Bar/trough generation on a natural beach. Journal of Geophysical Research, 101(C5): 12097-12110.

Tomasicchio, G.R., Alsina, J., Caceres, I., D'Alessandro, F., Fortes, C.J.E.M., Ilic, S., James, M.R., Nagler, L., Pinheiro, L.V., Sanchez-Arcilla, A., Sancho, F., Shaw, B. and Schüttrumpf, H., 2010. Dune erosion, overwash and breaching, Third International Conference on the Application of Physical Modelling to Port and Coastal Protection. CoastLab 10, Barcelona, Spain.

Tomasicchio, G.R., Sanchez-Arcilla, A., D'Alessandro, F., Ilic, S., James, M.R., Sancho, F., Fortes, C.J.E.M. and Schüttrumpf, H., 2011. Large-scale flume experiments on dune erosion processes. Journal of Hydraulic Research, 49, sup1: 20-30.

Uittenbogaard, R., Bosboom, J. and Kessel, T., 1999. Numerical simulation of wave-current driven sand transport, WL|Delft Hydraulics Delft, The Netherlands.

van der A, D.A., 2010. Effects of Acceleration Skewness on Oscillatory Boundary Layers and Sheet Flow Sand Transport. PhD thesis, University of Aberdeen, Aberdeen, UK, 205 pp.

van der A, D.A., O'Donoghue, T., Davies, A.G. and Ribberink, J.S., Submitted. Experimental study of the turbulent boundary layer in acceleration-skewed oscillatory flow.

van der A, D.A., O'Donoghue, T. and Ribberink, J.S., 2010. Measurements of sheet flow transport in acceleration-skewed oscillatory flow and comparison with practical formulations. Coastal Engineering, 57(3): 331-342.

van der A, D.A., O'Donoghue, T., Davies, A.G. and Ribberink, J.S., 2008. Effects of acceleration skewness on rough bed oscillatory boundary layer flow, 31st International Conference on Coastal Engineering. ASCE, Hamburg, Germany, pp. 1583-1595.

van der A, D.A., O'Donoghue, T. and Ribberink, J.S., 2009. Sheet flow sand transport processes in oscillatory flow with acceleration skewness, 6th International Conference on Coastal Dynamic. World Scientific, Tokyo, Japan, pp. 1-13.

van der Werf, J.J., Schretlen, J.J.L.M., Ribberink, J.S. and O'Donoghue, T., 2009. Database of full-scale laboratory experiments on wave-driven sand transport processes. Coastal Engineering, 56(7): 726-732.

van Rijn, L.C., 1984. Sediment Transport, Part I: Bed Load Transport. Journal of Hydraulic Engineering, 110(10): 1431-1456.

van Rijn, L.C., 1993. Principles of sediment transport in rivers, estuaries and coastal seas. Aqua Publications, Amsterdam.

van Rijn, L.C., 2007. Unified View of Sediment Transport by Currents and Waves. I: Initiation of Motion, Bed Roughness, and Bed-Load Transport. Journal of Hydraulic Engineering, 133(6): 649-667.

van Rijn, L.C., 2009. Prediction of dune erosion due to storms. Coastal Engineering, 56(4): 441-457.

van Thiel de Vries, J.S.M., van Gent, M.R.A., Walstra, D.J.R. and Reniers, A.J.H.M., 2008. Analysis of dune erosion processes in large-scale flume experiments. Coastal Engineering, 55(12): 1028-1040.

Vellinga, P., 1986. Beach and dune erosion during storm surges. PhD thesis, Delft University of Technology, Delft, The Netherlands, pp. 200.

Wang, Y.-H., 2007. Formula for predicting bedload transport rate in oscillatory sheet flows. Coastal Engineering, 54(8): 594-601.

Warner, J.C., Sherwood, C.R., Signell, R.P., Harris, C.K. and Arango, H.G., 2008. Development of a three-dimensional, regional, coupled wave, current, and sediment-transport model. Computers & Geosciences, 34(10): 1284-1306.

Watanabe, A. and Isobe, M., 1990. Sand transport rate under wave-current action, 22nd International Conference on Coastal Engineering. ASCE, Delft, The Netherlands, pp. 2495-2507.

Watanabe, A. and Sato, S., 2004. A sheet-flow transport rate formula for asymmetric, forward-leaning waves and currents, 29th International Conference on Coastal Engineering. ASCE, Lisbon, Portugal, pp. 1703-1714.

Wilson, K.C., 1966. Bed-load transport at high shear stress. ASCE J. Hydraulics Div., 92(HY6): 49-59.

Wilson, K.C., 1987. Analysis of Bed-Load Motion at High Shear Stress. Journal of Hydraulic Engineering, 113(1): 97-103.

Wilson, K.C., 1989. Friction of wave-induced sheet flow. Coastal Engineering, 12(4): 371-379.

Wilson, K.C., Andersen, J.S. and Shaw, J.K., 1995. Effects of wave asymmetry on sheet flow. Coastal Engineering, 25(3-4): 191-204.

Zala-Flores, N. and Sleath, J.F.A., 1998. Mobile layer in oscillatory sheet flow. Journal of Geophysical Research, 103(C6): 12783-12793.

Zyserman, J.A. and Fredsøe, J., 1994. Data Analysis of Bed Concentration of Suspended Sediment. Journal of Hydraulic Engineering, 120(9): 1021-1042.

Appendices

APPENDICES

A.1 Interpolation procedure

In the following, a short guide is provided, illustrating the approach used to obtain the values (r, ϕ) from the knowledge of (R, α). The latter key parameters can be obtained from the knowledge of the wave height, wave period, local water depth and bottom slope (e.g., Dibajnia et al., 2001; Tajima and Madsen, 2002; Tajima, 2004; and Elfrink et al., 2006). For the explanation one uses the example given in Section 4.3, of a wave with normalized wave length and wave height, respectively, of L/h=15 and H/h =0.4, propagating at 2 m depth over a beach with slope equal to 1:40 (Elfrink et al., 2006). The corresponding values of R and α are $R = 0.659$ and $\alpha = 0.278$. To find the corresponding pair (r, ϕ) values the following methodology is proposed:

i) Using Eq. (4.17) with $R = 0.659$ it is possible to estimate r for each ϕ of Table 4.1 by inverting such equation (yielding a 3rd-order polynomial) and finding its roots via Cardano's method. This method returns three solutions of r, but only the real solution within $0 < r < 1$ is accepted. Applying Eq. (4.19) for those values of r, one finds a set of α values. It is then possible to limit the range of ϕ within our domain ($-\pi/2 \le \phi \le 0$), verifying in which ϕ values $\alpha = 0.278$ is included. For $\alpha = 0.278$, we are restricted to $\phi = -\pi/4$ ($r = 0.7449$, $\alpha = 0.248$) and to $\phi = -\pi/3$ ($r = 0.6480$ and $\alpha = 0.308$). We proceed then with linear interpolation and find $\phi = -0.286\pi$ for $\alpha = 0.278$.

ii) An analogous procedure can be used starting with α, i.e., using Eq. (4.19) with $\alpha = 0.278$ it is possible to estimate r, for each ϕ of Table 4.3, via Cardano's method. Applying Eq. (4.17) with these values of r one calculates a set of R values, and delimitates the range of ϕ within our domain ($-\pi/2 \le \phi \le 0$), verifying the ϕ values in which $R = 0.659$ is included. For $\alpha = 0.278$ we are restricted to $\phi = -\pi/4$ ($r = 0.6704$ and $R = 0.637$) and to $\phi = -\pi/3$ ($r = 0.7300$ and $R = 0.689$). From linear interpolation, for $\alpha = 0.278$ we obtain $\phi = -0.292\pi$.

iii) The average value of ϕ, computed in i) and ii), is considered the final ($\phi \approx -0.29\pi$).

iv) The value of ϕ in step iii) is used to compute the final r. Firstly, the final values in step i) ($r = 0.7449$ and $r = 0.6480$ corresponding, respectively, to $\phi = -\pi/4$ and $\phi = -\pi/3$) are used to obtain a first solution ($r = 0.700$). Secondly, the final values in step ii) ($r = 0.6704$ and $r = 0.7300$ corresponding, respectively, to $\phi = -\pi/4$ and $\phi = -\pi/3$) are

used to obtain a second solution ($r = 0.698$). Then, the average value is considered the final approach ($r \approx 0.699$).

Following the above procedure, which is not exact, some errors arise as illustrated in Figure A.1 and Figure A.2. Both figures show that the largest errors occur for small values of r ($r < 0.1$). However, within the range $-\pi/2 \le \phi \le 0$ and $0 < r < 1$ the errors for predicting ϕ and r are relatively small. Averaging the errors for that domain, they correspond approximately to 3.4% and 2.5%, respectively.

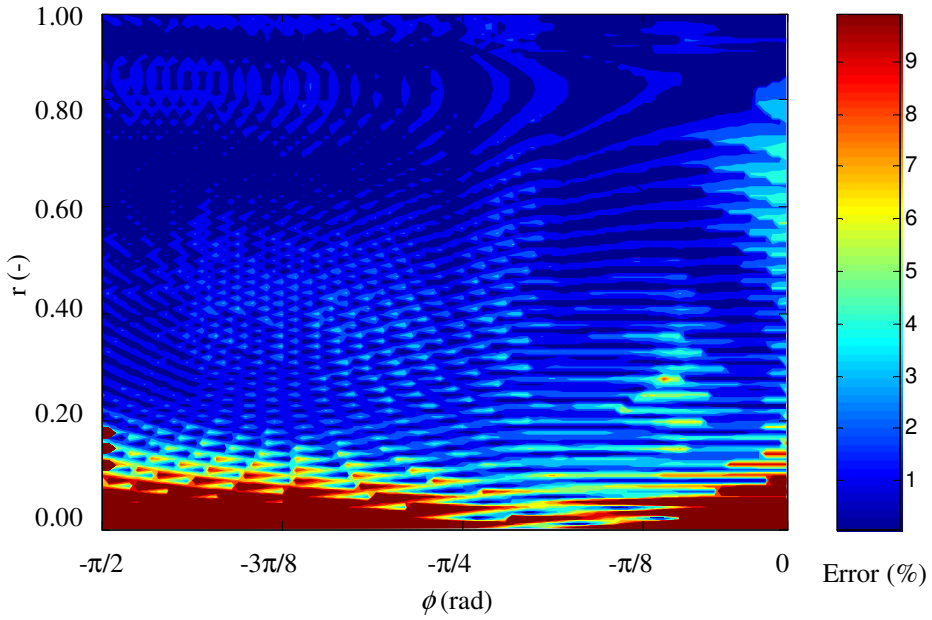

Figure A.1 – Error percentage for the prediction of ϕ using Eq.s (4.17)-(4.19).

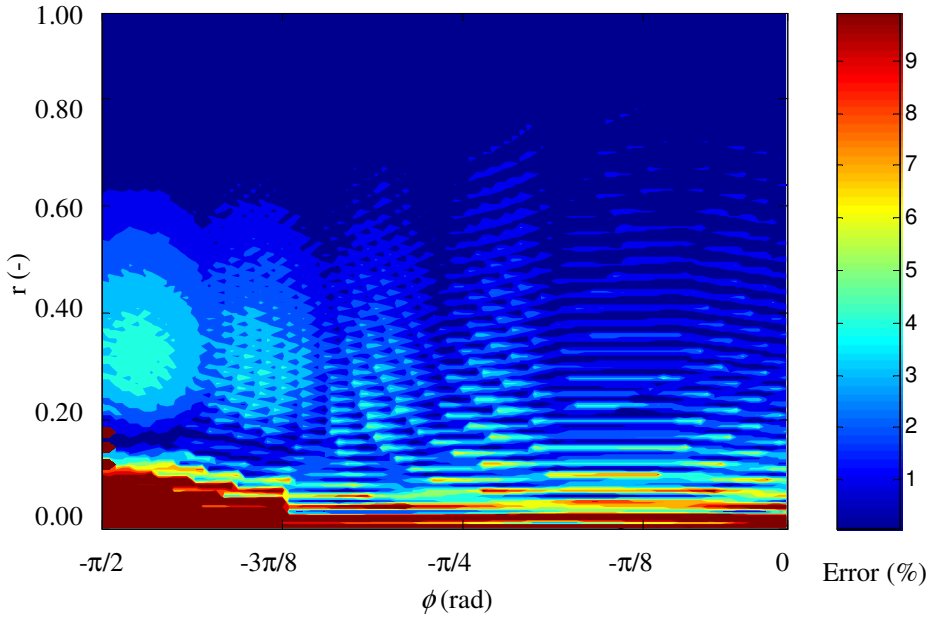

Figure A.2 – Error percentage for the prediction of r using Eq.s (4.17)-(4.19).

A.2 Frictional coefficient formulas

Bottom shear stress and turbulence in wave motion are crucial parameters for sediment transport. Like in the TRANSKEW laboratory experiment, often, natural beaches present turbulent boundary layers. However, turbulent boundary layer problems are an order of magnitude more difficult than laminar boundary layers, where the basic hydrodynamics of this flow remain unsolved and the results available are limited to semi-empirical formulas. The wave friction factor f_w is a dimensionless factor that links the bottom shear stress, to the free-stream velocity. From dimensional analysis, one can conclude that it depends on the Reynolds number and on the amplitude to roughness ratio A/k_s.

Attending to the different flow regimes and that the most common occurring in nature is the rough turbulent flow, several formulas rely only on the parameter A/k_s. Here, the roughnesses are so large that the important characteristic of the rough turbulent flow is that f_w is essentially independent of the Reynolds number, i.e.,

$$f_w = f_w\left(A/k_s\right). \tag{A.1}$$

Table A.1 synthesizes some wave friction coefficient formulas found in the literature that depend only on the relative roughness A/k_s. The predictive relationships were originated from previous theoretical and experimental results and some of them need to be solved iteratively for f_w. Figure A.3 summarizes the friction factors results as a function of the dimensionless parameter A/k_s. The results are presented for the range of values of TRANSKEW and demonstrate that there is considerable scatter in its estimates. Swart (1974) equation predicts the highest values of the selected equations. It is followed by Jonsson (1966), Madsen (1994) and Tanaka and Thu (1994) formulations which predict almost analogous values. The others formulae provide lower values, being the smallest results given by Kamphuis (1975). For the range of values presented and comparing with Swart's formulation, the magnitude of the estimates of the friction factor is smaller in the order of 58% to 84%.

Table A.1 – Wave friction factor formulas.

Authors	Friction coefficient expressions	Eq.
Jonsson (1966):	$\frac{1}{4\sqrt{f_w}} + log_{10}\left(\frac{1}{4\sqrt{f_w}}\right) = log_{10}\left(\frac{A}{k_s}\right) - 0.08$, $\frac{A}{k_s} > 1.57$	(A.2)
Swart (1974):	$f_w = exp\left[5.213\left(\frac{A}{k_s}\right)^{-0.194} - 5.977\right]$, $\frac{A}{k_s} > 1.57$ $f_{wi} = 0.3$, $\frac{A}{k_s} \le 1.57$	(A.3)
Kamphuis (1975):	$\frac{1}{4\sqrt{f_w}} + log_{10}\left(\frac{1}{4\sqrt{f_w}}\right) = \frac{4}{3} log_{10}\left(\frac{A}{k_s}\right) - 0.35$ With the explicit approximation for $\frac{A}{k_s} < 50$: $f_w = 0.4\left(\frac{A}{k_s}\right)^{-0.75}$	(A.4)
Nielsen (1992):	$f_w = exp\left[5.5\left(\frac{A}{k_s}\right)^{-0.2} - 6.3\right]$	(A.5)
Tanaka and Thu (1994):	$f_w = exp\left(5.743\left(\frac{A}{k_s}\right)^{-0.100} - 7.53\right)$	(A.6)
Madsen (1994):	$f_w = \begin{cases} exp\left(7.02\left(A/k_s\right)^{-0.078} - 8.82\right), & 0.2 < A/k_s < 10^2 \\ exp\left(5.61\left(A/k_s\right)^{-0.109} - 7.30\right), & 10^2 < A/k_s < 10^4 \\ exp\left(5.5\left(A/k_s\right)^{-0.120} - 7.02\right), & A/k_s < 10^6 \end{cases}$	(A.7)
Myrhaug et al. (2001):	$f_w = c\left(30\frac{A}{k_s}\right)^{-d}$, $\begin{cases} (c,d) = (1.39;0.52), 900 \le 30A/k_s \le 11000 \\ (c,d) = (0.112;0.25), 30A/k_s \ge 11000 \end{cases}$	(A.8)
Wang (2007):	$f_w = 2\kappa^2\left[\frac{1}{ln\left(A/k_s\right)}\right]^2$ where κ is the von Karman's constant taken as 0.407 .	(A.9)

The difference between the formulations is comprehensible in the way that even the existing measurements generally present some scatter. In addition, the estimated friction factors may differ from laboratory results depending on the nature of the roughness contribution, i.e., fixed grain roughness, mobile sediment grains or different bedform dimensions produced by waves. Consequently, those differences might lead to some deviations between the existing formulae, affecting significantly the magnitude of bottom shear stress parameterisations.

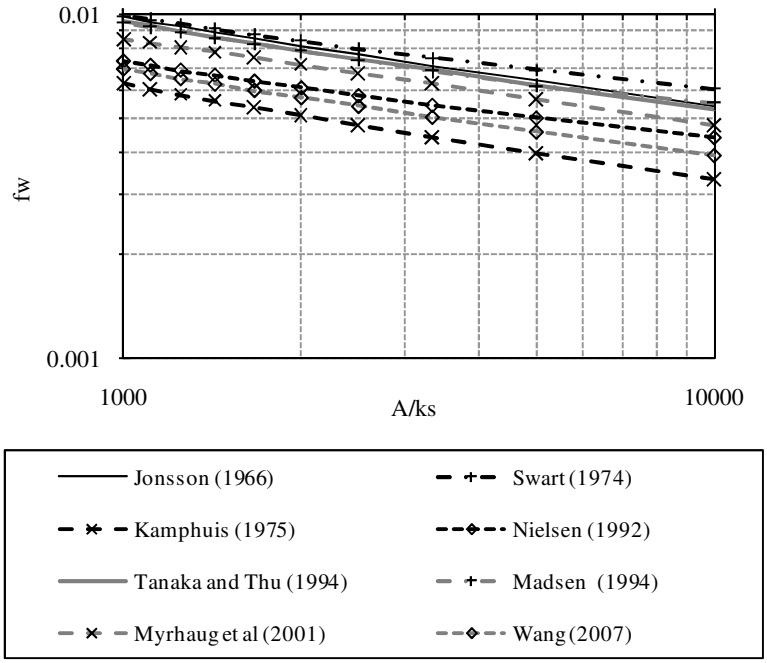

Figure A.3 – Evaluation of the wave friction factor with selected existing formulas (Jonsson, 1966; Swart, 1974; Kamphuis, 1975; Nielsen, 1992; Tanaka and Thu, 1994, Madsen, 1994; Myrhaug et al., 2001; and Wang, 2007).